THERMAL METROLOGY FOR WASTE HEAT SYSTEMS: THERMOELECTRICS TO PHASE CHANGE MATERIALS

A Dissertation

Submitted to the Faculty

of

Purdue University

by

Collier S. Miers

In Partial Fulfillment of the

Requirements for the Degree

of

Doctor of Philosophy

May 2019

Purdue University

West Lafayette, Indiana

THE PURDUE UNIVERSITY GRADUATE SCHOOL
STATEMENT OF DISSERTATION APPROVAL

Dr. Amy Marconnet, Chair

Department of Mechanical Engineering

Dr. John Howarter

Department of Materials Engineering

Department of Environmental and Ecological Engineering

Dr. Ali Shakouri

Director, Birck Nanotechnology Center

Department of Electrical and Computer Engineering

Dr. Ganesh Subbarayan

Department of Mechanical Engineering

Dr. Xianfan Xu

Department of Mechanical Engineering

Department of Electrical and Computer Engineering

Approved by:

Dr. Jay P. Gore

Head of the Departmental Graduate Program

To Catherine,

Thank you for all your love and support throughout this process.

I could not have done this without you.

ACKNOWLEDGMENTS

I would like to thank my wife, Catherine, who knows better than anyone what a demanding process this has been. I must thank my parents. Mom, all the late night projects and teaching me to keep going and push through things when they got hard paid off. Thank you for not losing it when you came home to yet another household appliance disassembled and a young boy with no clue how to put it back together yet. Dad, you taught me how to use tools, build things, and work around problems that arise in the process. Thanks for always taking the time to teach me about what you were doing and how to safely use tools to build things. It has saved my fingers more than once. John Carter, you are almost here as well. I am so proud of you and I am amazed by your brilliance even in our shared field. You will do amazing things and thank you for all the talks we have shared when I have called you with a problem. Elizabeth, you are always there when I need you to keep me grounded and put things in perspective. I appreciate it more than you know. Red, you have always been there for me and supported me in anything that I have done. You got me into cycling then helped me get a job as a bicycle mechanic. This lead directly into being a mechanical engineer, and I can't thank you enough for this. You taught me that showing up and working the hardest is the best way to get the job that you want, and this advice has never failed me.

Thank you Amy for believing in me and hiring me as your first student. You have been the best advisor I could have hoped for and I have been honored to help build the Marconnet Thermal & Energy Conversion (MTEC) Lab with you over the past six years. I am proud of what the lab has grown into during our time at Purdue and I look forward to what it will become as you continue to grow and improve it. I would also like to thank my committee for their support and guidance during my PhD.

Next, I want to thank my friends: Paxton, Ethan, Sean, and Evan. Y'all have all been there for me along this journey and I could not have made it through without each of you. Paxton, you specifically have seen the entire journey over the past 27 years and have been there at every step along the way to give me the support and encouragement I needed. It has made all the difference in the world to me for getting this far and I can't thank you enough for helping me through this.

I must also thank Brian Carroll, you were the first mentor I had in engineering, and because of your example and high standards for your own work, I chose to go to graduate school for heat transfer and pursue a career at Jet Propulsion Laboratory. You have taught me so much that I would have never learned in a class room, for which I am forever grateful.

Thank you Carlos Hidrovo, you gave me my first exposure to research and it was your initial guidance that started me down the path to graduate school. I learned so much from you while working in the Multiscale Thermal Fluids Laboratory (MTFL) and my life has been forever changed because of my time there.

Thank you Caroline Baker, you patiently helped me wade through all the "interesting" math that popped up in the last couple of years and also providing an outlet for Catherine and I to relax with you and Chris.

Thank you to all my labmates: Aalok Gaitonde, Albraa Alsaati, Yuqiang Zeng, David Cuadrado, Rajath Kantharaj, and Aaditya Candadai. We have made it through this together, and I am thankful for all your friendships.

Finally, I must thank all of the people that were in the trenches with me and put up with years of weird technical questions or that showed up at odd hours to help me troubleshoot a problem. Bert Gramelspacher, you have tirelessly answered all of my obscure electronics questions for over half a decade, and you have yet to run at the site of me. For that, I truly commend you! Tami Armstrong, you have always been willing to help me out in whatever way you can, from helping me find an instrument or component to getting me setup with whatever obscure equipment or tool I came to you looking for. On top of all of that, you make the best homemade marshmallows

I have ever had. Mike Bayless, you have gone above and beyond in helping me out with my systems at the Birck Nanotechnology Center, and I appreciate your practical contributions when helping me troubleshoot a problem. Additionally, I have learned so much from Dan Hosler, Kenny Schwartz, and Dave Lubelski over the years and I cannot thank you enough for all that you have taught me.

Ms. Sandy, you have helped me through many hard times and always encouraged me to keep pushing forward. Thank you for all that you do for us.

Funding and Support:

I would like to thank Professor Ali Shakouri and the Birck Nanotechnology Center for providing funding for the Z-Meter hardware.

Financial support for the portions of this dissertation relating to phase change materials provided by members of the Cooling Technologies Research Center, a graduated National Science Foundation Industry/University Cooperative Research Center at Purdue University, is gratefully acknowledged.

PREFACE

"More and more, we take for granted that work must be destitute of pleasure. More and more, we assume that if we want to be pleased we must wait until evening, or the weekend, or vacation, or retirement. ... In order to have leisure and pleasure, we have mechanized and automated and computerized our work. But what does this do but divide us ever more from our work and our products and, in the process, from one another and the world? ... If I could pick any rule of industrial economics to receive a thorough re-examination by our people, it would be the one that says that all hard physical work is 'drudgery' and not worth doing."

- Wendell Berry, "What Are People For?"

TABLE OF CONTENTS

Page

Page

LIST OF TABLES

LIST OF FIGURES

Figure Page

Figure Page

Figure Page

Figure Page

ABBREVIATIONS

ASTM	American Society for Testing and Materials
BNC	Birck Nanotechnology Center
BTU	British Thermal Unit
CLS	Ceramic Loading Shroud
CJC	Cold Junction Compensation
CTE	Coefficient of Thermal Expansion
DMM	Digital Multimeter
DOE	Design of Experiments
DSC	Differential Scanning Calorimetry
FEA	Finite Element Analysis
FET	Field Effect Transistor
F/T	Feedthrough
GUI	Graphical User Interface
HRS	Heat Rejection System
I^2C	Inter-Integrated Circuit
LLNL	Lawrence Livermore National Lab
MTEC	Marconnet Thermal and Energy Conversion (Lab)
NIST	National Institute of Standard and Technology
OFHC	Oxygen-Free High Conductivity
PCM	Phase Change Material
PtRTD	Platinum Resistance Temperature Detector
PV	Photovoltaic
PWM	Pulse Width Modulation
RTD	Resistance Temperature Detector
TAD	Tangent Alignment Device

TC	Thermocouple
TCR	Temperature Coefficient of Resistance
TDTR	Time Domain Thermoreflectance
TE	Thermoelectric
TEG	Thermoelectric Generator
TIM	Thermal Interface Material
TIP	Thermal Isolation Platform
TMEP	Thermal Management Evaluation Platform
TPRL	Thermophysical Properties Research Laboratory
TTV	Thermal Test Vehicle
UPS	Uninterruptible Power Supply
UQ	Uncertainty Quantification

Gases

Ar	Argon
He	Helium
N_2	Nitrogen

Materials

AlN	Aluminum Nitride
Al_2O_3	Aluminum Oxide
Bi_2Te_3	Bismuth Telluride
PbSe	Lead Selenide
PbTe	Lead Telluride
PEEK	Polyether Ether Ketone
SiGe	Silicon Germanium
ThO_2	Thorium Dioxide
ZrO_2	Zirconium Dioxide

ABSTRACT

Miers, Collier S. Ph.D., Purdue University, May 2019. Thermal Metrology for Waste Heat Systems: Thermoelectrics to Phase Change Materials. Major Professor: Amy M. Marconnet, School of Mechanical Engineering.

Accurate measurements are essential to further the advancement of a technical field. This sentiment is particularly true for the thermal sciences, where due to the indirect nature of temperature, the most critical physical quantity that we discuss is often grossly mismeasured. This leads to substantial spread in reported experimental data, which impedes progress. Here I present two systems for which a gap in current measurement systems or experimental practices exists. First, I detail the design and fabrication of a high-temperature Z-Meter which simultaneously measures pertinent thermoelectric properties. Then I present work done to improve the design of phase change material passive thermal management solutions and a new measurement platform allowing the direct comparison of performance across a wide range of thermal management designs.

In the first part of my dissertation, I design a Z-Meter system to evaluate the performance of thermoelectric materials under large temperature differences. Few systems exist for simultaneous measurement of thermal, electrical, and thermoelectric properties at high-temperatures ($>$ 400℃), which is crucial for high-temperature waste heat recovery applications. The Z-Meter simultaneously measures the three thermoelectric properties from which the figure of merit, ZT, is calculated. Traditionally, this technique has been employed utilizing a very small temperature difference across the sample (ΔT = 1-2℃) and test temperatures between 20-400℃; however, thermoelectric materials are typically subjected to large temperature gradients for favorable energy conversion. Additionally, high operating temperatures ($>$ 400℃) provide access to higher grade waste heat than is available at low temperatures.

It is critical that materials be characterized under conditions close to the targeted operating conditions, because the relevant properties possess strong temperature dependencies.

In this work, I focus on extending the measurement capabilities for a Z-Meter to higher temperatures ($\sim$ 1000℃). In order to accomplish this, I develop detailed 2D axisymmetric multi-physics finite element analysis (FEA) simulations of the system components and measurement process to extract simulation values at the probe locations in the system. This simulated "experimental" data is passed as the input for the uncertainty quantification (UQ) model to statistically compare design options, evaluate the impact of component modifications on the overall system performance, and to provide the quantitative data required to deselect options from the design space and determine the final Z-Meter design which minimizes the measurement error for ZT. The UQ model for the meter bars includes effects from radiative losses, contact resistances, thermoelectric effects, and interaction of electrical measurement signals in the bar. The detailed UQ model combined with the fully-coupled multi-physics simulations results provide a powerful platform to investigate the sensitivity of ZT to specific design variables (*e.g.*, component positioning, material selection, or sensor type) which is invaluable for determining the correct system design.

The system, as designed, is capable of sample hot side temperatures of 1000℃ with temperature gradients on the order of 500℃. The elevated temperature capability is necessary to fill a gap in characterization equipment for high-temperature thermoelectric applications. In order to maximize the accuracy and repeatability of high-temperature measurements, I instrumented the meter bars with fine gauge type-S thermocouples. The measurement system is capable of operating in high-vacuum to suppress convection losses or it can be backfilled with an inert gas permitting atmospheric control for testing under specific environments. This is the first Z-Meter to permit the adjustment of interfacial loading during the test without disturbing the test environment (temperature or pressure). This allows the user to maintain a more consistent contact pressure across a wide range of temperatures and provides the pos-

sibility for load dependent investigations of thermoelectric performance. Additionally, a triad of load cells provide *in situ* load monitoring and ensures uniform loading for the sample interface. The combination of simultaneous property measurement, high-temperature operation with large temperature gradients, user controlled mechanical loading, and a flexible operating environment provides opportunities to investigate high-temperature thermoelectric property dependencies and opens the doors to a new understanding of thermoelectrics for high-temperature waste heat recovery.

In the second part of this dissertation, I design and measure the performance of phase change material (PCM) composite heat sinks for passive thermal management of mobile devices. PCMs are effective at storing thermal energy and are attractive for use in electronics to smooth peak temperatures during periods of high demand; however, the use of PCMs has been somewhat limited due to the poor thermal properties of the materials. Here, I propose a design for a tunable composite PCM heat sink for passive thermal management in electronic systems and develop an improved test platform to directly compare performance between different designs and PCMs. The composite design leverages high conductivity pathways, which are machined into aluminum heat sinks, back-filled with PCM, and sealed for testing. Two package sizes (25 and 50 mm) are considered, with several internal fin structures (no fins, isogrid, and isokite). All designs are tested using the new thermal management evaluation platform (TMEP) developed to permit testing with realistic power profiles, increase user control of power maps (spatial and temporal), control interfacial loading, and allow *in situ* temperature measurement. The composite PCM heat sinks are benchmarked against solid aluminum packages of the same size to gauge the extent of the performance enhancement derived from using composite PCM structures. This study focuses on three commercially-available PCMs: PureTemp 42, PureTemp 68, and PlusICE S70. Performance is evaluated based on (1) the time it takes the test heater chip below each composite PCM package to reach the cut-off temperature of 95℃ and (2) the period of a full melt-regeneration cycle. A range of heat fluxes are considered in this study spanning 6.8 - 14.5 W/cm^2. The isokite design with PlusICE S70 extends

the time to reach 95℃ by 36.2% when compared to the solid package, while weighing 17.3% less, making it advantageous for mass-limited platforms and mobile devices.

This dissertation work develops unique measurement platforms. Careful attention to measurement precision and uncertainty quantification while designing these systems ensures the utmost system quality, highest measurement performance, and best functionality for the user. It is the first Z-Meter to have fully adjustable interfacial loading available during the experiment and pushes the temperature range and sample temperature gradient beyond existing systems enabling researchers to characterize materials under realistic operating conditions. In parallel, I developed a turn-key thermal management evaluation platform for performance testing of enhanced composite PCM heat sinks. The TMEP is a fully mature, user-ready system now available for testing thermal management solutions. This system provides full user control of a thermal test vehicle instrumented to allow individual control within an array of heaters for realistic testing patterns with an easy to use graphical user interface. Further, I developed a passive thermal management device to enhance performance and efficiency of passive PCM cooling solutions in mobile devices. The improvement in high-power operation time combined with the reduced weight compared to systems without latent heat storage makes these composite heat sinks advantageous for mobile device thermal management.

In summary, the core contributions of this dissertation include:
(1) A high temperature Z-Meter allowing the simultaneous measurement of the properties required to define the thermoelectric figure of merit, and
(2) Design and testing of an enhanced composite phase change material heat exchanger for passive thermal management of mobile devices. A new thermal management evaluation platform is developed and presented to facilitate accurate performance characterization for these designs.

1. INTRODUCTION

1.1 Motivation for Improved Thermal Metrology

The need for more efficient use of energy around the world is constantly driving advances in materials and processes, but how do we gauge the progress of these improvements? With the development of better materials comes the necessity for similarly advanced measurement techniques to support continued improvement. Thermal metrology is inherently challenging owing to the indirect nature of temperature measurement and the extensive background knowledge necessary to accurately conduct experiments. As such, many modern experiments and characterization methods used throughout the field suffer from very large, typically unacknowledged, uncertainty in temperature measurements. In this work, I address these common issues and provide some improvements by investigating two cases where thermal measurement techniques need further refinement: thermoelectrics (TEs) and phase change materials (PCMs).

1.2 Thermoelectrics

1.2.1 Motivation for Improved Thermoelectric Performance

Lawrence Livermore National Lab (LLNL) periodically quantifies the breakdown of energy production, usage, and waste in the United States. In particular, the LLNL 2018 study of energy mapping, as shown in Figure 1.1, reported that an estimated 101.2 Quads[1] of energy were used in the United States in 2018, and that 68.5 Quads of that energy, or approximately 68%, was lost as rejected energy, referred to as waste heat [1]. This quantity of waste heat is enormous - converting to Watt-hours that is 20.08 PW·h (10^{15} W·h). For comparison, the U.S. Energy Information Administration

[1]A Quad stands for one quadrillion British Thermal Units (BTUs) of energy.

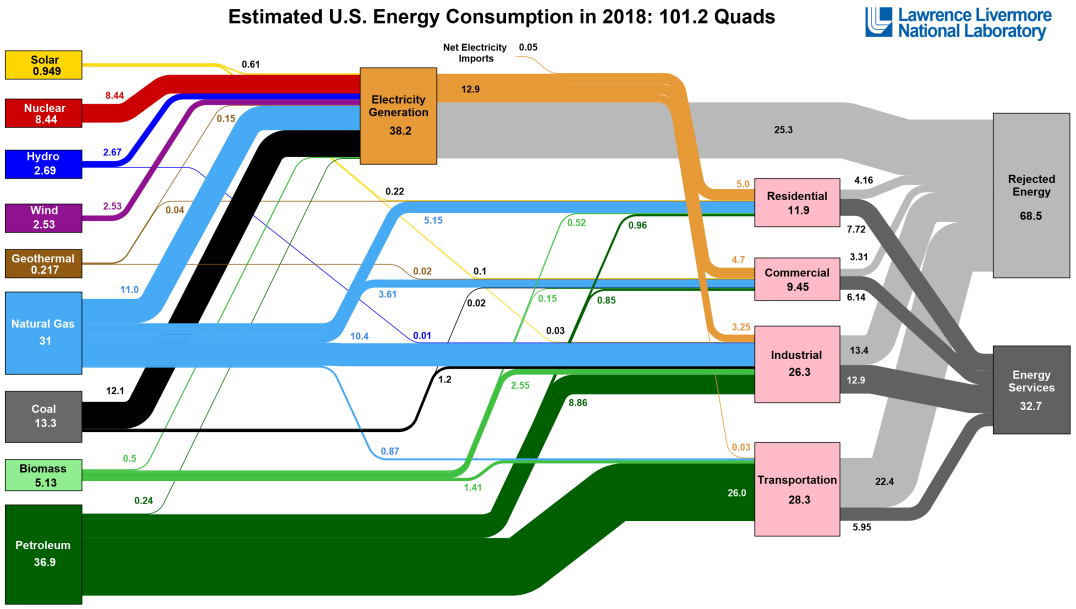

Source: LLNL March, 2019. Data is based on DOE/EIA MER (2018). If this information or a reproduction of it is used, credit must be given to the Lawrence Livermore National Laboratory and the Department of Energy, under whose auspices the work was performed. Distributed electricity represents only retail electricity sales and does not include self-generation. EIA reports consumption of renewable resources (i.e., hydro, wind, geothermal and solar) for electricity in BTU-equivalent values by assuming a typical fossil fuel plant heat rate. The efficiency of electricity production is calculated as the total retail electricity delivered divided by the primary energy input into electricity generation. End use efficiency is estimated as 65% for the residential sector, 65% for the commercial sector, 21% for the transportation sector and 49% for the industrial sector, which was updated in 2017 to reflect DOE's analysis of manufacturing. Totals may not equal sum of components due to independent rounding. LLNL-MI-410527

Figure 1.1. A Sankey diagram created by researchers at Lawrence Livermore National Laboratory showing the estimated energy usage, breakdown, and flow for the United States in 2018. Reproduced with permission from Lawrence Livermore National Laboratory.

reported the average annual electricity consumption for a U.S. residential customer in 2017 was approximately 12,000 kW·h [2]. Thus, the amount of energy lost as waste heat from 2018 alone could power an average household for more than 1.6 billion (10^9) years. This scale of wasted energy motivates many researchers around the world to make strides to develop advanced methods for utilizing waste heat. There are many technologies currently in use that work well to reclaim energy from waste heat sources, thus improving process efficiency, but these systems tend to be large, immobile, and are typically expensive to service. An alternative to these complex pieces of machinery comes in the form of something much smaller, highly mobile, and devoid of moving parts: a thermoelectric generator (TEG). TEGs are not a new technology and much research has focused around them for over fifty years in an

attempt to improve performance, but there still exist significant gaps in this field to be addressed.

1.2.2 Summary of Modern Improvement Efforts

The major downside to thermoelectrics is that they are relatively expensive compared to the energy produced with reasonable temperature gradients. In other words, TEGs have a relatively high $/w price when compared to competing alternative technologies such as photovoltaic (PV) cells [3]. Additionally, many of the materials that perform decently well in TEGs tend to be comprised of rare or toxic materials, which precludes wide-spread implementation. These devices still see service in situations that require long-term operation and reliability without maintenance, such as remote sensing or space missions. Even for the best thermoelectric materials, it is necessary to optimize module design and geometry to achieve the highest output. An alternative route is to optimize scalable processes and manufacturing capabilities to drive the cost of moderately efficient TEGs down, making the $/w for TEGs more competitive with PV cells and other alternative energy technologies.

1.2.3 Improved Metrology for Thermoelectrics

The advances in modification and tuning of material properties for improved thermoelectric performance are very promising, but when it comes to the coupled nature of thermoelectric materials, researchers have encountered some measurement challenges. The thermoelectric figure of merit,

$$ZT = \frac{S^2\sigma}{\kappa} \cdot \overline{T}, \tag{1.1}$$

is comprised of three separate properties: the Seebeck coefficient, S, electrical conductivity, σ, thermal conductivity, κ, and the mean temperature of the thermoelectric material, $\overline{T}$ [4]. Due to the standard measurement processes for these materials, researchers often use at least three separate instruments, and separate samples, to

perform the property characterizations required to evaluate the figure of merit. This can introduce considerable errors resulting from different sample compositions, fabricated sample geometry, contact conditions, and disparities in measurement conditions, environment, and losses. Thermoelectric materials cannot be assumed to be homogeneous throughout a lot or sample batch, thus even studies on samples taken from the same lot cannot be directly compared without addressing the error resulting from sample-to-sample variations. Small differences in fabricated geometry can be accurately measured and addresses as the geometry of the sample is typically required to perform property characterization. However, researchers should avoid aggregating data or directly comparing samples with disparate form factors (*e.g.*, use of bulk property measurement data to characterize a thin film or vice versa). If separate measurement methods are used to determine an aggregate property such as ZT, the sample must be measured in the same orientation for all properties. This means that it is generally not appropriate to mix different property values measured for the in-plane and cross-plane orientations to determine ZT. Even with all of these points addressed, a direct comparison between results from different techniques and/or systems requires the exact same measurement conditions, test environment, and losses. The compounded errors introduced from multiple measurement techniques and sample variability make the process of accurate thermoelectric property characterization extremely tedious. Careful consideration must be paid to a large number of test parameters and variable factors across several systems and samples to properly match data to form a composite ZT. Failure to adequately do this leads to erroneous values of ZT reported in literature and considerably impedes the feedback process for tuning new materials. An alternative to this separate property measurement is simultaneous property measurement on a single sample. This approach is attractive as it effectively removes errors stemming from sample variability and different operating conditions and measurement temperatures to form a temperature dependent property characterization for the constituents of ZT. The motivation behind the first part of this

dissertation is to present an overview of the design concerns and fabrication for such a simultaneous measurement system.

1.3 Phase Change Materials

Thermal management is critical for reliable operation of electronic devices. As the trend predicted by Moore's law continues, higher processor densities in electronics creates serious problems for efficiently removing heat [5]. This problem is compounded for portable electronics, as these devices are not only shrinking in size, but also have limited available power and options for rejecting the heat from the device to keep the junction temperature below a critical level of approximately 125℃ [6,7]. Traditionally active cooling schemes are utilized to remove heat from high-density electronics, but these techniques are not feasible for use in portable electronics due to size/weight, increased power requirements, and user experience limitations (based on comfort and safety). Therefore, to address this problem, passive thermal management schemes must be employed. Generally this involves a network of heat spreaders or heat pipes integrated into the device that help to move heat away from the processor locations diffusing the high temperatures and rejecting heat to the ambient through the screen or body of the device [8, 9]. Additionally, most portable electronics do not have sustained high computational loads, but rather short surges of computational demand. These brief surges result in high-temperature spikes inside the device while the heat is diffused and rejected. These periodic temperature spikes and large temperature swing thermal cycles are bad for component reliability, leading to premature failure. However, there exists a thermal management scheme well tailored for periodic loading of this nature: phase change material (PCM).

PCMs are well suited for use in portable electronics due to their passive operation, and combination of sensible heat storage with latent heat storage resulting from a phase transition. This combination yields a higher thermal storage capacity than possible with sensible heat storage devices of comparable volume. Additionally, during

this phase transition, the temperature of the PCM remains relatively constant, which is a desirable condition for extending the time for a system to reach a critical temperature. There remains a barrier to wide implementation of PCM in electronics: the poor thermal properties of many common PCMs [10]. Researchers have investigated approaches to quantify the effectiveness of PCM integration into electronics cooling both numerically and experimentally. A broad range of experimental approaches are considered in literature, many using different metrics by which to judge the operational performance for the PCM thermal management performance. This makes comparison of data for different approaches and materials extremely difficult. This combined with no standard method of testing these materials results in fragmented results that are unlikely to be stitched together to find a practical solution.

Past studies on PCMs built an understanding of specific processes involved in the implementation of composite PCM thermal management packages; however, it is very difficult to compare data between experiments and models, both of which typically apply to specific use cases. In order to better study performance of packaged PCM heat sinks, I propose a general test method allowing direct performance comparison across different types of PCMs and packages with realistic, quantifiable heating and *in situ* temperature measurements. The PCM portion of this dissertation first describes the methodology for PCM selection, then the design of the composite heat sinks, the development of a highly versatile test platform for performance testing, and finally presents results from testing commercial PCMs in the designed packages.

1.4 Scope of Work

Two main contributions of this thesis include:

(1) Improved metrology techniques that usher in new possibilities for thermal and thermoelectric characterization through truly unique measurement platforms that will serve to attract new collaborations, and

(2) Development of a passive thermal management device to enhance performance

and efficiency of cooling solutions in mobile devices.

Improved metrology techniques: In terms of the first aspect of the scope of work, this work focused on two systems:

- The completion of the Z-Meter fills a measurement gap in the field for **simultaneous property characterization of high-temperature thermoelectric materials**. As designed, the Z-Meter can operate with sample hot side temperatures of $\sim$ 1000 ℃, under large temperature gradients $\Delta T \sim$ 500℃, capable of a variety of testing atmospheres (air, vacuum, N_2, Ar, and He) and houses a load cell triad to provide *in situ* monitoring of the contact force to the sample. A unique feature to this Z-Meter is the ability to adjust the contact loading from outside the chamber, without breaking vacuum or purging the test environment. This means that pressure accurate pressure dependent contact studies are now possible at high temperatures. The system design was developed by constructing multi-physics simulations of the system components and measurement process, then using this model output as the input to an uncertainty propagation model. This tool enables powerful characterization capable of investigating unique problems and providing new directions for existing research with high temperature thermoelectrics.

  While the primary design focus for the Z-Meter is to simultaneously measure thermoelectric properties, this versatile tool is capable of so much more. The system is ASTM D5470 compliant making it ideal for high-temperature studies on both the thermal (and electrical) properties for thermal interface materials (TIMs). In addition to TIMs materials such as ceramic or glass insulator and wafers can be measured in the system. Finally, the system can be used for the characterization of an actual thermoelectric generator if it is small enough to fit well on the bar interface, otherwise, secondary bars could be made to expand the testing possibilities for the Z-Meter system.

- The developed **turn-key thermal management evaluation platform (TMEP)** for investigating active or passive thermal management technologies and which provides full user control over spatial and temporal power profiles, controllable interfacial loading, and in situ temperature monitoring within the test die. This system is built around a thermal test vehicle (TTV) and allows realistic power profiles and temperature maps to be applied simulating actual device conditions. This test system is fully automated and controlled through a custom, easy to use graphical user interface (GUI).

  Much like the Z-Meter, the TTV platform is very versatile and provides many options for value-added measurements by using this existing system. Beyond PCMs, it could be used to benchmark TIMs. Another valuable side-purpose of this system can be to use it for head-to-head comparison testing of passive versus active cooling technologies on the same TTV under the same conditions. Between the Z-Meter and the TTV, we can cover a very large range of TIMs research, from fundamental property measurements to simulated performance testing on the TTV or direct performance evaluation in head-to-head studies with other technologies.

Passive Thermal Management Solution: In terms of the second aspect of the scope of work, I developed a novel design for an enhanced composite PCM heat sink, which allows easy tuning of the structure during the design phase to maximize PCM heat sink performance for a large range of operating conditions. These heat sinks are the focus of a comparison study which would validate the performance of TTV platform. The home-built aluminum packages are combined with three off-the-shelf PCMs to test the design and the TTV system: PureTemp 42, PureTemp 68, and PlusICE S70. Two package sizes (25 and 50 mm) are considered and I present two enhanced package designs (isokite and isogrid) as well as two controls (no fins and solid package - no PCM). The main function of the control samples is to provide an

accurate and repeatable baseline to compare against. The tests were conducted at three heat fluxes: 7, 11, 14 $^{W}/_{cm^2}$, typical for current mobile electronic devices.

One metric to evaluate the composite PCM heat sinks it to compare the time that it takes for the maximum temperature on the test die to reach 95℃, which served as a cut-off temperature for these tests. The isokite design with PlusICE S70 extends the time to reach 95℃ by 36.2% when compared to the solid package, while weighing 17.3% less, making it advantageous for both mass-limited platforms (e.g. spacecraft or aerospace vehicles) and mobile devices. Further cycling studies and measurement of PCM sub-cooling during regeneration were also successful using the versatile set of tools I incorporated into the TMEP. The second part of my dissertation details the novel PCM heatsink designs, the operating user overview and details for using the TMEP, and presents the results of my study on the PCM heat sinks.

1.5 Overview

The remainder of this dissertation is organized into two parts: (I) thermoelectrics and (II) phase change materials.

The first part, containing chapters 2 - 6, focuses on simultaneous measurement of thermoelectric properties through the design and fabrication of a high-temperature Z-Meter. Chapter 2 provides a review of characterization techniques for thermoelectric properties, and an overview of the operating principles behind the Z-Meter measurement. In Chapter 3, I present the design and development of the Z-Meter in comprehensive detail. Chapter 4 lays out the data analysis for the Z-Meter measurement and presents a detailed uncertainty quantification model utilized throughout the instrument development process to motivate design choices. Chapter 5 presents the initial results for the Z-Meter system. Chapter 6 is a summary of the thermoelectric work for my dissertation. It also contains my proposed future directions for the Z-Meter and I suggest improvements for further enhancement of the system.

The second part, containing chapters 7 - 11, presents my work on performance evaluation of PCMs for use in passive thermal management of electronics. Chapter 7 provides background and motivates the need for improved performance evaluation of PCM thermal management in electronics. In Chapter 8, I present the tunable package design for enhanced composite PCM heat exchangers. Next, in Chapter 9, I describe the development of our thermal test vehicle (TTV) characterization platform to improve testing performance and versatility by permitting a single test system to be used for a wide range of operating conditions. In chapter 10, I present the data obtained for the performance of the PCM packages using the TTV characterization platform. In addition to the data on the performance of the composite PCM heat sinks for extension of operation time before reaching the thermal cut-off temperature, I also investigate the regeneration of the packages and measure the extent of sub-cooling experienced by the PCMs. Finally, chapter 11 documents my recommendations for future avenues to explore with the development of the composite PCM heat sinks.

PART I: SIMULTANEOUS THERMOELECTRIC PROPERTY MEASUREMENT

2. THERMOELECTRIC CHARACTERIZATION

This chapter first details some of the widely used techniques to measure the individual material properties that comprise the figure of merit, ZT. Then we introduce direct and simultaneous measurements of ZT focusing on the Z-Meter approach that will be further developed as part of this thesis.

2.1 Separate Property Characterization

2.1.1 Seebeck Coefficient

The measurement of the Seebeck coefficient is typically done one of two ways: the integral method or the differential method. The integral method requires the sample to be in wire form and is not practical for most thermoelectric materials, outside those used for thermocouples; therefore, it is not discussed in detail here, but can be found in literature [11]. The differential method is better suited for determining the Seebeck coefficient of bulk materials. In this method, a bulk sample is held under a known temperature gradient and the open circuit voltage is measured directly from probes on the surface of the sample. The ratio of the open circuit voltage to the temperature difference is the Seebeck coefficient,

$$S = \frac{V_{OC}}{\Delta T}. \tag{2.1}$$

The voltage and temperature difference must be determined at the exact same locations for the accurate determination of the Seebeck coefficient. It is imperative that consistent treatment of the definition of temperature difference compared to the direction of voltage measurement is observed, because this can easily result in an incorrect sign for the Seebeck coefficient. Additionally, note that the measured (relative) Seebeck coefficient will be different from the absolute Seebeck coefficient. This

is because the value measured is due to both the sample and any connecting leads which will also be under temperature gradients. The absolute Seebeck coefficient can be found by subtracting the system lead contribution [11, 12].

2.1.2 Electrical Conductivity

Electrical conductivity can be difficult to accurately measure due to the relatively high value of conductivity for good thermoelectric materials combined with the small sample thicknesses. Electrical conductivity or resistivity is typically measured using a four-wire Kelvin probe setup to eliminate electrical contributions from the measurement leads. Two probes supply current to be passed through the sample, while two more probes measure the voltage drop across the sample. When this technique is done for an isothermal sample, making sure to keep the sense current low to minimize any impacts from Joule heating, the resistance of the sample can be measured directly; however, this requires the sample to be brought into an isothermal state, while the Seebeck coefficient and thermal conductivity measurements both require thermal gradients. A further complication of this measurement is the presence of Peltier heating, $q = {}^{I}/\pi$ which heats or cools at the contact junctions between dissimilar metals when a current is passed through them.

Since it is not practical to measure the electrical conductivity under isothermal conditions, it is then natural to consider measurement under the same temperature gradient required by the other two property measurements. Thermoelectric materials have a substantial Seebeck coefficient, so the total voltage drop measured across a thermoelectric sample under a temperature gradient will be the sum of both the ohmic and Seebeck voltages:

$$V_{tot} = V_{ohm} + S \cdot \Delta T, \tag{2.2}$$

where V_{tot} is the total measured voltage and V_{ohm} is the ohmic voltage drop across the sample. It is not uncommon for the ohmic voltage contribution to be of the same order as the Seebeck voltage in thermoelectrics [12]. These effects can be separated

by fast measurements and current reversal. If the measurement is performed in approximately 1-2 seconds, then the time for Peltier heating to develop is minimized. Additionally, if the current direction is switched (with a fixed temperature gradient), the contribution of the Seebeck voltage can essentially be eliminated to yield a more accurate measurement of the ohmic voltage [13, 14]:

$$V_{Ohm} = \frac{[V_{I^+} + S\Delta T] - [V_{I^-} + S\Delta T]}{2}. \tag{2.3}$$

A precision resistor (0.1%) in series with the sample is often used to accurately measure the sense current used.

2.1.3 Thermal Conductivity

Thermal conductivity is generally the most challenging property to characterize accurately of the three properties that make up ZT. There are many ways of measuring thermal conductivity, and three of the most commonly used methods for measuring thermal conductivity of thermoelectric materials are briefly presented here.

The 3ω Method

The 3ω method is an effective to measure thermal conductivity. It is very accurate and minimizes issues of contact resistance through the use of periodic heating at the sample surface. In this method, a current at frequency ω is supplied to a heater line that is deposited and patterned on the surface of the material. Joule heating and, thus, the temperature variation of the heater line occur at twice the heating frequency, 2ω. The heater line also functions as a temperature sensor since the metal is typically chosen such that it has a strong temperature coefficient of resistance (TCR), *e.g.*, platinum or palladium. The resistance change of this metal line with temperature occurs at frequency 2ω matching that of the temperature oscillations. The resulting measured voltage across the heater line (*i.e.*, the supplied current oscillating at 1ω multiplied by the resistance oscillating at 2ω) includes both 1ω and 3ω harmonic

components. The third harmonic voltage is directly related to the amplitude of the temperature oscillations of the heater on the sample surface. The amplitudes of the temperature oscillations depend on the properties of the underlying material and the contact resistance. Sweeping through a range of frequencies enables extraction of thermal conductivity. This technique is discussed in great detail in my Master's thesis [15], and I refer the reader to it for additional information on this technique [16–24].

Laser Flash

The laser flash method measures the thermal diffusivity, α, and specific heat, C_P of the sample. The relationship between thermal conductivity and thermal diffusivity is, $\alpha = \kappa/\rho C_P$, where ρ is the density. This measurement is performed by irradiating the face of a sample with a sub-millisecond laser pulse, while observing the opposite side of the sample with an infrared photodetector that measures the temperature rise. The thermal diffusivity is determined from the evolution of the backside temperature with time. The specific relationship between the temperature evolution and diffusivity depends on the system and how many non-ideal measurement parameters are taken into account. The original proposed method assumes and isotropic sample with adiabatic boundary conditions [25].

The specific heat can either be measured simultaneously during the laser flash measurement by knowing the absolute temperature rise of the sample based on the amount of heat input. However, uncertainty in the absorptivity of the sample can lead to significant uncertainty in heat capacity with this method. Thus, it is common for the sample to subsequently be measured using a differential scanning calorimeter (DSC) to determine the heat capacity of the material at all necessary measurement temperatures separately from the laser flash measurement. In a DSC measurement, a known standard material, the sample, and an empty DSC pan are subjected to the same heat fluxes and the differential power required to heat the known standard

material, sample, and empty pan at the same rate are recorded. The results for the empty pan are used to correct for the impact of the materials being housed in measurement pans for the system. Then based upon masses of the standard and sample, and the known specific heat of the standard material, the specific heat for the sample is computed.

Reference Bar Method

The reference bar method compares the thermal gradients in an sample with unknown properties to the thermal gradient in reference bars of known thermal conductivity. This method is widely used for the measurement of thermal interface materials and other solids with relatively low thermal conductivities.

Specifically, the sample is sandwiched between two bars of the reference material and 1D conduction is assumed between two bar faces . Typically, the reference bars are metallic and instrumented with several temperature sensors along the axis. These measurement points provide known temperatures at known distance increments along the bar. Paring this information with the known thermal conductivity of the reference bar, the heat flow through the bar and thus through the sample can be determined using Fourier's law:

$$q = -\kappa A_C \frac{\partial T}{\partial z}. \tag{2.4}$$

Both the top and bottom bars holding the sample are used as reference bars for monitoring heat flow through the sample, as shown in Figure 2.1. Specifically, if the heat transfer rates in the top and bottom bar match, this must be the same heat transferred through the sample. If the heat transfer rates in the top and bottom bars do not match, this indicates a departure from ideal operation, and a higher order model must be employed to account for losses along the bars and from the sample.

The temperature profile is extrapolated in each reference bar to the sample-reference interface to estimate the temperature drop across the sample. Knowing

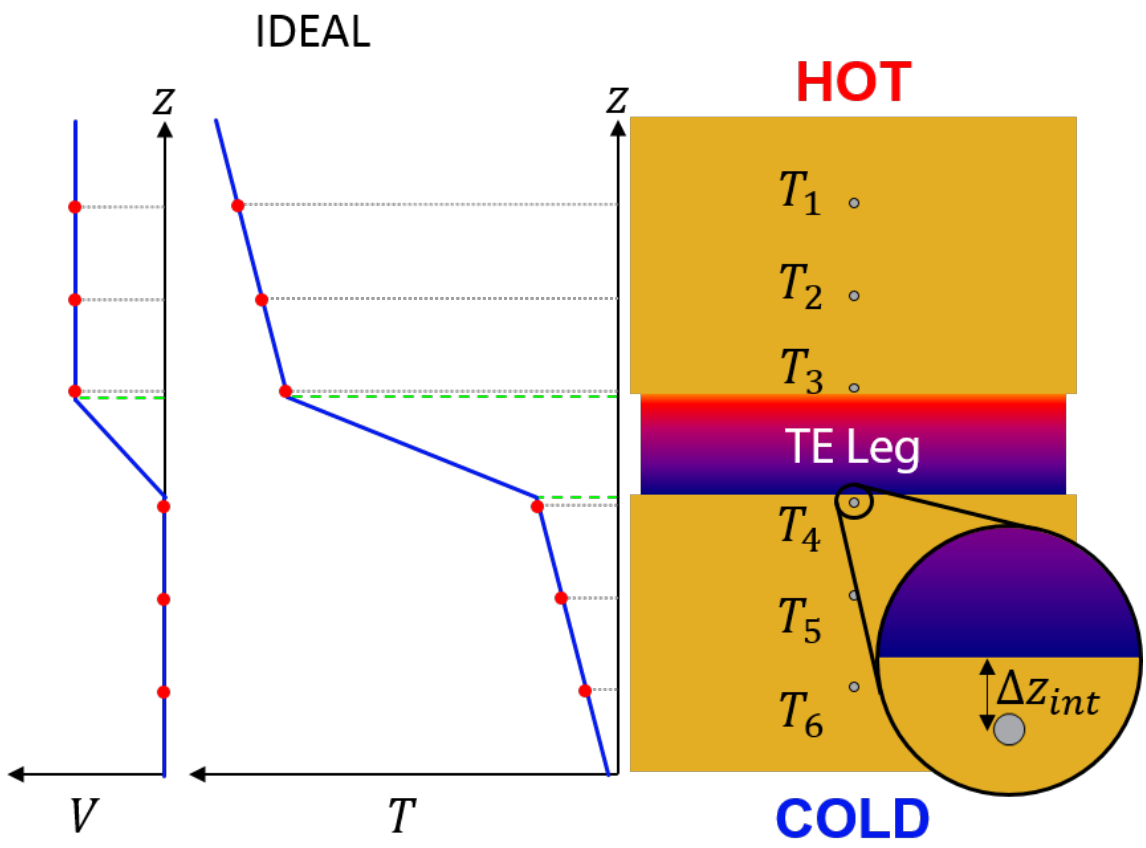

Figure 2.1. Idealized schematic of the reference bar method the showing temperature profile (without losses) and measurement locations. Note that this example system includes probes for both voltage and temperature to enable measuement of thermal and electric properties.

the heat flow through the sample and the temperature drop across the sample allows the thermal conductivity of the sample to be determined.

Note that extremely smooth and flat interfaces are required to minimize contact resistance at the sample. The ASTM D5470-17 standard calls for the surfaces to be smooth within 0.4 microns and parallel to within 5 microns and specifies a contact pressure between 0.69 MPa (100 psi) and 3.4 MPa (500 psi) [26].

2.2 Need for Simultaneous Measurements of TEs

Traditionally, the parameters for the figure of merit, ZT, have been measured individually, then combined to form a composite ZT, but this often involves conducting at least three separate experiments on at least three separate samples while trying to maintain the same testing conditions and sample consistency. This often leads to unacknowledged sizable errors for the reported measurement and certainly is more time/labor intensive for the researcher. Additionally, articles have reported data with the properties measured in varying configurations,*i.e.*, electrical properties are measured *in-plane*, while the thermal properties are measured in the *cross-plane* configuration [27]. This occurs due to the difficulty of *cross-plane* electrical characterization and *in-plane* thermal conductivity measurements, but this superposition of measurement properties is not a valid measurement for thermoelectric materials as they tend to be highly anisotropic and cannot be generalized with this compiled measurement approach.

Even under ideal comparison conditions, large variability can still exist in the measurement of TE properties. Wang *et al.* [28, 29] demonstrated this in a round-robin study, published in 2013, investigating the inter-laboratory repeatability of thermoelectric material characterization. This study used two sets of p-type Bi_2Te_3 samples, tested at seven labs around the world using the same instruments: laser flash systems from Anter Corp or Netzsch Manufacturers within valid calibration periods. The sample variance was 1.54%, but the measurement variance for the thermal diffusivity measurement alone was 6.8% at 300 K and rose rapidly to over 14% at 475 K [29]. This study highlights the measurement complexity of thermoelectric properties and the necessity of careful consideration and system design when it comes to their measurement. If measured properties vary this much for a well controlled study, imagine the variance for all the studies reported in literature. Simultaneous measurements will not solve every measurement problem with thermoelectrics, but

they can provide a better controlled platform for the measurements and help to reduce the uncertainty and variance of measured properties for new materials.

2.3 Z-Meter Overview

2.3.1 Description of System Operation

A Z-Meter is an instrument that is used to simultaneously measure, on one sample, the three thermoelectric properties, S, σ, and κ, from which the figure of merit, ZT, is calculated [30]. This instrument consists, at its most basic level, of two bars of a material with known properties arranged axially, between which the thermoelectric sample is clamped. One end of the bar assembly is heated, while the other is cooled, thus inducing heat flow through the bars and sample. Temperature sensors are installed at known distances along the bars to determine the heat flow, as the thermal conductivity of the bar material is well characterized with temperature. The bars are also equipped with electrical connections to permit the electrical properties across the sample to be monitored. Traditionally, this technique has been employed utilizing a very small temperature difference across the sample ($\Delta T \approx 1 - 2$℃) and test temperatures between approximately 20 - 400℃, but thermoelectric materials must generally have sizable temperature gradients across them to achieve desirable performance [31, 32]. Therefore, the best way to evaluate the performance of the materials under large temperature differences is to characterize them under such gradients [33].

2.3.2 Background/Prior-Art

In 1955, E.H. Putley [34] described an apparatus to measure the thermoelectric properties of lead selenide (PbSe) and lead telluride (PbTe). Putley welded dual leads of 203.2 μm diameter platinum wire at each end of a sample, then brought these four leads out to electrical connections to permit current to be run directly through the sample, or passed through a pair of leads to create a temperature difference across

the sample via resistive heating. Four type-K thermocouples of 50.8 μm diameter were welded directly to the sample to ensure low resistance ohmic contacts and measure both the axial and transverse temperature differences. Additionally, each axial or transverse pair of thermocouples was used as potential probes to measure the potential differences. Measurements at elevated temperatures were made by placing the sample holder inside a furnace made from a heater wound around a silica tube [35]. This apparatus could directly measure the electrical resistivity, utilize the small temperature difference to determine the Seebeck coefficient, and calculate the thermal conductivity from steady-state, adiabatic conditions. Independently, T.C. Harman [36, 37] proposed a method which also utilized a temperature difference created by the Peltier effect, and showed that the figure of merit could be directly determined from a ratio of the absolute Seebeck voltage and the ohmic voltage of the sample,

$$ZT = \frac{V_{Seebeck}}{V_{ohmic}}. \tag{2.5}$$

The transient Harman technique is widely used to directly determine ZT for thermoelectric materials, but is limited to small temperature differences [38–40].

The first Z-Meter was created by L. S. Phillips [41] circa 1965. The lack of integrated characterization methods for thermoelectric materials at elevated temperatures, 100 - 600℃, such as those found in direct conversion nuclear power generators, motivated his work. The developed design was capable of generating temperature gradients across the sample of ∼10℃ for thermal conductivity and ∼100℃ for Seebeck coefficient measurements. While this system permitted the use of a single system to carry out the necessary measurements for determining ZT, the measurements were still performed separately. Muller [42] was the first to construct a Z-Meter with the capabilities for measurements under large temperature gradients. Several other researchers have created Z-Meters as summarized in Table 2.1, but the system that sparked the inspiration for this work was started by Mayer [43, 44], then improved by Amatya [33]. Their high-temperature Z-Meter system has many of the same goals as my system design, but due to the thermal losses within their system, they were not able to reach the desired high temperatures.

The high-temperature Z-Meter of Mayer and Amatya [33, 43, 44] was capable of large $\sim$ 250℃ temperature gradients and simultaneous measurements to extract all three thermoelectric parameters. Additionally, it permitted the direct measurement of conversion efficiency and the power density for a single thermoelectric leg. This system was capable of high-vacuum operation, although outgassing issues prevented them from achieving their desired vacuum level. The heat source was a HeatWave Labs button heater with a temperature controller capable of stable $\pm$1℃ temperature control at temperatures up to 1200℃. However, the maximum reported hot side temperature achieved in the system was 440℃. The system was designed using a single-sided copper reference bar placed below the sample and instrumented with type K thermocouples. Gold plating the copper bar reduced radiation losses at high temperatures. The electrical resistivity was measured using the traditional DC voltage sweep with a Kelvin probe configuration integrated into the bars and an active load similar to that described by Müller [42]. This active load permitted load matching to measure the maximum efficiency and to determine the electrical conductivity from the load matched condition. But, they noted that the powered FET load matching circuit had higher electrical parasitics than the traditional Kelvin approach [33]. Finally, this system had a piezoelectric strain gauge integrated for measurement of the interfacial loading at the sample.

The work in this dissertation differs from past work in that I have designed the system with the primary intent of reaching high temperatures, up to 1000℃ with large temperature gradients ($\sim$ 500℃) across the sample. A major contribution of this system is the careful thermal design and target of achieving high temperatures from the outset. This permitted all components to be designed specifically to enable the system to achieve high temperatures. I utilize a vacuum controlled environment to minimize convection losses, but also take great pains to minimize my outgassing budget to achieve these low vacuum levels and preserve the cleanliness of the system avoiding contamination. This is particularly critical for the high-accuracy temperature sensors, which are subject to contamination in a high-vacuum environment if

cleanliness standards are not maintained, discussed more in Section 3.4. This is accomplished through adherence to high vacuum design practices, material selection, cleaning procedures, and installation practices. Our system also has a triad of load cells for monitoring loading uniformity during testing, and due to a novel loading scheme for Z-Meters, the system also permits modification of the interfacial loading without disturbing the system environment or breaking vacuum. Finally a nearly continuous data acquisition scheme (less than 200 ms between complete measurement sweeps) is utilized, which does not require that sample temperatures be equilibrated during the testing run for property measurements to be collected permitting future use in investigating slow transient heating or cooling cases. This system fills a need for high temperature simultaneous property characterization at Purdue University and will serve as a valuable tool for researchers here as and collaborators around the world.

Table 2.1. Comparison table of all previous Z-Meter systems. Reprinted from Amatya, R., Mayer, P. M., & Ram, R. J. (2012). High temperature Z-meter setup for characterizing thermoelectric material under large temperature gradient. Review of Scientific Instruments, 83(7), 075117., with the permission of AIP Publishing.

Z-Meter	T_{Hot} [℃]	ΔT [℃]	Heat Flux Meas.	Electrical Resistivity
Classical Arrangement [41] (1965)	600℃	$\sim$ 10℃ (κ) $\sim$ 100℃ (S)	Pyrometer	DC Voltage Isothermal
Transient Z-Meter [30] (1990)	700℃	-	Heat Flow Meter	Fast DC (Square Wave) Voltage
Graded TE Measurement [42] (1998)	500℃	385℃	Nickel Reference Bar	Variable Load Resistor Circuit
Effective ZT Measurement [45] (2009)	200℃	160℃	Heat Flux Sensor	AC Method (4-Wire)
Commercial "Z-Meter" TEC Microsystems	110℃	65℃	N/A	AC Method
High-Temperature Z-Meter [33, 43, 44] (2007)	440℃	255℃	Au-Plated Cu Reference Bar Type K TCs	DC Voltage (4-Wire) Active Load
Low-Cost Z-Meter [46] (2014)	112℃	-	Cu Reference Bar Type K TCs	-
Purdue Z-Meter [47] (2018)	1000℃	500℃	Polished Mo Reference Bar Type S TCs	Fast DC (Square Wave) 4-Wire

3. Z-METER DESIGN

3.1 Design Overview/Set Up

This chapter details the design process of the Z-Meter system and subcomponents. I start by explaining the system constraints and primary design metrics. I then move through the approximate design process explaining design decisions and thought process for the benefit of the reader working to recreate or expand upon this work. The approximate order of the system design is as follows:

1. Determine an appropriate sample size and shape for maximum versatility and widest use within the system.

2. Design the meter bar and identify the key features for development of an accurate reference bar design.

3. Evaluate temperature sensing technologies, select the appropriate sensor type, and expound upon my sensor design and fabrication process.

4. Discuss details of the electrical measurements in the Z-Meter system: Seebeck coefficient and electrical resistivity.

5. Explain heater operation, power capabilities, and present mechanical loading limitations which dictate a shift in system architecture. I then chronicle my feature design and solution process to protect the heater and provide adequate thermal isolation.

6. Present the thermal radiation shielding scheme for the instrument, outline the advantages and disadvantages of implementing radiative loss suppression components within the measurement system, and delineate the heat shield design process.

7. Introduce the design, operation, component selection, and fabrication of the heat rejection system for the Z-Meter system. This includes a discussion of the pumped flow loop utilized for heat removal from the vacuum chamber, suggested cold plate features, design of vacuum and atmospheric flow tube assemblies, and detailed pressure drop calculations for system operation.

8. Illustrate mechanical loading challenges and requirements within the system for accurate long-term operation. Proffer a novel design feature for Z-Meter systems which enhances measurement throughput, while providing improved *in situ* load monitoring.

9. Set forth key design features and practices for components operating in high vacuum environments. Elaborate on the vacuum system, instrumentation, procedures, and operational considerations.

10. Present the remaining aspects necessary for realizing a high-accuracy measurement system, which are all too frequently over looked, including: Component and vacuum feedthrough layout, cabling and wiring harnesses, system level noise reduction techniques, and a discussion of the electronic instruments, the settings necessary for accurate measurement of signals in this system, and how they are used to perform this measurement.

3.1.1 System Design Metrics

The overall system measurement requirements and operational metrics are the major driving factors in the Z-Meter design. This system is filling a gap that currently exists at Purdue and many other institutions for accurate high-temperature thermoelectric material characterization. The target operating temperature is 1000°C for the hot side of the sample. In addition to achieving the high-temperature point, another primary goal of the system is to provide simultaneous property characterization for thermoelectric materials under large temperature gradients. This requirement stems

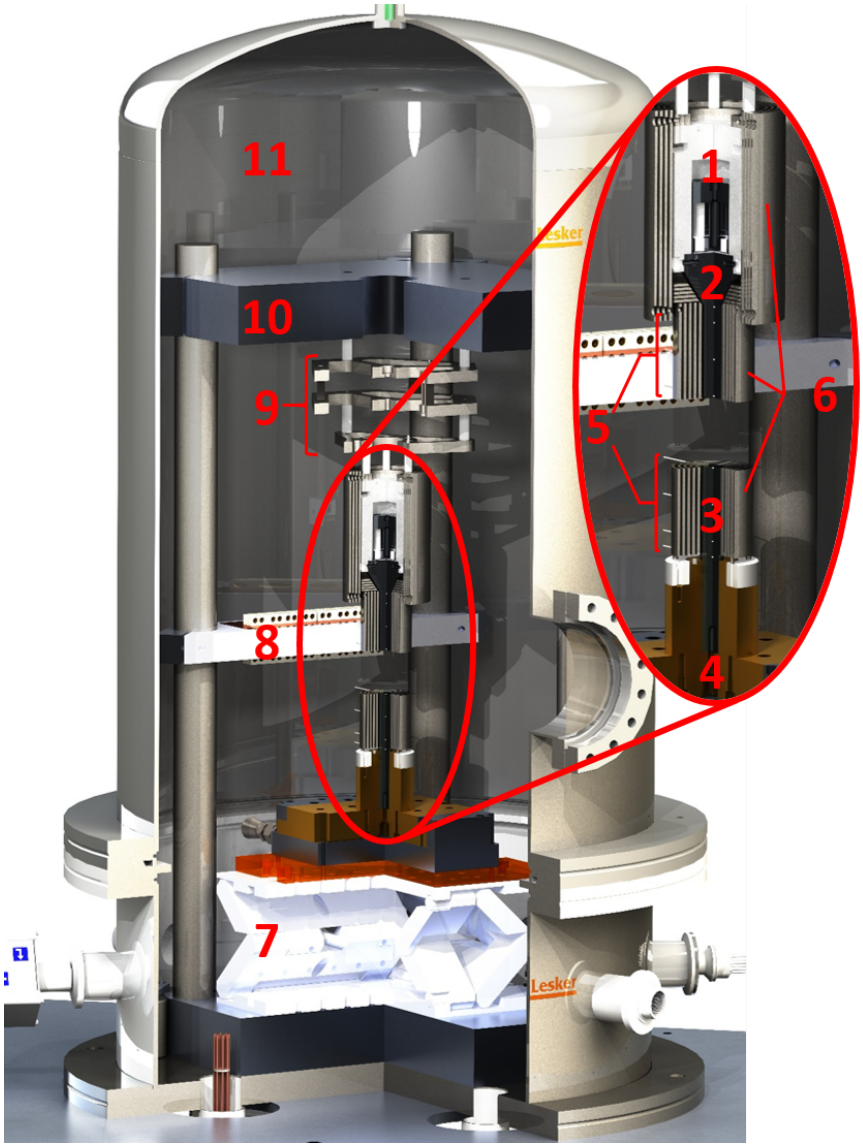

Figure 3.1. CAD rendering of the Z-Meter measurement system sectioned for clear view of system components. The enlarged detail view shows the meter bars which the sample is inserted between and clamped in place. System components are tagged for clarity: (1.) Button heater with ceramic loading shroud, (2.) Upper molybdenum meter bar, (3.) Lower molybdenum meter bar, (4.) Cold-plate and lower meter bar mount, (5.) Distributed temperature and electrical sensor probes mounted in both meter bars, (6.) Banked, annular, polished stainless steel radiation shields, (7.) High capacity lab-jack, (8.) Isothermal connection terminals for cold junction compensation, (9.) Thermal isolation platforms with three load cells mounted between the top two platforms, (10.) Load frame, (11.) High vacuum chamber.

from the fact that actual TEGs operate under large temperature differences to increase efficiency, so it is necessary to characterize new materials being designed under such conditions. This system will be a user system open to all members of the Birck Nanotechnology Center (BNC) at Purdue University. As such, it is imperative that the system be intuitive and user friendly, accept a common sample size, and allow the characterization of a wide range of sample thicknesses. Additionally, we have recognized the need for versatility in research systems and have imposed a requirement of maintaining compliance with the ASTM D5470 test standard commonly used for thermal interface material (TIM) characterization. This is not the main goal of the system, but it can be attained without compromising primary project goals and is a value-added system feature permitting a wider user pool access to the standard measurement technique.

3.2 Sample Size

It is important to consider ease of use when designing a measurement system. This includes designing for a common sample size and minimizing sample preparation. Additionally, secondary validation of measurements using an independent method are critical for a robust system design. After a survey of locally available test equipment and sample requirements, a sample size of ⌀12.50 mm (0.500 in.) is selected to best accommodate secondary testing. This size is selected as it is the required sample geometry for the laser flash measurement systems used by Thermophysical Properties Research Labs (TPRL), located in West Lafayette, IN. TPRL is a well established leader in the field of thermal measurements, dating back to wide recognition of their material testing in Thermophysical Properties of Matter - the TPRC Data Series by Touloukian *et al.* [48] published in 1970. In addition to secondary testing at TPRL, with some further processing the ⌀12.50 mm sample puck can be used for time domain thermo-reflectance (TDTR) or 3ω measurements of thermal conductivity. These

factors combined with the fact that many groups use half-inch dies for compaction and sintering of new materials made this a well-balanced choice for the Z-Meter.

3.3 Meter Bars

3.3.1 Materials

The first step in a materials selection process is to clearly define the requirements for the material and specify the desired property behavior. Due to the nature of the Z-Meter measurement, there are many types of properties that must be considered: thermal, electrical, and mechanical.

Thermal Properties

The first requirement to consider is select the material for the material bar considering thermal properties: thermal conductivity, thermal expansion, emissivity and radiative losses, and melting temperature.

First, the thermal conductivity of the meter bars determines the thermal gradients used for measurement of heat flow along the bars. ASTM D5470 recommends that the bar thermal conductivity be greater than 50 W/(m·K), which is also required to achieve high-temperatures at the sample interface. The selection of a thermal conductivity is complicated for this application as it requires a balance between two opposing factors. A high thermal conductivity is desired to reach high-temperatures at the sample interface, but the thermal conductivity must also be low enough to resolve a measurable temperature gradient between the temperature probe locations. Additionally, since the meter bar method requires approximate 1-D conduction in the bars, the thermal conductivity of the material must be high.

Second, since this system is designed to operate at high-temperatures, the change of the size of the material (*i.e.* thermal expansion) must be considered over this range as well. Large size changes with temperature lead to increase thermal stresses,

and can impact the alignment within the system. The cross-sectional area is a key constituent in the determination of the thermal conductivity, but if the bar dimensions change drastically with temperature, then this variation of conduction area can lead to over-estimation of measured thermal conductivity. Additionally, if the meter bars expand with temperature, the thermal contact between the temperature sensors and the bar can be degraded substantially due to enlargement of the probe insertion well. This indicates that the coefficient of thermal expansion is another critical property to be considered in the material selection process for the meter bars.

Third, thermal losses from the reference bars are important to accurate property characterization of the sample and at high-temperatures, radiative losses can be substantial. In order to achieve high-temperatures, radiative losses must be suppressed as much as possible. This can be done by adding thermal shielding, but a good way to minimize this problem from the beginning is to target materials with low emissivities over the temperature range of operation. Emissivities can sometimes be adapted to a more suitable range through mechanical polishing and/or deposition of a low emissivity material such as gold or platinum, but at high-temperatures, surface coatings such as these can cause problems such as phase transition of the coating or inter-diffusion of the reference bar material with the coating. Inter-diffusion can cause the calibrated thermal properties of the reference bar to shift over prolonged periods of operation at high-temperatures.

Finally, it is important for the material to have a high melting temperature and a low intrinsic vapor pressure. Operation at high-temperatures requires a material of a considerably higher melting point to avoid holding the material above its recrystallization temperature for too long, which can lead to excessive grain growth and result in materials becoming too ductile for practical application in a mechanical loading system. The recrystallization temperature for a materials can be generally estimated as approximately 40% of the melting point for the material [49].

Electrical and Thermoelectric Properties

The Z-Meter utilizes the reference bar not only for use in thermal property characterization, but also as electrical probes to the sample. Since electrical properties are being measured through the meter bars, the electrical properties of the bars themselves are important to consider for material selection. The first property to evaluate is the electrical resistivity of the material. The measurement of electrical resistance to determine resistivity for thin thermoelectric materials often involves very small quantities since good thermoelectric materials have high high electrical conductivity and the thin sample form factors leads to small resistances. The electrical conductivity of the meter bars must be sufficiently high so as to not dominate the measurement of resistance in the sample. Another critical set of properties to consider are the thermoelectric properties of the bar material. One of the main properties of interest for measurement in the Z-Meter is the Seebeck coefficient. As discussed in Section 2.1.1, the Seebeck coefficient describes the development of a voltage potential due to temperature difference in an open circuit. It is important for the meter bars to have a low (and approximately constant) Seebeck coefficient to permit accurate measurements of the voltage drop across the sample without interference from the emf generated within the measurement bars themselves.

Mechanical Properties

Mechanical properties for high-temperature materials are especially important when the system is going to be applying a mechanical load to compress sample under test. As materials approach their melting temperatures, their mechanical properties quickly decline. As discussed above, extended operation at temperatures over $\sim 40\%$ of the melting temperature for the material result in ductile materials (annealing). These materials lose much of their elasticity and hardness, which is detrimental for bars that must transfer a load to a sample, but not deform themselves. Therefore, a high hardness value and a high elastic modulus are desired. Another mechanical

property to consider is thermal creep which is the time-dependent deformation under an applied load. Creep deformation is often a problem for materials operating at elevated temperatures, which can deform component geometry over time and damage system sensors or components.

Discussion of Material Selection

Evaluation of Materials in Existing Reference Bar Systems

A typical starting point for materials selection is to survey what has been used previously to accomplish the task. Copper [33,50,51] and aluminum [52] have traditionally been used for meter bars due to their excellent thermal properties. Stainless steel [52] has even seen use in reference bar systems, although it is not as common. While these materials can be found in previous systems throughout literature, we find that in driving the operating temperature of the system higher, we reach a point where these materials are no longer feasible options for the meter bars.

The high thermal diffusivities of copper and aluminum make them very attractive for use as meter bars since it is easy to obtain the necessary operating conditions for the meter bar technique: $\sim$ 1D heat flow and uniform temperature profile for a given cross-section. Both materials have high thermal conductivities which limits the temperature gradients present between temperature sensors, but with careful geometric and thermal design this problem can be overcome by using appropriately sensitive temperature probes. Stainless steel permits steeper temperature gradients to be resolved due to a lower thermal conductivity, which can help compensate for limited sensor accuracy in some systems, but limits the heat flow through the bar to the sample. The problem with stainless steel is that it has poor thermal conductivity, typically two orders of magnitude lower than that of oxygen free high conductivity (OFHC) copper and approximately one order of magnitude lower than common aluminum alloys (6061-T6), making it extremely difficult to construct a reference bar which satisfies the meter bar operation conditions.

Copper and aluminum alloys have high coefficients of thermal expansion (CTEs), which means that these materials will expand/contract considerably during the course of a full test cycle due to the wide temperature range. While we leverage this property for intimately mating the base components, using a thermal interference fit to obtain excellent contact between the lower reference bar and the copper base mounting plate, any change in size of the meter bars is undesirable as it is difficult to characterize the exact degree of change for all points on the bar. Thermal expansion for stainless steel is much less of an issue than for copper or aluminum, but over large temperature ranges can still impose significant errors within the measurement. Traditionally we think of a material growing uniformly due to the CTE as it is heated, but this is not necessarily the case after the part has been machined and has different features. Therefore, we target materials with a low CTE for any parts within the system that will experience significant temperature swings. This helps to ensure that bar shape and probe holes maintain the desired dimensions throughout the test. In certain cases, limited thermal deformation can be accommodated and corrected for in the data analysis, but it is not ideal.

Copper and aluminum are both very soft metals which leads to contact surfaces easily damaged by sample loading, meaning surfaces must be polished regularly and over time the meter bars will need to be replaced more frequently due to surface wear and wall thinning between the sample interface and the temperature probe located in extreme proximity to the surface. Stainless steel, in general, is less prone to deformation or oxidation than either copper or aluminum. Most stainless steels are sufficiently hard as to not have an issue with interface damage for most materials of interest.

The electrical properties for copper and aluminum are excellent; they both have very low resistivities and Seebeck coefficients. The electrical properties for stainless steels are not as favorable, with a resistivity of 1.5 order of magnitude higher than those for copper or aluminum, and while the Seebeck coefficient is still low compared

to thermoelectric materials to be measured, it is higher than those for copper or aluminum.

Mechanical strength of the material must be considered at these elevated temperatures. Thermal creep can lead to deformation of the meter bar over time, especially as materials are operated at temperatures approaching their melting point. Aluminum alloys melt around 650℃, while copper melts at approximately 1080℃ [53]. While the melting point for many stainless steels is much higher, $\sim$ 1400℃ [53], portions of the loaded meter bar are designed to operate at temperatures up to 1200℃. This would mean operation under load at approximately 86% of the material melting temperature, which is not suggested for long term system performance. It is clear that these traditionally used options will not work for the meter bar material in the Z-Meter due to operating temperatures alone.

Evaluation of Alternative Reference Bar Materials

Since traditionally used materials are not an option due to the elevated temperature range, we first targeted materials known to operate well at high-temperatures, then sorted from there as to which had the proper combination of properties to make them suitable for use in the Z-Meter. There is a wide range of materials capable of operation at high-temperatures, and countless alloys designed for specific high-temperature applications, but a balance of the properties to suit the measurement proved more difficult.

Many different materials are considered for the meter bar materials. In lieu of an extended discussion of each material individually, key material property plots are included to highlight comparison between materials. After evaluation of the materials shown in Figures 3.2 - 3.4, we determined that the best suited materials were refractory materials, specifically: tungsten, molybdenum, and their alloys (not listed in figures). I decide to use a pure material instead of an alloy owing to a lack of reliable data on the drift in thermal and electrical properties of the bar due to prolonged operation at high-temperatures in a vacuum environment. Even small

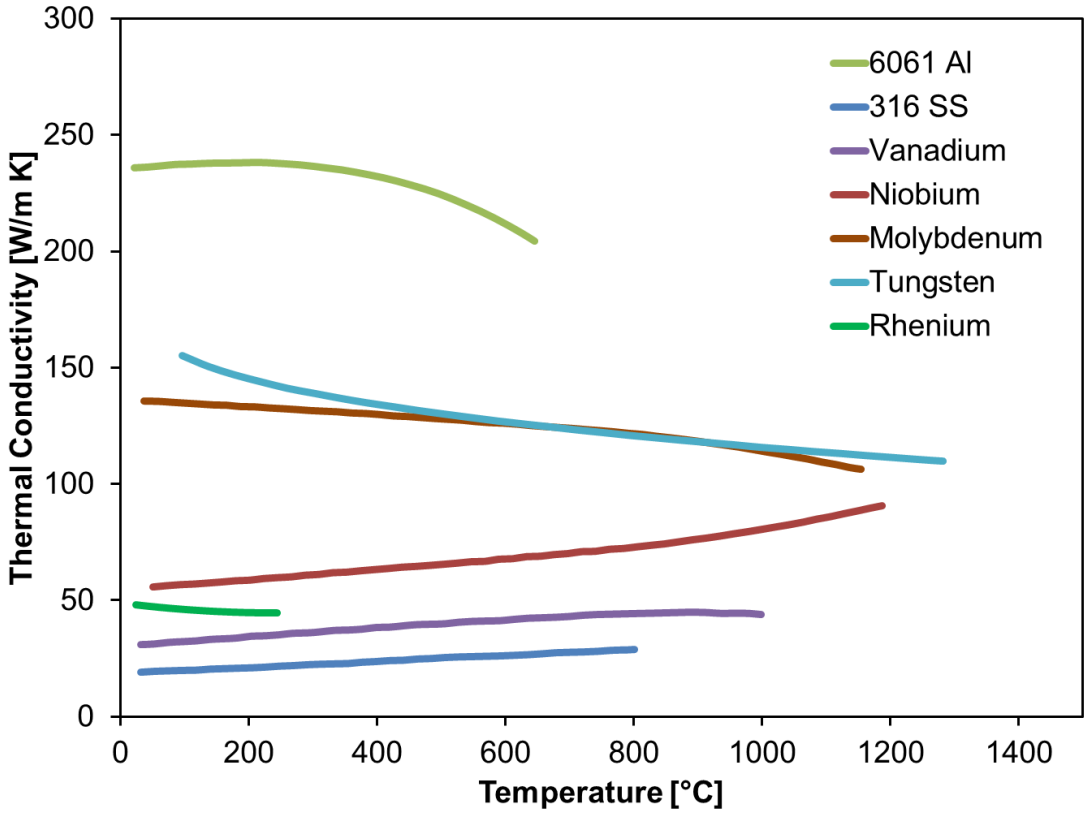

Figure 3.2. Thermal conductivity of potential reference bar materials [48, 54–56].

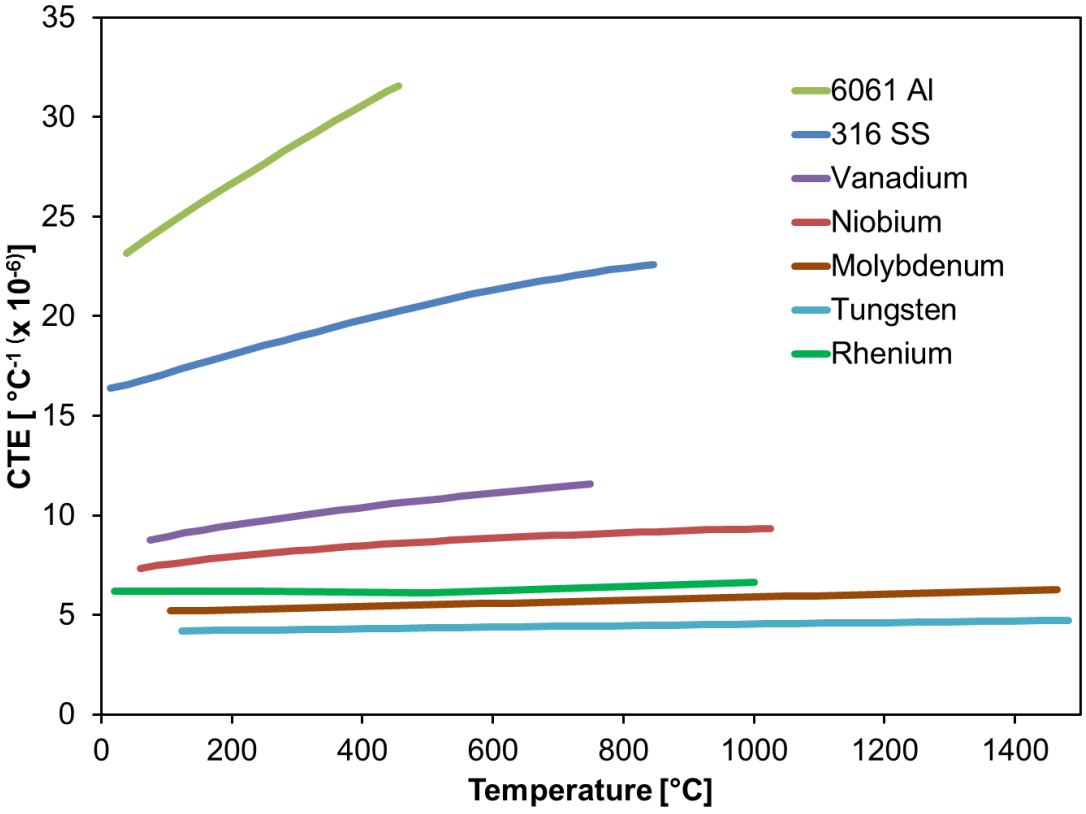

Figure 3.3. Coefficient of thermal expansion (CTE) of potential reference bar materials [54, 55, 57].

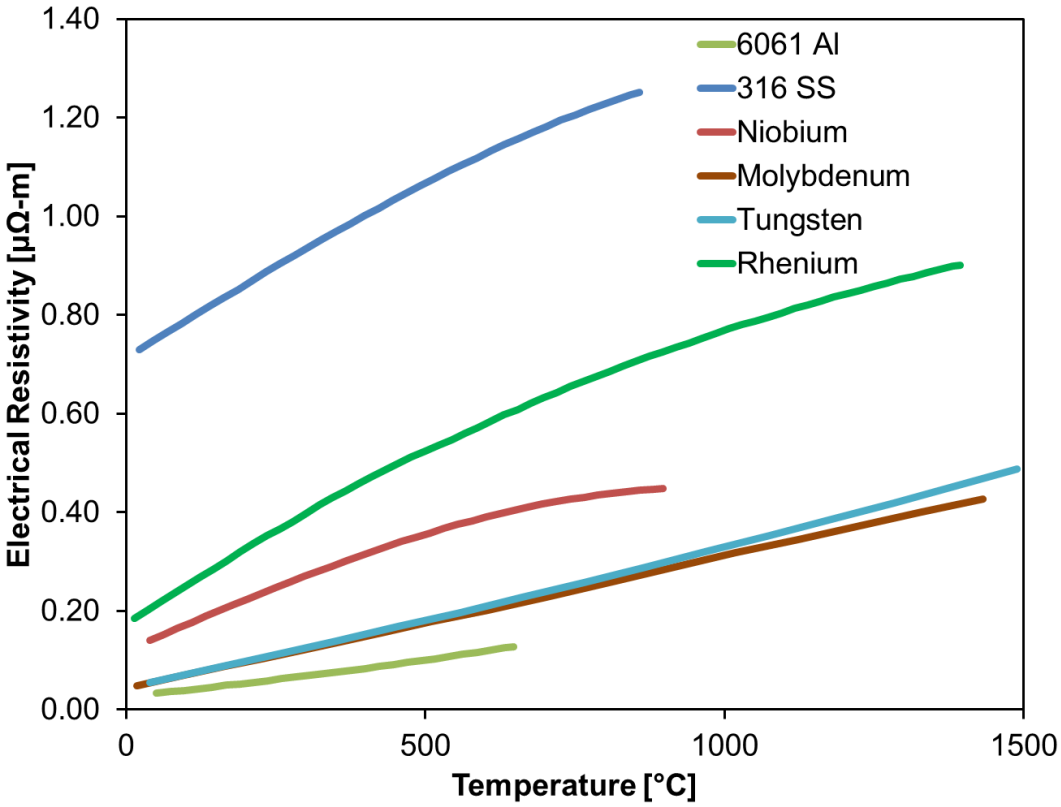

Figure 3.4. Electrical resistivity of potential reference bar materials [54–56].

persistent deviations over time can compound into substantial measurement errors due to unexpected aging characteristics of an alloy material.

I compare tungsten and molybdenum for use as a meter bar. Tungsten has a slightly higher thermal conductivity, a lower CTE, and has a comparable electrical resistivity to molybdenum across much of the operational temperature range, but the electrical resistivity for tungsten does increase faster than molybdenum with temperature. These two materials have a favorable balance of desired properties: relatively high thermal conductivities, low electrical resistivities and CTEs across the temperature range, both are very stable and robust at high-temperatures, and have impeccable creep resistance. There is a measurable Seebeck effect for both materials, but it is of the same order as the Seebeck coefficient for copper, and the magnitude of the Seebeck coefficient for both tungsten and molybdenum is less than that for platinum or palladium as shown in Figure 3.5. In addition to the properties already discussed, we must also briefly mention the comparison of typical emissivities for these materials. Figure 3.6 shows nominal emissivity ranges with temperature for the tungsten and molybdenum materials in the as delivered state, having precision ground surfaces. The materials undergo machining and polishing prior to use, but this serves as a baseline comparison between the two materials. The precision ground surfaces are smooth, but not polished; therefore, we anticipate the actual emissivities for the bar in operation to be less than the values provided from the manufacturer (Plansee) for both materials [54, 55, 58].

Based on these facts, tungsten has a slight advantage over molybdenum from a materials selection perspective; however, this does not take into account the material machinability. Ultimately, we elected to use molybdenum to improve machinability of the meter bars. Tungsten is very difficult to machine accurately due to its hardness and the degree of work hardening that occurs during the machining process. Molybdenum is still a difficult material to machine, but it has better machinability than tungsten, while still possessing the desired combination of thermal, electrical, and mechanical properties. After material selection, the remaining system components

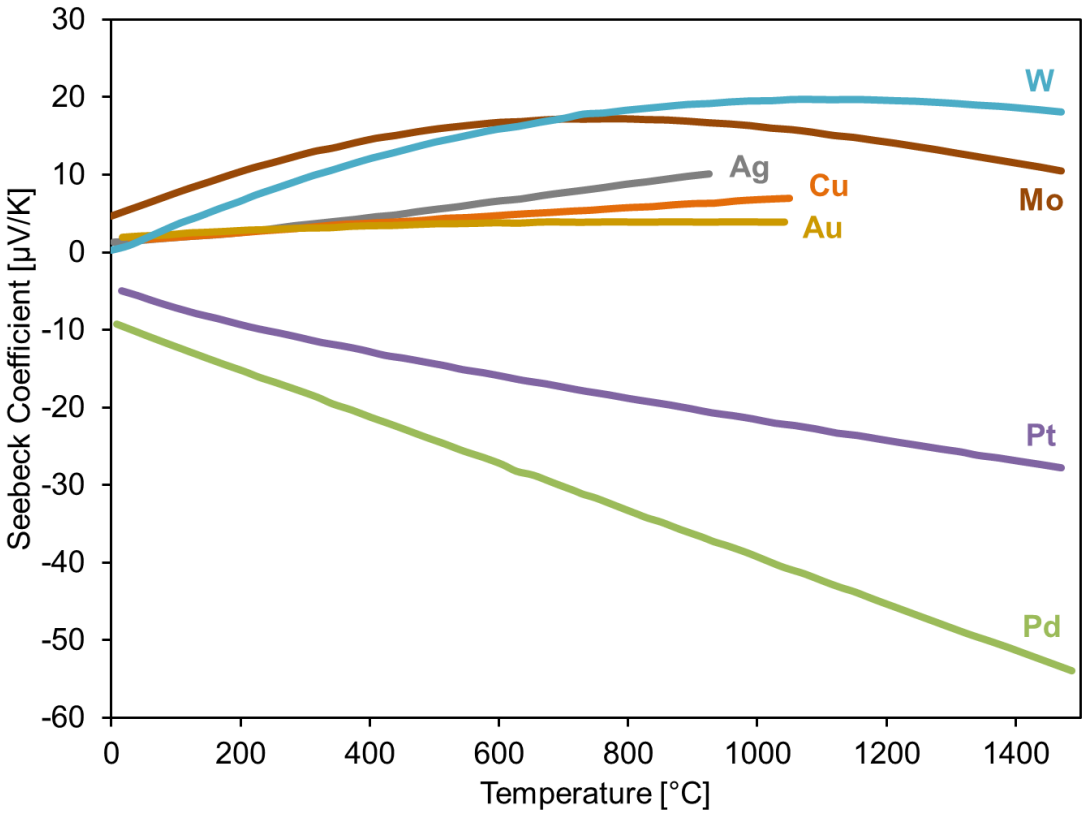

Figure 3.5. Seebeck coefficient of potential reference bar materials [59, 60].

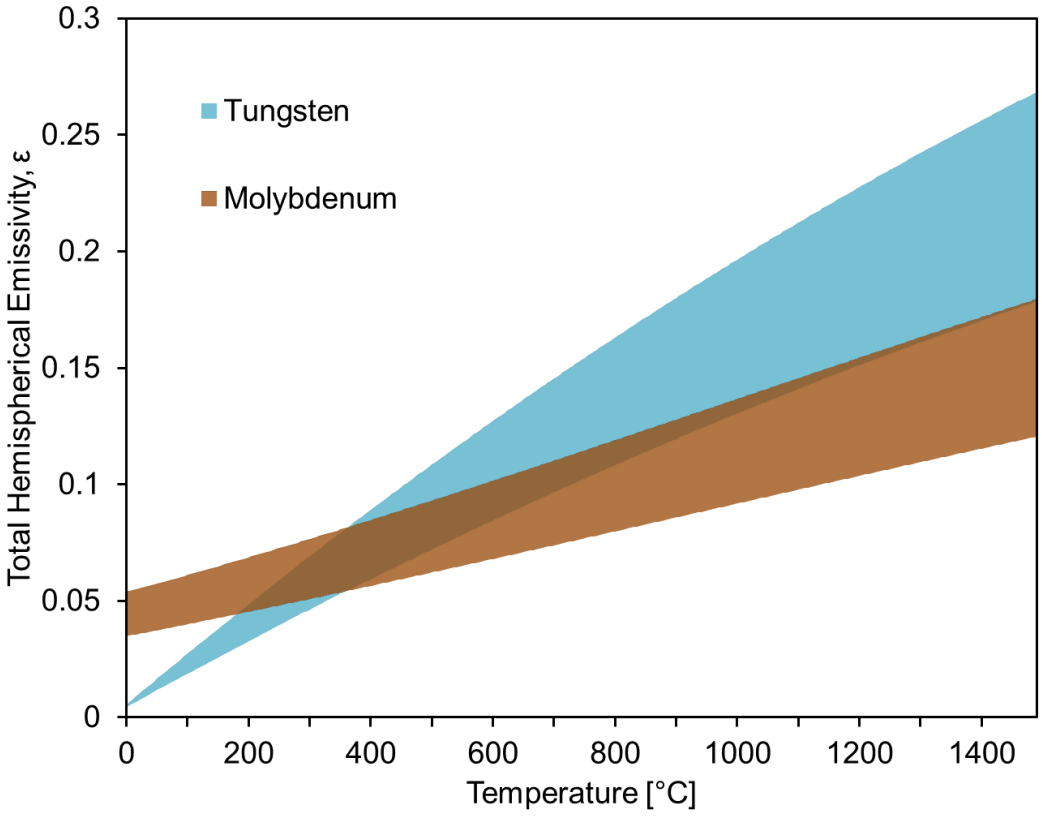

Figure 3.6. Total hemispherical emissivity of potential reference bar materials with as-received ground surface finish [54, 55].

and assemblies must be evaluated thoroughly and iterated upon to achieve a fully mature design for the measurement system.

3.3.2 Geometry of the Reference Bars

The reference bars are carefully designed to achieve approximately 1D heat flow, meaning that the temperature in the bar does not vary radially within a given cross-section. This is done by ensuring that the local bar Biot number is small:

$$Bi = \frac{h \cdot D_B}{2\kappa_B} < 0.1, \tag{3.1}$$

where h is the heat transfer coefficient describing the losses from the radial surfaces of the bar, D_B is the bar diameter, and κ_B is the thermal conductivity of the bar. Due to the high-temperatures during testing, the experiment must be conducted under vacuum conditions for multiple reasons: (1) to suppress convective losses from the assembly, which would drive the Biot number out of the targeted range, and (2) at these temperatures, oxidation of many materials occurs quickly and violently, thus necessitating that experiments be conducted under high vacuum conditions (10^{-6} Torr). Once the condition of a small Biot number is satisfied, the temperature gradient along the bar must be measured without significantly disturbing the 1D temperature profile within the bar and with high accuracy.

As detailed in Section 3.3.1, material properties are paramount in the design of the meter bar. A high conductivity material will need longer separations between measurement locations due to the reduced thermal gradient and finite probe sensitivity. Therefore, it is essential to select a material that has a high enough thermal conductivity to satisfy the condition of a small local Biot number ensuring a uniform temperature profile within the cross-section at each location along the axis of the bar, but low enough to resolve a temperature gradient along the bar. In addition to thermal conductivity, thermal expansion must also be considered when determining sensor spacing as the system operates over large temperature ranges, which can lead to significant changes in geometry during the course of the test for some materials. Accuracy of the temperature sensor is also important as less accurate sensors will require further spacing to obtain a sufficient thermal gradient along the bar. Probe size needs to be minimized to avoid major disturbances in the thermal profile within the bar, and local losses at probe points due to conductance along the probe.

In addition to the impact that material properties have upon the bar, the actual sizing of the bar itself is critical to accurate measurements and involves several competing design factors to achieve optimal bar sizing. The bar diameter cannot be too large, because it will make it difficult to maintain a sufficiently small Biot number due to the increase in the surface area for radiative losses. As the bar radius is increased,

a more powerful heater is required to maintain necessary temperature gradients for the measurement. Also, large bar diameters require large sample diameters, which is not always possible. Alternatively, as the bar diameter is reduced, the impact of parasitic losses and distortions in the uniform cross-sectional thermal profile are worse due to the measurement probes, because the probes can only be reduced in size to a certain point, then the relative size of the probe to the bar can result in considerable distortions of the profile. I use common sample sizes as a means to reduce the design space to specific sizes for consideration.

I selected a sample size of ⌀ 12.7 mm (0.500 in.) as this is a commonly used sample puck size for materials development, and it allows auxiliary testing with other property measurement systems available around Purdue, such as Laser Flash. After the sample size is selected, the meter bars are selected to be slightly oversized to the sample at ⌀ 13.08 mm (0.515 in.) to provide approximately 3% clearance around the edges of the sample. This is done to simplify the alignment of the sample and the bars and helps to ensure the full sample interfacial area is active in the measurement instead of only engaging some portion of the area due to misalignment. The length of the meter bars is prescribed by the required spacing between temperature sensors for accurate measurement of the thermal gradient along the bar across the entire temperature range. Many factors impact the necessary spacing of temperature sensors including: material properties of the bar, accuracy of the temperature sensor and probe sizes/conductances.

3.4 Temperature Measurement and Sensors

A general overview of the temperature sensor technologies considered for use in the Z-Meter is presented, followed by a description of the selection process for the chosen sensors. The potential temperature sensor technologies can be broken up into two major groups non-contact and contact measurements.

3.4.1 Review of Non-Contact Thermal Sensors

Non-contact measurements are attractive because there is nothing physically touching the reference bar, which avoids disturbing the thermal profile and prevents probe conductance losses. Bolometers are first considered due to their size and ability to mount inside of a heat shield without necessity of a gap in the heat shield exposing the bar surface to higher losses. Such use would require custom fabrication of miniature platinum foil bolometers coated with platinum black to enhance the absorption. Due to the high-temperature coefficient of resistance (TCR) for the platinum foil, the increase in temperature due to the absorption from the bar would cause a change in the measured resistance of the foil. This technology was quickly deemed as ill-fitted to this process as bolometers perform better when the incoming radiation is chopped into a low frequency ($\sim$ 10 Hz) [61], and it would not be feasible to install chopper windows to be actuated inside of the heat shields. A similar technology, but one not requiring a chopped radiation signal is a thermopile detector and are often used in spectral or total radiation pyrometers [61]. A thermopile is essentially a number of differential thermocouples connected in series between a surface of unknown temperature (with low thermal mass) and a uniform temperature reference surface to measure the temperature difference. This permits higher sensitivity than a differential thermocouple alone and only two of the thermocouples experience large temperature gradients which limits the impact of inhomogeneities in the leads. However, it requires an increased area to make the series connections between the two surfaces and the thermocouples must be constructed from ultra fine wire to limit heat flow [60]. The voltage measured by a thermopile is given by

$$V_{out} = n(V_S(T) - V_S(T_0)), \tag{3.2}$$

where n is the number of thermocouples used, V_S is the Seebeck voltage measured at the unknown temperature, T, and the reference temperature, T_0 [61, 62]. As such, thermopiles also require the measurement of the reference temperature. The configuration of these sensors could lend itself well to such non-contact measurements.

Custom annular ring shaped sensors could be fabricated and attached at known positions along the inner surface of the heat shields, using the shield as a reference surface, but due to limitations on smallest size possible for feasible manufacturing while maintaining high-temperature compatibility, and further complication of added wiring in the limited space within the radiation shielding, we decided that sensors such as bolometers or thermopile pyrometers were not feasible for local installation inside of the heat shields.

Next we evaluate the use of infrared pyrometers for measurement of bar temperature. Infrared pyrometers measure the incident radiation by focusing it through a lens onto a thermopile detector, using the same operating principle as discussed above. The issues that quickly arise from this measurement method are access to the bar surface requiring radiation shields to be removed and increasing losses. Additionally, the pyrometer would need to be located outside of the chamber due to the vacuum environment, limiting the field of view of the bar to that which can be seen through the vacuum view port as depicted in Figure 3.7. The pyrometer can be scanned along the axis of the bar, but at the distance required by the radius of the chamber, the spot size for the measurement is too large. This precluded the use of infrared pyrometers for measurement of bar temperatures.

The final option for non-contact measurement of bar temperature was to use an infrared camera to measure the temperature map for the bars and sample visible through the viewport to the bell jar. The use of an IR camera is attractive, because it provides additional information about the temperature of the sample and permits contact resistances to be measured directly from the thermal map by considering the temperature jumps recorded at the interfaces in the images. However some difficulties do exist. The radiation shielding around the sample and portions of the bars must be removed to provide a view of the surfaces, an infrared transparent viewport is required to permit external measurement with an infrared camera, and the working distance of the camera from outside the chamber makes imaging of the bar sample interfaces challenging. The required resolution combined with the minimum working

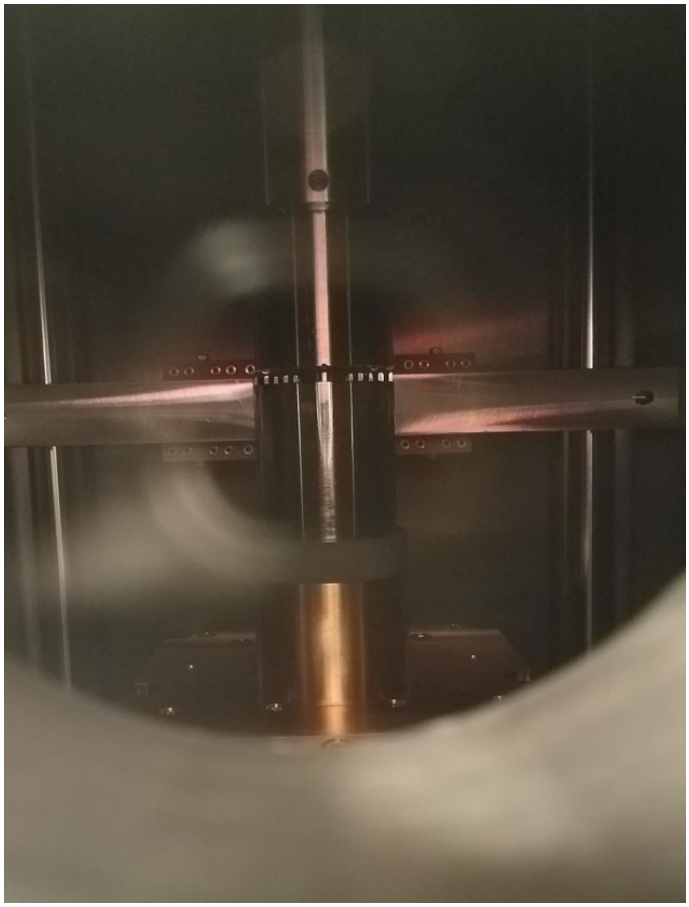

Figure 3.7. View of the sample and meter bars through the front vacuum viewport of the Z-Meter. Any infrared (IR) detector would have to operate from this location and require magnifying optics for accurate measurement of the thermal interface temperature drops and to resolve an accurate temperature profile along the sample.

distance due to the chamber viewport location require a considerable investment in infrared imaging camera and optics, which at this time are beyond the budget of this project. However, due to the benefits to be gained by having an infrared temperature map of the sample and interfaces, the system is designed in such a way that future compatibility with infrared measurement is possible by installing an appropriate viewport, camera, and optics. The sample location is aligned with the level of the viewport, and the radiation shields can be removed or modified to reveal the area visible in the field of view from the chamber window.

Once the non-contact options for temperature measurement were exhausted, the more traditional contact sensor technologies were investigated. The benefits to these sensors is that they are readily available, and generally much cheaper than the non-contact technologies. However, since these sensors require contact with the body of interest for the measurement, they can have a significant impact upon the process being measured if not carefully selected and installed.

Due to the indirect nature of temperature measurement, we are reliant upon the response of other properties that we can measure to temperature allowing us to infer the temperature within the system. One of the most widely exploited temperature-property relationships is that between temperature and electrical resistance. In many materials, the strong dependence of electrical resistance upon temperature can be easily leveraged to determine device temperature by passing a small current through a resistive device and monitoring the voltage level. Two main types of thermal sensors utilize this operating principle: thermistors and resistance temperature detectors.

3.4.2 Review of Contact Thermal Sensors

Thermistors

A thermistor, originally called a thermally sensitive resistor, is a semiconductor material that has a strong sensitivity of its resistance to changes in temperature and started to be commercially manufactured circa 1930 [63]. There are two main types of thermistors, positive temperature coefficient (PTC) and negative temperature coefficient (NTC). It is generally the NTC type thermistor which is used for temperature measurement, meaning the resistance of the sensor decreases with increasing temperature. While this operating principle is somewhat similar to that of RTDs, discussed next, thermistors devices are often orders of magnitude more sensitive to temperature changes [61]. First-order approximations can be applied accurately to describe the resistance-temperature relationship over small temperature regions, but to accurately describe the behavior of a thermistor over a wider temperature range, the non-linear

behavior of the thermistor's resistance must be captured in greater detail. A commonly used equation to describe the sensor response is the Steinhart-Hart third-order approximation

$$T = \left[a + bln(R) + c(ln(R))^3\right]^{-1}, \tag{3.3}$$

where a, b, and c are the Steinhart-Hart parameters defined during device calibration, T is the absolute temperature, and R is the electrical resistance. It is common to see Eqn.3.3 presented with a β parameter. This is done by setting $a = \left(\frac{1}{T_0}\right) - \left(\frac{1}{\beta}\right) \cdot ln(R_0)$, $b = \frac{1}{B}$, and $c = 0$, where R_0 is the resistance measured at $T_0 = 298.15\ K$ (25℃), which yields [63]: $\frac{1}{T} = \frac{1}{T_0} + \frac{1}{B} ln\left(\frac{R}{R_0}\right)$. Solving for temperature

$$T = \frac{\beta}{ln\left(\frac{R}{R_0 \cdot e^{-\beta/T_0}}\right)}, \tag{3.4}$$

which can be used in combination with the information given from the manufacturer's calibration if the β parameter is reported.

Despite this high sensitivity certain attributes of thermistors make them ill suited for use in the Z-Meter. Typically thermistors are selected to cover a relatively narrow range of temperatures due to the non-linearity of their response, nominally 0℃ to 100℃. While some thermistors are available with a larger range, none will cover the entire operating range of the Z-Meter. Many manufacturers list the maximum operating temperature for thermistors between 150℃ and 300℃ [64]. This narrow band of use precludes thermistors as a viable option for instrumenting the reference bars in the Z-Meter.

Resistance Temperature Detectors (RTDs)

When considering thermistors, we observed that the semiconductor material has a strong non-linear response with changes in temperature. This makes thermistors very sensitive to temperature changes, but only accurate over small temperature ranges. Resistance temperature detectors (RTDs) also work by utilizing the relationship between temperature and resistance for a material, but RTDs employ pure metals for

this purpose. The resistance response to temperature changes of pure metals is much less sensitive to temperature changes than that of the semiconductors used in thermistors, but with careful material selection, it can still be very accurate and hold this accurate relationship across a wide range of temperatures.

All metals experience an increase in electrical resistance with temperature, but only a few materials have the desired properties for use as RTDs. The temperature coefficient of resistance (TCR), α_{TCR}, is used to describe the slope of the relationship between resistance and temperature. The TCR can be approximated as constant over small ranges for some materials, but for other materials or any material over a wide temperature range, the TCR can itself take on a temperature dependence. In addition to requiring a strong, stable TCR, an RTD should also have a large nominal resistance for improved measurement stability and accuracy. This is because the signal level of the RTD, voltage drop measured with some specified sense current, is proportional to sensor resistance; therefore, a favorable RTD material will have a high TCR and a high resistivity. Materials with low resistivities can still be used as RTDs, but actions must be taken to ensure accurate temperature measurement [65].

The sensor resistance must be large (100 - 1000 Ω) for accurate temperature measurement since the product of TCR and nominal device resistance determines the sensitivity, which must be done geometrically. The electrical resistance can be increased by extending the conductor length and or reducing the conductor cross-sectional area, both of these can be problematic for implementation in a RTD. First, extending the conductor length requires considerably more material be used, which can increase the size of the sensor, slow the thermal response, and decrease the positional resolution of temperature measurement due to the larger sensor size. Alternatively the cross-sectional area of the conductor can be reduced to constrict current flow, thus increasing the resistance without adding more material to the sensor, but as conductors get smaller, they tend to be less durable and sensors are prone to damage or failure.

The operating principle of a RTD is the resistance measured for a device can be used to determine the temperature based on a calibration curve describing the resistance behavior across a temperature range. At the atomic scale, the temperature of a material is described through vibration of the atoms and molecules that comprise the material. Therefore, using Debye's theory of specific heat, the vibrational modes can be included yielding the Debye Temperature:

$$\theta_D = \frac{\hbar\omega_D}{k_B} \tag{3.5}$$

where $\hbar$ is Planck's constant, ω_D is the cutoff frequency, and k_B is Boltzmann's constant [66]. Ziman [67] shows that the Debye temperature can be used to determine the degree of dependence of resistance on temperature. If the temperature is high, ${}^{\theta_D}/_{T} << 1$, the resistance is proportional to temperature, but for low temperatures, ${}^{\theta_D}/_{T} >> 1$, and the resistance is proportional to T^5.

The Debye temperature for platinum is 240K from Table 3.1, so ${}^{\theta_D T}/_{<} < 1$, indicating the resistivity should scale linearly with temperature,

$$R(T) = R_0[1 + \alpha_{TCR}(T - T_0)], \tag{3.6}$$

where R_0 is a reference resistance taken at T_0, usually 0℃, and α_{TCR} is the temperature coefficient of resistance (TCR) [69]. Platinum is the most common metal used in RTDs, owing to its nearly linear TCR from -200℃ to 600℃, long-term stability, and material durability. Tungsten is another material that is used for RTDs, but in practice is generally only employed in high-temperature applications (T > 600℃) because it is acutely brittle and challenging to work. Additionally, some nickel alloy materials are use due to their low cost, but these exhibit high degrees of non-linearity and are subject to measurement drift during use [60]. Platinum is recommended for use in RTDs to be used in applications requiring accurate measurements and long life of the sensor.

As we are working in the Debye high-temperature limit, we have stated that the resistivity should have a linear scaling with temperature, but Fig. 3.8 shows a slightly

Table 3.1. Debye temperatures tabulated from low temperature heat capacity measurements. Unless otherwise noted, data is sourced from Kittel [66] *Indicates Hook and Hall [68].

Solid Material	θ_D $[K]$	Solid Material	θ_D $[K]$
Cs	38	Zr	291
Rb	56	Ga	320
Hg	71.9	Zn	327
Tl	78.5	Cu	343
K	91	Li	344
Pb	105	Sc	360
In	108	V	380
Ba	110	Mg	400
Bi	119	W	400
La	142	Mn	410
Sr	147	Ti	420
Na	158	Ir	420
Au	165	Al	428
Sn	200	Re	430
Cd	209	Co	445
Ag	225	Ni	450
Ca	230	Mo	450
KCl *	235	Fe	470
Ta	240	Rh	480
Pt	240	Os	500
Hf	252	Ru	600
Pd	274	Cr	630
Nb	275	Be	1440
Y	280	C (Diamond) *	2230

non-linear trend to the data. This discrepancy comes from the Debye prediction being for 100% pure platinum, while in practice trace amounts of contaminants are likely to be present. A linear relation still serves as a reasonable approximation of the temperature-resistance relationship across small temperature ranges; however, for precise measurements a higher order equation should be used, which accounts for non-linearities in the temperature-resistance relationship. When operating in larger temperature ranges, it is recommended to use a second order polynomial calibration equation as it better captures the slight non-linearity in the resistance - temperature relationship for platinum [69].

$$R(T) = R_0(-5.8 \times 10^{-7}T^2 + 39.08 \times 10^{-4}T + 1)\ \Omega \tag{3.7}$$

He shows that it can yield an accuracy better than 0.01℃ within a temperature range of 20 - 630℃; however, any impurities or variations between devices will introduce measurement uncertainty. As such, it is advisable to carefully calibrate each RTD for maximum accuracy of temperature measurements.

In addition to impurities or variations in the resistance sensing material leading to measurement uncertainty, the method of measurement can greatly impact the accuracy of the measurement. PtRTDs permit accurate measurement of temperature due to the relationship between temperature and resistance as described by eq(3.6-3.7) and shown in Figure 3.8; however, since RTDs require a current flow to measure resistance, the leads contribute to the measured resistance of the device if the voltage difference is taken where the current is introduced. Figure 3.9 illustrates the difference in the layout of the different measurement configurations for determining the resistance of the RTD. The two wire measurement method, Figure 3.9(a), will yield a measurement dependent on the characteristics of the lead wires which must be accounted for in the determination of temperature based upon resistance; however, in the four wire measurement scheme, Figure 3.9(b), the voltage drop across the device is measured via separate probes. This separate measurement of voltage minimizes the current that flows through the voltage sensing lines thus reducing the effect of the voltage leads. It is for this reason that the four wire technique is typically employed

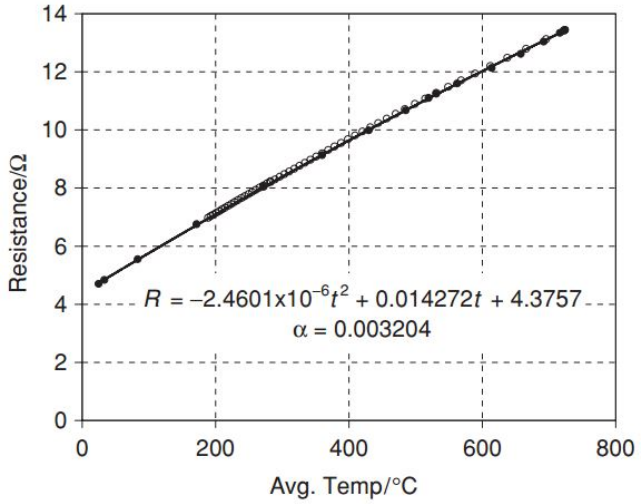

Figure 3.8. Resistance versus temperature curve showing the capabilities of a thin film PtRTD to perform temperature measurements. Measurements made at 5 minute intervals where solid dots are the heating points, while the open circles represent data collected during cooling. Pt = 0.77 μm thick, 900°C N_2 anneal [70].

to accurately measure resistances; however, the 2-wire technique can still be applied accurately in situations where number of wires or connections must be minimized. Application of the two-lead RTD measurement requires careful consideration of the contributions from the lead wires and appropriate adjustment of measurements to account for the lead resistance.

Thermocouples

While RTDs provide accurate and repeatable measurements up to a much higher temperature than what is achievable with thermistors, commercially available options are not available that will reach the desired temperatures in packages small enough to integrate into the reference bar without major distortion of the thermal profiles. The accuracy of RTDs will be leveraged else where in the system to provide refer-

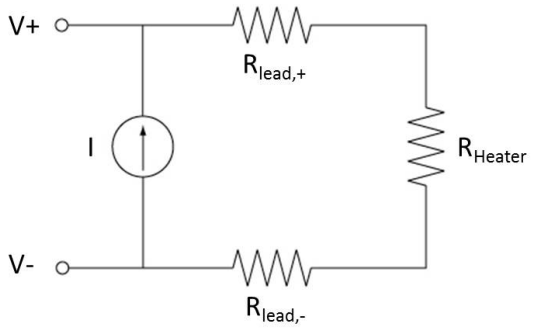

(a) Two wire resistance measurement electrical schematic.

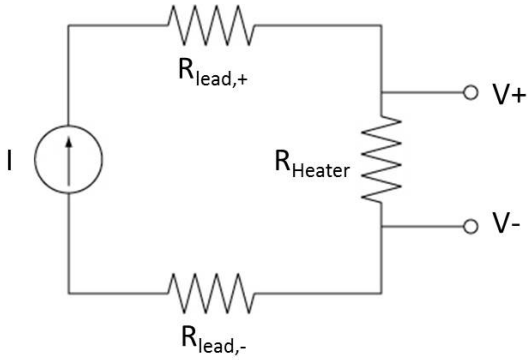

(b) Four Wire (Kelvin) resistance measurement electrical schematic.

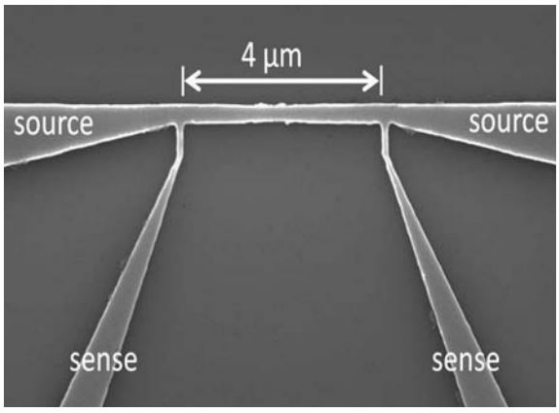

(c) Simple four wire sensing geometry implemented for temperature sensing for a thin film PtRTD [71]. Figure is reproduced under the permissions of the Open Access Publishing Agreement. © Optical Society of America

Figure 3.9. Comparison of resistance measurement configurations: (a),(b) schematically and an actual thin-film RTD.

ence temperature readings for the selected thermal sensor type, thermocouples, as discussed in the section detailing the cold junction compensation scheme.

Thermocouples are the most widely used form of temperature sensor due to their ruggedness, ease of implementation, and generally low cost. A thermocouple is physically a very simple sensor, two dissimilar wire joined together at the measurement

end. As such, the thermocouple can be tailored to the precise application maximizing the measurement accuracy for the specific system. Wire diameter can be selected to optimize the balance between probe conductance losses and response-time with drift, mechanical robustness, and long service life [59]. Thermocouple probes can be designed to be flexible for moderate temperature operation, rugged for durability, and easy to install for easy system maintenance; additionally, they are capable of measurement across a wide temperature range and are not subject to self-heating errors as seen with thermistors or RTDs [72].

In both thermistors and RTDs, the sensor operated based on a change in the resistivity of the material with temperature, allowing the resistance change to be monitored and mapped to a temperature relation. The operation of thermocouples is rather different due to the thermoelectric effects. When a thermocouple experiences a temperature difference between the ends, the Seebeck effect induces a current flow proportional to the temperature gradient. When the electro-motive force (emf) generated by this current flow is measured, a relationship can be determined between the emf and the temperature difference between the ends of the thermocouple. Determination of absolute temperature measurements requires the knowledge of the end of the thermocouple at which the emf is measured, also referred to as the cold junction. The major attraction of thermocouples is the simplicity, availability, and flexibility to specify a particular type of thermocouple to meet measurement requirements.

There is a vast array of thermocouples types for which published data is available, all made from distinct combinations of dissimilar metals and each with a slightly different purpose. In this wide range of thermocouple combinations, only twenty pairs are commonly used [59, 73]. Currently eight types of thermocouples are standardized under the international temperature scale of 1990 (ITS-90) [74], detailed in Table 3.2.

Five of the eight standard thermocouple types (E, J, K, N, and T) belong to a group called base metal thermocouples and all utilize nickel in at least one thermoelement. The alloys used for these thermocouples make them ill-suited for high-temperature measurement as intercomponent diffusion and preferential phase tran-

sition of lower melting point materials within the alloys cause substantial drifts in calibration. Additionally, these materials are known to readily oxidize at high-temperatures complicating or prohibiting the annealing process necessary to remove mechanically induced inhomogeneities [60].

Table 3.2. Standard thermocouple types and operating conditions [59–61].

Type	Thermoelements		Composition (wt%)		Temperature Range		$S\left(\overline{T}_{mean}\right)$	$S\left(T_{max}\right)$
	Positive	Negative	Positive	Negative	[°C]		$[\mu V/K]$	$[\mu V/K]$
E	Chromel	Constantan	Ni-9.5%Cr-0.5%Si	Cu-44%Ni	-270	1000	60	75.2
J	Iron	Constantan[1]	∼99.5%Fe	Cu-44%Ni*	-210	1200	55	28.6
T	Copper	Constantan	∼99.5%Cu	Cu-44%Ni	-270	400	37.5	61.8
K	Chromel	Alumel	Ni-9.5%Cr-0.5%Si	Ni-5%(Si,Mn,Al)	-270	1372	35	36.5
N	Nicrosil	Nisil	Ni-14.2%Cr-1.4%Si	Ni-4.4%Si-0.1%Mg	-270	1300	31	37.2
R	Pt-13%Rh	Pt	Pt-29.6±0.2%Rh	Pt-6.12±0.02%Rh	-50	1768	11	13.9
S	Pt-10%Rh	Pt	Pt-29.6±0.2%Rh	∼99.99%Pt	-50	1768	10	11.9
B	Pt-30%Rh	Pt-6%Rh	Pt-29.6±0.2%Rh	∼99.99%Pt	0	1820	7.5	11.7

[1]Constantan listed for type-J is not interchangeable with those for types-E or type-T.

Table 3.3. Non-standard thermocouple types and operating conditions [59–61].

Type	Composition (wt%)		Temperature Range		$S\left[\overline{T}_{mean}\right]$	$S\left[T_{max}\right]$
	Positive	Negative	[°C]		$[\mu V/K]$	$[\mu V/K]$
G	W	W-26%Re	300	2400	16.7	12.1
C	W-3%Re	W-25%Re	0	2400	17.1	9.9
D	W-5%Re	W-26%Re	0	2400	16	8.8
	Pt-20%Rh	Pt-5%Rh	0	1770	6.8	9.9
	Pt-40%Rh	Pt-20%Rh	0	1850	2.5	4.7
	Pt-13%Rh	Pt-1%Rh	0	1770	9.9	12.2
	Pt-15%Ir	Pd	0	1550	12	13.6
	Pt-5%Mo	Pt-0.1%Mo	0	1550	29	30
	Ir-40%Rh	Ir	0	2190	5.3	5.6
	Ir-50%Rh	Ir	0	2140	5.7	6.2
	Ir-60%Rh	Ir	0	2090	5.2	5
Platinel II (1786/1503)	Pd-31%Pt-14%Au	Au-35%Pd	0	1360	42.5	35.5
Platinel I (1813/1503)	Pd-14%Pt-3%Au	Au-35%Pd	0	1360	41.9	33.1
Geminol	Ni-20%Cr	Ni-3%Si	-18	1260	18.7	22.2
Tophel II/Nial II	Ni-10%Cr	Ni-2.5%Si	0	1260	40	36
Hoskins 3-G-345/3-G-196	3-G-345	3-G-196	0	1260	40.7	36
19 Alloy/20 Alloy	Ni	Ni-Mo	0	1260	55	59

Platinum-based Thermocouples

Thermocouples in this subclass are mainly used for precision laboratory measurements, calibration, and high-temperature measurements (T > 1000℃) due to their long life and minimal drift in calibration. The platinum-based thermocouples are the most stable of the standard types, but the pure platinum legs in both the R and S types is also the most sensitive to contamination of all the standard thermoelements [59].

Platinum-based thermocouples are more resistant to oxidation, permit measurement a higher temperatures, and for high-temperature measurements in air, have proved to be more reproducible than their base-metal counterparts. These thermocouples should not be used in reducing atmospheres nor in the presence of vapors. Generally metals protect themselves against these vapors by a native oxide layer, but platinum's resistance to oxidation leaves it vulnerable to contamination [75]. These noble metal thermocouples should not be inserted directly into metallic protection tubes as impurities can diffuse into the pure platinum leg. Darling and Selman [76] have detailed the effects of low oxygen partial pressure (vacuum) on type-S thermocouples in contact with Al_2O_3 (alumina) ceramic insulator at high-temperatures for extended operation. They find that vacuum environments accelerate the time to failure and the drift rate of type-S thermocouples when compared to operation in air, but find that around 1000℃ and below that the critical failure mode is due to impurities from the ceramic protection tubes. Within a standard oxidizing environment, platinum based thermocouples do not react with respect to refractory oxides, but when held below a critical level of vacuum, acute reactions can occur. Under these conditions constituents of the refractory dissociate (Al_2O_3, ZrO_2, and ThO_2), oxygen is generated, and platinum extracts the available metals from the refractories to form dilute alloys, but effects are much worse for small particle size refractories in contact with the metal (*i.e.* compacted powder insulation) [76]. While not optimal, the reactions that occur between platinum and pure alumina are not severe enough to

prevent effective use of these together in vacuum environments [76]. Another study on performance of noble metal thermocouples at high-temperatures in vacuum found that while the type-R thermocouples failed or drifted beyond the desirable bounds before their targeted 10,000 hour life goal, they still performed well for shorter periods of time. After approximately 1,600 - 2,000 hours of operation in vacuum at 1327℃ (1600 K), the type-R thermocouple had drifted between -1.5 to -4.7 K [77]. This drift will be considerably higher than what will be seen in the Z-Meter system because degradation and rapid grain growth occur most rapidly in the platinum thermocouples for temperatures over 1200℃ [59, 72], which should not be exceeded in the Z-Meter system.

Selection of Thermocouple Type

The primary sensors in the Z-Meter are type-S (Pt/Pt-10%Rh) thermocouples. Type-S thermocouples are used as an ITS-90 measurement standard for determining temperatures between 630.74℃ and the freezing point of gold (1064.43℃) [72]. This type of thermocouple is selected over the more widely used type-K thermocouple due to accuracy improvements with the type-S, but primarily due to the substantial drift seen in type-K thermocouples after prolonged use at high-temperatures and the serious issue of "green rot" [60]. Preferential oxidation or "green rot" corrosion happens for type-K thermocouples used in reducing atmospheres or vacuum. The chromium in the positive Chromel®(Ni-9.5%Cr-0.5%Si) thermoelement will oxidize forming chromium oxide, which appears as a green scale on the wire. This transitions the chromel wire from non-magnetic to magnetic and reduces the e.m.f. of the thermoelement resulting in a low temperature reading [59, 60]. In the case of type-S thermocouples, as long as they are properly annealed and fixtured in pure, contaminant free, housings for insulation, their performance at high-temperatures is quite good. The only drawback of type-S thermocouples is that they tend to have some drift issues when operated in vacuum environments. Type-B (Pt-30%Rh/Pt-6%Rh) ther-

mocouples are more stable in vacuum, and less susceptible to excessive grain growth at high-temperatures than either type-R (Pt-13%Rh/Pt) or type-S (Pt-10%Rh/Pt) as type-B has Pt-Rh alloys for both thermoelements, instead of the pure platinum negative lead used in both type-R and type-S thermocouples, resulting in more stable material properties and restricted grain growth at high-temperatures. However, type-B thermocouples have a very low emf at temperatures below 450℃, which becomes negligible between 0 - 50℃. While this can be nice since it does not require CJC for the sensors due to negligible fluctuations at room temperature, it means that these sensors cannot be used for reliable measurements beneath 450℃. This will not work because we need to keep the cold plate at 150℃ or less. The bar could be instrumented with different thermocouple types or sizes through out the zones of different temperature, and mechanical requirements. Material or diameter graded thermocouples such as this could further improve measurement performance within the system, but it would come at a price of substantially increasing the complexity of system management. The use of different thermocouple pairs along the meter bars would work perfectly fine for measurements of the system, and could be used to reduce sensor cost by confining the noble metal thermocouples only to the regions that truly require them. However, considering all aspects of the design and evaluating the available long term property data, type-S thermocouples are chosen for use in the Z-Meter. They are the standard measurement type chosen for high-accuracy reference measurements at high-temperatures, and considerable data is available on their operation and drift at high-temperatures in vacuum. Additionally, they will work well over the entire range of temperatures needed for the Z-Meter.

3.4.3 Design of Thermocouple Probes

The primary goal of thermocouple probe design is the accurate temperature measurement within the bar while minimizing impact on thermal profile impact due to probes. This is accomplished with fine gauge (40 AWG/80μm) type-S (Pt-10%Rh

vs. Pt) thermocouples housed in high-purity, 99.8%, alumina, double-bore sheaths [59,78]. Each probe sheath is 50.8 mm (2.000 in) long to minimize the temperature at which the thermocouple wires exit the sheath to avoid bends in areas of high thermal gradients, and helps to reduce conduction losses through the probes [60]. The thermocouple probes are mounted radially into the bar to probe the center temperature at prescribed distances along each bar. They are installed with an insertion depth of 7.3 mm (0.287 in). All bar thermocouple probes are aligned to the rear of the bar to avoid interference with the user during sample loading. No thermocouples are mounted in the sample to prevent distortion of the properties under investigations, and to simplify sample preparation which helps prevent complicated operating procedures from introducing additional error into the measurement. The two thermocouple probes closest to the sample interfaces have been further enhanced by milling a small relief down the outside of the sheath, which allows the tungsten electrical voltage contact to be tightly wound and fixed at the tip of the probe, while being easily routed out of the hole. This is done to ensure that the temperature of the point of voltage measurement is known precisely. The probes used for supplying the electrical sense current for measuring electrical conductivity have been carefully positioned at the extreme ends of the top and bottom meter bars to prevent localized distortions of the thermal and electrical profiles from impacting neighboring sensors.

3.4.4 Fabrication Procedure for Thermocouple Probes

The legs of the thermoelements are purposefully cut to different lengths for the purpose of easy polarity identification during the installation process. Each positive thermoelement (Pt-10%Rh) is cut to be approximately 12.5 mm (0.5 inches) longer than the negative thermoelement. The thermoelements are trimmed to the same length immediately before calibration. The difference in hardness between the pure platinum thermoelement (40 HV), and the Pt-10%Rh (85 HV) is used to verify the polarity of the leg prior to installation [75]. This is verified by holding the non-

Table 3.4. Recommended upper temperature limits for protected thermocouples. Reproduced, with permission from Park, R. M., & Hoersch, H. M. (1993). ASTM-MANL-12 — Manual on the Use of Thermocouples in Temperature Measurement: 4th Edition., copyright ASTM International, 100 Barr Harbor Drive, West Conshohocken, PA 19428.

Upper Temperature Limits for Various Wire Sizes (AWG), [°C]						
	No. 8	No. 14	No. 20	No. 24	No. 28	No. 30
Thermocouple Type	3.25 mm	1.63 mm	0.81 mm	0.51 mm	0.33 mm	0.25 mm
	0.128 in.	0.064 in.	0.032 in.	0.020 in.	0.013 in.	0.010 in.
T	-	370	260	200	200	150
J	760	590	480	370	370	320
E	870	650	540	430	430	370
K and N	1260	1090	980	870	870	760
R and S	-	-	-	1480	-	-
B	-	-	-	1700	-	-
C	-	-	-	2315	-	-

welded ends of the two wires between the thumb and forefinger of a gloved hand with about 100 mm (2.0 inches) protruding and gently press the two ends against against the back of another gloved hand. The negative thermoelement (pure platinum) will deflect considerably more than the positive thermoelement. This is done gently to avoid large deformations which might work harden the recently annealed wires. Any work hardening that occurs from this small test will have minimal impact due to the negligible temperature gradients in the wires at the cold junction compensation terminals. An alternative method is to simply connect the probe to a digital multimeter and heat the tip of the probe slightly with a heat gun. If the polarity is correct, then the voltage reading will increase, but if the polarity is reversed, the voltage reading will decrease. The thermocouple probe fabrication process is very detailed and a thorough step-by-step process description is provided for the reader

in Appendix A. This is done to aid with future instrumentation of the system when probe replacement is required.

Since the temperatures in the system will not exceed 1300℃, the drift in the thermocouples is due to two reversible processes over different regions of the temperature gradient zone. Low temperature hysteresis occurs due to the oxidation of rhodium in the positive (Pt-10%Rh), occurring around 450℃, and high-temperature hysteresis due to order/disorder arrangement of dissimilar atoms, lattice vacancies, and other defects which establish equilibrium levels quickly at high-temperatures, centered on 800℃ [59]. These effects (low and high-temperature hysteresis) occur in opposite directions; therefore, partial compensation occurs.

Above 1000℃, changes occur due to grain growth, the relief of cold work, and other microstructural changes. The rates of these types of changes decreases with time, thus it is possible to anneal the thermocouples prior to use to minimize changes. Cold-work affects the Seebeck coefficient and can lead to significant change due to handling and installation of the wires (particularly in the double bore sheathing). Most of the cold-work can be removed with a 1 hour anneal at 1100℃, but the Pt-Rh leg will retain some residual effects. Rhodium oxidizes above 500℃ and the oxide (Rh_2O_3) dissociates above 900℃ [60]. This results in a reduction in the Seebeck coefficient from 500 - 900℃, with the greatest impact at 800℃. After heating to 1000℃ the oxide dissociates rapidly and the Seebeck coefficient recovers [59]. The formation of the rhodium oxide is thus reversible and can potentially cause hysteresis.

Probe Details:

The thermocouple probes are fabricated in-house, using fine gauge (40 AWG/80 μm) Type-S, Pt-10%Rh vs. Pt, thermocouple wire (Omega SP10R-003), housed in high-purity, 99.8%, alumina, double-bore sheaths[2] (Omega TRX-005132-6). The wires are joined using a carbon electrode arc in an Argon shielding gas [61]. Each probe sheath is approximately 50 mm (2.000 in) long to minimize the temperature at which the thermocouple wires exit the sheath to avoid bends in areas of high thermal gradi-

[2]IDs: 127 μm (0.005 in), OD: 889 μ m (0.035 in)

ents, and helps to reduce conduction losses through the probes [59, 60, 78]. They are installed into the meter bars with an insertion depth of 7.3 mm (0.287 in). This depth is designed to center the thermocouple junction on the axis of the reference bar adjusting appropriately for the radius of the alumina potting cement used to seal the end of the probe after fabrication (Ceramabond 569).

3.5 Electrical Measurements

Due to the multiphysics nature of these measurements, many things happen simultaneously to accurately gather data during the experiment. Since the end goal of the system is to measure ZT, we know that three properties must be measured: Seebeck coefficient S, electrical conductivity σ_{elec}, and thermal conductivity κ. The Seebeck coefficient is determined by measuring the open circuit voltage across the sample while it is held under a thermal gradient:

$$S = \frac{\Delta V_{OC}}{\Delta T}. \tag{3.8}$$

It is crucial that the ΔT must be determined only across the sample, as interfacial conductances and probe offsets can adversely impact the measurement of the Seebeck coefficient. This requires characterization of the bar and sample interfaces to accurately account for both thermal and electric contact effects.

Electrical conductivity has traditionally been measured by bringing the sample to an isothermal state at the desired temperatures, then using a four-probe electrical measurement to determine the cross-plane resistivity of the sample. Bringing the sample to an isothermal state in this system would preclude the simultaneous measurement of the properties as thermal gradients are required for the remaining properties. Therefore, a four-probe DC electrical measurement is still conducted, but an external current source is used to perform a current sweep, while maintaining a fixed temperature difference across the sample. Utilizing a sweep of sensing currents through the sample, the voltage as a function of current can be used to evaluate electrical conductivity. It is important to keep the supplied current level small enough

to avoid Joule heating during the measurement or the voltage must be corrected based on the measured Seebeck Coefficient and sample temperature gradients. In general, the extrapolated intersection of the linear trend to the vertical voltage axis gives a secondary measured value for the Seebeck Coefficient, while the slope of the trend provides the ohmic resistance of the sample. The electrical conductivity can be calculated as

$$\sigma_{elec} = \frac{L_S}{R \cdot A_{C,S}}. \tag{3.9}$$

Note that in my selected materials, with large temperature gradients across the sample the ohmic contribution to the measured voltage drop is small compared to the Seebeck contribution, and ultimately even the relatively small variations in temperature with increasing current can significantly impact the data extraction for the electrical conductivity. Thus, we must evaluate a sweep across a range of currents and account for the varying Seebeck contribution when analyzing the electrical conductivity.

3.6 Heater

The heater used for this project is an Ultra High Vacuum (UHV) button heater with heat shield (P/N: 101251-01) manufactured by HeatWave Labs. The heater face (⌀ 1 in.), body, and stem are constructed of molybdenum. The resistive heating element is potted inside the molybdenum body using high-purity alumina potting cement and one lead of the heating element is internally brazed to the heater body, using the molybdenum as the electrical return for the current supplied to the heater. The heater is designed with a thin walled molybdenum stem that extends from the back of the heater body to provide thermal isolation and a mounting point for the heater. This molybdenum stem is mounted into the base of the heat shield assembly using two set screws. The heat shield assembly provides side and rear radiation shielding, a polished stainless steel body and molybdenum rear shields, for the heater to help increase efficiency by reducing radiative losses and incorporates a threaded bolt pattern for mounting the assembly in the system.

The heater is designed for UHV operation at temperatures up to 1200℃, with negligible outgassing, for operation periods exceeding 10,000 hours. Table 3.5 shows the nominal operating points for the button heater. The maximum design power for the heater is 190 W, which if used with the controller in the 16 V mode, yields a maximum operating current, $I_{max} = P_{max}/V = 11.875\ A$. The current level is further limited by the operating limits of the vacuum feedthroughs (F/Ts). The power F/T (Lesker P/N: EFT02V5068B) has a limit of 10 A per pin. A type-K thermocouple probe, 1.5

Table 3.5. Power table for the HeatWave Labs button heater, showing nominal operating points.

Temperature [℃]	900	1000	1100	1200
Voltage [V]	8.5	10.90	13.60	16.00
Current [A]	5.80	6.60	7.50	8.00
Power [W]	49.00	73.00	102.00	128.00

inches in length, is mounted inside of the stem of the heater contacting the back face of the heater and secured in place using radial set screws from the heat shield assembly, with the thermocouple leads extending from the back of the heat shield assembly. This thermocouple probe is used in conjunction with the HeatWave Labs temperature controller and power supply unit (P/N: 101303-23B). This proportional-integral-derivative (PID) temperature controller (Watlow P/N: PM6R1FA-1AAAAAC) permits programming of ramp and soak profiles for lower system stresses at startup compared to applying full power to the heater immediately. Autotuning is supported, but is not used for this system. Instead the PID controller is manually tuned to maximize performance for this particular system, with an achievable absolute accuracy of ± 1℃. The controller uses an oversized solid-state relay (SSR) for precise control and long life. Built-in fault protection incorporated in the form of a separate over-temperature alarm set point and an independent mechanical relay in series with the solid-state control relay. Since full high-temperature characterization runs will take many hours,

this feature is critical for the safety of the system as it permits safe remote operation and monitoring. If the critical temperature set point is reached, it trips the mechanical relay cutting power to the heater and preventing system damage due to temperatures exceeding design metrics. Additionally, the internal silicon-controlled rectifier (SCR) is short-circuit protected using a conventional fast acting 20 amp cartridge fuse (rear access) and a circuit breaker on the front panel provides over current protection to the system. Finally, the system is set up with a chamber interlock to provide open loop protection disabling the heater power if the chamber open is open.

This heater is designed as a non-contact radiation heater. This radiation gap provides very uniform heating to thin substrates, but a significant portion of the heater power is lost due to the surface properties of the heater and reference bar, as molybdenum's absorptivity of radiation in the 2 - 10 μm range is not sufficient to balance the system losses and achieve a hot side temperature of 1000℃ for the sample. A COMSOL multiphysics simulation is used to help model the radiative transport from the heater face to the bar and losses in the system. The heater face was set at 1200℃, the bar was held in close proximity ($\sim$ 0.5 mm) to the heater face, a 3 mm thick stand-in sample of lead telluride was installed between the upper/lower reference bars, and the cold plate temperature was set fixed at 200℃. The reference bar is approximated as a gray body and a total hemispherical emissivity of 0.1 is assigned to the top surface [79]. Without any modifications, at steady state, the top of the reference bar is about 600℃.

Due to the high-temperatures of the system and operation in vacuum, the available options for high emissivity surface coatings are limited and reliability data for high-temperature vacuum operation is even more scarce. After reasonable options for surface enhancement were exhausted, the remaining option was to operate the heater in contact with the bar. There are two major problems with this: heater passivation and mechanical loading.

3.6.1 Heater Passivation

The first problem is that the heater body is the current return path for the heater elements. This current would interfere with the low level electrical measurements across the sample, so the heater must be electrically insulated from the bar, while maximizing the thermal contact. The high-temperatures preclude the use of available electrically insulating thermal interface materials (TIMs) and high-temperature TIMs are mostly metallic foils which do not provide electrical insulation. Next I consider a direct deposition of a passivation coating on the heater face. This is attractive since it will electrically insulate the face of the heater while still providing an adequate thermal conductance pathway to the bar. The reason this passivation method is not implemented is the lack of long term durability and stability data for these films operating intermittently at high-temperatures in vacuum. Concern about damage to the film and electrical break through to the bar is a major concern, since the thermocouple probes, heat shields, and upper meter bar must be removed to access the heater. This would require the thermocouples to be recalibrated or replaced if grain growth in the platinum thermoelement progressed to the extent that it is too brittle to remove or install without damage to the probe.

The next best option is to use an intermediate material which is electrically insulating, but maintains a high thermal conductivity. The first obvious candidate for a high thermal conductivity electrical insulator is diamond, but due to availability and cost, this is not a suitable material for the system; however, there are two main materials that are commonly used in such applications: aluminum nitride (AlN) and beryllium oxide (BeO). Aluminum nitride has a thermal conductivity of 20 $W/m^2 \cdot K$ at approximately 750°C [80] and provides adequate electrical insulation from the heater face. Based on the trend for the thermal conductivity of AlN at 750°C, I expect the the value to be even lower than 20 $W/m^2 \cdot K$ for temperatures of order 1000°C. Alternatively, BeO has a thermal conductivity of 20 - 50 $W/m^2 \cdot K$ at 1000°C [80], while maintaining a sufficient electrical resistance. While the fired ceramic form of BeO is

safe for handling and use, BeO dust is carcinogenic and can cause Berylliosis through inhalation of or contact of dust containing beryllium with skin [81]. This electrical isolation disk is located inside an area of the chamber which is only accessible through a major system disassembly, and the probability of the BeO breaking is minimal since it is fully supported on both faces between the button heater and the upper reference bar. Due to the favorable properties and limited choice of other available materials, BeO is selected to use in the Z-Meter. The BeO (BeOceramic-5050048FG, MTI Corp.) is >99% pure and is ground to a thickness of 483 μm (0.019 in) with a surface roughness of 15-30 μm on each side. In order to enhance the thermal contact between the heater, BeO and reference bar, both sides of the BeO substrate are metallized with platinum to act as a high temperature TIM. The edge is scraped after deposition to avoid bridging of the metallized faces and guarantee electrical isolation between the two faces. This addresses the issue of the heater body being the current return for the heater driving current, but the mechanical loading of heater must still be addressed.

3.6.2 Mechanical Loading Bypass – Ceramic Loading Shroud

The heater body is mounted into the shield assembly by a very thin walled molybdenum stem that protrudes from the rear of the heater. This stem serves as a mounting point for the heater, houses the type-K thermocouple for feedback to the PID temperature controller, and serves as a means of thermal isolation for the heater body from the heat shield assembly and auxiliary fixturing. While this stem provides superb performance for the design conditions of the radiative heater, this feature may not be mechanically robust enough to comply with the full range of loadings prescribed in ASTM D5470, 0.069 - 3.400 MPa (10 - 500 psi) [26].

It is necessary to check that the heater stem is mechanically able to take the loading. This is done by considering column buckling for a hollow cylinder. The exact dimensions for the construction of the heater are not publicly available from

the HeatWave Labs, but through measurements of the heater features, we are able to estimate a range for the stem wall thicknesses: 0.254 mm to 1.27 mm (0.01 in. to 0.05 in.). This calculation initially assumes that the hollow cylinder is under perfect axial loading conditions (no eccentric loading). First the stem must be classified as a long column or an intermediate column to determine if the Euler formula for long columns or the Johnson formula for intermediate columns is applicable. This is important because Euler's formula for long columns will over predict the buckling failure load for intermediate columns. The applicable equation is determined by examining the slenderness ratio,

$$SR = \frac{L_e}{r_g}, \tag{3.10}$$

where $L_e = K \cdot L$ is the effective length which the original length, L, multiplied by the effective length factor, K, to account for the types of end connections (pinned, fixed, sliding, etc...), and r_g is the radius of gyration. The value at which the column transitions from a long column to an intermediate column is defined by the critical slenderness ratio

$$SR_{cr} = \sqrt{\frac{2\pi^2 E}{K^2 \sigma_y}}, \tag{3.11}$$

where E is the modulus of elasticity, K is the effective length factor, and σ_y is the yield strength. The critical slenderness ratio is defined as the value for the slenderness ratio for which the critical Euler stress, σ_{cr}, is equal to one-half of the material yield stress.

Some properties of the reference bar are required to evaluate Eq.3.10 and 3.11. The temperature dependent Elastic modulus and yield strength are obtained from the molybdenum supplier [54] . The plots are digitized using a code to extract the

plotted data from the scaled axes [82]. This data is then fit to polynomial equations for each property:

$$\begin{aligned} E(T,℃) &= -2.56545 \cdot 10^{-8}T^3 + 4.33749 \cdot 10^{-5}T^2 - 0.06988T + 331.22574\ GPa \\ \sigma_y(T,℃) &= 2.43424 \cdot 10^{-12}T^5 - 6.45742 \cdot 10^{-9}T^4 + 5.67750 \cdot 10^{-6}T^3 - ... \\ &\quad ... - 0.00179T^2 - 0.28415T + 580.94386\ MPa \\ \alpha_{CTE}(T,℃) &= 7.83673 \cdot 10^{-10}T + 5.10450 \cdot 10^{-6}\ \frac{m}{m \cdot ℃} \end{aligned} \tag{3.12}$$

where the Elastic modulus is fit with a third order polynomial and the yield strength is fit with a fifth order polynomial. The density is not provided as a function of temperature, so it must be inferred from given properties. The change in density with temperature is due to the change in volume with temperature. Since the coefficient of thermal expansion (CTE) is very low for molybdenum, nominally $5.5 \cdot 10^{-6}$ m/(m·K) [54], we can assume the expansion behavior of the stem is linear. The density of the molybdenum at room temperature is ρ_0=10200 kg/m^3, which yields the mass of the stem, m, when multiplied by the volume at room temperature. Considering a linear change in dimension with temperature, $\frac{\Delta L}{L} = \alpha_{CTE}\Delta T$, we determine the volume change with temperature as

$$\begin{aligned} A_C(T) &= \pi \left[(r_o(1 + \alpha_{CTE}(T)\Delta T))^2 - (r_i(1 + \alpha_{CTE}(T)\Delta T))^2 \right], \\ L(T) &= L(1 + \alpha_{CTE}(T)\Delta T), \\ V(T) &= A_C(T) \cdot L(T). \end{aligned} \tag{3.13}$$

With the impact of temperature on volume known, density is readily found by dividing the mass of the stem, which does not change, by the volume at each temperature to determine the density as a function of temperature:

$$\rho(T) = \frac{m}{V(T)}. \tag{3.14}$$

The radius of gyration can by found as, $r_g = \sqrt{I/A_C}$, where I is the area moment of inertia and A_C is the cross-sectional area. The area moment of inertia and radius of gyration for a hollow cylinder aligned with the axial direction are

$$\begin{aligned} I(T) &= 2\pi\rho L \int_{r_i}^{r_o} r^3 dr = \frac{\pi}{2}\rho(T)L(T)\left[r_o^4(T) - r_i^4(T)\right], \text{ and} \\ r_g(T) &= \sqrt{\frac{I(T)}{A_C(T)}} = \left[\frac{\rho(T)L(T)}{2}[r_o^2(T) + r_i^2(T)]\right]^{1/2}. \end{aligned} \tag{3.15}$$

Since the base of the stem is welded to the heater body and the other end is clamped in the heat shield assembly, it is appropriate to use fixed end conditions, and the American Institute of Steel Construction (AISC) recommended effective length condition, K = 0.65 (the theoretical value for both ends fixed is K = 0.5, but the AISC value has been shown to have good agreement with experiments and it builds in a slight safety factor) [83]. Calculations for the slenderness ratio yields values in the range, $0.3373 \leq SR \leq 0.4080$. Comparing these with the values obtained for the critical slenderness ratio, $167.52 \leq SR_{cr} \leq 321.26$. It is clear from this result that the stem can be evaluated as a long column. The critical load for a long column,

$$P_{cr}(T) = \frac{\pi^2 EI}{L_e^2} = \frac{\pi^3\rho(T)E(T)}{1.30}\left[r_o^4(T) - r_i^4(T)\right]. \tag{3.16}$$

Calculating the critical load across the range of possible wall thicknesses and over the entire measurement range of temperatures, as shown in Figure 3.10 we see that implementing the range of loadings necessary for the ASTM D5470 standard, loading up to 3.40 MPa, will exceed the critical loading for the stem at the high end of the operating temperatures. It is then necessary to incorporate a protection into the system design for the heater stem to avoid damage during system operation. This problem would be compounded for actual operation as this prediction does not include any eccentric loading effects, which would make the problem significantly worse.

The molybdenum heater stem is not designed for the levels of loading that are present in the system and is extremely sensitive to eccentric loading; therefore, the design must bypass the heater and load the bar directly to avoid damage. In addition to mechanical robustness, the loading structure must also have a low thermal

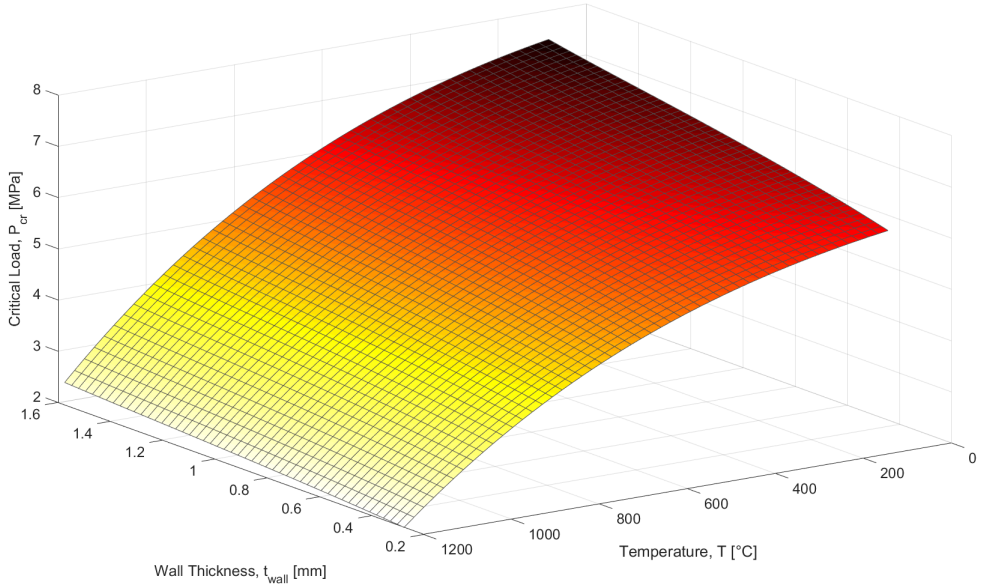

Figure 3.10. Plot shows the calculated critical loading level that will result in buckling over a range of possible stem wall thicknesses and over the entire range of operation temperatures. This calculation is based on the assumption of a perfect axially loaded hollow cylinder with both ends fixed, using AISC recommended effective length condition, K=0.65. Prescribed loadings for ASTM D5470 go up to 3.400 MPa, which is above the critical loading level for high-temperatures; therefore, buckling is possible.

conductivity to help reduces losses from the bar, and have a low CTE to avoid negatively impacting the reference bar alignment due to CTE mismatch during operation. In order to meet these operational requirements for the system, we designed a ceramic loading shroud (CLS) that the heater and heat shield assembly is mounted inside, with light preload for good contact with the bar, and the CLS becomes the mounting fixture for the upper reference bar. Finite element analysis of the CLS is carried out using material properties for the case of high-temperature operation. A design loading condition of 6.89 MPa ($\sim$ 1000 psi) provides a reasonable safety factor due to uncertainty in the as-fired properties of the ceramic used. Originally

we specify alumina ceramic for the CLS, but due to the machinability of alumina, we substituted alumina silicate ceramic. This material is not as good for thermal isolation as the alumina, but it allowed the part to be machined with standard tooling rather than requiring specialized diamond retooling. However, the long term effects of high-temperature contact between the alumina silicate and molybdenum are unknown. There is the potential for some silicon diffusion from the ceramic into the molybdenum after extended periods of high-temperature operation, but this impact is monitored by strictly adhering to a regular validation test schedule using a known properties sample. If the results drift from the known properties of the validation sample, the sensors and probes will be recalibrated. If the drift persists, the bar will be examined for drift from its calibrated property state.

In addition to the ceramic loading shroud, three tiers of thermal isolation platforms (TIPs) are used to mount the heater assembly from the top of the load frame. This is necessary to aid in the thermal isolation of the heater, directing the majority of the heat flow through the reference bars and sample while minimizing thermal losses to the load frame. Each tier of the TIP assembly is machined from 304 stainless steel. Stainless steel is selected over aluminum, which is about six times cheaper to machine, due to the lower conductivity of the 304SS, the higher rigidity which permits thinner features to be used further restricting the geometric heat flow pathways, while not compromising the mechanical integrity of the components. Each tier is connected with three ceramic standoffs. This scheme is selected because three points are required to fully constrain a platform, any more connections than this just add more conductance pathways for thermal losses. The only exception to this is the mounting between the CLS and the first TIP, the fixture ring. The mounting of the CLS required placement of through holes for bolts within 1-1.5 bolt hole diameters of the end of the cylinder, and necessitated undercutting of a lip around the edge for installation and space for the box wrench and nuts during installation. Due to these requirements, high localized stress concentrations are observed during FEM modeling of the CLS. I chose to address this issue by decreasing the size of the bolts used, thus decreasing

the clearance holes required in the CLS, and to accommodate the increased loads on each smaller bolt cross-section, more bolts were added. The net effect of loaded cross-sectional area is almost exactly the same, but reducing the bolt diameter permits a more uniform distribution of the load around the CLS and the smaller holes reduce the stress concentration near the outer edges of the CLS. Additionally, a 304SS load distribution ring is incorporated between the ceramic standoffs and the CLS which further helps to reduce stress concentration areas in the CLS, but also serves as the mounting point for the radiation shields. The mounting bolts from the fixture ring pass through the load distribution ring and and top lip of the CLS to be secured with titanium nuts on the underside of the CLS mounting lip. Titanium nuts were chosen to avoid the danger of galling between the 316 SS bolt and a stainless steel nut since the high-temperatures preclude the use of anti-seize in the vacuum environment. The other two tiers of the TIP assembly are discussed further in the section detailing design for thermal isolation within the system, 3.6.4.

3.6.3 Heater Wiring

The heater must be wired to the high-current feedthrough to supply power to the heater during operation. The heater supply/return conductors must be appropriately sized to handle the current levels required for the heater operation, but must be small enough to minimize the thermal losses through the conductor from the high-temperature heater. Power connections to the heater are simple enough: one connection is made to the supply line protruding from the back of the heat shield assembly, using a beryllium copper inline barrel connector (Lesker P/N: FTAIBC058), with a 20 A current rating and a maximum rated operating temperature of 400℃, while the other connection must be made to the heater body for the current return. This connection is made via a #6 non-insulated, R-type, nickel-plated OFHC copper ring terminal secured against the back face of the heat shield assembly using a nut threaded onto one of the mounting bolts.

The maximum operating current is 10 A, limited by the single pin current rating of the power F/T for the vacuum chamber. It is possible to raise this limit if additional heater power is required in the future by wiring multiple pins in parallel per conductor through the F/T. There are seven remaining pins in the F/T available for future use to increase current limit if needed, but a single pin is used per conductor at this time. The next task is to select appropriately sized connection wires for the heater supply and return. Several key items must be considered here. First, the conductors must be capable of carrying the current load in the vacuum environment. Second, the voltage drop along the total length of the wire cannot be too high. Third, the thermal leakage pathway for conductance losses from the heater along the wires must be minimized.

Selection of the correct wire size is fairly straight forward for operation in normal operating conditions. There are current capacity tables and the wire size can be directly selected from the current rating; however, these standard tables are not directly applicable to use in vacuum. The current capacity for a wire is defined to prevent the wire from getting too hot and melting its insulation or melting. So for use in vacuum, the wire will not be able to reject as much heat as one in air, because no convective cooling. This means the current capacity of the wire will need to be derated for use in a vacuum environment. The same is true for use in high-temperature environments, a wire cannot carry as much current at high-temperatures as at low temperatures due to limited heat rejection. Using the information regarding vacuum and high-temperature derating of current capacity from MIL-STD-975 and NASA/TM-1991-102179 , we build a model to estimate the thermal conductance and voltage drop in the heater connection wire. The 1-D model considers the electrical re-

sistance and thermal conductance of copper wire. Temperature dependent properties are considered, where

$$\begin{aligned} \kappa_{Cu}(T,℃) &= 8.181 \cdot 10^{-10}T^4 - 1.538 \cdot 10^{-6}T^3 + 8.906 \cdot 10^{-4}T^2 - ... \\ &\quad ...0.223T + 403.042 \ \frac{W}{m \cdot K}, \\ rho_{Cu} &= 1.68 \cdot 10^{-8} \ \Omega \cdot m, \text{ and} \\ \alpha_{TCR} &= 3.9 \cdot 10^{-3} \ ℃^{-1}. \end{aligned} \tag{3.17}$$

Since we are just modeling the conditions on the back face of the heat shield assembly, temperatures are on the order of 200 - 250℃[3], so the electrical resistance is approximated as having a linear dependence through the TCR to these values. The temperature dependent electrical resistance is defined as,

$$R_{Cu}(T,℃) = \frac{\rho_{Cu}L}{A_C}\left(1 + \alpha_{TCR}(T - T_0)\right), \tag{3.18}$$

where ρ_{Cu} is the electrical resistivity taken at room temperature (T_0). This resistance is used with the maximum design current to determine the worst case voltage drop across the leads to the heater by using Ohm's law. Next the thermal conductance must be considered for the wire to minimize heat losses from the heater. The thermal conductance is the reciprocal of the thermal resistance,

$$G = \frac{1}{R_{th}} = \frac{\kappa A_C}{L}. \tag{3.19}$$

The wire diameters used in the analysis are standard sizes corresponding to the American Wire Gauge (AWG). The AWG diameter is defined as

$$d_n = 0.005in. \cdot 92^{\frac{36-n}{39}} = 0.127mm \cdot 92^{\frac{36-n}{39}}, \tag{3.20}$$

where n is the gauge number [84]. Using Eq.3.18 and 3.19 we determine that that 14 AWG wire has the best balance between thermal conductance losses and this size is optimal for minimizing both heat losses and voltage drop at the same time, shown in Figure 3.11. While 14 AWG is shown to be the best balance for minimizing voltage

[3]This range is based on conversations with the company about the operation of the heater.

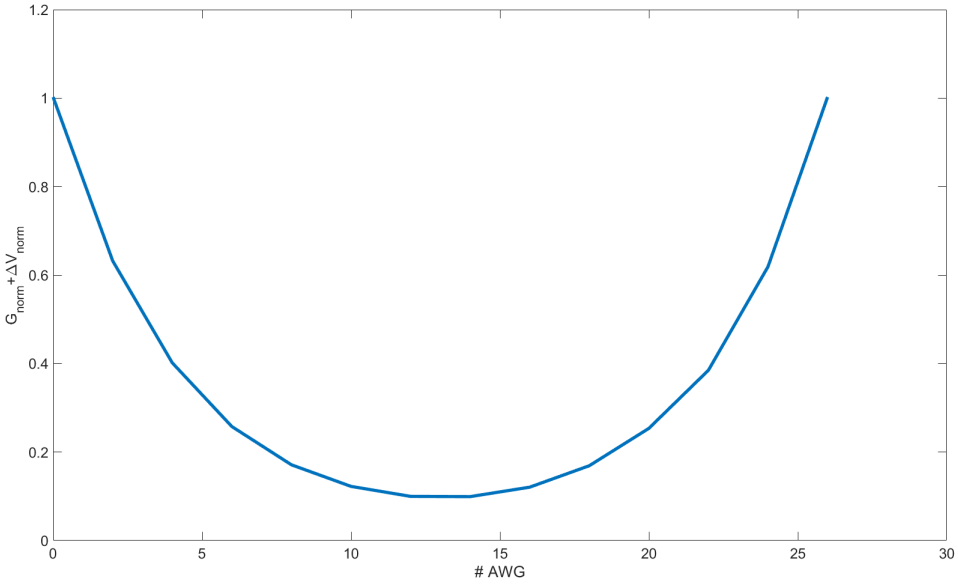

Figure 3.11. Minimizing the heat conductance losses and voltage drop for the heater wiring. The optimal point is found to be at 14 AWG, but the thermal losses for the system are more critical than a slightly higher voltage drop, so 16 AWG is chosen to help minimize the thermal losses from the heater while still keeping a reasonably low electrical resistance for the heater power control loop.

drop and thermal conductance together, the thermal losses are more critical to the system operation, so long as the voltage drop is not unreasonable. After further analysis and inspection, we determined that 16 AWG stranded OFHC copper wire with Teflon (PTFE) insulation will be adequate for use in vacuum as it has a derated current capacity of 13.0 A, providing a 30% safety factor. A smaller wire, 18 AWG, was considered, but it only has a derated current value of 9.2 A. While these estimates for current rating are conservative, the 18 AWG would not leave any safety factor in the system, so it was not selected. Selection of a wire size smaller than the co-optimal point indicated by Figure 3.11 does mean a higher voltage drop for the control loop, but the estimated voltage drop for the entire loop, approximately 10 feet (3.05 m), is

392 mV. This is only 2.45% of the supply voltage level of 16V, so the voltage drop will not have a noticeable impact on the performance of the system. Due to the limited heater power available and the size of the system we take great pains to minimize thermal losses and direct as much of the heater power through the reference bar as possible. The optimization of heater leads is just a small part of this effort which will be detailed next.

3.6.4 Thermal Isolation

The limited heater power in the system is important, because if sizable heat leaks exist, the sample will not reach the target operating temperatures. Additionally, even if the heater power was not the limiting factor, it is good design practice for a precision measurement to confine heat flow to the region of measurement. This is because as the heat leaks to the rest of the system thermal expansion can shift bar alignment, load cells are elevated out of their rated operating range, and system components/wiring can be damaged due to high-temperatures. So thermal isolation of the heater and upper reference bar are critical to system performance. The thermal isolation platform (TIP) assembly was introduced in Section 3.6.2 to highlight the design of the interface between the CLS and the TIP assembly. Figure 3.12 shows the TIP assembly at the top of the load frame. Each level is connected using alumina silicate ceramic standoffs with vented bolts to hold the platforms together. The vented bolts are not used here for void volume venting like in blind holes, but rather they are used since they have a reduced thermal conductance as compared with solid bolts, which further helps to isolate the high-temperature region from the rest of the system.

3.7 Thermal Radiation Shielding

Losses due to fixturing and radiation prevent the bar from reaching high-temperatures. The losses due to fixturing are addressed through careful design of the TIP assem-

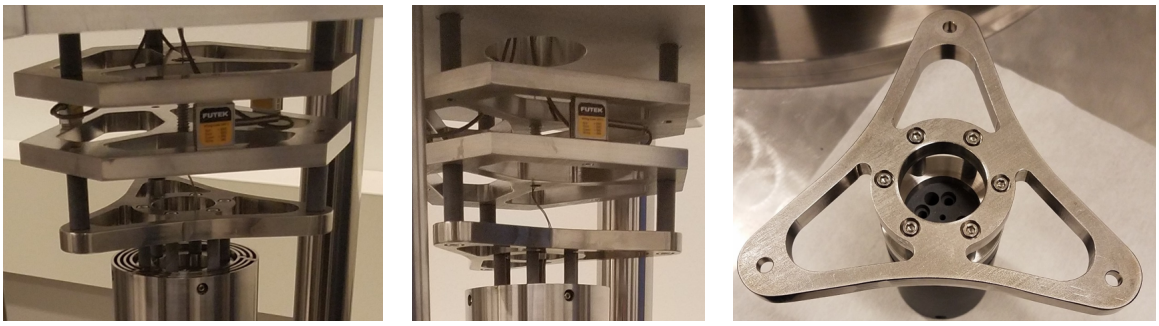

(a) TIPA 1 (b) TIPA 2 (c) Fixture Ring

Figure 3.12. A tiered design is adopted for thermal isolation of the upper bar and heater. Here the thermal isolation platform (TIP) assembly is shown. The top two layers of the TIP assembly house the load cell triad. Each tier is connected using alumina silicate ceramic standoffs with vented bolts to hold the platforms together.

bly, heater wiring, and probe conductance, now we address the radiation losses. One way to reduce losses due to radiation at high-temperatures is to reduce the surface emissivity through polishing or application of a low emissivity surface coating. The bars have been polished, which reduces the emissivity from that shown in Figure 3.6 to a value of approximately 0.05 at 1000℃ [79]. Another way to suppress thermal radiative losses is to add radiation shields around the bars to reduce the temperature of the surroundings seen by the surface of the reference bar.

3.7.1 Overview of design for banked radiation shields

The vacuum environment suppresses most convection losses, and it is easy to verify that the effects of air conduction under this high vacuum environment are negligible. The thermal conductivity of nitrogen at 1 $\mu Torr$ is many orders of magnitude lower than that of the bar, thus the impact of any losses due to gas conduction will be substantially below my measurement sensitivity. The remaining mode of heat transfer to consider for losses is radiation, which is quite significant in my analysis due to the high-temperatures. Radiation occurs for any surface that has thermal energy, *i.e.* has

a temperature above absolute zero, but radiative losses are generally only significant for cases of large temperature differences, which is the case in this system. The top meter bar is heated to approximately 1400 K, but is enclosed in a vacuum chamber which must have the walls kept cooler than 343 K (70℃) to comply with ASTM C1055-03 for safe operating temperatures for equipment accessible to humans [85]. As a further safety precaution and comfort consideration for the researchers using the system, the target operating temperature for the exterior chamber wall is set to 40℃. This creates a significant temperature difference under which radiative losses can influence the measurement. The solution is to add radiation shielding layers between the central bar and the chamber walls to reduce radiative losses from the bar.

3.7.2 Shield Design

The required number of shields is determined by considering the trade-off between available space and the diminishing returns of adding more shields. Figure 3.13 shows the percent reduction in radiative heat transfer against the case without any shielding. A clear benefit is seen for the initial shields, but the shielding improvement sees an asymptotic limit as the number of shields increases.

Conduction along the shield leads to re-radiation from the shield to the bottom bar acting as a thermal shunt around the sample. This is problematic because the heat flow through the sample is based upon heat flow through the upper and lower meter bars. If some heat from the upper bar is bypassing the sample by means of the heat shield, this will significantly impact the measured value for thermal conductivity. Additionally, a single shield would require excessive platform movement for sample loading and block the view for sample-bar alignment with the upper reference bar. In order to address this issue, the shield is split into several banks to minimize the problem of axial shield conduction resulting in re-radiation from a hotter shield to bar/sample. While the division of the thermal shielding into banks greatly improves

performance, it does not completely solve the issue of re-radiation from the shield to the bar. This is because the inner-most layer of each shield approaches the average temperature for the bar it is around as the system goes to steady state. The average temperature for the bar is by definition hotter than the coldest point on the bar which results in parallel pathways for heat flow along the bars. One path is the desired conduction pathway used to measure the heat flow through the sample, but the other pathway involves the radiation from the bar to the heat shield at the top where it is hottest, then the shield rises in temperature, becoming hotter than the lower portion of the bar, and radiates heat back to the bar at the lower portions. This problem is most noticeable at the highest operating temperatures. I take measures to minimize this issue by using materials with low thermal conductivities (316 SS) and polishing the surfaces of the shields to reduce emissivity. Due to the design, the shields are thicker than is ideal, but this was required to reliably weld each shield bank together for mounting in the system. Thinner shield thicknesses could improve system performance by reducing the axial conduction along the shield.

Based upon size and manufacturing limitations, banks of five shields are installed around the meter bars, while a bank of four shields is installed around the upper ceramic loading shroud. This banked shielding scheme provides a 99.9% reduction in radiative losses over the case of zero shields. These shields are installed in three separate banks to limit the effects from reradiation from the shield to the bar. Segmenting the shields serves to provide isolated shielding for the heater, upper bar, and lower bar respectively. The addition of the shields drastically reduces the impact of the radiative losses upon the measurement parameters and allows the system to reach higher operating temperatures at the sample interface with the power available to the heater. However, even with the shields in place, radiation still must be accounted for during the analysis.

Three banks of concentric radiation shields are used in the Z-Meter. The largest attaches to the load distribution ring at the top of the ceramic loading shroud (CLS) to suppress radiation losses from the shroud. The upper radiation shield bank is

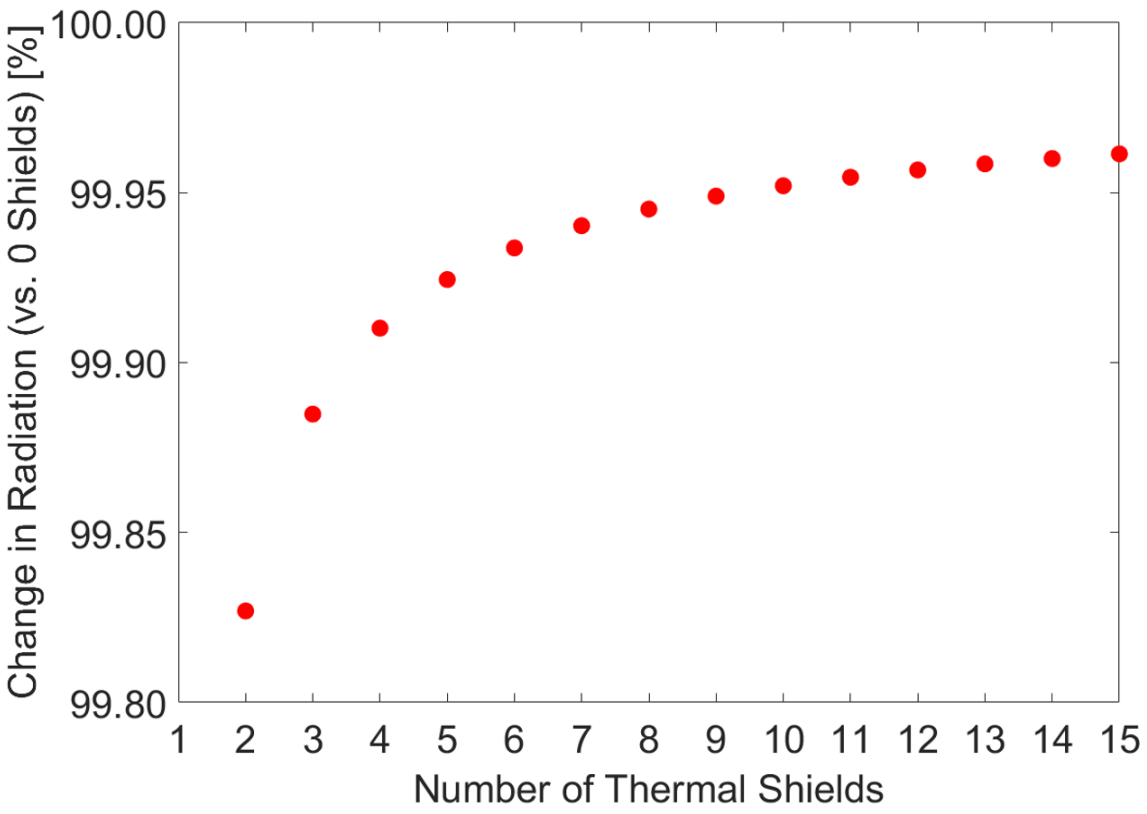

Figure 3.13. Percent change in radiative heat flow as a function of the number of shields added compared to the case of no shields. This calculation is for a Molybdenum bar with surface emissivity $\varepsilon_{Mo} = 0.1$ and a 304L stainless steel shield with a surface emissivity of $\varepsilon_{SS} = 0.075$. The spacing between shields was held constant at 5 mm.

contoured to the shape of the upper reference bar with both horizontal and vertical shields. This is necessary to minimize heating of the shield assembly from the necked region of the meter bar which otherwise is exposed to the end and axial view of the concentric shields. This upper bar shield assembly is mounted to the CLS shield bank by use of doubly threaded joints. Doubly threaded joints are when both bodies being joined are threaded. Typically bolted joints have a through-hole and a threaded hole, or two through holes and a nut is used both of which allow the joint to be compressed creating a strong fastening point. A doubly threaded joint locks the distance between

Figure 3.14. The three banks of concentric radiation shields used in the Z-Meter. The upper bank for the ceramic loading shroud (CLS) also serves as the mount for the upper bar shield.

two bodies since the fastener engages in both holes. When this is done from multiple sides of the cylinder, it fixes the upper radiation shield bank in the center of the CLS shield bank. In addition to providing a clean and compact mounting scheme in the system, it also serves as an effect means of further thermal isolation of the upper shield bank. This mounting requires specific layers of the shield assemblies to be threaded. The CLS shield bank has through holes on the outer three layers, while the inner-most shield is threaded for all four holes at the top and at the bottom (eight total).

Only three points are required to fix and define the position of the shields, but achieving 120° repeatable alignment across all nine vertical layers that comprise the CLS and upper bar banks proved to be unfeasible. Due to the precision alignment required to successfully mate parts in this manner, four holes were drilled. While

(a) Upper Bar Heat Shield - Bottom View

(b) Upper Bar Heat Shield - Top View

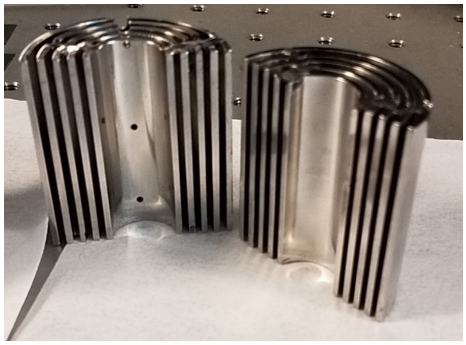

(c) Lower Bar Heat Shield - Split

Figure 3.15. The banked heat shields are constructed of concentric polished stainless steel tubes TIG welded together in three locations at the top and three at the bottom to minimize conduction pathways between the shields while maintaining structural form. The top of the upper bar shield bank is contoured with horizontal shields to prevent the necked portion of the reference bar from radiating energy to the outer shield layers. The lower shield bank is split to make installation and alignment of the sample easier.

it is difficult to achieve repeatable 120° angular positioning across all shield layers during manual machining, parallel or perpendicular alignment to other hole locations is substantially easier.

Concentric alignment of the upper bar shield bank to the CLS shield bank is crucial because there is little clearance between the inside of the upper bar bank and the surface of the bar. The detailed alignment procedure for the shields is included in Appendix D.

3.8 Mechanical Loading

This system is the first Z-Meter system to permit *in situ* adjustment of sample interfacial loading without breaking vacuum. This is important as it allows the contact to be monitored during a test, and adjusted between test runs to keep the loading at the optimal value over the entire temperature range, since loading will increase as

the temperature increases due to thermal expansion of system components. Alternatively, the adjustment can be used to change the loading completely and investigate the pressure dependence of the sample and contacts.

3.9 Load Frame and Loading Mechanism

Due to the geometry and over hanging lip of the vacuum service well, the base of the load frame had to be substantially undersized for the bottom of the chamber (to permit it to fit past the lip of the service well), leaving no direct means of securing the frame in place or confining it to the center of the chamber. The problem this presents is serious, the high power vacuum F/T for the heater lead is exposed on the inside of the chamber. I have implemented a detailed standard operating procedure (SOP), which takes steps to keep the user from having any power available to the chamber while the hoist is up (chamber is open) through use of a system interlocks hardwired to the heater power supply. Additionally, we have a mechanical relay which automatically opens, cutting power to the system, if the chamber is opened and the heater control unit is powered on. However, if the aluminum base of the load frame somehow shifts and comes in contact with the exposed power feed through, for instance while the chamber is open and something gets moved, the user might not notice as there is no power applied to the feed through since the chamber is open, but if they then close the chamber and try to apply power to the heater, the load frame now forms a conductive pathway from the feed through to the chamber walls, the cart, and adjacent equipment which could put the user at risk of injury. There are several safety precautions built into the system such as 20 amp fast blow cartridge fuses for fault protection against short circuit events and a circuit breaker on the front panel of the heater temperature controller protects from over current as previously discussed at the beginning of Section 3.6. The chamber will be grounded as a further safety precaution. User safety is my primary concern, which is why we felt it necessary to leverage the system design to minimize all possible risks to the users. If it is possible

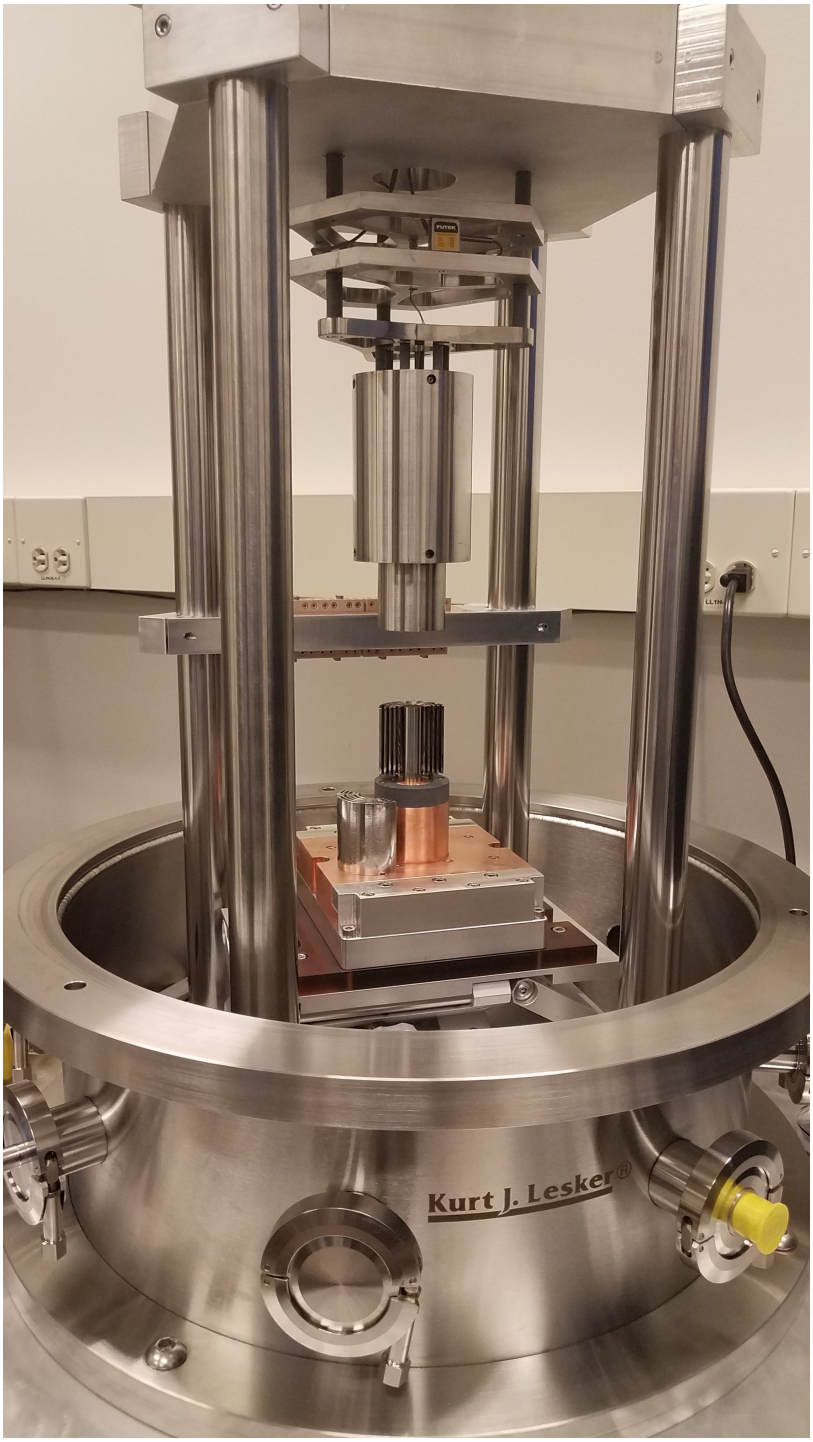

Figure 3.16. Z-Meter system during assembly. Here the split lower shield is clearly visible. This permits better access to the user for sample installation and alignment to the lower bar. The shields sit on precision mounting pins in the alumina silicate mounting ring on the lower copper bar mount.

for the load frame to contact a live power lead, then the risk is unacceptable even with the layers of safety precautions as safety devices can fail or a user could be in contact with part of the metal cart or outside of the chamber when they turn on the heater power supply. In short, an unconstrained design for the load frame in the vacuum system carries a possibility of injury, which must be minimized to create the safest tool possible for the user and protect the tool from damage. I address this serious problem with multiple layers of redundancies to ensure complete user safety and optimal system operation. First, after the load frame plates were machined, we masked the sides, the machined boss mount surfaces for interfacing with the load frame bars, and plugged the threaded holes using set screws to protect the threads from damage. Then, we bead blasted the large top and bottom areas to create a uniform, slightly textured surface. This textured surface is less prone to sliding on the machined service well base plate than a smoothly machined surface, especially when the textured surface is combined with the heavy weight of the load frame. Bead blasting is utilized instead of sand blasting because utilizing the small glass beads provides a more uniform finish. It is important to mask the boss faces where the load frame bars mount to preserve the precision flat surface carefully machined to ensure perpendicularity between all for bars and the frame base to guarantee a precise fit with the top platen. The importance of masking the sides, particularly the radii, of the frame base is directly related to the next layer of redundant safety.

The bead blasting of the frame base provides some improvement to the safety of the system, but it does not actually keep the load frame centered in the service well. This is important for several reasons, first, there are dozens of small diameter signal cables that are connected between terminals on the load frame and the electrical F/Ts of the vacuum chamber. These cables are delicate due to their size and should not be strained by pulling on them through the movement of the load frame in the system. Similarly the flexible convoluted metal tubing used to bridge the dynamic gap between the in-vacuum tube assemblies and the cold plate mounted on the lab jack require very thin walls to maintain such flexibility. In addition to the convoluted

tubes, there are orbital welds in the heat rejection system (HRS) in-vacuum tube assemblies. These tube assemblies are routed around the load frame and mounted in two insulating clamps on the back to prevent the movement of the lab jack from pulling on the cantilevered tubes and subjecting the welds to bending moments. Subjecting orbital welded tubing assemblies to bending moments from the load frame being moved around repeatedly combined with the high pressure differentials that the tube experiences during operation in vacuum, puts the system at a high risk for a coolant leak into the vacuum environment. Therefore, it is essential that the load frame is fixed in position inside the chamber.

The base of the load frame is made from a 2.000 inch thick plate of 6061-T6 aluminum, which cannot be welded in place inside the 304 stainless steel vacuum chamber using standard welding methods. Stainless threaded boss tabs could be welded into the system, then components secured to these, but it could limit future versatility of the system for adaptation to new components or testing methodologies. Instead we developed a novel system to confine the load frame to the correct central position and prevent its translation withing the service well without any form of attachment to the service well. Utilizing a similar concept to kinematic mounts often seen in optical systems, we are able to position the load frame in the center of the service well and keep it from coming into contact with any of the vacuum F/Ts. This mounting system leverages the inner curved surface of the vacuum service well, the base of the load frame with my carefully designed radii, and four pairs of spacing cylinders to place around the base. I machine pairs of ($\varnothing$ 1.500 in.) stainless steel cylindrical spacers, to the same height as the thickness of the load frame base (2.000 in.), from the same stock used to turn the load frame bars. I chamfer the bottom edge to avoid any contact with internal welds on the vacuum chamber, drill and thread holes on top of these spacer cylinders, and connect each of the pairs with an aluminum rigid coupler using a vented hex drive flat head screw. These couplers hold the cylinders the perfect distance apart for each to make one line of contact with the wall of the service well and the another contact line with the radius of

the load frame base. The tangent alignment devices (TADs) drop in and lift out, without tools or disassembly of other parts of the system. They are designed this way to avoid the need for additional assembly or disassembly inside the vacuum chamber where fastener might be dropped and roll into the port where the turbo-molecular pump is at the back of the chamber. Additional precautions and features implemented for the protection of the turbo-molecular pump are discussed in Section 3.11.2. Implementation of the TADs creates a system that cannot be easily shifted into a high power electrical F/T resulting in a more robust design and a safer system.

Another concern for the experiment is the alignment of the bars to the sample, so great care is taken during the fabrication and assembly of system components to maintain alignment within the ASTM D5470 specification of bar faces being parallel to within 5 μm [26]. All parts are toleranced in such a way as to minimize the impact of tolerance stacking and insure proper bar alignment; however, there is some variability that must exist in a system with this many parts which are connected between the mounting for the top and bottom bars. Each of these parts that must be connected has some variability built into its final position in the system due mainly to the through hole tolerances when assembling the components. Instead of drastically increasing machining costs by holding extreme tolerances for all components throughout the system, we elected to hold consistently tight tolerances, but not over machine the system to accomplish my alignment goals. Instead, we assemble the system, then utilize the available few thousandth of an inch in play for both the top and bottom bar assemblies to bring the bars into alignment. A detailed procedure for bar alignment is presented in Appendix C. This procedure was completed verifying that the bar faces are parallel to within 5.08 μm (0.0002 in.), further refinement of this procedure could be achieved by using a 0.0001 in. step go/no-go gauge instead of a 0.0002 in. step.

Finally, the system must be capable of axial loading of the sample and bars to overcome the interfacial contact resistance for the electrical and thermal measurements. A loading system, shown in Figure 3.16, capable of applying interfacial pressures up

to 10 MPa at the sample was designed and implemented. The design of this loading system departs from all previous Z-Meters in that it keeps the top bar fixed and moves the bottom bar to provide loading to the sample. This feature proves to be very important for many reasons throughout the system. The most noticeable improvement is that this design permits the loading control to be easily moved outside of the vacuum chamber by connecting the lab jack (Newport 281-V6[4]) lead screw to a rotary F/T via a sliding universal joint and two precision axles allowing the user to adjust the interfacial loading without breaking vacuum or cooling the system down. Holding the top bar fixed and only moving the bottom bar is advantageous for many other reasons as well. Now that the top bar is fixed, it eliminates the need for linear/sleeve bearings to be installed for the top plate, as is common for other systems. This eliminates the slight play that exists in sliding bearing setups and avoids the necessity of compliant bearing mounts to avoid jamming of bearings/guide rails during movement. Additionally, to achieve interfacial pressures of 10 MPa, a considerable amount of weight, approximately 136 kg (300 lbs), would need to be applied to a dead-weight style system where the top bar provides the loading. Moving this much weight into/out of the system can be dangerous since it must be lifted to a height of over 1.5 m (5 ft) to install it on top of the load frame. Incorporation of the lab jack into the loading design makes the system less prone to damage of someone dropping the upper assembly and bar into the lower bar, or injuring themselves while moving the assembly into place. Some previous systems use a screw loading system, and while this is much safer than the dead-weight design, it still requires the vacuum chamber to be vented for adjustment and prohibits adjustment of the load during the test. In contrast to previous system, my bottom actuated loading design makes alignment of the sample much easier due to the fine adjustment of the sample loading with a control knob and the user being able to keep the sample in view while dialing in the bar contact.

[4]This is a high-vacuum compatible version of the standard high capacity 281 lab jack.

An added benefit of the bottom actuated loading bar is it minimizes any movement of very the thin thermocouple lines for the highest temperature sensors due to increased error resulting from any cold working and induced strain in the thermocouple leads. A consequence of moving the bar actuation to the bottom of the chamber is that the cold plate for the heat rejection system (HRS) must now move up and down, thus requiring flexible fluid lines in the vacuum system. This minor complication is addressed in Section 3.10 detailing the HRS design.

A triad of high vacuum compatible s-beam load cells (FUTEK LSB200 - QSH01649) are installed to measure *in situ* axial loading of the sample. Our design incorporates three load cells to achieve optimal system performance for measuring the interfacial load. Dividing the load improves the measurement accuracy over that possible with a single load cell because sensors with a smaller range and higher accuracy can be used, thus reducing the overall measurement error for the axial load. The reason for using three load cells was to fully constrain the meter bar, but avoid over constraint of the system. Unlike the use of one or two mounting points, three points of contact fully constrain the column location, but do not over constrain it like a quad mount would do. Avoiding over constraints in system mounting helps to prevent offsets between the applied load and load measured due to physical constraint. Finally, the use of several load cells spaced around the loaded column permits monitoring of load uniformity throughout the test, as any eccentric loading will be registered by a change in loading between the triad.

3.10 Heat Rejection System

The heat rejection system (HRS) consists of a pumped fluid loop to remove heat from the bottom of the bar through a cold plate and reject this heat outside the chamber at the chiller. The cold plate (MaxQ 001-MXQ-01) is aluminum, with internal heat transfer enhancing fins, as shown in the sectioned view, Figure 3.19, and is friction stir welded to form a high quality weld which will not leak or fatigue over-

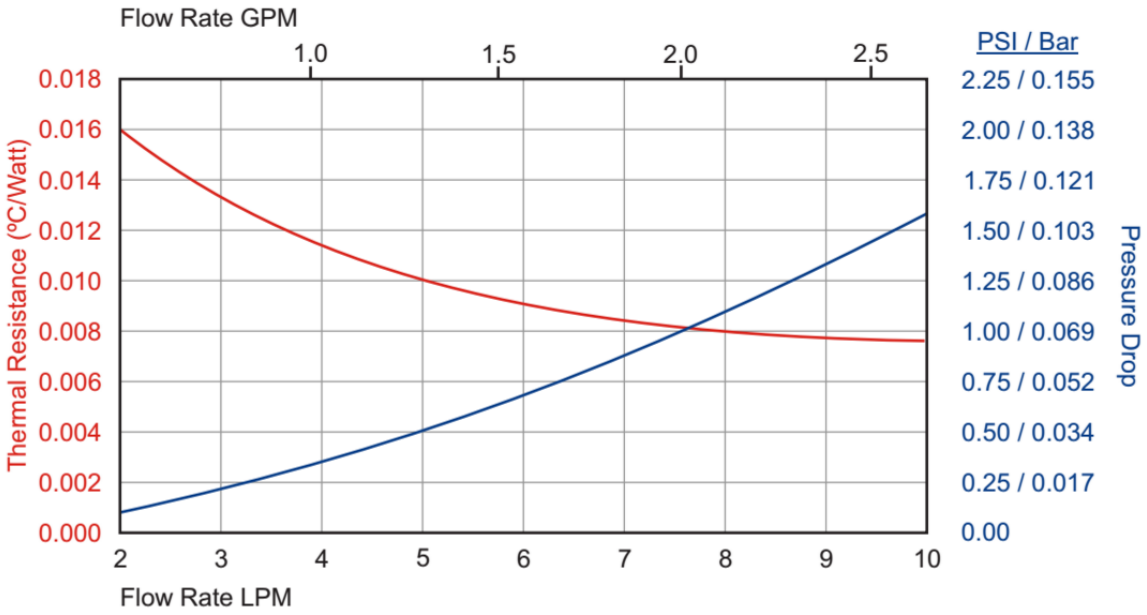

Figure 3.17. The performance curve for the MaxQ coldplate (001-MXQ-01) for a 50% ethylene glycol/water coolant mixture. The thermal resistance values are calculated based upon the difference between the maximum coldplate temperature and fluid inlet temperature. The pressure drop calculations include two 1/4-18 NPT hose barb fittings. Courtesy of MaxQ Technology [86].

time even with normal loading of the surface at high-temperatures. The surface of the cold plate is machined flat to within 0.025 / 25.4 mm with a maximum finished surface roughness of 0.8 μm. This ensures good thermal between the cold plate and the copper mounting base for the bar.

3.10.1 System Flow Tubing

An often over looked design element is the routing of the fluid lines for removing heat from a chamber, but this can prove an important part of the system design. First consider tubing on the outside of the vacuum chamber. The tubes will reach temperatures of around 150℃ which means that sensitive signal conductors must be

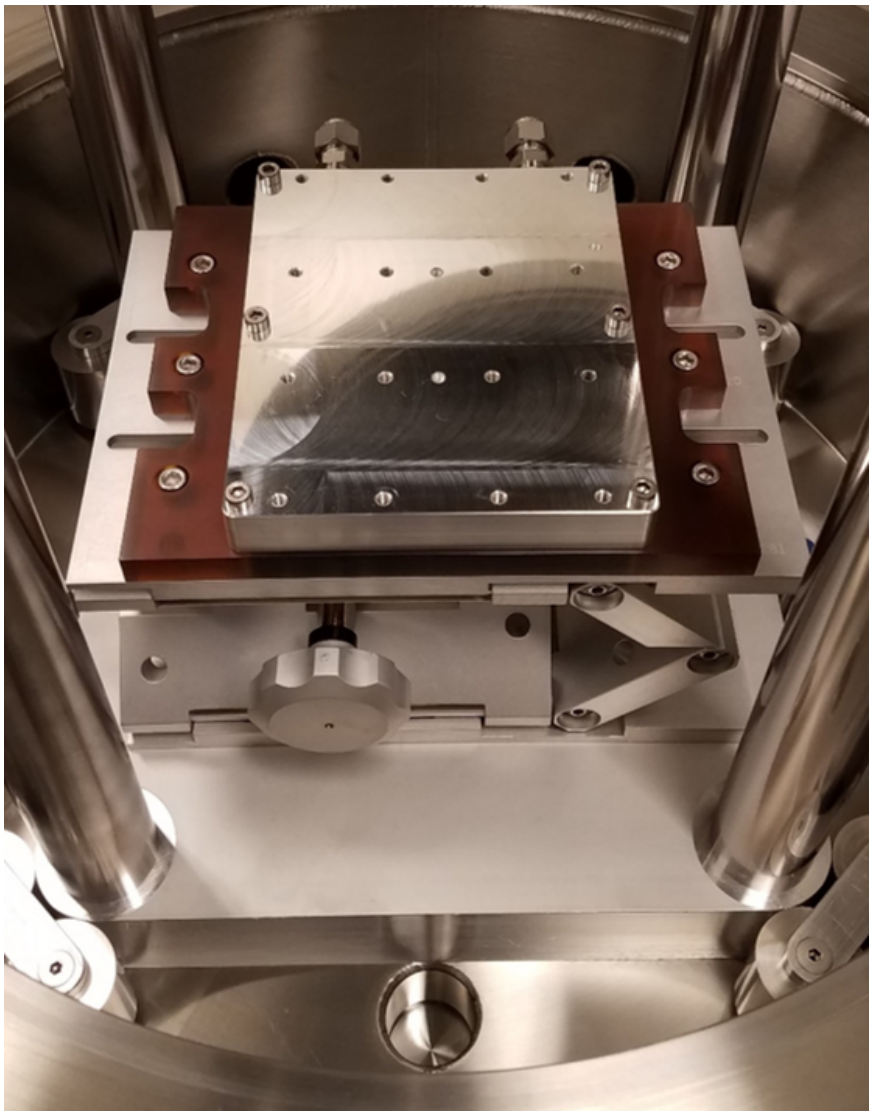

Figure 3.18. View of coldplate surface, machined flat to within $^{0.025}/_{25.4}$ mm, with a maximum surface roughness of 0.8 μm for good thermal contact with copper base mount. The top has threaded holes distributed over the face to keep the surface in intimate thermal contact. The shallow holes seen on this surface in three places are where the friction stir weld joints were inspected, these void volumes are vented from channels on the bottom of the copper base plate to avoid slow virtual leaks.

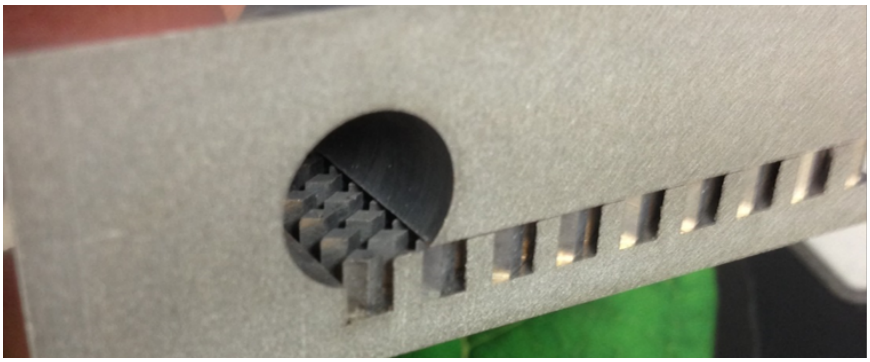

(a) View of fins inside this model of MaxQ coldplate.

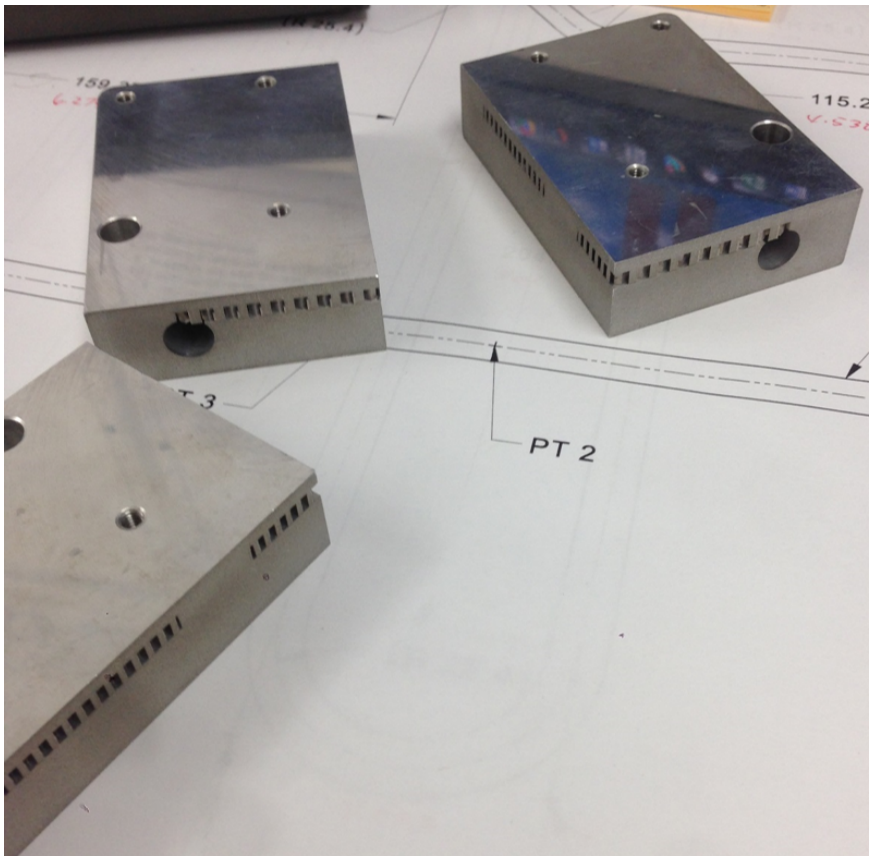

(b) View showing flow manifolds and fin structures.

Figure 3.19. Sectioned view of the same model coldplate showing internal heat transfer grid in the central region and flow distribution channels down the sides. The joints where the top plate is laid in after internal machining are not visible due to the high-quality of the friction stir weld. Courtesy of MaxQ Technology [86].

kept away from these lines to avoid impacting signal quality as the line heats up. All tube routes were designed to enter the chamber from the bottom of the cart which minimizes the exposure to the operator to hot tubes. In addition to routing the tubes away from operator accessible areas, a thick rubberized fiberglass insulation sleeve is added to the outside of all tubing to provide another safety barrier. Tubing inside the vacuum chamber is slightly more complicated as space is limited and the vacuum environment is not conducive to using traditional insulation sleeves to protect wiring from the flow tubing. Wiring inside the chamber is routed to avoid proximity to the hot fluid return line from the cold plate. The HRS tubing is routed to bring rigid tubing as close to the cold plate as possible, but since the cold plate must vertically with the lower bar, flexible lengths of tubing are required. Convoluted stainless steel tubing allows a vacuum tight flexible connection in the limited space inside the chamber. It is critical when installing a flexible metal fluid line that motion be constrained to a single plane to avoid twisting of the fluid line during movement. Tubing bends are avoided within three tube diameters of an orbital weld or connector location which helps to minimize leaks within the system. A ceramic port break is installed on the HRS fluid outlet F/T as a thermal standoff to reduce the heating of the chamber walls.

3.11 Vacuum Environment/System

Vacuum environments are commonly used during thermal property measurement to suppress convective losses from the sample and probes. Exact relations for pressure dependence of convection loss can be determined by considering the effects of momentum and heat transfer through rarefied gases, for a detailed treatment please consult the work by Jousten [49] for a thorough overview of the process. After consulting the calculations detailed by Jousten, it is apparent that a vacuum level of $< 1 \times 10^{-3}$ Torr is required to suppress the majority of convective losses. While further decreasing the vacuum pressure will help further decrease any convective losses, it

also leads to a marked increase in the contact resistances within the system. The requires a delicate balance between preventing convection losses from the bar and maintaining favorable contact conditions. The high operating temperatures for some system components poses a further complicating factor as these parts will readily oxidize at such high-temperatures in the presence of O_2.

In order to address this problem and keep the system free from damage, while still maintaining favorable thermal contacts, the system has been designed to allow the user to operate at higher pressures that would be possible with O_2 in the atmosphere through the use of an inert gas atmosphere. This allows the user to pull a hard vacuum (1×10^{-6} to 5×10^{-5} Torr) to sufficiently reduce the O_2 levels in the chamber, then backfill the chamber with an inert gas to bring the chamber up to a pressure level that has adequate thermal contact with the sample but still suppresses the convective losses from the meter bar. Typically this backfill pressure is approximately 1×10^{-3} Torr. The backfill gas is plumbed for N_2 from the building supply lines, but can easily be switched to any high-purity, inert, compressed gas by connecting the 1/4 in. Swagelok fitting to a K-Bottle regulator. The backfill gas pressure should be set to a level of 0.15 MPa (7.3 psiG) [87].

3.11.1 Design to Minimize Virtual Leaks

In a vacuum chamber, air is pumped out of the enclosure to create a volume of low pressure (vacuum); however, what about the volumes of air that cannot easily leave the chamber? These void volumes are trapped in some enclosed portion of the design and slowly leak out over time to leave the system, but in doing this it raises the system pressure slightly over time. This is called a virtual leak.

It is important to minimize virtual leaks because they can be damaging to the system since the pressure differentials can be quite high, and the presence of virtual leaks makes it more difficult to run an experiment as longer pump down times are required to obtain the ultimate vacuum level. These void volumes are often at the

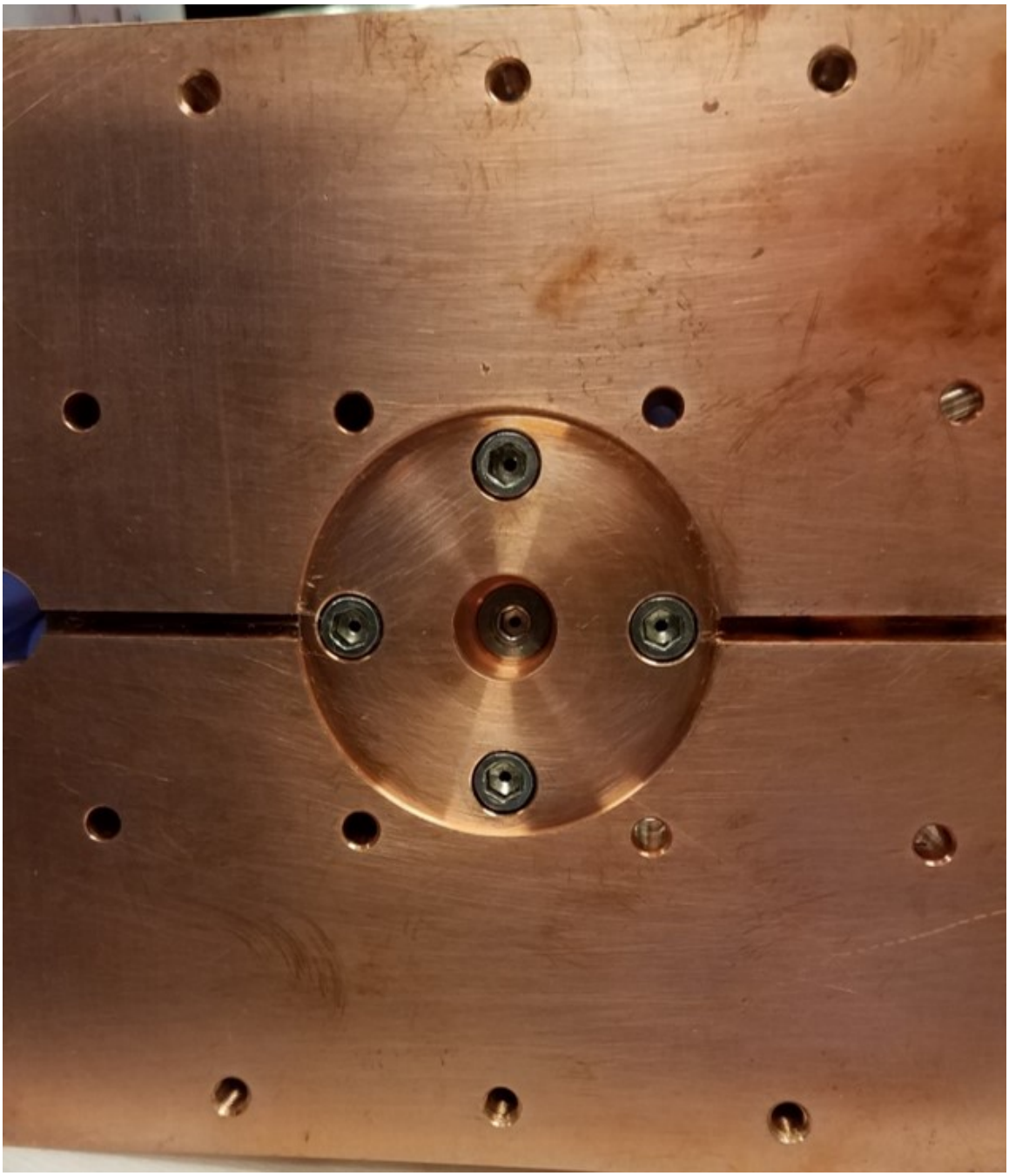

Figure 3.20. A view of the bottom of the copper mounting base that interfaces with the cold plate. This shows the effects take to properly vent all dead volumes for use in vacuum and minimize virtual leaks.

bottom of blind holes, or small cavities between bolted interfaces. Design for minimization of virtual leaks simply seeks to minimize regions of trapped gas. This can be accomplished by using through holes wherever possible in the design (this also typically helps to reduce machining costs). If blind holes are required, vented hardware should be used or a venting channel should be machined to relieve the void volume at the bottom of the blind hole. This can be done by drilling a small hole from another face to provide a path for the gas to escape from the trapped void volume. Finally, special attention must be paid to bolted interfaces, as these can often contain captured voids. In the cases where a bolted interface must cover a pocket or tops of blind holes, such as shown in Figure 3.20, then venting channels must be added to allows the gas to freely escape during vacuum pump-down.

3.11.2 Vacuum System Configuration

Finally, the selection of the vacuum system components themselves can have a major impact on the quality of the system vacuum. I chose a dry scroll pump (Edwards nxDs10i) as this provides an oil free pump for roughing the system to avoid the potential problem of oil backstreaming and contaminating the system. This model also has an integrated non-return valve which protects the system from being vented in the event of a power failure. This system protection is critical for the Z-Meter system because with very long equilibration times for high-temperatures. While the facility where this system is located does run with uninterruptible power supplies (UPS) to certain lab instruments, it is always a good idea to have a redundant system in place to ensure that the system is not accidentally vented while the bar is still hot and damaged, for instance if there was a power outage while a test was running at a high-temperature. Dry scroll pumps are an excellent option for low-maintenance and quiet pump operation in a small lab space. Additionally, due to the way a scroll pump operates, it is inherently a low-vibration pump design. This is important because the roughing pump needs to be mounted on the same cart as the Z-Meter to fit

in the lab space. As an added layer of prevention, we added further vibration isolation mounting pads to minimize any impact from the roughing pump on the measurement system.

In addition to a roughing pump, we also utilize a turbo-molecular pump (Osaka TG450F) connected directly to the 8 in. conflat mounting port on the bottom of the vacuum service well. This pump comes with an inlet baffle screen to prevent debris from falling into the opening from the chamber, but the stock screen has openings that are large enough to let small screws from the system fall into the inlet of the turbo pump. In order to prevent accidental damage of the turbo pump, an auxiliary screen constructed from copper was added, which reduced the mesh size by approximately a factor of four. This provides a sufficiently small mesh size to catch any bolts from the system before the enter into the turbo pump. While the protection of the pump is critical to proper system operation, the addition of this auxiliary screen does reduce the vacuum conductance proportionally to the reduction in input area. This was a necessary price to pay for system protection, and the system still reaches a vacuum level of approximately 5×10^{-5} Torr in thirty minutes.

The final components that make up the core of the vacuum system are the vacuum pressure gauges. I utilize a dual gauge scheme to provide better pressure measurement over the wide range of operation pressures. I have installed both a wide range convection gauge (KJL275316) for the range 1×10^{-4} to 1,000 Torr and an ionization gauge (KJLC392402YD) for 1×10^{-9} to 1×10^{-2} Torr. This dual gauge approach allows for accurate pressure measurement over the entire range of system operating pressures. The ionization gauge is equipped with a Yttria filament (IG4YD) instead of a tungsten filament, because Yttria filaments are more robust and provide for longer accurate operating lives under the rigors of typical lab usage. These gauges work well with other operating fluid besides Nitrogen/Air, but require the user to apply a sensitivity correction factor to the displayed reading from the ionization gauge to account for the different gas. Sensitivity correction factors for this ionization gauge are included in Table 3.6. These factors are applied as follows to a reading to correct for

Table 3.6. Ion gauge sensitivity correction factors for selected gases [88].

Gas	Correction Factor
Air	1.00
Ar	1.29
CO_2	1.42
He	0.18
N_2	1.00

another working gas. If the gas being used is He, and the gauge displays a pressure reading of 1×10^{-6} Torr, then the user must determine the appropriate correction factor from Table 3.6, which is 0.18 for He, and apply this to the displayed pressure to find the corrected pressure reading:

$$P_{He} = \frac{1.0 \times 10^{-6}\ Torr}{0.18} = 5.6 \times 10^{-6}\ Torr. \tag{3.21}$$

3.12 General System Configuration Considerations

3.12.1 Cabling

Cable layout and construction is carefully designed in this system to minimize noise pickup. I utilize individually shielded, silver plated copper, twisted pairs with PTFE insulation for all critical electrical connections. External cables are laid up into wiring harnesses which are carefully tied to minimize noise pickup loops between leads. Each wiring harness is run from the instrumentation rack to the Z-Meter cart, then secured in place to avoid microphonics, cable vibrations in a magnetic field resulting in an induced emf by vibrations of conductors causing fluctuations in the stray capacitance between two conductors. This is the reason that all wires are twisted and tied into appropriately grouped wiring harnesses then laid out and secured to prevent excess movement during the experiment.

The wiring harnesses themselves are also separated to preserve signal integrity. Low level DC signals have a separate harness from power signals, and are also separate from the digital communications harness. The separate harnesses are also routed to maximize physical separation between cable runs, and where crossing is necessary, harnesses are crossed at 90° to minimize impact on the low level signals. Cable entry to the rear of the equipment rack is organized using rails that permit highly configurable mounting positions to keep signal types separate, but also provide strain relief for the cables prior to entering the instruments. This level of cable organization is extended to the selection of the feedthrough locations inside the vacuum chamber.

The placement of low level signal feedthroughs is done in such a manner as to isolate them as much as possible from hot liquid feedthroughs, power feedthroughs, and mechanical rotary feedthroughs. Additionally, the placement of the signal feedthroughs is done to place them as close to the instrumentation rack as possible and further reduce the length of the wiring harnesses. The Z-Meter is designed and assembled in compliance with NASA-STD-8739.4, which governs crimp contacts and reliable connections. As such, Mil-spec twist-lock circular connectors are used for external low level signal connection, which provides excellent reliability in connection and ample electrical shielding at the connections. Internal connections are made with special vacuum compatible PEEK and stainless steel circular connectors. The internal and external connectors utilize MS3476(MB16)-MIL-DTL-26482, Series 2 crimp connectors. Crimp connections are made with a DMC AFM8 (M22520/2-01) crimp tool and the K18 positioner head. This crimping tool is calibrated to meet MIL specifications governing install of aerospace crimp connections.

3.12.2 Noise

First, consider the type-S thermocouples. Common noise can be picked up in both measurement leads (thermo-elements), which is why the leads are always kept in close proximity and the gap between the conductors is minimized to avoid inde-

pendent or out-of-phase noise between the lines. I set up the voltage measurements for the thermocouples as differential measurements to help eliminate this common noise pickup. High purity (99.8%) alumina dual bore sheathing is used for the type-S thermocouples. The purity of the material is critical as impurity leaching from materials in contact with the pure platinum at high-temperatures is the largest contributor to sensor drift, which is due to a change in material composition. The measurement junction of the thermocouples is inert arc welded using carbon electrode for the added quality of the joint, and it allows the joint to be better centered at the end of the sheath and encased in high purity alumina potting cement to electrically isolate the thermocouple form the bar. Additionally, all cabling external to the vacuum chamber is run as individually shielded twisted pairs. The cable shield is connected to the same clean ground reference as that of the thermocouples.

Special care is taken to avoid thermal gradients at any lead wire connections to minimize added thermoelectric noise from dissimilar contacts. This is accomplished by mounting connection terminals on thick isothermal copper plates which act as heat sinks and act to suppress thermal gradients across connections. This is the same layout as the cold junction compensation (CJC) block, but the CJC also has precision PtRTDs mounted between every two terminal block pair to precisely know the temperature at each individual connection terminal pair and properly compensate the signal. Solder joints are avoided throughout the system for two reasons. In vacuum solder can easily contaminate the system due to its vapor pressure and the low operating pressure of the chamber, but solder can also contribute additional noise at contacts. Solder can introduce excess noise at contacts due to impurities or residual flux that was not fully removed. Additionally, perfectly repeatable solder joints are incredibly hard to achieve especially across different installation days and even worse with more than one installer. This can lead to variations that stack up throughout the system and thus major contributions from excess noise. It is common practice in the aerospace industry to avoid solder joints for wiring when possible and instead utilize crimp contacts, which provide reliable, clean, and highly repeatable

connections. As previously mentioned, the Z-Meter is assembled in compliance with NASA-STD-8739.4 to ensure reliable connections.

In addition to the possibility of a dry solder joint or contamination adding to the measurement noise, solder also adds a dissimilar metal at the contact point and can have large contributions to thermoelectric noise in the system if thermal gradients are present. These factors drove the minimization of solder contacts within the system to only those present in the extension of the PtRTD leads, which was done with high purity, lead and cadmium free solder under extremely clean conditions. All connection points are thermally anchored to a copper plate to avoid thermal gradients across the junctions. The PtRTDs are designed as two wire connections, instead of splicing two additional sense wires into the leads of all RTDs, we instead calibrated for the lead resistance at several temperatures and current levels to apply as a correction in post processing of the data. The sense current will be optimized during sensor calibration to maximize the signal-to-noise ratio while minimizing self heating.

Much of what is done for the thermocouples is also done for the electrical leads for the sample voltage measurement. It is still connected through the CJC terminals to monitor the junction temperature and compensate for any temperature fluctuations that might impact the measurements. In the voltage measurements, the leads are required to be in electrical contact with the bar, which means there will be dissimilar metal contacts with large temperature gradients. This thermoelectric noise is removed from the system by taking a measurement, reversing the measurement polarity, and then taking another measurement. By combining these two measurements, the impact of the thermoelectric noise is easily removed.

Reducing noise at the instrument is accomplished by utilizing long integration times for the A/D converter. The system has a slow response, so it is not a problem to have integration times of 1-2 seconds (maximum integration time for instrument) which drastically reduces noise. Readings are averaged across intervals of 10 seconds to further reduce noise, as noise decreases proportionally to the square root of the number of averaged samples [89, 90]. It is also important to select an appropriate

measurement range as performing measurements at the edge of gain region has the largest gain errors. The digital multimeters (DMMs) are configured as follows:

- Resolution is set to maximum precision in slow mode (long integration time)
- Input resistance is set to >10GΩ for best DC voltage accuracy
- Math null is used to remove interconnection offset for DC voltage measurements

In addition to these settings, auto-zero is used to remove the offset voltages present on the multimeters circuitry. Auto-zero works by internally disconnecting the input signal following each measurement and recording a zero reading to subtract from the preceding measurement readings. A single point, star grounding scheme is utilized for tying into the clean instrumentation ground at the Birck Nanotechnology Center (BNC). This grounding scheme utilizes a single low impedance bus bar as the direct connection interface for each instrument that requires an instrumentation ground reference and shield references.

3.12.3 Electronic Measurement Instruments

Temperature measurement is performed in voltage mode rather than direct temperature measurement mode to improve reading accuracy [91]. A custom cold junction block mounted inside of the chamber is used rather than electronic cold junction compensation for further error reduction in temperature readings [59]. One platinum resistance temperature detector (Honeywell HRTS-5760-B-U-0-12) is used for each thermocouple channel pair on the internal cold junction block and these values are used for cold junction compensation. Voltage measurements for Seebeck and electrical conductivity are taken using the Agilent 3458A as a dedicated instrument for voltage measurements across the sample, so the uncertainties for these measurements are based upon the calibrated accuracy of this instrument within the appropriate voltage measurement ranges [92].

4. ANALYSIS AND UNCERTAINTY QUANTIFICATION

4.1 Analysis

Due to the multiphysics nature of these measurements, many things must happen simultaneously to accurately gather data during the experiment. Since the end goal of the system is to measure ZT, we know that three properties must be measured: Seebeck coefficient (S), electrical conductivity (σ), and thermal conductivity (κ). The Seebeck coefficient is determined by measuring the open circuit voltage across the sample while it is held under a thermal gradient:

$$S = \frac{\Delta V_{OC}}{\Delta T}. \tag{4.1}$$

It is crucial that the ΔT must be determined only across the sample, as interfacial conductances and probe offsets can adversely impact the measurement of the Seebeck coefficient. This requires characterization of the bar and sample interfaces to accurately account for both thermal and electric contact effects. Since the determination of temperatures at the contact interfaces is not always easy and can require extensive characterization of contact behavior, we also present a secondary means of determining the Seebeck coefficient from the test data for the electrical conductivity.

Electrical conductivity has traditionally been measured by bringing the sample to an isothermal state at the desired temperatures, then using a four-probe electrical measurement to determine the cross-plane resistivity of the sample. Bringing the

This chapter is based largely on an ITHERM conference paper written by the author in 2018.

sample to an isothermal state in this system would preclude the simultaneous measurement of the properties as thermal gradients are required for both the Seebeck coefficient and the thermal conductivity. Therefore, we need a means of extracting the electrical resistivity while holding the sample under a thermal gradient. The drawback to this is that the measured electric potential across the sample will be comprised of the ohmic voltage drop for the sample and the Seebeck voltage from the temperature gradient.

$$V_{tot} = V_{ohm} + S\Delta T \tag{4.2}$$

In order to address this issue, we sweep through different levels of sense current that is passed through the sample, and the voltage measured as a function of current can be used to evaluate electrical conductivity. At each current level, we measure the voltage drop for current flow in both directions through the sample, with the current direction being switched with a frequency of 0.5 - 1 Hz. This frequency is selected as it provides a long enough time for the electrical readings to stabilize but is faster than the thermal response time of the system and minimizes contributions from Peltier heating in the sample. Another advantage of measuring the voltage drop with current flowing in both directions, is that the effect from the Seebeck voltage can be cancelled out. This is because the Seebeck voltage is developed due to the temperature gradient applied to the sample, since we reverse the current direction, but the temperature gradient stays fixed, we will be able to account for the Seebeck voltage contribution and eliminate it from the voltage reading by averaging it out [13, 14]:

$$V_{Ohm} = \frac{[V_{I^+} + S\Delta T] - [V_{I^-} + S\Delta T]}{2}. \tag{4.3}$$

It is also important to keep the supplied current level small enough to avoid Joule heating during the measurement to avoid modifying the temperature gradient imposed by the Z-Meter. A final benefit to the voltage versus current sweep method for measuring the electrical conductivity is that it has a built in means of determining the Seebeck voltage. When the voltage response with current is plotted, the slope

of the line is the ohmic resistance (R_{ohm}) for the sample, but the y-intercept is the Seebeck voltage. The electrical conductivity can be calculated as

$$\sigma = \frac{L_S}{R_{ohm} \cdot A_{C,S}}. \tag{4.4}$$

Finally, the thermal conductivity of the sample must be determined by using the meter bar method. In this measurement, it is paramount that the heat flow in the meter bars is well characterized, all losses are accounted for, and the analysis adjusted for these losses. The heat flow through the sample is unknown, but under perfect conditions (no losses) it will be the same as the heat flow through the meter bars themselves. Since the thermal conductivity of the meter bars has been well characterized across the full temperature range of operation and the temperatures at known spacings along the bar are measured accurately during the experiment, Fourier's law provides the heat flow through the bars as:

$$q = -\kappa_B A_{C,B} \frac{\Delta T}{\Delta Z}. \tag{4.5}$$

If we know the heat flow through the bar above the sample, and that through the bar below the sample, then averaging these will provide a good estimate of the heat flow through the sample; in-fact, the ASTM D5470 measurement standard was recently updated and now states [93],

> 6.4.4 If the heat flow meter bars are used on both the hot and cold surfaces, guard heaters and thermal insulation is not required and the heat flow through the test specimen is computed as the average heat flow through both meter bars.

However, while this might be sufficient for measuring the heat flow and determining an effective thermal conductivity, it does not provide sufficient accuracy to permit accurate extrapolation to the interface temperatures to accurately determine the Seebeck coefficient.

In order to properly determine the temperature profile in the meter bars, we must develop a heat transfer model that accounts for conduction along the bar, and radiation losses from the surface. Figure 4.1 shows a schematic that depicts a cylindrical

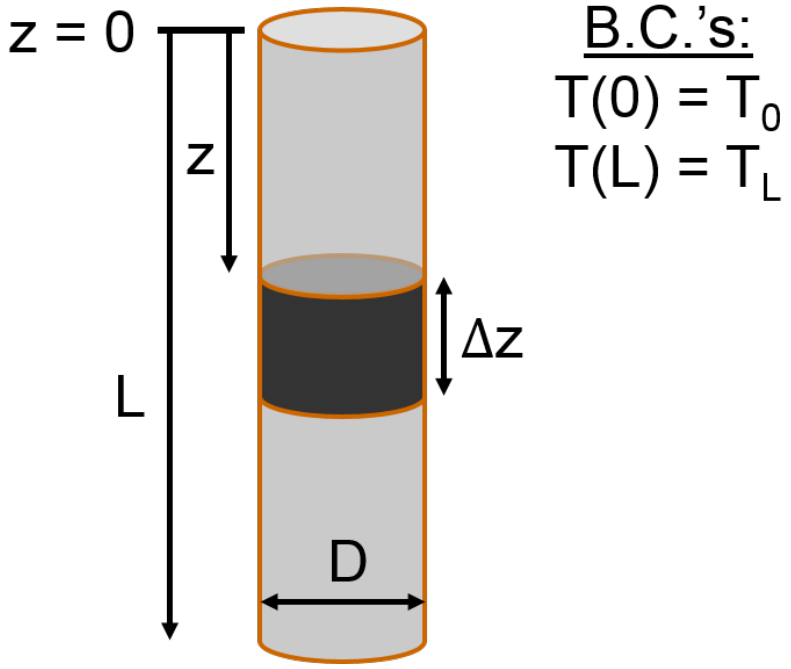

Figure 4.1. A schematic view of the model developed to account for thermal radiative losses.

bar of diameter D and length L. The following model is based upon the following general assumptions:

- Bar is at steady state
- 1-D Conduction in bar (uniform cross-sectional temperature profile)
- Surface losses are due only to radiation (no convection in the vacuum chamber)
- Bar radius is constant with length and not a function of temperature
- Surface emissivity is constant
- Diameter of bar is small compared to that of the vacuum chamber (T_{surr})
- No heat generation within the bar.

Since the diameter of the fin is much smaller than that of the vacuum chamber that it is enclosed in, the surroundings can be treated as a black body at constant

temperature, T_{surr}. Considering the energy balance for the discrete element shown in Figure 4.1,

$$q_z - q_{z+\Delta z} = q_{rad}, \tag{4.6}$$

where $q|_z$ and $q|_{z+\Delta z}$ are, respectively, the heat flow into and out-of the discrete element through the bar cross-sectional area, A_C. The surface losses due to radiation for the discrete element can be described as $q_{rad} = \varepsilon A_S \sigma (T^4 - T_{surr}^4)$, where $A_S = \pi D \Delta z$. If we divide both sides by Δz,

$$\frac{q_z - q_{z+\Delta z}}{\Delta z} = \varepsilon \pi D \sigma (T^4 - T_{surr}^4), \tag{4.7}$$

and then noting that the left hand side of the equation is Newton's difference quotient for q at z and taking the limit as $\Delta z \to 0$

$$\lim_{\Delta z \to 0} \frac{-(q(z+\Delta z) - q(z))}{\Delta z} = \lim_{\Delta z \to 0} \varepsilon \pi D \sigma (T^4 - T_{surr}^4), \tag{4.8}$$

we see the left hand side is the definition of the derivative of q at z. Applying the squeeze theorem to the right hand side and noting that this part is continuous in the interval $[z,\, z + \Delta z]$, we get:

$$-\frac{dq}{dz} = \varepsilon \pi D \sigma (T^4 - T_{surr}^4). \tag{4.9}$$

Then substituting Fourier's law, $q = -\kappa A_C \frac{dT}{dz}$, into the equation, we end up with:

$$\frac{d}{dz}\left(\kappa(T)\frac{dT}{dz}\right) = -\frac{\varepsilon \pi D \sigma (T^4 - T_{surr}^4)}{A_C}, \tag{4.10}$$

where $\kappa(T)$ is a function of temperature. Due to the temperature dependence of the thermal conductivity and the specific boundary conditions we have for this situation, this equation does not lend itself to an easily obtained closed-form solution; however, we can set it up for numerical integration to obtain the temperature profile between the two known points.

If we substitute Fourier's law into (4.7), we have:

$$-\kappa A_c \left.\frac{dT}{dz}\right|_z - \left(-\kappa A_c \left.\frac{dT}{dz}\right|_{z+dz}\right) = \varepsilon \sigma A_s (T^4 - T_{surr}^4), \tag{4.11}$$

which can be discretized

$$-\kappa_i A_c \frac{T_i - T_{i-1}}{\Delta z} - \left(-\kappa_i A_c \frac{T_{i+1} - T_i}{\Delta z}\right) - \varepsilon\sigma P \Delta z (T_i^4 - T_{surr}^4) = 0 \tag{4.12}$$

$$\Rightarrow \qquad T_{i+1} - 2T_i + T_{i-1} - \frac{\varepsilon\sigma P \Delta z}{\kappa_i A_C}(T_i^4 - T_{surr}^4) = 0, \tag{4.13}$$

and finally linearizing (4.13), we get

$$T_{i+1} + \left(-2 - \frac{\varepsilon\sigma P \Delta z^2}{\kappa_i A_C} T_i^3\right) T_i + T_{i-1} = -\frac{\varepsilon\sigma P \Delta z^2}{\kappa_i A_C} T_{surr}^4. \tag{4.14}$$

This equation can be solved within the data analysis loop in MATLAB by providing initial guesses for the solution, which are based on a linear profile between the known temperature boundary conditions at $z = 0$ and $z = L$.

The final factor to consider is the losses at the interfaces to the sample, which are generally described through contact conductances

$$h_{total} = h_{cond} + h_{rad} + h_{gap}, \tag{4.15}$$

where the total conductance is comprised of three conductances: conduction through the contacting areas, radiative transport across the interface, and gap conductance or conduction through the gas filled pockets at the interface [94]. The contact conduction is treated with a geometric deformation model for the interfaces of surfaces. These values are assumed to be independent and normally distributed having probability density function:

$$p(y) = \frac{e^{-\frac{y^2}{2\sigma^2}}}{\sigma\sqrt{2\pi}}. \tag{4.16}$$

In the probability density function given by (4.16), σ represents the standard deviation height, and is defined by

$$\sigma = \left[\frac{1}{L}\int_0^L y^2 dx\right]^{1/2} = \left[\int_{-\infty}^{\infty} y^2 p(y) dy\right]^{1/2}. \tag{4.17}$$

This model considers the distribution of the roughness features at a surface depending on the standard deviation of surface height, σ, and effective absolute surface slope, m, of the asperities, both of which are obtained from a profilometer measurement [94].

The real contact area, A_r is reduced from that which is obtained by using the bar or sample cross-sectional areas, otherwise known as the apparent contact area, A_a. The relative real contact area can be defined as [95]

$$\frac{A_r}{A_a} = \left(\frac{a}{b}\right)^2 \frac{1}{2} erfc(x), \tag{4.18}$$

where a is the mean contact-spot radius, b is the mean cylinder diameter, and $erfc(x)$ is the complimentary error function of $x = \frac{Y}{\sqrt{2}\sigma}$. Two rough surfaces in contact can be evaluated as one rough surface, with equivalent roughness and slope, in contact with and penetrating a perfectly smooth surface. The ratio, $\frac{Y}{\sigma}$ is called the relative mean plane separation and describes the average separation distance the rough and smooth surfaces when plastic deformation occurs at the peaks of the asperities. Mantelli [94] defines the contact-spot density for such a case,

$$n = \frac{1}{16}(\frac{m}{\sigma})^2 e^{x^2} erfc(x), \tag{4.19}$$

and the mean contact-spot radius as,

$$a = \sqrt{\frac{8}{\pi}} \frac{\sigma}{m} e^{x^2} erfc(x). \tag{4.20}$$

In order to use this model, the equivalent roughness and slope for the single rough surface as defined by the actual properties for the two surfaces are given as $\sigma = \sigma_1^2 + \sigma_2^2$ and $m^2 = m_1^2 + m_2^2$ respectively.

This analysis is then carried forward to determine interfacial conduction lengths and areas based upon the probable interfacial contact conditions established by the geometric deformation model. Yovanovich proposed a correlation that captures the physics due to thermal, geometric, and deformation effects found in the above model that is widely used to describe contact conductance [94, 95]:

$$\frac{h_c}{\bar{\kappa}} \frac{\sigma}{m} = 1.25 \left(\frac{P_{Load}}{H_C}\right)^{0.95} \tag{4.21}$$

where $\bar{\kappa} = \frac{(2\kappa_1\kappa_2)}{(\kappa_1+\kappa_2)}$ is the harmonic mean of the thermal conductivities of the two materials at the interface, σ/m is the surface roughness parameter(given in μm), P_{Load}

is the applied contact pressure, (given in Pa), and H_C is the surface microhardness. This model agrees to within 1.5% of the full model in the range $2 \leq {}^{Y}/_{\sigma} \leq 4.75$, yet it is much more compact for ease of implementation [95]. Solving for the geometric constriction conductance,

$$h_c = 1.25\bar{\kappa}\frac{m}{\sigma}\left(\frac{P_{Load}}{H_C}\right)^{0.95}. \tag{4.22}$$

This fully defines the conduction constriction contact conductance. The remaining two contact conductances, h_{rad} and h_{gap}, are still required to fully describe the contact behavior. The impact of these two effects is easy to show by formulating equations to describe heat transfer between two parallel plates separated by an evacuated space [96]

$$\Delta T = \frac{2-\alpha}{\alpha}\frac{2\gamma}{\gamma+1}\frac{\lambda}{Pr}\frac{(T_{int,U} - T_{int,L} - 2\Delta T)}{z_{gap}}, \tag{4.23}$$

where ΔT is the temperature difference between gas molecules adjacent to the wall and the temperature of the molecules that make up the wall, α is the thermal accommodation coefficient to account for the different ways various gas molecules interact with disparate surface materials at low pressures, $\gamma = \frac{C_P}{C_V}$ is the ratio of specific heats, $\lambda = 2.27 \times 10^{-5}\frac{T[K]}{p[Pa]}$ is an approximation for the mean free path of air molecules (kinetic theory is used to obtain relationships to account for using another gas in the system), Pr is the Prandtl number, and z_{gap} is the gap separation distance. Rearranging equation 4.23 and solving for the the temperature jump at the wall,

$$\Delta T = \frac{\frac{2-\alpha}{\alpha}\cdot\frac{2\gamma}{\gamma+1}\cdot\frac{\lambda}{Pr}(T_{int,U} - T_{int,L})}{(L + 2(\frac{2-\alpha}{\alpha}\cdot\frac{2\gamma}{\gamma+1}\cdot\frac{\lambda}{Pr}))} \tag{4.24}$$

allows the conduction heat transfer through the low-density space to be defined as

$$\overset{"}{q}_{gap} = \kappa_{Gas}\frac{T1 - T2 - 2\Delta T}{z_{gap}}, \tag{4.25}$$

which can be directly related to the gap conductance as,

$$h_{gap} = \frac{\overset{"}{q}_{gap}}{\Delta T} = \frac{\kappa_{Gas}(T_1 - T_2 - 2\Delta T)}{z_{gap}\ \Delta T}. \tag{4.26}$$

Finally, the radiation contribution across the gap can then be included by approximating the interface as two infinite parallel planes,

$$\overset{"}{q}_{rad} = \frac{\sigma_B(T_1^4 - T_2^4)}{\frac{1}{\varepsilon_1} + \frac{1}{\varepsilon_2} - 1}, \tag{4.27}$$

where σ_B is the Stefan-Boltzmann constant, and ε_i are the emissivities of the two surfaces. The radiative conductance is defined similarly to that for gap conductance,

$$h_{rad} = \frac{\overset{"}{q}_{rad}}{\Delta T} = \frac{\sigma_B(T_1^4 - T_2^4)}{(\frac{1}{\varepsilon_1} + \frac{1}{\varepsilon_2} - 1)\ \Delta T}. \tag{4.28}$$

Now that all of the necessary factors are defined, we combine (4.22), (4.26) and (4.28) to define the total interfacial conductance:

$$h_{tot} = 1.25\bar{\kappa}\frac{m}{\sigma}\left(\frac{P_{Load}}{H_C}\right)^{0.95} + \frac{\kappa_{Gas}(T_1 - T_2 - 2\Delta T)}{z_{gap}\ \Delta T} + \frac{\sigma_B(T_1^4 - T_2^4)}{(\frac{1}{\varepsilon_1} + \frac{1}{\varepsilon_2} - 1)\ \Delta T}. \tag{4.29}$$

This relation allows the thermal conductivity of a sample to be estimated without direct characterization of the interface resistances; however, this can results in sizeable errors if the interfacial properties used to define the model are not perfect. It is highly recommended to perform additional experiments aimed specifically at characterizing the impact of the interfaces, *e.g.*, thickness dependent measurements. Running an experiment with the same set points, and loading conditions, but changing the material thickness allows a direct comparison of differences in the measured value that ideally stem only from the difference in the thermal resistance of the sample. To maximize the effectiveness of this comparativew measurement method, efforts should be taken to minimize the sample variance between the difference thickness samples. The samples should be fabricated at the same time and under the same conditions to help limit any differences between the test results for the different samples to the effects of the thickness only.

Now all the terms needed to define the figure of merit are now known from measured quantities. The next step in the design process is to consider the impact of uncertainties in the measured experimental parameters upon the final answer.

4.2 Uncertainty Quantification

There are many inputs (*e.g.*, material properties and geometry) required to obtain κ, σ, S, and ZT from the measured data. Their associated uncertainties, plus the uncertainties in measured quantities like temperature and voltage, must be considered when extracting properties from measured data. This section details how values are obtained and how the uncertainties are determined and how uncertainty distributions are assigned.

Geometry: All system geometry is measured with a coordinate measurement machine in the Purdue Mechanical Engineering Technology Metrology Lab. The rated accuracy for the system at the time of use was 1.27 μm (0.00005 in.). The values measured by the CMM are the result of many repeated measurements averaged to determine the mean values for all dimensions of interest, for this reason it has a normal uncertainty distribution assigned to it. The sample thickness is measured using a Mitutoyo Digital thickness Indicator (543-472B) mounted to a calibrated granite reference surface (Mitutoyo 517-890). This is a grade A, 8 $\times$ 6 in. granite reference surface, with a flatness accuracy of 2.54 μm (0.0001 in.). The rated accuracy for this instrument is 2.54 μm (0.0001 in.). The sample diameter is measured with a Starrett outside micrometer (230FL), with a rated accuracy of 2.54 μm (0.0001 in.). The inner diameter of the radiation shields is measured with a Starrett dial caliper (3202), with a rated accuracy of 25.4 μm (0.001 in.). With all precision geometric measurements surface cleanliness is absolutely critical to perform accurate measurements. All parts are triple solvent cleaned prior to performing these measurements to ensure that surface debris does not bias the measurement. Likewise, all instruments are wiped down gently with a lint free clean room wipe, moistened with 200 proof ethanol prior to use.

Input Material Properties: Values and the distribution of uncertainty for material properties to estimate corrections for system operation such as thermal conductivities (not the Mo bar conductivities), emissivities, electrical resistivities, and

Seebeck coefficients are taken from tabulated literature sources [48,53,54,56,59,78,79, 97–100]. The thermal properties that are critical to the accuracy of the system, such as the thermal conductivity for the top and bottom bars, have been independently measured for the specific material stock used to fabricate each bar by Thermophysical Properties Research Laboratory (TPRL) in West Lafayette, IN. The results of this testing are detailed in section 5.1.

Temperatures: Temperature measurement uncertainties are based upon calibrated accuracies for the type-S thermocouple sensors used with a Keithley 2700 and 7708 multiplexer card in voltage measurement mode [60, 78]. Temperature measurement is performed in voltage mode rather than direct temperature measurement mode to improve reading accuracy [91]. A custom, dual sided, cold junction block mounted inside of the chamber, as shown in Figure 4.2, is used rather than electronic cold junction compensation for further error reduction in temperature readings [59]. One PtRTD (Honeywell HRTS-5760-B-U-0-12) is installed for each pair of thermocouple channels on the internal cold junction block. These highly accurate RTDs are used to compensate for the temperature of the terminals where the small diameter thermocouple wires are transitioned to more robust copper wiring for connection to the main signal cable harnesses to the instrumentation rack.

Voltages: Voltage measurements for Seebeck and electrical conductivity are taken using the Agilent 3458A as a dedicated instrument for electrical measurements across the sample, so the uncertainties for these measurements are based upon the calibrated accuracy of this instrument within the appropriate voltage measurement ranges [92].

4.3 Numerical Model for UQ

A MATLAB based uncertainty quantification tool (from UQ-Labs [101]) is used to evaluate the impact of uncertainty in these inputs on the extracted material properties for the sample. To do so during design, a multi-physics numerical model is created of the Z-meter system including heat losses, contact effects, and measurement currents.

This model generates simulated measurement data (voltages and temperatures) used to calculate the material properties with the data extraction techniques described above that can then be directly compared to the parameters input to the computational model (κ, σ, and S).

Briefly, a 2D axisymmetric model in COMSOL Multiphysics mimics the experimental process and provides mock experimental data for the analysis of the accuracy of the measurement technique. The simulation is fully coupled with electrical, thermal, and thermoelectric physics. Temperature-dependent properties are used for the meter bars. Point probes are added to the model to act as sensors to gather data from the locations that will have sensors in the physical Z-Meter system. The vacuum chamber and heat shields are modeled as part of the system, allowing surface-to-surface radiation to be considered for internal surfaces. Figure 4.3 shows the numerical COMSOL data plotted for locations along the central axis of the bars, with the measurement probe locations indicated. The sample is located in the center of the two reference bars and is of sufficiently lower thermal conductivity that the majority of the temperature drop in the system occurs across the sample itself. The measurement points (red circles) correspond to the actual measurement locations in the physical system, and these are the locations where the MATLAB script samples the temperature distribution to obtain data as it would come from the experiment. The effects of radiation losses are apparent in the non-linear profile as shown in Figure 4.3.

In this evaluation, the electrical properties of the sample in the COMSOL model are fixed as constants for lead telluride (PbTe): $S_{COMSOL} = 1.87 \times 10^{-4}\ \frac{V}{K}$ and $\sigma_{elec,COMSOL} = 6.0976 \times 10^{4}\ \frac{S}{m}$, while the thermal conductivity is varied in the range expected for modified materials: $k_{COMSOL} = 0.1 - 10.0\ \frac{W}{m \cdot K}$. Please note that while the properties for PbTe are used for this numerical study, the melting point of PbTe is only 924℃, so it would not be possible to actually perform these experiments at the temperatures shown. However, this is merely meant to serve as an investigative study of the system performance and measurement uncertainty, where the PbTe is just a stand-in material to use for rough property values. Further, it is important to note

that this range of thermal conductivities far exceeds that which would be obtained from nano-structuring of a real material like PbTe, but this serves to show the performance and limits of the system across a wide range of thermal conductivities since thermal conductivity directly impacts the temperature difference across the sample. Table 4.1 shows the impact of the sample thermal conductivity on the total measurement uncertainties. The uncertainty in the measurement of the Seebeck coefficient is low, but does have a slight increasing trend as the sample thermal conductivity is increased. This is primarily due to the fact that samples with higher thermal conductivities will result in smaller temperature differences across the sample. A smaller temperature difference across the sample means that the Seebeck voltage is lower and more difficult to measure accurately.

4.4 Uncertainty Analysis: Methods & Results

The uncertainty analysis briefly mentioned in the previous section is coded in MATLAB using the UQ-Lab uncertainty quantification package [101]. After defining the model inputs of interest (geometry, temperatures, voltage measurements and material properties) and assigning each input an appropriate probability distribution for its uncertainty, a sampling scheme is selected to formulate a data set with which to investigate the uncertainty of the parameters of interest. UQ-Lab provides the user with a choice of four common sampling schemes: Monte Carlo, Latin Hypercube, Sobol, or Halton. Evaluating the sampling methods within this model, the Monte Carlo sampling is the fastest across all runs, but also had the largest sampling error for a constant sample size of 100,000 samples. Sampling error here refers to biases in the sampling routine that lead to errors in rebuilding the input distributions for validation data sets. The Latin Hypercube method has the smallest sampling error, but it would not run for the standard 100,000 comparison run that the other methods were checked with. If the sample size gets too large for the Latin Hypercube method, then the code crashes. This is not a problem once a smaller number of samples is

input. The Sobol sampling scheme provides the next lowest sampling error and is very stable for the range of input values evaluated.

Comparing the values predicted through this uncertainty propagation model to the values that are input in the simulation shows the agreement between the "measured" and actual values as compared in Figure 4.5. Compared to standard experimental design with numerical models, the UQ-based approach gives us not only the value of the extracted properties at the nominal input values, but also the uncertainty in the measurements.

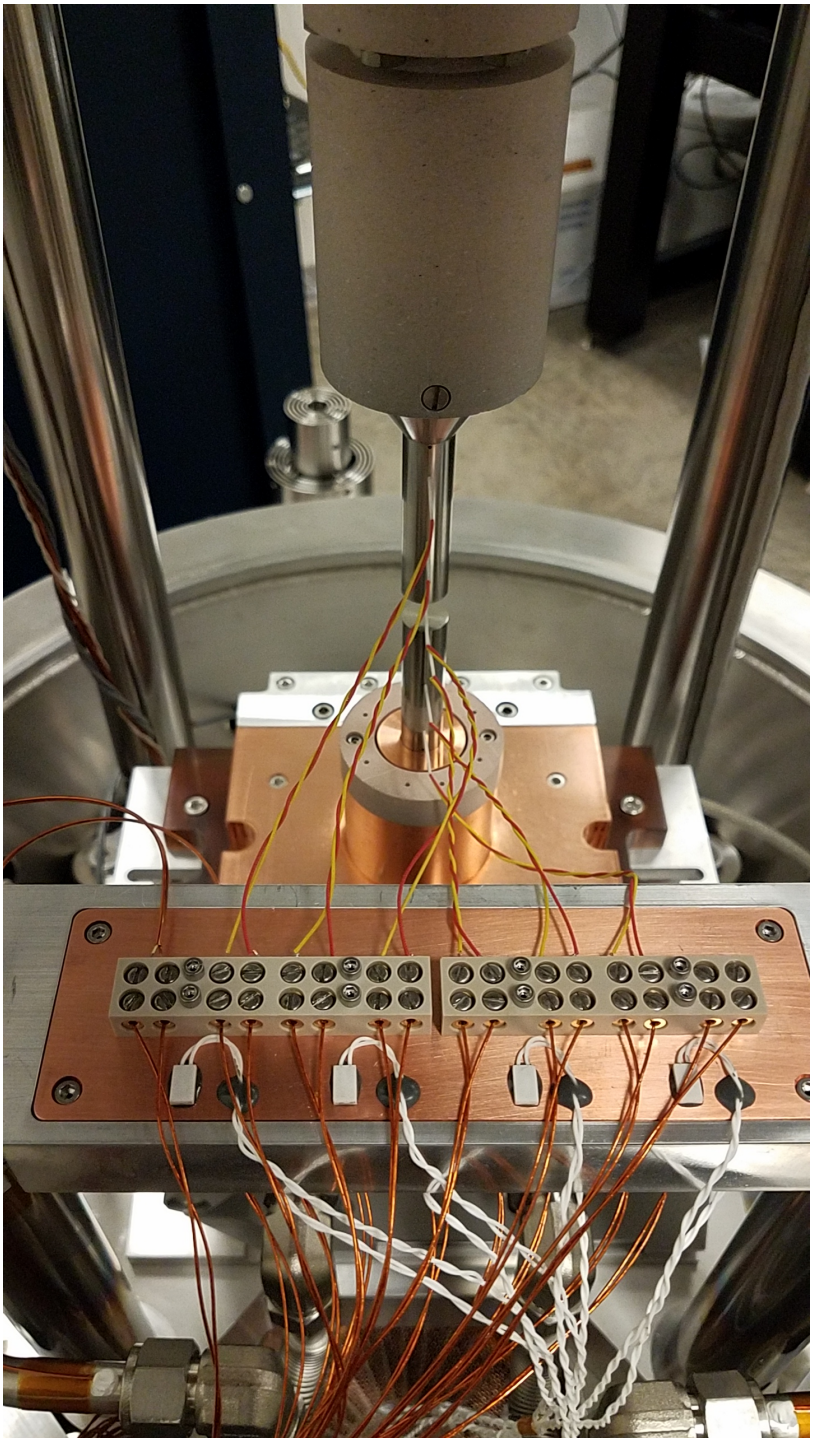

Figure 4.2. View of the top of the custom cold junction compensation block inside the vacuum chamber. There is one platinum RTD (HRTS-5760-B-U-0-12) installed for every two junctions to provide accurate local readings for all junctions. There are another sixteen terminal on the bottom of the block with another four PtRTDs bonded for monitoring.

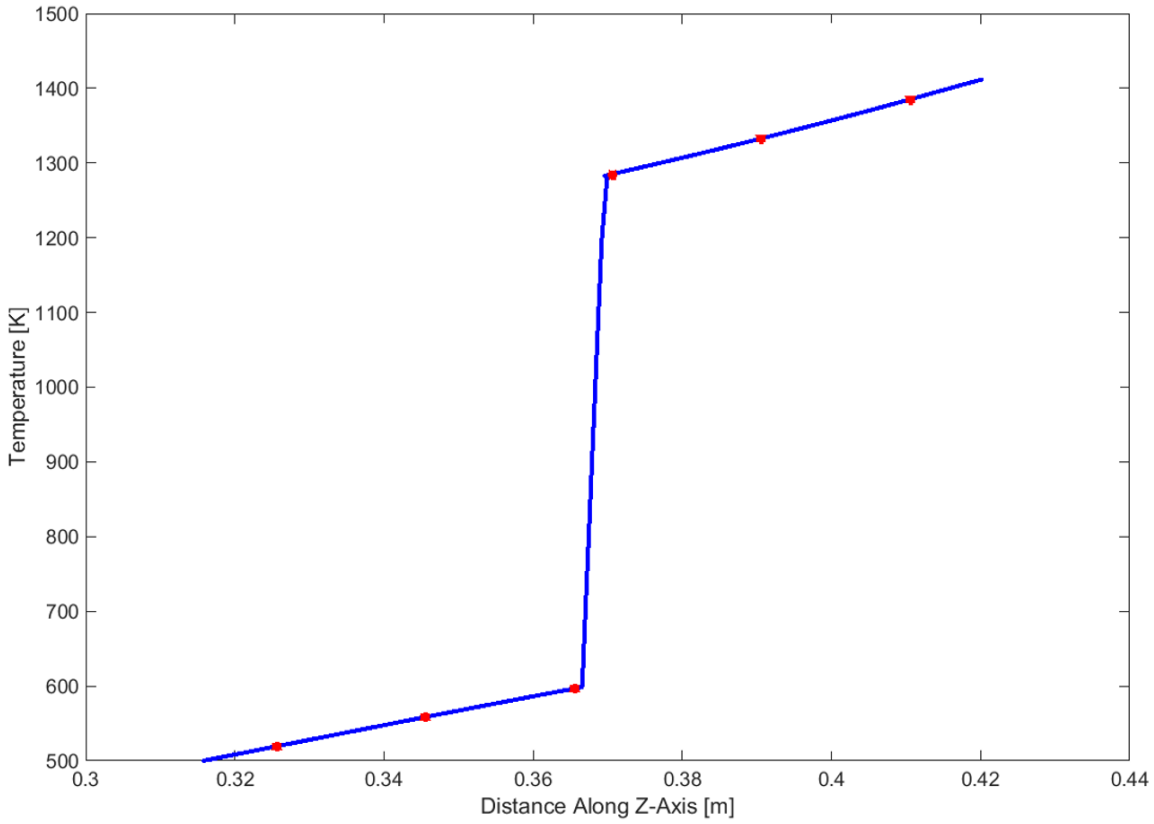

Figure 4.3. Temperature profile within the reference bar - sample - reference bar assembly computed with COMSOL (blue line) and extracted for use in calculation of properties (red points).

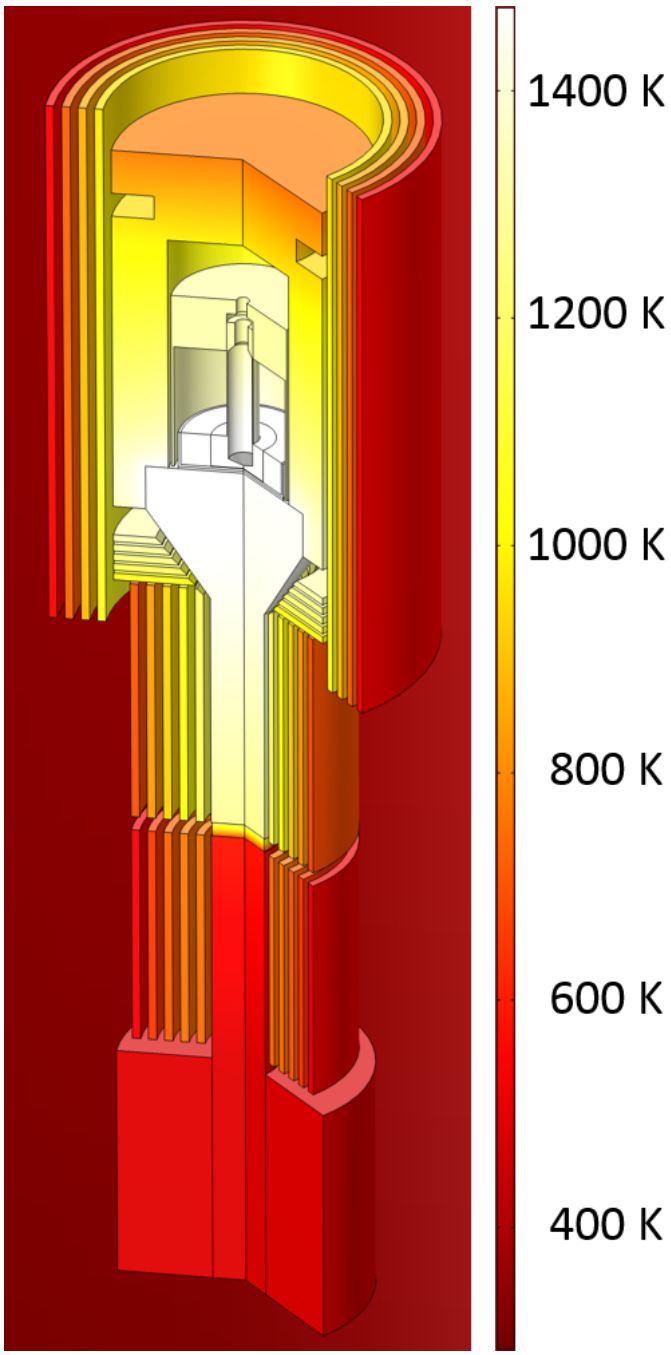

Figure 4.4. Numerical simulation results for the temperature distribution within a sectioned view of the Z-Meter system. Here the three banks of concentric radiation shields are clearly visible around the central meter bars. Above the upper meter bar, the button heater assembly and ceramic loading shroud are included as components in the model to more accurately estimate thermal losses for the system.

Table 4.1. Extracted Seebeck Coefficient, electrical conductivity, thermal conductivity, and ZT and associated error as a function of simulated input thermal conductivity of the sample. In this model, S_S and $\sigma_{S,elec}$ are kept fixed, while the thermal conductivity κ_S is varied.

$T_{heater}[K]$	$k_{S,COMSOL}$	$S_S\,[V/K]$	$\%Err\ S_S$	$\sigma_{S,elec}\,[S/m]$	$\%Err\ \sigma_S$	$\kappa_S\,[W/(m\cdot K)]$	$\%Err\ \kappa_S$	$ZT\,[-]$	$\%Err\ ZT_S$	$\overline{T}_{Sample}\,[K]$
1473	0.5	$1.871\cdot10^{-4}$	0.04%	$6.369\cdot10^{4}$	4.46%	0.580	15.98%	3.646	9.80%	947.675
	1.0	$1.871\cdot10^{-4}$	0.06%	$6.369\cdot10^{4}$	4.46%	1.080	8.01%	1.944	3.13%	940.937
	5.0	$1.874\cdot10^{-4}$	0.23%	$6.369\cdot10^{4}$	4.46%	5.114	2.27%	0.403	2.65%	919.557
	10.0	$1.879\cdot10^{-4}$	0.46%	$6.369\cdot10^{4}$	4.46%	10.190	1.90%	0.201	3.49%	912.426

4.5 UQ Summary

A detailed uncertainty propagation model based upon numerical multi-physics simulations is presented to characterize the measurement error in the Z-Meter system. Although the results of this study do not directly correspond to a physical material, it provides valuable data for addressing measurement concerns during the final phases of the instrument fabrication and construction. This model and uncertainty analysis enables a better understanding of the real impact of design choices upon the final measurement uncertainty of the instrument. Ultimately, detailed UQ should be integrated early in the design process to minimize the uncertainty in measured parameters and utilized to provide guidance for system modifications and improvements to be implemented.

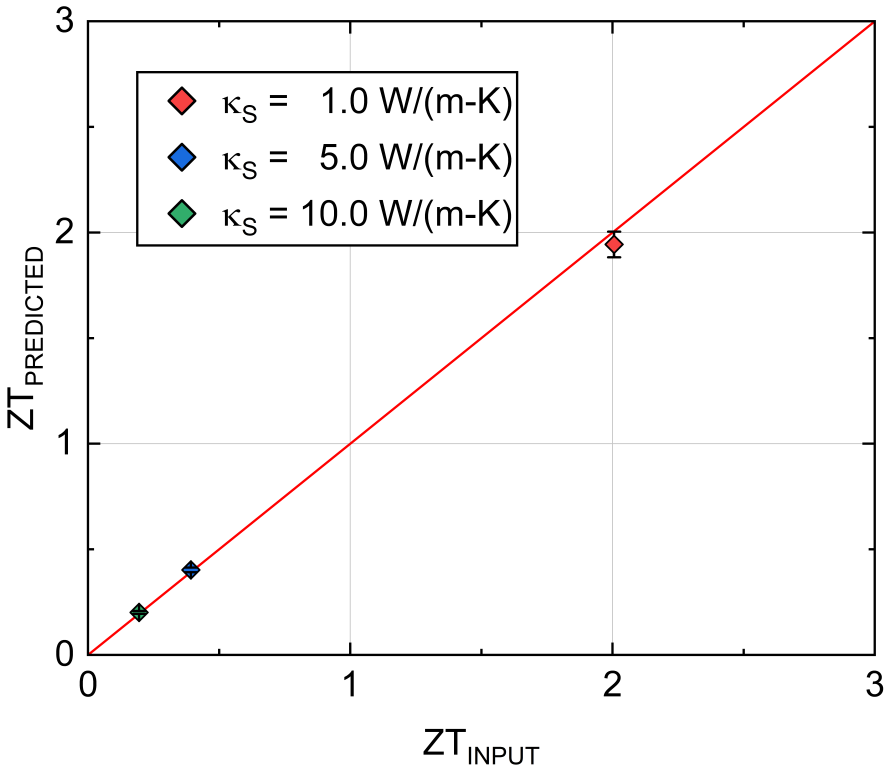

Figure 4.5. Extracted ZT with from the numerical model with uncertainty propagation as a function of the ZT input into the COMSOL model showing good agreement between the results of the uncertainty propagation model and the input value of ZT in the simulations. The different data points represent changing the thermal conductivity to mimic the material being enhanced through reduction of the thermal conductivity. The Seebeck coefficient and electrical resistivity are held constant between tests to investigate the system's performance in measuring the thermal conductivity of the sample across a range of input values.

5. RESULTS

Several validation steps are required prior to measuring unknown materials with this new measurement tool. First, we propose verifying the system works for each property independently, then for thermoelectric materials. Initial validation steps presented here focus on the reference bar thermal properties using the Z-meter tool and shed light that the interfaces are crucial to characterize. Future work will include validation with thermal reference materials across a range of thermal conductivities, then move to electrical and Seebeck coefficient characterization.

5.1 Calibration of Reference Bar Material Properties

The molybdenum used as the reference bar materials is characterized by the Thermophysical Properties Research Lab (TPRL) in West Lafayette, IN. This provides a NIST traceable measurement of the thermal conductivity for the reference bar from room temperature to 1200℃. This characterization is performed using the laser flash method to determine the thermal diffusivity, α (ASTM E1461). The laser flash system at TPRL consists of a Korad K2 laser, in a high vacuum chamber with optical viewports for sample access, a tantalum tube heater surround a sample holding fixture in which the sample under test is mounted, and an infrared (IR) detector for monitoring the temperature response at the back surface of the sample [102]. Then the specific heat, C_P is measured across the full temperature range as well using a Netzsch model 404 differential scanning calorimeter (ASTM 1269), taking care to use precisely the same measurement points. A NIST traceable sapphire measurement standard is utilized for the known standard to evaluate the measurement against. A general overview of both the laser flash technique and the DSC measurement technique is provided in Section 2.1.3. The bulk density, ρ, of the material was calculated

from the sample's geometry and mass. The thermal conductivity can be calculated from these values as

$$\kappa(T) = \alpha(T) \cdot C_P(T) \cdot \rho. \tag{5.1}$$

Please note that in this analysis, the thermal expansion of the molybdenum sample is neglected because the coefficient of thermal expansion for the material is small meaning the dimensions of the sample will not change significantly with temperature.

Table 5.1. Results from molybdenum reference bar characterization by TPRL, where sample A is the material for the upper bar.

Sample Description	Temperature [°C]	Density [kg/m^3]	Specific Heat [J/kg-K]	Thermal Diffusivity [m^2/s]	Thermal Conductivity [W/m-K]
A	23	73.4	10076	252.8	5.36E-05
	50	122	10076	255.6	5.24E-05
	100	212	10076	259.8	5.00E-05
	200	392	10076	267.0	4.60E-05
	300	572	10076	273.4	4.36E-05
	400	752	10076	279.7	4.14E-05
	500	932	10076	285.1	4.02E-05
	600	1112	10076	290.0	3.88E-05
	700	1292	10076	294.8	3.76E-05
	800	1472	10076	299.7	3.63E-05
	900	1652	10076	305.1	3.53E-05
	1000	1832	10076	311.2	3.42E-05
	1100	2012	10076	318.3	3.29E-05
	1200	2192	10076	326.8	3.18E-05

Table 5.2. Results from molybdenum reference bar characterization by TPRL, where sample B is the material for the lower bar.

Sample Description	Temperature [°C]	Density [kg/m^3]	Specific Heat [J/kg-K]	Thermal Diffusivity [m^2/s]	Thermal Conductivity [W/m-K]
B	23	73.4	10129.2	253.3	5.42E-05
	50	122	10129.2	256.0	5.29E-05
	100	212	10129.2	260.3	5.05E-05
	200	392	10129.2	267.9	4.64E-05
	300	572	10129.2	274.5	4.43E-05
	400	752	10129.2	280.8	4.21E-05
	500	932	10129.2	286.2	4.08E-05
	600	1112	10129.2	291.2	3.94E-05
	700	1292	10129.2	296.0	3.84E-05
	800	1472	10129.2	300.9	3.69E-05
	900	1652	10129.2	306.2	3.56E-05
	1000	1832	10129.2	312.3	3.47E-05
	1100	2012	10129.2	319.5	3.35E-05
	1200	2192	10129.2	328.0	3.23E-05

5.2 Determination of Interfacial Contact Resistance

In order to start characterizing the system, we tested the thermal contact resistance of the interfaces by contacting the bars directly and performing a measurement. The results directly show the impact of contact resistance since there is only the single interface and not a sample. Figure 5.1 shows the raw data collected during a Z-Meter test. These are the temperatures for each thermocouple in the meter bars and are used to directly determine the heat flow in the sample. Each heater power level is run until the reference bar thermocouples reach steady state, which here is defined as reaching a variance of less than 0.05℃ over a period of 10 minutes. This running variance is monitored and recorded by the software and notifies the user when steady state is reached. At this time, the user must still manually input the heater power increase, which is why some steady state periods are held for longer than others. There is a portion of the data that decreases from roughly 10,000 to 13,000 seconds, this is due to an internal safety interlock that was tripped because the heater was outputting the maximum power and the temperature was not increasing quickly enough. Once the interlock is tripped, it shuts off power to the heater to protect the system from run-away heating. This parameter can be adjusted or completely disabled, but it is advised for safe operation of the system in the event that the control thermocouple becomes damaged. In this case, it indicates that the thermal resistance of the contact interface is not sufficient to achieve higher temperatures in the system with the available heater power. This interlock was disabled and reset just before 13,000 seconds, where the temperature is seen to climb back to approximately the value before the interlock trip. Evaluation of the raw temperature data permits the heat flow in each bar to be determined. This heat flow, with the known temperature difference across the interface between the bars yields a measured range of interface resistance values shown in Figure 5.2. It is important to note that these values are dependent upon the surface roughness and micro-hardness of both the bars, the interfacial loading, the measurement temperature, and the vacuum pressure. These results cannot be directly

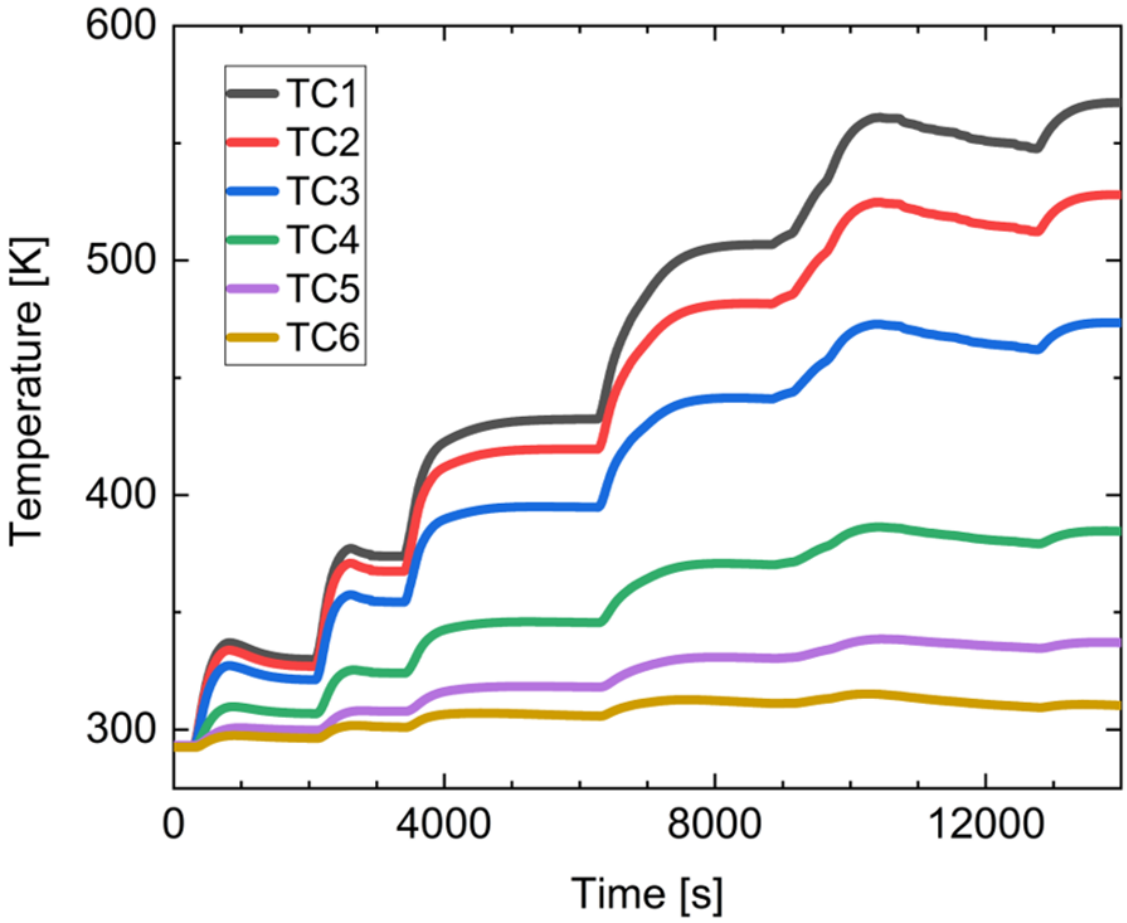

Figure 5.1. The raw temperature data for the thermocouples in both the top and bottom reference bars during a bar-to-bar direct contact test to measure the effects of contact resistance. Each heater power is run until the bar thermocouples reach steady state (variance <0.05℃ over 10 minutes), but the user still must manually change the heater set point which is why some steady regions are longer than others.

applied to other cases of loading, but the model shows reasonable agreement without fitting parameters. The accuracy of this model will continue to be enhanced by further measurements of surface properties for the bars and future samples: complete surface roughness maps (peak asperity and slope) using a high accuracy profilometer, mapping the temperature dependence of emissivity and absorptivity for the bar surfaces, and depth dependent micro-hardness. At this time, the surface roughness of

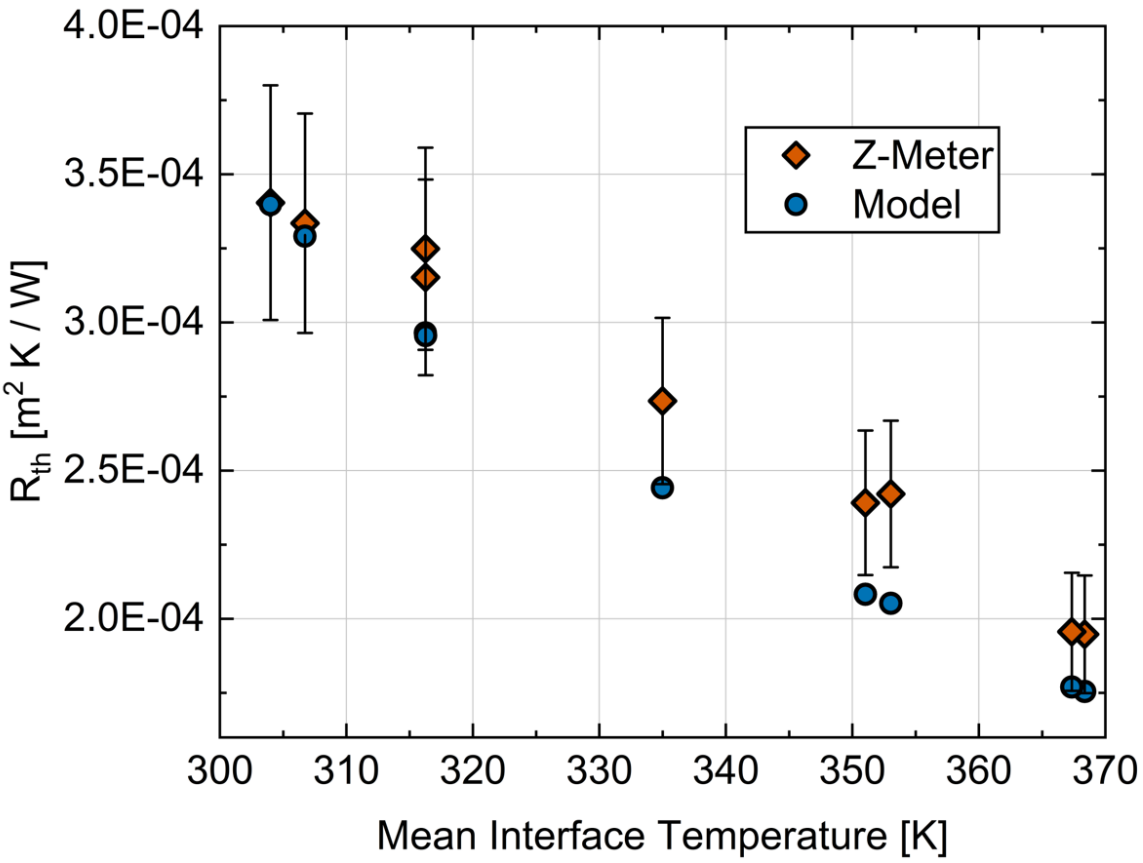

Figure 5.2. Plot showing the thermal contact resistance measured for the bar-to-bar contact case compared to the predicted contact resistance using the contact model developed in chapter 4.

the bars is estimated based upon the polish grit and the uniformity of the reflecting surface, while all other values are based upon data from literature. Further development and benchmark testing of the system for property measurement performance are still required once suitable thermoelectric materials can be obtained.

6. Z-METER SUMMARY

6.1 Development of a high temperature Z-Meter user system for BNC

The Z-Meter was designed and built as a user tool for the Birck Nanotechnology Center (BNC), to fill a gap in characterization capabilities for high-temperature thermoelectric materials. The Z-Meter permits simultaneous measurement of the constitutive properties of the figure of merit, $ZT = \frac{S^2\sigma}{\kappa}T$, between 0 - 1000℃, with large temperature differences ($\Delta T \sim 500$℃).

The completion of this system provides simultaneous property characterization for thermoelectric materials at high-temperatures, under large temperature gradients, and controlled atmospheres. Thermoelectric samples with thicknesses ranging from thin wafers ($\sim$ 100s μm) to large bulk samples ($\sim$ 10 cm) are easily accommodated, without any necessary sensor mounting in the samples. The instrument is capable of *in situ* monitoring of interfacial loading $>$ 10.5 MPa (1522 psi), which is fully user adjustable without breaking vacuum. This allows users to easily adapt the interfacial loading to keep it constant when changing temperatures (accounting for effects of thermal expansion in the system) or to investigate the effects of contact resistance by sweeping through a range of contact pressures. The system provides the freedom of specifying the testing environment, which permits the study of atmospheric effects on material performance: inert gases, high vacuum, or air (see note on use in air, Section 6.2). A detailed uncertainty quantification prediction model is presented to drive the design decisions through out the Z-Meter build and provide a strong platform for accurate data analysis of measured samples.

6.2 Recommendations for Future Development of the Z-Meter System

Probes

It will be necessary to enlarge the thermocouple probe mounting holes in meter bars. The current holes, ⌀0.035 in., are designed to accommodate a 1/32 in. dual bore alumina sheath to protect the thermocouples inside the bar; however, the available dual bore alumina sheathing is slightly oversized, ⌀0.035 in., from the nominal advertised diameter, ⌀0.03125 in., most likely due to expansion of the sheaths during firing. Other suppliers have been contacted, and it seems that most available dual bore ceramic sheaths have a tolerance of ± 5% or ± 0.015 in., whichever is greater. Currently the 1/32 in. sheaths are manually fit to each bar location by reducing the sheath diameter to ∼ 0.033 in., providing a close fit, but still allowing the probe to be inserted. This complicated fitting process (see Appendix A) results in probes which are very fragile and often break during installation.

As a starting point, the existing bar holes of ⌀0.035 in. should be reamed to ∼ ⌀0.037 in. to allow the full diameter sheaths to be used in the probe fabrication process. Adapting the bar to accept full diameter probe sheaths has numerous advantages for the system, including: much faster probe fabrication, increased probe strength by using the full diameter sheath (∼ 6% more diameter than currently installed probes), improved repeatability, and higher yields for manufactured probes as many probes are broken during the fitting process. In addition to the benefits for the probe fabrication, the interface between the probes and the meter bar will be improved as well. At this time, the holes are in an as-drilled state with an estimated average roughness of 1 - 6 μ m, after reaming the estimated average roughness will be reduced to 0.5 - 2 μ m. This will help to improve the thermal and electrical contact between the probes and the bars.

While reaming the existing hole diameters will provide a vast improvement in system usability, it does not address a key issue with the current operation. The existing leads for the type-S thermocouples have a diameter of 0.003 in., which is

good for reducing thermal losses from the bar, but results in extremely fragile probe leads due to the properties of platinum. The biggest problem is encountered with the pure platinum negative lead as it often fails due to work-hardening during handling or after installation during use. At this time, all of the thermocouples installed in the system have been changed to 40 AWG (⌀0.003 in.) type-K special limits of error (SLE) thermocouples which are installed in the ⌀1/32 in. sheaths. The type-S thermocouples were removed due to the high failure rate and lack of stability in the leads due to unavoidable damage inherent to their installation. While the wire diameter for the type-K is the same as that for the type-S, the mechanical properties of the type-K alloys are much more resilient to assembly and installation than those of the platinum used in type-S thermocouples. Type-K SLE thermocouples are an appropriate option for use in the Z-Meter as they allow the probe size to be kept small, thus minimizing point losses at each probe location. This comes at the cost of reduced absolute accuracy, higher drift rates with high-temperature usage, and propensity for 'green rot' in the positive leg (chromel) of the thermocouple. 'Green rot' refers to the preferential volatilisation of chromium in the at low pressures and high temperatures. As the oxidation consumes the chromium in the positive leg, it becomes magnetic which causes a negative voltage drift in the sensor ($\sim$ 30%). Eventually the positive lead will fail mechanically due to the compromised material structure. Even without 'green rot,' drift rates in type-K thermocouples are much higher than those for the noble-metal thermocouples as detailed in Section 3.4.2. Type N thermocouples are formulated to overcome the issues faced by type-K sensors. The use of type-N thermocouples can substantially delay the onset of significant drift in the system. Type-K thermocouples have shown drifts of approximately 175 μV after 200 hours at 1200℃, while type-N thermocouples in the same test experienced only 20 μV of drift after 200 hours at 1200℃ in the same test, please note these values are for a test performed between 8 AWG type-K and N thermocouples and should not be taken as drift values for small diameter wires [60]. Despite the improvements of type-N thermocouples, all of the standard thermocouples will experience significant drift

at high temperatures with the problem being exacerbated by operation in vacuum, temperature cycling of the system, and the small wire diameters. The smaller the wire diameter, the more prone the leads are to contamination, drift, and failure. All of these factors reveal that if small diameter thermocouples are continued to be used in this system, then it is crucial that a proactive sensor replacement schedule be in place and it be strictly adhered to in order to preserve the accuracy of the Z-Meter measurements.

While all standard thermocouple types experience drift in vacuum at high temperatures, the performance of platinum based thermocouples is far better than that of the base metal types. The problem with platinum thermocouples of very small wire diameter is that they are too fragile and cannot be practically handled, installed, or used reliably. Increasing the wire diameter to the maximum size ($\varnothing$0.005 in.) that will fit the current probe size will help slightly, but this will still be very difficult to assemble and install. Bentley recommends a 24 AWG ($\varnothing$0.020 in. or 0.5 mm) for the best balance in stability, cost, and ease of handling [59], but this size thermocouple will create much larger thermal parasitics in the bar. While stability/probe robustness and minimizing thermal losses are at odds, a compromise can be reached. It is vital that the probes function as they are supposed to within the system and that they can be effectively installed as needed; without this, the system is not going to function properly to conduct the desired measurements. I propose removing the bars from the system and drilling new holes on the face 180° from the existing holes to accommodate larger probes. The new probe locations should be shifted away from the bar interfaces by a sufficient amount to avoid bit deviation during drilling of the closest hole to the interface and maintain the 2 cm spacing between the next two holes. The current supply probe locations can be adjusted for the bit size to avoid contacting the angled portion of the top bar or the copper mounting base of the lower bar, but do not need to maintain a strict relative spacing to the other holes. The probe positions must be adjusted for several reasons: 1.) if not adjusted, they will match up with the original probe holes on the other side and create a stepped (dual

diameter) through hole, 2.) drilling a larger hole at the same set back spacing from the interface as the small probe may not provide sufficient material to fully encompass the new hole, 3.) drilling a hole very close to the edge of a part often results in deflection of the drill bit towards the interface due to the thermal loading during the drilling process. I recommend increasing the probe size to $\varnothing 1/16$ in. as this will greatly strengthen the probe sheath itself, but also permit the use of thermocouple leads as large as 27 AWG ($\varnothing 0.015$ in.). While a larger lead will increase the losses from the measurement locations along the bar, it is necessary to achieve proper system operation. Further testing should be conducted for both probe fabrication and installation to determine the optimum size for thermocouple leads not based solely upon heat transfer and losses, but rather balancing thermal losses with ease of handling, contamination resistance, and durability of the assembled probe. As the wire diameter is increased, the probe conductance losses may no longer be negligible in the measurement. I propose incorporating a combined immersion and lead wire model at the mounting location of each probe to account for the added thermal losses [61, 64]. The use of these models helps to account for the losses at each probe as the probe size increases and allows appropriate corrections to be applied to the data based on physical models of what is happening in the system rather than simply adding a fitting parameter to a numerical code.

Due to the uncertainty in the probe size, we suggest purchasing several packages of $\varnothing 1/16$ in. probes at the same time, and waiting to drill the mounting holes until the sheaths arrive. If all the sheaths are coming from the same lot, the variance in the diameters should be much smaller than the listed $\pm$ 5% or $\pm$ 0.015 in. (whichever is greater). The new bar holes should be drilled approximately 0.002 in. larger than the nominal diameter for the sheath lot. It takes approximately 16 - 20 in. of total sheath length to fully instrument the thermocouples, voltage probes, and current connections to the bar. I would recommend ordering five times this length to provide a sufficient back stock of sheath material for future probes in the system. If additional sheaths are required in the future, the best practice will be to contact the company prior

to placing an order and communicate that sheaths in the size range [$\varnothing_{MountingHole}$ - 0.004 in. to $\varnothing_{MountingHole}$ - 0.002 in.] are required. They should be able to tell you if their current stock will fall within this range prior to placing the order.

Operation in Air at High Temperatures

Upper temperature limitations are enacted for use in air to avoid oxidation of system components. The system is designed to avoid problems with oxidation, even when operating at high temperatures in air, but insufficient system operation data is available at this time to permit full scale heating in air. The biggest limiting factor for temperature operation in air will be the convective losses and heating of the load cells above the bars as the hot air rises. Additionally, prior to any testing above 100℃ in an air environment, the copper mount for the lower bar must be plated to avoid rapid oxidation of this surface. In addition to the complications added by oxidation concerns, operation in a non-vacuum air environment can introduce significant convection losses along the bar and will require extensive modeling to accurately correct the data for this effect.

Heater

The current system design will work to achieve temperatures as high as 1000℃ for the sample hot-side, but it will only be able to accomplish this for specific samples with sufficiently low thermal conductivity due to the available heater power. The current heater was purchased when the initial idea of a high-temperature Z-Meter at Purdue was started by a previous group, but not pursued further. This heater has a maximum rated power output of 190 W, as shown in Table 3.5, which is not a lot of power for such a large system. I have made it work for the purposes of proving the operational concept of the system, but ideally a much more powerful heater, on the order of 1 kW should be installed in the Z-Meter to allow a more complete range of thermal conductivities and temperature differences across the sample to be tested. I have spoken with Heat Wave Labs, the manufacturer of the original heater, and there

are drop in replacements that would work with the existing system and shielding, but would replace the button heater with a cartridge heater providing 500 - 1,000 W of heating power. In addition to this, we highly recommend that a future heater not have the return power lead internally brazed, but rather have two power leads and leave the surface of the heater isolated to remove the need for the aluminun nitride (AlN) isolation disk between the heater and upper meter bar.

Another potential issue to be addressed with the heater are the preload springs behind the heater shield assembly inside of the ceramic loading shroud that help to keep the heater face in good thermal contact with the AlN isolation disk and the upper bar. These are just typical 316SS compression springs and are not specifically designed for high temperature operation. A typical maximum operating temperatures for a spring of this type is approximately 275℃. Based on some conversations during the early design phase of this project with the manufacturer of the heater (Heat Wave Labs), the expected back side of the heater shield is $\sim$ 200 - 300 ℃ for a heater face temperature of 1200℃. This put us very close to the operating range of the regular springs, so we elected to test the system before going to a more extreme solution. Note that implementation of the estimated heater internal geometry and shielding within my multi-physics models showed that the back of the heater shield predicted temperatures much higher than 300℃, but we chose to move forward with the construction of the system based on the manufacturer's recommendations - performing validation tests for ourselves to compare the maximum expected temperature range provided by the manufacturer with that from my models. After initial tests while monitoring the back of the heater shield temperature, we observed temperatures consistent with the multi-physics models which greatly exceeded the 300℃ mark for the back of the heater shield. Operation for long at these temperatures will result in spring relaxation and permanent deformation, thus rendering the springs useless for keeping the heater in good thermal contact with the bar. Therefore, we propose two solution paths, which we plan to implement at the earliest possible opportunity.

The first solution option is to either source or fabricate high-temperature compression springs. Diamond wire spring company offers Inconel 718 springs which are rated for a maximum operation temperature of 593℃, which might be sufficient as the highest temperature we have currently observed for the back of the heater shield is 608℃. However this still puts these springs over their maximum operation temperature. Inconel spring are also advertised by Yost Superior as being operational up to 871℃. But both of these companies typically manufacture large runs of parts and may not be able to produce only four springs for us. An alternative to buying custom springs is to make my own high temperature springs. The details of the proposed process are included in Appendix B. The second solution option is to forgo the use of springs all together and instead install rigid ceramic stand-offs that are precisely sized to keep the heater face in firm contact with the AlN and the upper bar surface. If this is pursued, two small radial holes should be drilled in the ceramic loading shroud to allow an allen wrench to be used to tighten and loosen the mounting set screws for the button heater and make fine adjustments to perfect the fit.

Additional Heater Interlocks

During testing, we have noticed that the temperatures of the load cell platforms above the bar increase with increasing heater set point as expected, but feel that we must raise this concern here for future researchers. These load cells are temperature compensated up to 71℃ (160°F), and can be further operated to 93℃ (200°F) by applying a temperature shift span and zero. However, the load cells can be quickly damaged if they are allowed to reach temperatures above 93℃. It is critical that the researcher keep an eye on the temperature of the lower mount for the load cells to ensure that the temperature does not get too hot and damage the load cells ($T_{LoadCell} >$ 93℃) or bias the data if 71℃ $\leq T_{LoadCell} \leq$ 93℃ and the proper corrections are not applied. A software heater interlock should be applied to shut off the heater output if the temperature of the load cells reaches 90℃. A similar hard cut-off point of 150℃ should be defined for the temperature of the cold plate to avoid exceeding the

rated fluid temperature or chiller operation range. Currently these temperatures are monitored by the user and they must manually respond and physically turn off the heater. This is not a good idea for long-term multi-user utilization of the system. Currently the mechanical heater interlock is wired to the insulation temperature for the current supply lead for the heater. Since a PTFE insulated wire is used, this insulation cannot get above 200℃, but significant rises have not be observed as of yet at that location. It might be a better idea to change the mechanical safety limit for the heater to monitor the temperature of the load cell lower platform to help protect these sensors.

Chiller Limited System

The maximum operating point for the chiller is 150℃, thus limiting the temperature of the cold plate inside the chamber to this same value. This fixed maximum temperature of the cold plate in contact with the copper lower bar mount makes it difficult to achieve elevated lower bar temperatures and requires that any high temperature measurements be carried out under very large temperature gradients. I have designed a thermal stand-off platform to be installed between the copper lower bar mount and the cold plate, which will serve as a means of elevating the lower bar temperature while still complying with the required upper temperature limits for the cold plate. If a new chiller is being considered which will permit the fluid temperature to be raised significantly, recall that the liquid feedthroughs into the vacuum chamber are all metal and will heat up quickly. This will also expose the vacuum seals to these same high temperatures, which they are not designed to handle. This can be addressed through the installation of all metal ring seals, which will still provide vacuum level seals via an all-metal o-ring replacement for a KF vacuum flange.

Non-Contact Temperature Mapping

A final system improvement could be the incorporation of an infrared (IR) camera to image the bar interfaces and the sample. This will allow the user to determine

the thermal gradient along the sample directly and account for contact resistances by imaging a short distance of the meter bar as well to map the temperature drop across the bar-sample interface. In addition to the IR camera, and a suitable magnification lens with an appropriate field of view, the system would need to have the current 6 in. CF flanged zero length quartz (fused silica) viewport replaced with an IR transparent window. The IR transparent window is required to allow the appropriate wavelengths to transmit through the material without substantial losses. Materials such as sapphire, calcium fluoride (CaF_2), magnesium fluoride (MgF_2) or zinc selenide ($ZnSe$) are commonly used for IR transparent viewports in vacuum systems. These IR transparent viewports are less common in the 6 in. size CF flange, so a zero length flange plate adaptor may be required to reduce the 6 in. CF flange to a more readily available 4.5 in. CF flange zero length viewport.

PART II: PHASE CHANGE MATERIAL IN SITU CHARACTERIZATION

7. APPLICATIONS, MATERIALS, AND MEASUREMENTS

Phase change materials (PCMs) are used for numerous applications of thermal energy storage: keeping beverages cold in a cooler full of ice on a hot day, capturing solar energy for storage and later use to heat water [103–106], as a means of controlling the climate within our buildings and homes via integration into building materials [107–111], and incorporation into furniture within those homes [112]. Beyond housing and homewares, PCMs are utilized even further to help maintain proper operating conditions in situations where power requirement are critical, precluding typical thermal management strategies. Passive thermal management using PCMs has been long utilized in the design and construction of aerospace vehicles and spacecraft as a means of storing thermal energy for later use, damping of high power events to preserve local temperature profiles, or as a means of providing short-term tactical thermal management in a volume and mass efficient package [113–116]. The investigation of PCM design and application in spacecraft is particularly insightful, because in these systems, heat from high-power-dissipating electronic must be removed, there is no free convection, and volume/weight are highly controlled [115]. Wax based PCM thermal control systems were used successfully on the Lunar Roving Vehicles (LRVs) for the Apollo 15, 16, and 17 missions to the moon, shown in Figure 7.1(a). Three main systems of the LRV utilized passive thermal management using PCMs: the Signal Processing Unit (SPU) and batteries, the Drive Control Electronics (DCE), and the Lunar Communications Relay Unit (LCRU) [118]. Passive thermal management with PCMs was targeted due to the periodic nature of the usage demand on this mission. The primary thermal loads were only present during operation by the astronauts, then after these "sorties" the heat could be rejected from the LRV via radiator panels allowing the PCM to solidify and prepare for the next cycle [117].

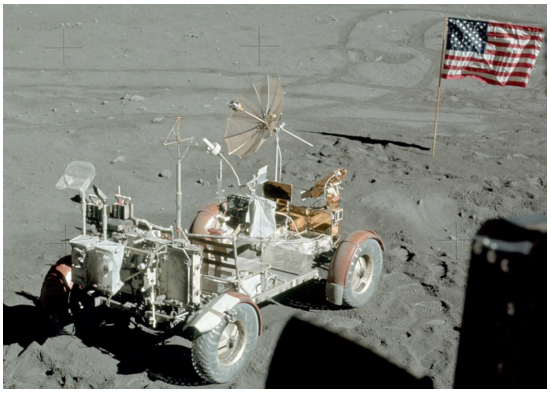

(a) LRV during Apollo 17 mission

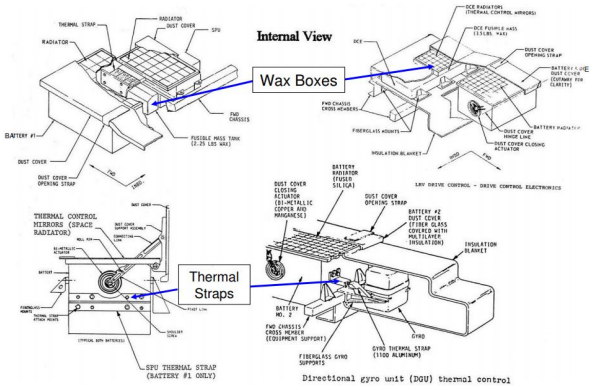

(b) LRV forward chassis electronics [117]

Figure 7.1. Lunar Rover Vehicle (LRV) during the Apollo 17 moon mission. Passive thermal management using PCMs was used in three key systems: 1.) the Signal Processing Unit (SPU) and batteries, 2.) the Drive Control Electronics (DCE), and 3.) the Lunar Communications Relay Unit (LCRU) [118, 119]. Images obtained from NASA and their use is permitted under the general permissions of NASA media guidelines.

7.1 Passive Thermal Management

Parallels can be drawn between design for spacecraft and similar design constraints faced in thermal management in portable electronics. Both applications have high-power densities requiring spreading and dissipation elsewhere, natural convection cannot be used directly to cool the device, and significant size and weight constraints. Please note, portable electronics utilize natural convective cooling on the outside of the device for heat rejection, but it is not appreciable inside the device. With device power densities growing ever higher, static thermal management designs which target and design for worst case operating conditions are no longer favorable due to the high temperatures swings during cycling, which can lead to component failure.

PCMs are attractive for passive thermal management because they are compact, versatile, and dampen peak system thermal loads through the latent heat of phase change. Implementation of PCMs can reduce system weight and thermal load requirements since the peak temperatures are smoothed by the phase change process.

This permits the system to be designed for an average load rather than peak/worst-case loading. Since most portable electronics do not have sustained high loads, but rather short surges of high usage, PCMs are well suited for use to extend the time of peak operating power while keeping temperatures below critical levels. After the peak system load subsides, the PCM has time to dissipate this energy without impacting the perceived performance of the device. Implementation of PCMs within portable electronics helps to increase component reliability because temperature swings are smoothed and components no longer see the very high temperatures from the short heat surges, such as those due to computational sprinting.

7.2 Performance of Phase Change Materials

7.2.1 PCM Selection

Numerous PCMs exist with a wide range of thermophysical properties. Here, PCMs are selected to provide insight into the factors that govern PCM performance in thermal management applications. The primary properties to consider in the selection of PCMs include: melting temperature (T_M), thermal conductivity (κ), latent heat (L), heat capacity (C_p), and mass density (ρ). The PCM options are first narrowed by targeting a specific range of operating temperatures. This work focuses on an operating temperature range from 30 - 95℃, and a melting point is selected to fall within this envelope. A primary focus of melting around 70℃ is selected to allow adequate time for melting while maintaining a sufficiently high phase transition point. This allows regeneration to occur quickly, making the latent heat available for repeated cycle loading. Additionally, a lower melting point material, $T_M \sim 40$℃, is included in the study to highlight the impact this parameter has on system performance. Commercially available PCMs are considered with melting points that are approximately the values targeted. Final selection is based upon a relative ranking of the different materials using the cooling figure of merit proposed by Shamberger and colleagues [120, 121].

Cooling Capacity Figure of Merit

It is vital to have a metric of material performance, independent of system architecture, as means of rapid comparison between different materials. The main points of interest when investigating PCMs for passive thermal management are: melting temperature (T_M), latent heat of fusion, (L), and cooling capacity, (q). In this instance, cooling capacity refers to the instantaneous rate of heat transfer into the component. Both melting temperature and latent heat are intrinsic material properties and can easily be tabulated for comparison; however, cooling capacity is typically very dependent on the shape of the physical system and the boundary conditions. Typically, engineers have utilized the thermal conductivity as the third metric for comparison and ranking of approximate cooling capacity for a PCM; however, this neglects the contributions of the other properties contributing to thermal performance such as latent heat of fusion, material density, or the heat capacity of the material. Shamberger [120, 121] recently proposed a new cooling capacity figure of merit,

$$FoM_q \sim \kappa_l L_v, \tag{7.1}$$

where κ_l is the thermal conductivity of the liquid phase and L_v is the volumetric latent heat. This relative comparison between performance potential for different PCMs is valid when considering a narrow band of temperatures, approximately $\pm$ 10℃, on either side of the material melting temperature. Since, in many applications, PCMs are approximately isothermal during melting and utilization of their latent heat, this is a good comparison point between materials.

The relative rankings, plus consideration of availability in small sample sizes, are used to select three PCMs for analysis: (1) a high FoM_q salt hydrate material with a melting point of 70℃, PlusICE S70, (2) a lower FoM_q organic PCM with a melting temperature close to that of the salt hydrate at 68℃, PureTemp 68, and (3) another organic PCM in the same product family with a melting temperature of 42℃, PureTemp 42, to compare the impact of melting point.

7.2.2 Enhancing PCM Thermal Conductivity

Despite their usefulness, PCMs have some implementation roadblocks to overcome to enable their wide use as a primary thermal management solution for electronics, which mainly center around poor thermal properties. Much of the body of PCM research for thermal management addresses the issue of low thermal properties, specifically enhancement of PCM thermal conductivity. A popular approach to enhance the thermal conductivity of PCMs is to integrate the PCM into high conductivity structures. Chintakrinda *et al.* [122] compared the effectiveness of three different thermal conductivity enhancers (aluminum foam, graphite foam, and graphite nanofibers) infiltrated with a paraffin wax, for heat fluxes from 1.9 - 11.6 W/cm^2. They found that the addition of 11 wt% graphite nanofibers to the paraffin wax provided the most effective temperature control of their base heating platform at low power levels ($\sim$ 2 W/cm^2), but as the heat flux was increased, the effectiveness of this approach decreased. At higher heat fluxes (5 - 11 W/cm^2), they showed the use of high conductivity foams vastly improved the performance of the heat sink in reducing the temperature of the heated base; however, they did not observe any noticeable impact by the addition of the PCM to the heat sink. This showed that while the foam provided a high-conductivity pathway through the PCM, the interface between the foam and PCM was not sufficient for adequate heat transfer to the PCM, and thus did not provide effective utilization of the latent heat in the PCM. Similar to the heat spreading benefits of high-conductivity foams, metallic fins provide high conductivity pathways through the low conductivity PCM with the added benefit of precise structure control and increased interfacial areas [123]. Bentilla *et al.* [124] compared the performance of high conductivity filling structures (*e.g.*, foams, wools, and honeycombs) finding honeycomb structures to be the most effective due to the the continuous, regular, high conductivity structure, combined with large interfacial areas and small PCM thicknesses. This conclusion was echoed by Mahmoud *et al.* [125], given the good performance, light weight, and ease of implementation of a honeycomb core.

At the onset of heating, the PCMs absorb heat via sensible heating increasing in temperature until they reach their melting point. Then, the latent heat of phase change allows a significant amount of heat to be absorbed into the PCM with minimal temperature increase until the PCM is fully exhausted. This is desirable for electronics as it smooths or dampens potential temperature spikes during high-heat flux events by keeping the temperature close to the melting temperature. However, these materials typically suffer from low thermal conductivities making them difficult to implement in actual devices due to the concern of overheating after the latent heat storage capacity is exhausted. One approach to address this utilizes a heat sink or heat spreader design in which the PCM is integrated, thus effectively distributing heat throughout the low conductivity PCM.

Much research into PCM implementation for passive thermal management has involved finned heat sinks. Some studies concentrate on fin density, finding that increasing the number of pin fins is an effective way to enhance heat transfer to PCMs in high-power systems [126–128], while others target the fin shape to optimize the best interfacial shape to maximize heat transfer from the heat sink structure to the PCM [129]. Gurrum *et al.* [130] incorporated metallic PCM into microchannels (see Figure 7.2(b)) and studied the impact of periodic power cycling, determining that the correlation between channel size and system performance was heavily dependent upon the thermal conductivity of the PCM. Krishnan *et al.* [131] confirmed the conclusion reached by Bentilla *et al.* [124] that long thin cavities for PCM provide better effectiveness for system cooling. This is because there is a smaller depth of PCM through which the heat must conduct to fully access and utilize the complete volume of material for phase change. Extensive reviews of additional materials and techniques pursued for thermal conductivity enhancement of PCMs are available in literature [10, 123].

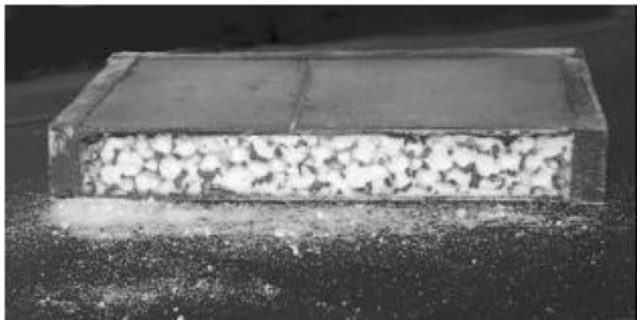

(a) Metal foam [132]

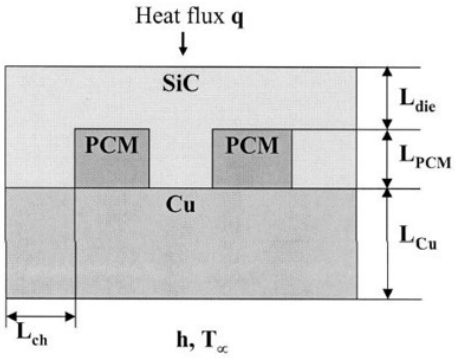

(b) Microchannels [130]

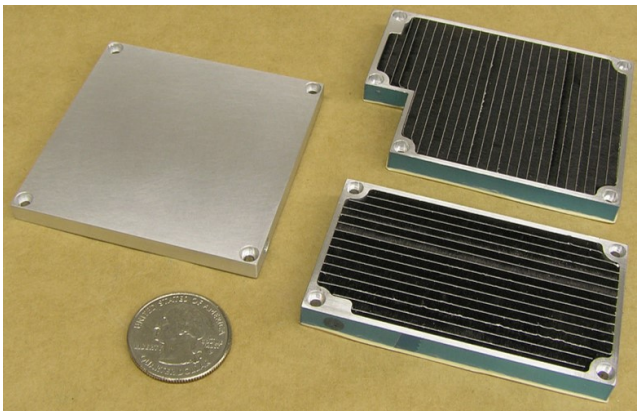

(c) Fins [133]

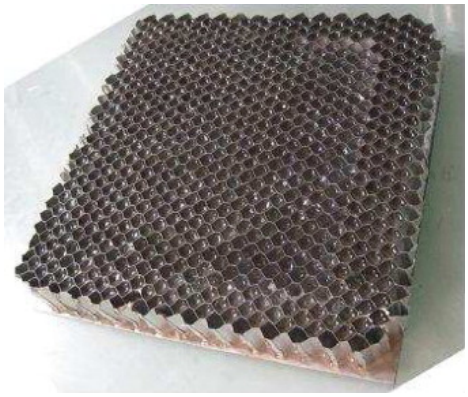

(d) Honeycomb structure [134]

Figure 7.2. High conductivity filler structures and integrated architectures boost the effective thermal conductivity of the PCM in the system. Panel 7.2(a) reprinted from *Proceedings of 2000 ASME IMECE: Undergraduate Research and Design in Heat Transfer*, C.A. Bauer and R.A. Wirtz, Thermal Characterization of a Compact Passive Thermal Energy Storage Device, 2000, with permission from ASME. Panel 7.2(b) reprinted from *Numerical Heat Transfer, Part A: Applications*, Vol. **42**/8, S.P. Gurrum, Y.K. Joshi, and J. Kim, Thermal Management of High Temperature Pulsed Electronics using Metallic Phase Change Materials, 2002, Taylor & Francis, with permission of the publisher. Panel 7.2(c) reproduced with permission of KULR Technologies. Panel 7.2(d) reprinted from *Energy and Buildings*, Vol. **43**/1, C. Hasse, M. Grenet, A. Bontemps, R. Dendievel and H. Salle, Realization, test and modelling of honeycomb wallboards containing a Phase Change Material, 232-238, 2011, with permission from Elsevier.

7.2.3 Characterization of PCM Performance

Advancement of PCM technology for practical integration in portable electronics for thermal management requires careful property testing and characterization of PCMs under dynamic thermal operating conditions. Much work has focused on numerical modeling of PCMs [123, 135] and designs for thermal management [129, 136], but studies focused on testing of integrated devices under realistic operating conditions have fallen short. On the other hand, property testing is typically conducted ex situ and a wealth of data exists for various PCMs that can be combined with models to predict performance. Differential scanning calorimetry (DSC) can be used to determine the melting temperature and latent heat of fusion for new PCMs. Dynamic response DSC can measure thermal conductivity with errors of approximately ± 10% for materials in the range of 0.5 - 2.0 $^{W}/_{m \cdot K}$, provided the assumptions laid out by Merzlyakov and Schick [137] are valid for the particular measurement. Alternatively, some researchers utilize hot disk thermal analyzers [138, 139], hot wire methods [140–146], or the reference bar method [147, 148] for measurement of thermal conductivity of the PCM alone.

While testing of discrete PCM samples to determine the intrinsic material properties is valuable in developing high performance materials, it does not capture the actual performance of the enhanced heat exchanger package. This must be done using carefully controlled test platforms. For example, Hodes *et al.* [149] utilized a Kapton® heater to emulate the chip in a portable handset and measured the time it took for the PCM temperature to reach specific levels. This highlighted the insulating effect of PCMs after the latent heat has been fully exhausted, which leads to rapid temperature rises. Luo *et al.* [150] installed a heater inside of a mobile phone to mimic realistic operation conditions. Temperature measurements throughout the various components of the phone showed conduction was the dominant mode of heat transfer within the phone architecture. Tan *et al.* [151] experimentally investigated the impact of including fins within the PCM. Their test setup consisted of four heater

modules mounted on top of a plate with a PCM cavity under each heater to approximate conditions within a personal digital assistant (PDA).

Note that the heaters used in these experiments are typically large, requiring the heat flux be applied over a majority, if not all, of the PCM package, and the data acquisition relies upon auxiliary temperature sensors external to the chip die, which do not provide an *in situ* view of the package performance. Thus, my system aims to address these issues by utilizing the same form factor for the heater as found in actual systems, but with user controlled heating and integrated temperature sensors to better represent actual chip measurements and provide streamlined testing procedures.

These past studies are important to build an understanding of specific processes involved with implementation of composite PCM thermal management packages; however, it is very difficult to compare data between experiments. The heaters used are typically large applying the heat flux over a majority, if not all, of the PCM package, and data acquisition relies upon external or auxiliary temperature sensors. There is a need for rigorous testing of phase change material based heat sinks in realistic application configurations.

In this portion of my dissertation, I develop and characterize composite PCM heat sinks to improve the performance of these heat sinks for use in passive thermal management of portable electronics. In Chapter 8, I detail the design of the enhanced composite PCM heat sinks and discuss the key parameters to consider when designing a composite PCM heat sink. Then, in Chapter 9 to better investigate the performance of PCM packages, I develop a general test method allowing performance to be compared directly across different types of PCMs and packages for user specified (spatial and temporal) power profiles, quantifiable heating, realistic test conditions, controllable interfacial loading, and *in situ* temperature measurements inside the chip to represent the measurement location of sensors in an actual chip die. Chapter 10 presents the performance results from the testing of the enhanced PCM heat sinks using the the improved TTV test bed.

8. PERFORMANCE EVALUATION FOR PCM THERMAL MANAGEMENT

This chapter describes the design of small-scale PCM heat sinks for integration into portable electronic devices and the design of a thermal test vehicle (TTV) for characterization of PCM heat sinks.

8.1 Package Design and Development

Building off previous work to optimize heat exchanger fins for composite PCM packaging, we design a range of packaging options to be evaluated by the new test rig to highlight differences in performance. Previous studies indicated that honeycomb structures provided good thermal conductivity enhancement for PCMs [124–128]. Leveraging this, we establish some design guidelines to help address inefficiencies in previous designs. Integrating metallic structures (*e.g.*, foam, wool or honeycomb) into a PCM typically results in poor thermal contact with the outer package leading to large thermal resistances. On the other hand, monolithic integration of the package and the thermal conductivity enhancement structure eliminates the contact problems. Further, the package is most responsive to sudden changes in heat input when the cavities of PCM are narrow with lots of surface area interfacing with the high conductivity structure. These high aspect ratio PCM pockets maximize the surface area to volume ratio between the PCM and thermal conductivity enhancement structure.

Here, we propose a novel, highly configurable package design for use as a composite PCM-heat exchanger. This design leverages a standard external package size which can be established early in the system level design for the portable electronic device. This would guarantee favorable positioning of the thermal management system, while allowing continued development of the internal structure of the package to adapt to other changes in the design cycle for the device. The designer can op-

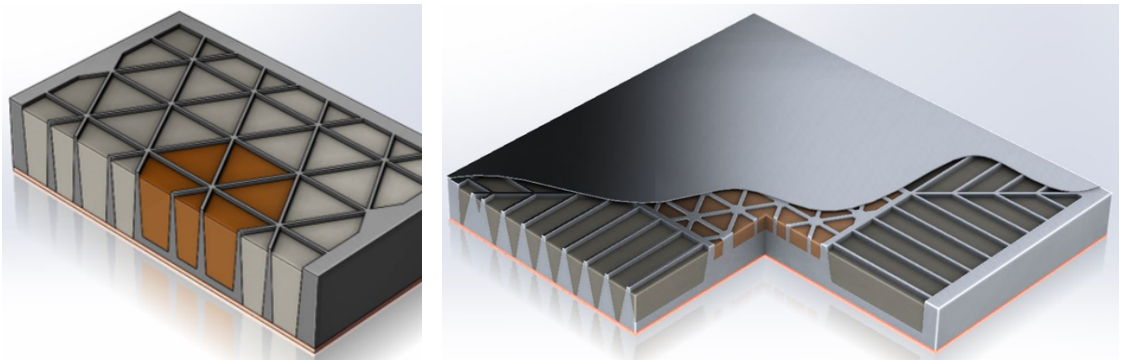

(a) 25 mm package (b) 50 mm package

Figure 8.1. The proposed tunable architecture PCM package design concepts demonstrate how a standard external package size can be specifically tuned for different families of chips without impacting the mechanical infrastructure around it. Local confinement of small PCM volumes permits the use of multiple PCMs to target different performance zones within the package. This compartmentalization also permits increased base thickness in key high power areas of the chip to promote better heat spreading. Note both figures are sectioned to better show internal package features. The top seal has been completely removed from panel (a) showing the 25 mm package. Panel (b) illustrates a larger 50 mm package with thicker central heat spreader and multiple PCMs.

timize the thermal management package layout for specific power maps or thermal requirements of individual chip families. Figure 8.1 illustrates the tunable package architecture. The tight working volumes are based upon a honeycomb pattern subdivided into isogrid or isokite deltoid structures further augmenting the surface area to volume ratio beyond that studied with traditional honeycomb enhancements. A benefit of my discrete PCM region based design, shown in Figure 8.1(a), is that not all partitioned volumes within the package need to be the same depth. A PCM volume with a shallower depth, such as those shown in orange of Figure 8.1(a) and 8.1(b), is advantageous for high-power density regions of chips because the thicker base acts as a heat spreader. Additionally, the thickness of the isostructure walls can be increased in areas of high heat flux to promote enhanced local heat spreading. These tech-

niques for localized heat spreading boost design performance without requiring all of the walls or the entire base of the package to be thicker, which would significantly reduce the available volume of PCM. In an extreme case, where a region of heat flux is high enough that the PCM will not have time to change phase prior to the chip reaching the thermal cut-off temperature, a portion of the PCM package could be left as solid metal, providing a continuous high conductivity path from the chip to the rejection surface at the top of the package. This spreading path quickly removes heat from the chip surface while still providing the benefit of latent heat storage from the PCM in the remaining volume of the package. In addition to the design benefits of localized heat spreaders, the size and shape of the PCM volumes can be optimized to the specific power map of each application. As an example of this, Figure 8.1(b) shows the inclusion of radial spreading troughs to promote uniform heat spreading through-out the package, while maximizing the total volume of PCM available for latent heat storage. Since the PCM volumes are discrete, this also permits multiple PCMs to be employed within the same package without concerns of mixing or sedimentation between materials. The extent of possible performance enhancements gained by introducing multiple PCMs will be addressed in future studies.

Applying these design metrics to the conceptual designs shown in Figure 8.1, we develop a range of proposed package designs for performance testing. I select package sizes of 25 and 50 mm square at a thickness of 5 mm for investigation. This helps to limit the study to the effects of the internal structure, and these common sizes allow results to be better compared to past and future work. As discussed for the conceptual design, the package layout can be easily tuned to the power map of the specific chip in a particular system. Our novel geometries seek to augment the performance of traditional PCM heat exchanger layouts by reducing the heat transfer resistance from the die to the center of the PCM volumes. This allows faster response time to surge power demands, while maintaining adequate heat spreading throughout the package. In this study, we design packages for a uniform power map to investigate the worst case scenario of setting the entire chip at the highest heat flux,

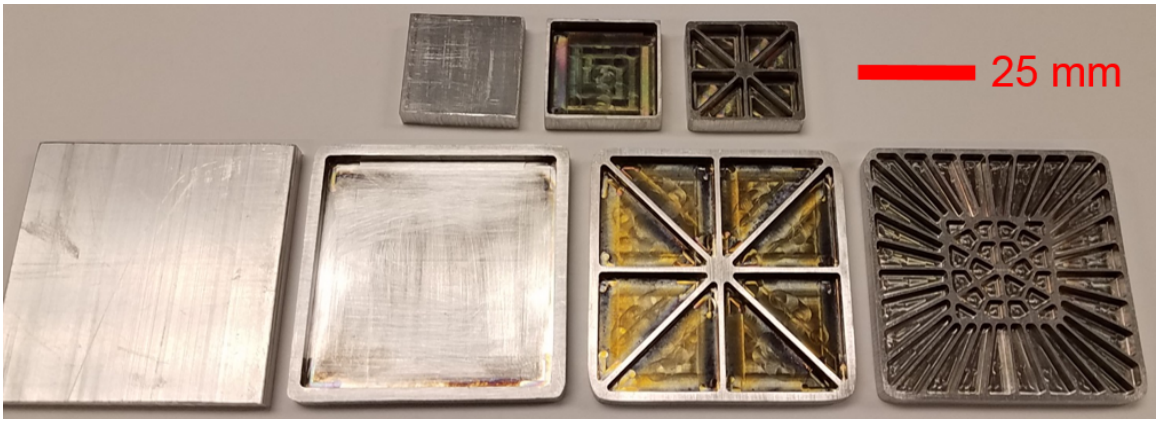

Figure 8.2. Overview of the different package designs compared in this study. All packages are 5 mm thick and machined from 6061 aluminum. Those in the top row are 25 × 25 mm, while the bottom row are 50 × 50 mm. The left-most package in both rows is the solid aluminum block the same size as the composite samples, used as a performance comparison benchmark with sensible heating only. Both the 25 and 50 mm package designs have a no fin case (second from the left) and an isogrid based fin design. The 50 mm package has one additional design based upon isokite deltoid fins (bottom row, far right). This isokite design highlights the key design features of the package design that can be used to tune and optimize packages for specific power maps and applications.

but in practice could easily be tuned for the specific hot spots to provide even greater performance benefits from the added PCM storage volume. Based upon these design concepts, we evaluate two separate manufacturing approaches for package fabrication: bottom-up and top-down.

8.2 Bottom-Up Approach

A bottom-up approach is additive, the composite heat exchanger is built up by introducing material to build the structure up to the final design. This approach permits a high degree of design freedom and is not constrained by typical machining operations. In fact, the heat exchanger would be built layer-by-layer using high

thermal conductivity metal foils, laser cut into shape and ultrasonically welded together utilizing the Fabrisonic R220 ultrasonic welding machine in Purdue's Herrick Laboratory.

8.2.1 Ultrasonic Welding

The ultrasonic welding process creates a solid-state bond between the layers of foil at low temperatures (no melting). The process is detailed in Figure 8.3(b). This consists of breaking the native oxide layer, bringing the two materials into intimate contact such that localized asperities yield and collapse due to high frequency vibrations from the horn (roller), then heat and pressure create a high strength metal-metal solid state bond [152]. While heat is required to form the solid state weld, it is a very low heat compared to traditional bonding processes. The peak temperature for this process for an aluminum-aluminum bond is less than 120℃.

To design the structure for this assembly technique, a slicer program sub-divides the 3D CAD solid model of the heat exchanger. These programs are typically used for preparation of 3D printer builds, but work well here to define discrete layers of the design based on the 150 μm thickness of the foil used to form the layers. This metal foil stock is laser cut to form each layer of the component stack, then the layers are carefully aligned on the Fabrisonic welding platform using a custom designed alignment pin tooling plate to ensure proper layer alignment. Due to the low temperature of the ultrasonic welding process, PCM can be introduced into the heat exchanger at any of the intermediate steps, and can even be sealed within the package with further layers added on top of it. A general representation of such a heat exchanger design can be seen in Figure 8.4, where the thin void layers are clearly visible in the right image.

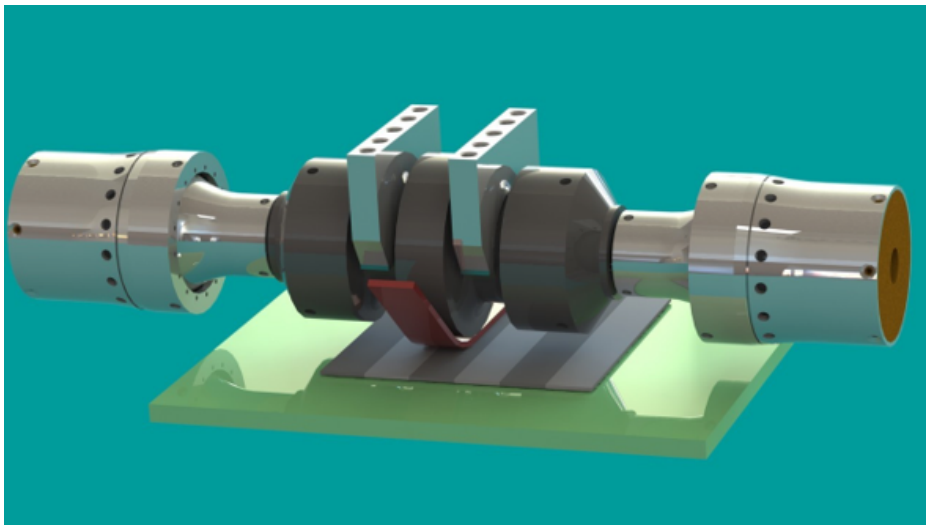

(a) Ultrasonic welding horn bonds foil

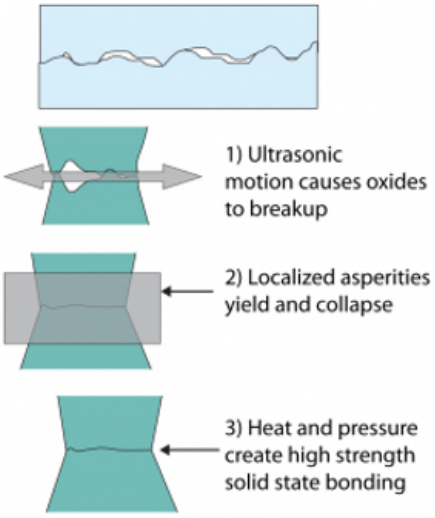

(b) Welding process

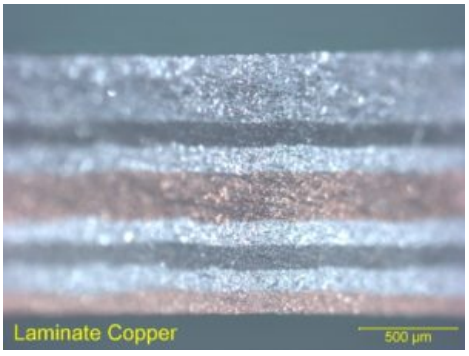

(c) Bonding of dissimilar materials

Figure 8.3. The weld is formed by ultrasonically removing the native oxide layers, bringing the materials into close contact such that the local roughness features yield and flatten due to high frequency vibrations from the horn, and then the heat and high pressure forms high strength metal-metal solid state bonds. The required applied heat is very low: for aluminum, the report peak temperature is less than 120℃. This process can easily be used to weld dissimilar materials to provide a wider range of design options for the heat exchanger structure. Figures courtesy of Fabrisonic [152].

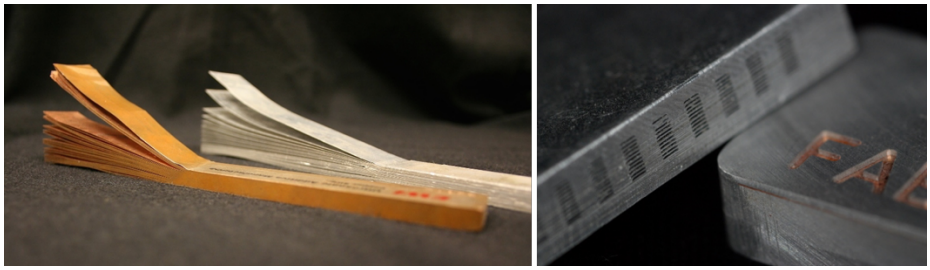

Figure 8.4. (left) Fabrisonic demo samples showing the result of the process prior to trimming the excess foil stock off the part. (right) Example of a heat exchanger fabricated with this technique. Note the voids within the cross-section through which fluid could flow (or in my work, PCM could be embedded). Figures courtesy of Fabrisonic [152].

8.2.2 Challenges of Implementing the Bottom-Up Approach

The possibilities for the performance enhancement with the Fabrisonic system are great, but implementing this approach has introduced some major road blocks to success. The system available on campus is older and lacks the top-end automation and integrated machining capabilities. This means that instead of the foil being continuously introduced from a roll where it is held under constant pressure, aligned, bonded, then cut in place, we must do each step manually. The main problem with this is the need to cut each layer's pattern prior to tensioning the foil. The pneumatic control of the tensioning pistons on our system is not fine enough to prevent the initial tension impulse from ripping the reduced cross-section of the foil. Wider foils were considered but due to the narrow width for the horn of the machine, wrinkling of the foil created problems for the subsequent layers to be bonded on top. These problems would be solved using Fabrisonic's newer automated machines (SonicLayer), but would require further investigation and tuning to use the available equipment.

8.3 Top-Down Approach

The top down approach to package design and fabrication is a standard process for heat exchangers. This involves subtractive machining (*e.g.* milling), casting, or

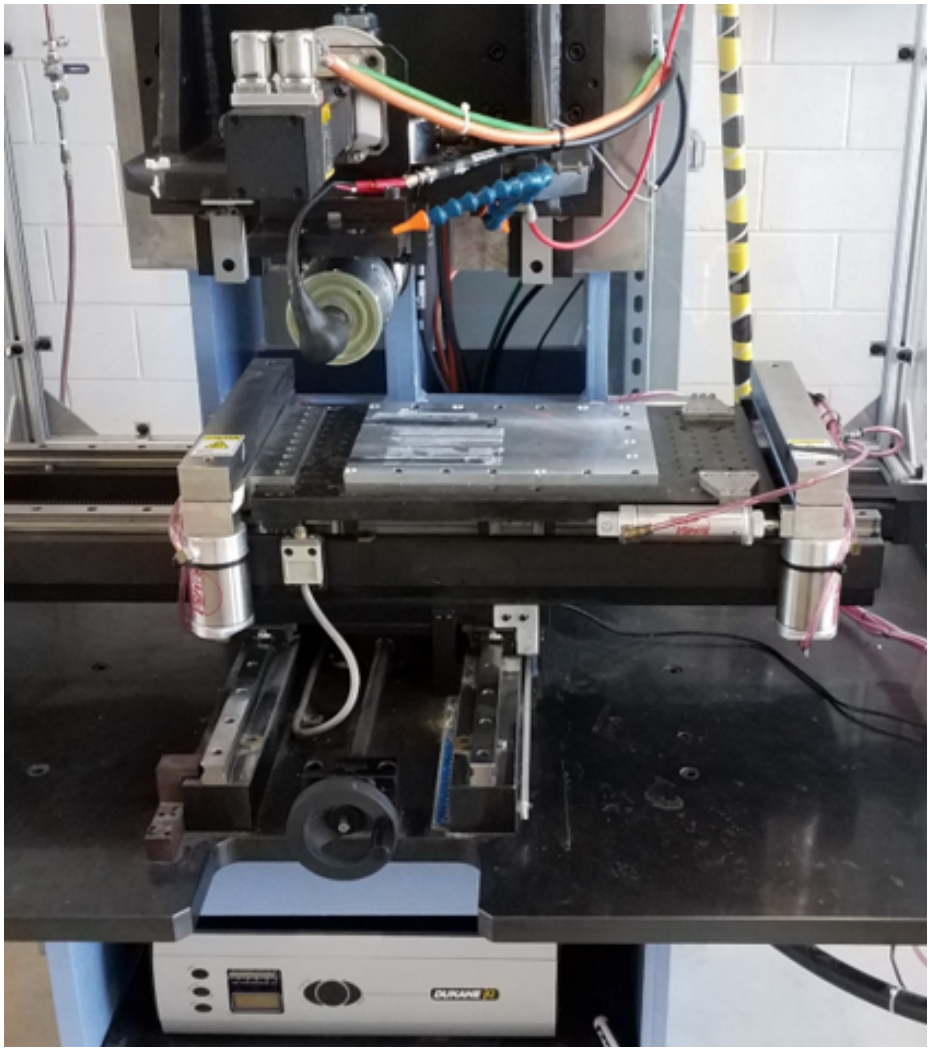

Figure 8.5. Fabrisonic system build platform. Pneumatic pistons clamp the foil to secure it, then stretch it to hold it flat along the build plate.

molding to fabricate the designs. It is typically limited by machinability of the solid portion and/or how the PCMs can be later integrated into the structure after all machining is done. Subtractive manufacturing is the most widely used approach as it permits the solid component of the heat exchangers to be cast or machined, then filled with PCM separately. The benefits of this method come from the established practices, supply chains, and technicians in place already for its implementation; however, PCM volumes must be large enough to permit easy introduction of PCM

throughout all voids from the top or some single fill port. Additionally, feature sizes and wall thicknesses are constrained by the production tolerance limits of CNC machines or the casting feature resolution. This method typically only employs a single material to avoid poor interfacial properties between dissimilar material bonds.

The top-down approach provides a good baseline for evaluation of the new PCM test platform presented in Chapter 9. Our novel feature geometries seek to augment the performance of traditional PCM heat exchanger layouts by reducing the heat transfer resistance from the die to the center of the PCM volumes, thus allowing faster response time to surge power demands. I utilize CNC machining to produce arrays of packages based upon the composite designs detailed above. These features are designed to comply with standard CNC machining rapid prototyping tolerances, $\pm$ 25 μm ($\pm$ 0.01 in), maintaining wall thicknesses of at least 50 μm (0.02 in), and a specified finish cutter diameter of $^1/_{16}$ in to yield inner corner radii of $\sim$80 μm. This is done to help mitigate the cost of machining many packages with contoured, small features. Here, the packages are sealed with a Kapton® film to prevent material degradation during testing and better simulate actual operating conditions. In practice, they can be sealed via ultrasonic welding to permanently attach metal lids without overheating the PCM inside.

8.4 Predicted Package Performance

The package designs are evaluated using a 3D, transient COMSOL multiphysics simulation to predict expected performance. The square geometry is reduced to $^1/_8$ using symmetry as shown in Figure 8.6. The kite deltoids have not been modeled at this time due to the inability to accurately include them within a symmetric $^1/_8$ segment of the package. Inclusion of these will require a $^1/_4$ model. A uniform heat flux of 7 $^W/_{cm^2}$, based upon the average power density of recently released mobile phone processors, is applied through a central square of size 25 $|times$ 25 mm on the back surface of the package. Convective boundary conditions are assumed for the

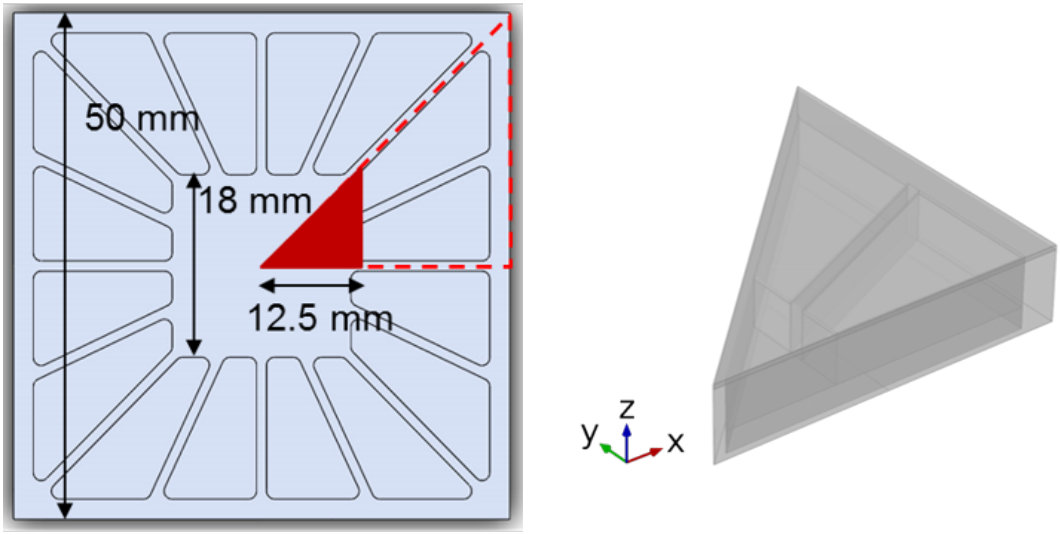

(a) Top view of package geometry

(b) 3d model of the reduced simulated domain

Figure 8.6. Schematic of the COMSOL model showing the simplified package design under review.

top and side surfaces, where a constant convective coefficient of 15 $^{W}/_{m^2 \cdot K}$ is used to represent a general natural convective cooling condition to ambient air at 293 K.

The material of the package is specified as 6063 Aluminum using temperature dependent properties included within the COMSOL material library. The PCM is defined based upon the properties of Climsel C70 defined in Table 8.1. The PCM is filled into the voids in the package to within 0.5 mm of the top surface to be consistent with the clearance needed in a real package for volumetric expansion of the PCM after phase change. The phase change process is modeled using the apparent heat capacity method integrated within the heat transfer module in COMSOL. A 300 μm top sheet of aluminum is added to the package to represent two layer of foil ultrasonically welded to seal the system.

One metric of interest is the time to reach a particular cut off temperature. By monitoring the hottest point in the package over time, we can compare the relative performance of packages with different designs and PCMs. Results of the simulations

Table 8.1. Data used for material properties of Climsel C70 in numerical COMSOL study.

Property	**Value**
Density	1400 $^{kg}/_{m^3}$
Latent Heat	282.9 $^{kJ}/_{kg}$
Specific Heat	3.6 $^{kJ}/_{kg \cdot K}$
Thermal Conductivity	0.6 $^{W}/_{m \cdot K}$

looking at the added effect of the PCM for this geometry, and compared to a full solid volume of aluminum, are included in Table 8.2. Clearly, the PCM (Climsel C70) improves the time to reach 100℃ compared to the empty package and even the solid Aluminum block for the tested heat flux.

Table 8.2. Results of COMSOL study.

Package	**Time to 100℃**
Empty	35 s
Solid	60 s
Climsel C70 (0.93 g)	102 s

The goal of my proposed test packages is to allow direct comparisons to be made between effects of internal design changes upon package performance. Existing performance evaluation platforms of PCM performance in electronics thermal management have not been able to couple realistic operation values, such as heat flux, power profiles, and PCB heat spreading, with a well-controlled scientific experiment. In the next chapter a new testing system is presented aiming specifically to address these long standing problems in PCM experiments.

9. *IN SITU* MEASUREMENT PLATFORM

9.1 Thermal Test Vehicle

To evaluate the PCM heat sink performance, we develop a generalized thermal management evaluation platform (TMEP) based on a thermal test vehicle (TTV), shown in Figure 9.1. This system permits accurate control of not only heater power, but also the spatial and temporal power map across the chip, which allows high power densities to be used. The TTV contains a 5 $\times$ 5 array of heaters within a test die that is approximately 21 $\times$ 21 mm. Additionally, this TTV is integrated with an array of platinum resistance temperature detectors (RTDs) to measure the temperature distribution across the internal surface of the test chip. These RTDs are representative of the integrated temperature sensors in actual processor dies. An inter-integrated circuit (I^2C) addressable pulse width modulation (PWM) control board was fabricated to permit individual control of all the TTV heaters using a single DC power supply (HP 6428B). Such control allows the user to develop and run any power profile or thermal cycling test desired. Interfacial loading between the PCM package and the TTV interface is also controllable for consistency and permits investigation into the effects of contact resistance between the PCM package and chip die. External natural convection effects are minimized by the installation of a thick polyether ether ketone (PEEK) insulating plate above the package, which is used for normal loading of the package to the die. The PEEK plate overhangs the PCM package enough to create a region surrounding the package with a very low Grashof number. This suppresses the convective losses from the package and better matches the conditions of operation in a small enclosure, such as the case in portable electronics.

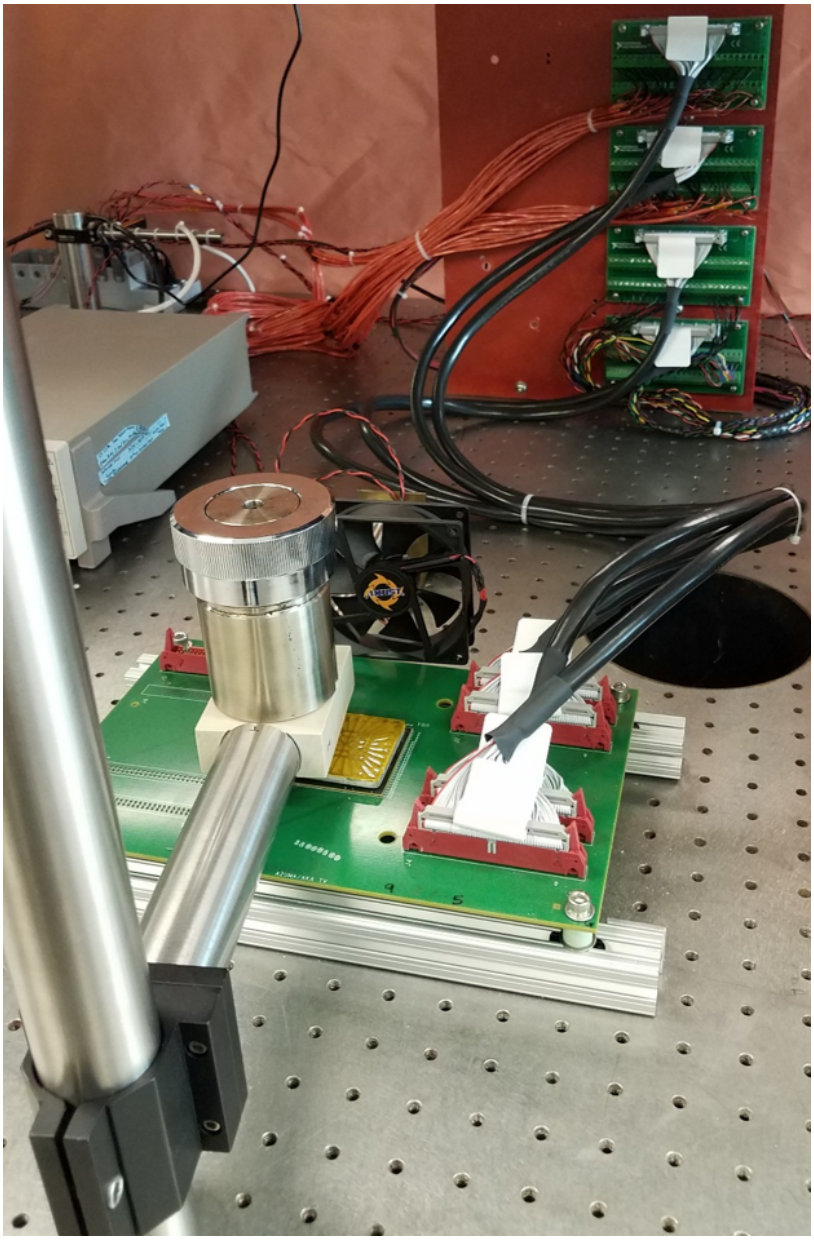

Figure 9.1. Thermal test vehicle (TTV) and experimental peripherals. Note, loading fixture is elevated and rotated out of position slightly to provide a better overall view of the TTV and package mounting. The fan is included to assure that all packages are quickly cooled back to ambient temperature when the temperature falls below 30℃ after all cycles have been completed. The fan is not active during any other portion of the cycle test.

System control and data acquisition are fully automated via LabVIEW with an Arduino-MATLAB interface to address and control the serial commands sent to the PWM matrix array. An intuitive graphical user interface (GUI) was created to give the user full control of the power profiles, both spatial and temporal. This GUI allows the user to select from pre-programmed spatial power maps, based upon common hot-spot configurations, for the test procedure, or the user can input their own custom spatial power map through the custom power map tab of the GUI. In addition to the spatial control of the TTV power map, the user has full control of the heater cycle period and number of cycles applied through the controls of the GUI.

Results for melting and solidification cycles are monitored using an NI cDAQ-9178 chassis with several specialized modules: a voltage module (NI 9205) for monitoring power to the heaters, a universal analog input module (NI 9219) for four-wire monitoring of internal RTDs, and a thermocouple module (NI 9213) for monitoring system and ambient temperatures. Additionally, a Keithley 2701 digital multimeter (DMM) equipped with two 20 channel multiplexer cards (Keithley 7700) provides four-wire monitoring of additional internal RTDs. The experiments provide information about the effectiveness of the PCM packages for extending the operation time before reaching the critical temperature.

A 0.5 mm thick thermal interface material (TIM) pad, Artic Thermal Pad ($\kappa =$ 6 W/cm^2), provides repeatable installation conditions for each package test, with a new pad installed for each package/PCM combination, as shown in Figure 9.3. The pads are cut oversized, 25 $\times$ 25 mm, for the die to avoid any errors associated with pad misalignment during installation.

9.2 Experimental Methodology

Prior to the start of an experiment, the masses of the empty packages, PCM filled packages, and PCM filled and sealed packages are recorded for each individual sample. The interfacial load value for all tests is set to 69 kPa ($\sim$ 10 psi) and

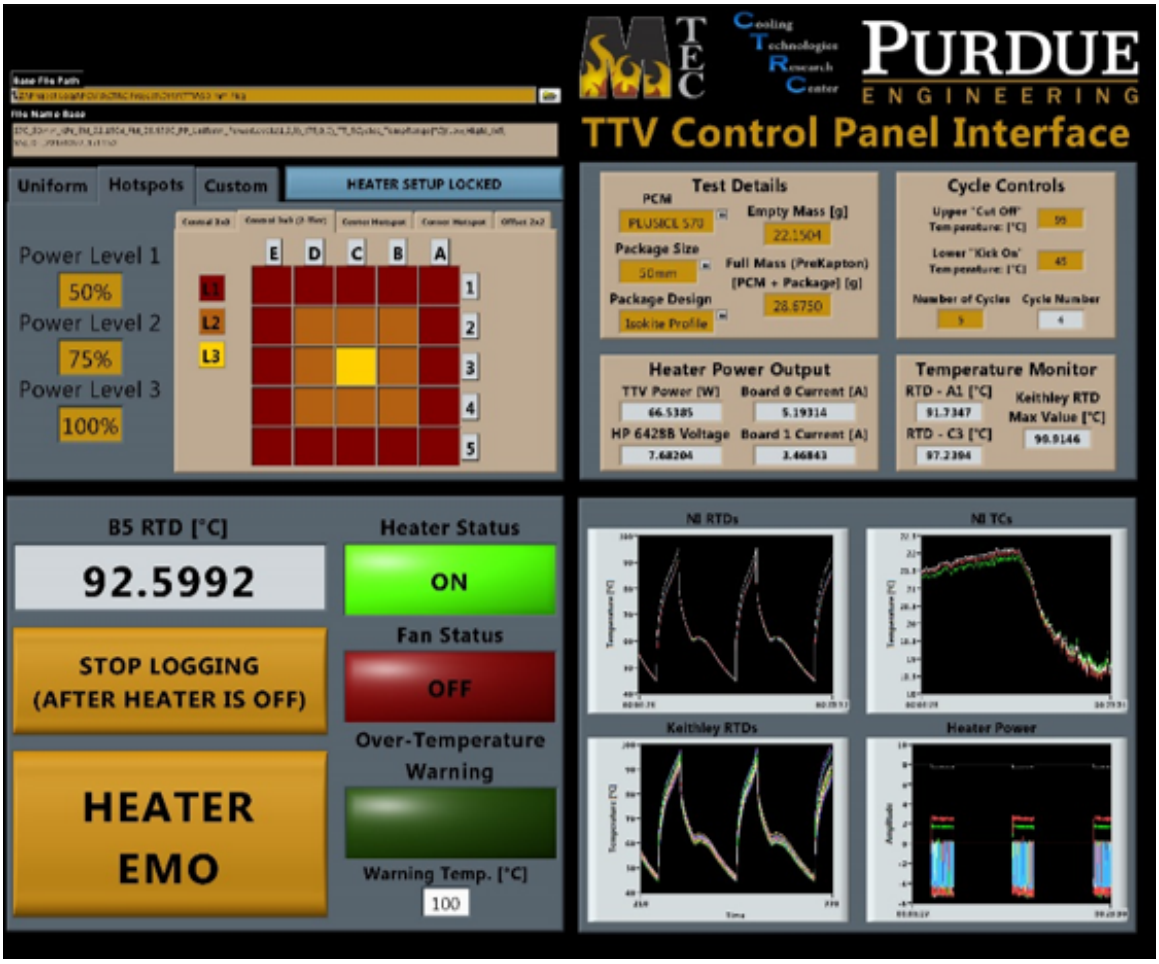

Figure 9.2. A view of the custom graphical user interface (GUI) created to allow users to intuitively interact with the test platform and easily run experiments. It has pre-programmed power profiles with different layouts of common hot-spot configurations, or it permits the user to enter their own custom spatial layout. Additionally, this GUI provides the user full control over the period of the heating cycles and the number of cycles to apply during the test.

remains constant for all tests. During an experiment, many values are monitored and recorded to fully capture the performance of the composite PCM heat sink. First, the die temperature map is logged using the internal RTDs throughout the TTV chip. Additionally, thermocouples monitor system and ambient temperatures to

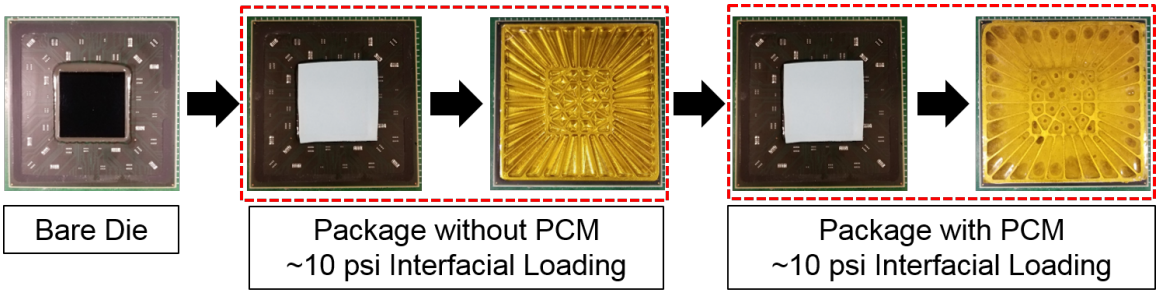

Figure 9.3. Overview of the test progression for each test package. First the response of the bare die is measured, then the control cases without PCM are measured (machined packages without PCM and solid aluminum packages), and then the package with the PCM integrated is tested. A new thermal pad is applied each time a package is changed for consistency.

better account for thermal losses. The power supplied to the heaters is also monitored via current sense resistors and logging of the supply output voltage.

The test parameters for the experiments are chosen to investigate specific operation regions for a target device or chip. In this study, uniform power maps are considered. The uniform test conditions evaluate a range of heat fluxes from 6.8 - 14.5 W/cm^2. The test power cycles are designed to operate like an active thermal throttling scheme, commonly employed in electronics, allowing processors to exceed typical clock speeds for a short period of time (surge processing) until the die temperature rises above a specified limit. When the die surpasses the cut-off temperature, $T_{cut-off}$, the power is reduced to keep the processor at a safe operating temperature. Once the temperature drops beneath a lower temperature set point, the processor is allowed to go back to high-power operation again. In this study, $T_{cut-off}$ is set at 95°C to avoid damage to the TTV, and the temperature to allow the high-power cycle to restart is 30°C. This lower temperature choice is somewhat arbitrary for the purposes of these tests, but is chosen to show the performance of the composite PCM heat sink across a broad range of potential operating temperature conditions. The number of cycles to complete is another user defined parameter. Five cycles are chosen for this

study as this captures the full behavior of a design-material combination, which shows the nature of the melt and regeneration behavior during operation.

The sequence of events during a test is as follows. The test starts with a 30 second period to confirm equilibrium conditions in the die and package. This ensures that each test starts from a steady state ambient condition. After initial equilibrium is confirmed, power is supplied to all the heaters at the specified levels for each location. Heating continues until the maximum die temperature increases above 95℃. At that point, the power to the heaters is shut off allowing the die and package cool naturally via heat spreading and dissipation through the TTV. It is important to note that temperatures are monitored continuously throughout all phases of the test to capture both melting and regeneration behavior. When all die temperatures decrease below 30℃, one of two things happens: (1) if the current cycle number is less than the set number of test cycles, then the heaters turn back on and the heating/cooling period repeats, (2) if the current cycle number is equal to the total number of test cycles set by the user, then the package continues to cool naturally back to the ambient starting temperature and the test is complete.

The testing procedure for each design and material combination consists of several stages. First, baseline tests (without PCM) are carried out to provide a comparison point for the composite PCM heat sinks. These baseline tests, carried out for all power levels, consist of the following cases: bare die (no added thermal management), solid aluminum packages (both 25 and 50 mm square by 5 mm thick), and each package design sealed without the PCM fill. Regular tests consider all package designs with each of the PCMs added to compare performance between sizes, designs, and PCMs. Multiple tests are run for all baseline and PCM filled cases, with the results averaged for each case.

10. EVALUATION OF PCM PACKAGES

Figure 10.1 shows the evolution of the die temperature with respect to time during the test of the 50 mm isokite package design containing PlusICE S70 PCM at a heat flux of 7.5 W/cm^2. The red region highlights melting during the heating phase, and the blue area denotes regeneration during cooling. Heating ceases once the max die temperature reaches 95℃. Due to the thermal resistance between the TTV die and the temperature of the PCM, melting appears to occur at a higher temperature than 70℃. This same phenomena is also observed during regeneration, with the apparent regeneration temperature depressed below the melting point during cooling; however, there is minor sub-cooling observed as shown by the small peak in Figure 10.1 during solidification. This peak occurs because sub-cooling allows the PCM temperature to reach a temperature below the phase change temperature of the PCM. Then upon the initiation of regeneration, the PCM releases the latent energy stored during melting to undergo a liquid-to-solid change of phase. This release of energy means that the increase in heat flow from the package, through the die, causes the internal chip temperature to rise again resulting in a small temperature peak associated with sub-cooling during regeneration.

Figure 10.2 shows the time to 95℃ for different packages and power levels. As a guide to interpreting the results, first consider a single package size, PCM type, and power level (for instance, the 50 mm package with PureTemp 68, at ~ 7.3 $^{W}/_{cm^2}$ shown in the top right corner of the image). As predicted, the addition of fins (*e.g.*, isogrid and isokite package designs) significantly enhances conduction pathways through the PCM and improves the performance (*i.e.*, the time to 95℃) of the composite PCM package. Additionally, the packages with higher surface area to volume ratios (*e.g.*, isokite) generally performed better than the finless or isogrid packages in all test cases except for the PureTemp 42 at the lowest heat flux level. The PureTemp 42 with

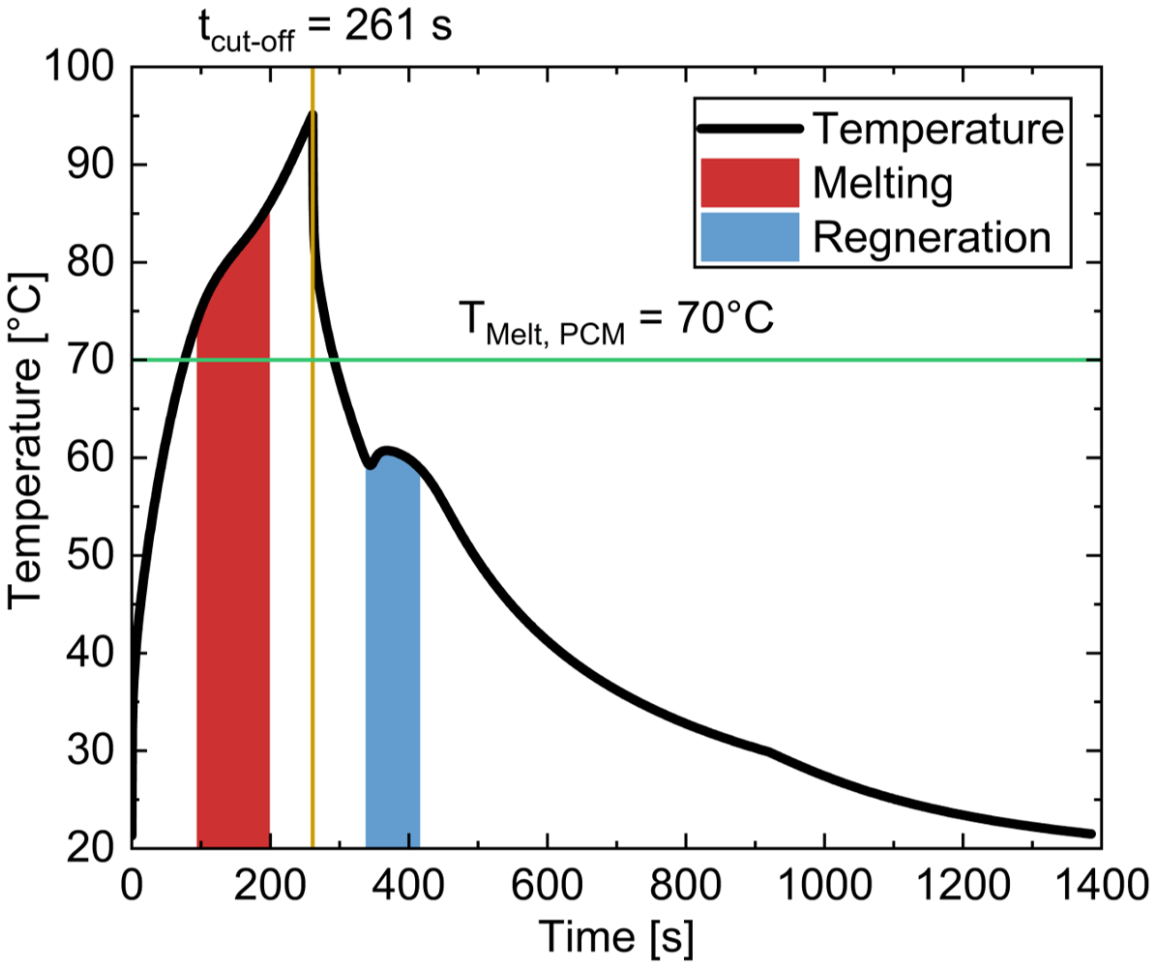

Figure 10.1. Temperature evolution for the 50 mm isokite package design filled with PlusICE S70 PCM at a heat flux of 7.5 W/cm^2. Temporal regions during melting and regeneration are highlighted in red and blue, respectively, and and the time to reach the cut-off temperature of 70℃ is indicated.

the isogrid design has better performance than the PureTemp 42 isokite design for the lowest heat flux level, but this result does not hold at higher heat fluxes due to the interplay between melting timescale and heating rate. At the lower heat flux, the PureTemp 42 can accommodate the heating load of $\sim 7.3\ W/cm^2$ and has a longer period over which to absorb the thermal energy. In the case of the PureTemp 42 in the isokite design at the $7.3 \pm 0.5\ W/cm^2$ heat flux, the PCM is fully exhausted long

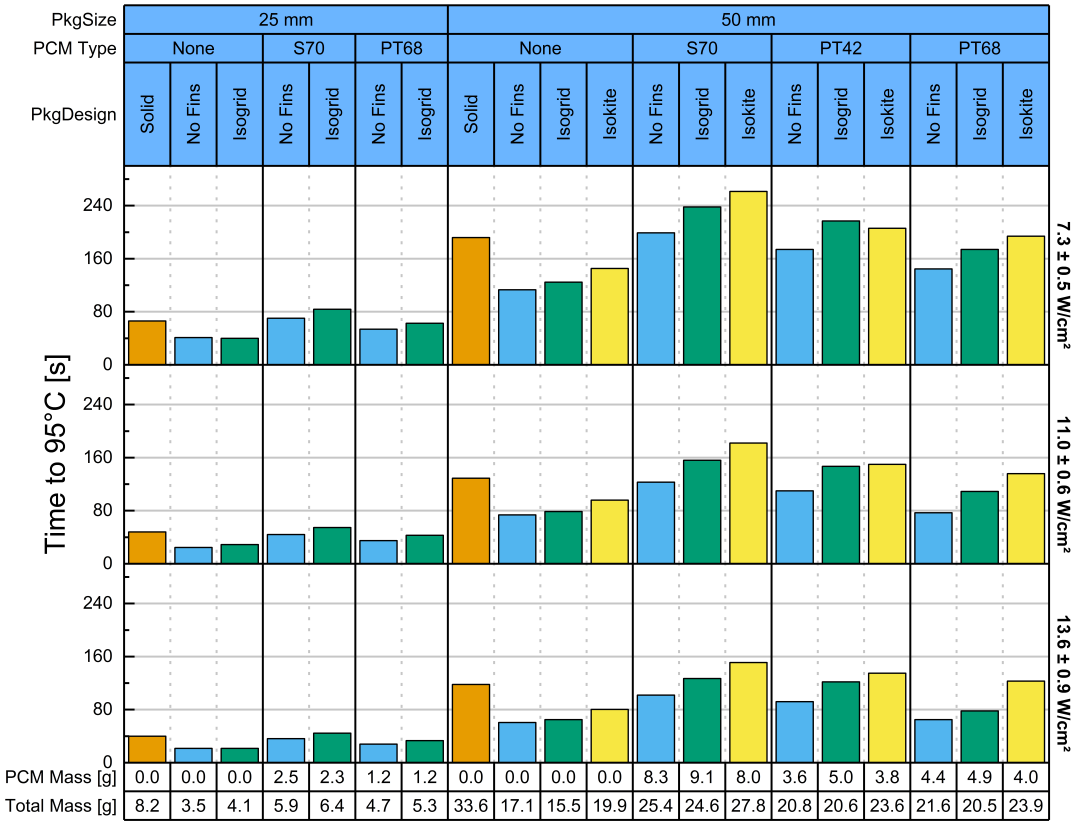

Figure 10.2. Time for each heat sink to reach the cut-off temperature of 95°C. The results are split and grouped first by package size (25 and 50 mm); then clustered by the type of PCM in the package during the test. A PCM type of "None" indicates a package is tested without PCM, while "S70", "PT42" and "PT68" signify the use of PlusICE S70, PureTemp 42 and PureTemp 68, respectively. The different color bars represent the individual package designs. "Solid" packages (orange) are a solid mass of aluminum with the same overall dimensions as the PCM heat sink packages, whereas "No Fins" packages (blue), "Isogrid" packages (green) and "Isokite" packages (yellow) have the indicated fin structures. Each row of bar charts represents a different power level as indicated by the labels on the right hand side. The mass of PCM and the total mass of each package is listed below the bar charts.

before the cut-off temperature is reached; therefore, it is beneficial for the package to have the extra volume of PCM allowed by the isogrid design. At higher heat fluxes, the energy absorption of PureTemp 42 cannot keep pace with the heating rate, thus the latent heat of the PCM is not exhausted prior to the chip reaching the $T_{cut-off}$, which renders the surplus PCM volume in the isogrid case useless. The trade-off between the enhanced response of the isokite design and the added PCM capacity of the isogrid design is a clear point to consider during package design for a specific operating load and material combination.

Now, consider one package size and type while increasing the heat flux (*i.e.*, look down across a column). As expected, the time to 95°C decreases with increasing heating rate. While Figure 10.2 provides detailed information about the performance of all the different package designs and material combinations at each heat flux level, quantitative trends are not immediately clear. Figure 10.3 provides an overview of the performance trends for each package design and material combination as the heat flux is increased. An important feature to note is the convergence of the individual design performances as the heat flux increases. This is expected due to the rate at which the PCM can accept heating from the die. It is clear from Figures 10.2 and 10.3 that increasing surface area and decreasing each PCM volume thickness results in a faster and more effective response for the PCM composite heat exchanger. Additionally, the convergence of designs with increasing heat flux highlights the impact that increased power loads have on enhancement features and PCM selection. This further emphasizes the importance of a tunable package to permit easy design modifications for high power systems.

Another major design consideration is the melting temperature itself, as observed by comparing the response of PureTemp 42 to that of PureTemp 68. The thermophysical properties, except melting temperature, are very similar for these two materials, but PureTemp 42 provides a longer operating time before reaching 95°C than PureTemp 68 due to the lower melting point. While this looks to be advantageous during the heating cycles, the impact on the regeneration phase must be

considered. A lower melting point requires a longer cooling time before full regeneration occurs thus requiring a longer regeneration period than PureTemp 68 with its higher melting temperature. Therefore, if the operating conditions require infrequent surges of thermal energy to be buffered, a PCM with a lower melting temperature can provide a longer time to reach $T_{cut-off}$ than a material with a higher melting temperature, provided all other thermophysical properties are comparable. However, as the cycling tests show in Figure 10.4, cases requiring regular thermal cycles would benefit more from the higher melting temperature which decreases the regeneration time and results in a shorter total cycle period (melting and regeneration), than from a slightly longer time to $T_{cut-off}$.

In all cases, the salt hydrate PCM, PlusICE S70, performed better than the organic PCMs. This result is expected due to the higher cooling figure of merit for PlusICE S70 compared to the PureTemp materials; however, a common barrier to implementation of salt hydrate materials in practical applications is a propensity for sub-cooling during regeneration. Sub-cooling, or the delay of the phase transition from liquid to solid beneath the melting temperature, is often a major issue for cycling of salt hydrate PCMs and must be investigated to determine if the augmented performance of the PlusICE S70 comes at a high price during regeneration.

The regeneration portion of the thermal cycle is critical for operation in devices. The desired behavior of a PCM during cycling allows the heat to be absorbed quickly and effectively into the available PCM volume, which allows complete melting to take place and provides maximum energy storage during a dynamic heating event; however, this is only half of the picture. It is also essential for the PCM to effectively reject the stored thermal energy after heating to allow quick cooling beneath the melting temperature which permits the liquid to solidify and be ready to absorb more thermal energy during the next heating cycle. If a PCM experiences sub-cooling, the regeneration process is delayed and the cycle period is extended. PlusICE S70 is specifically formulated to include nucleation-promoting components which minimize the degree of sub-cooling. During cycle tests for PlusICE S70, a sub-cooling of less

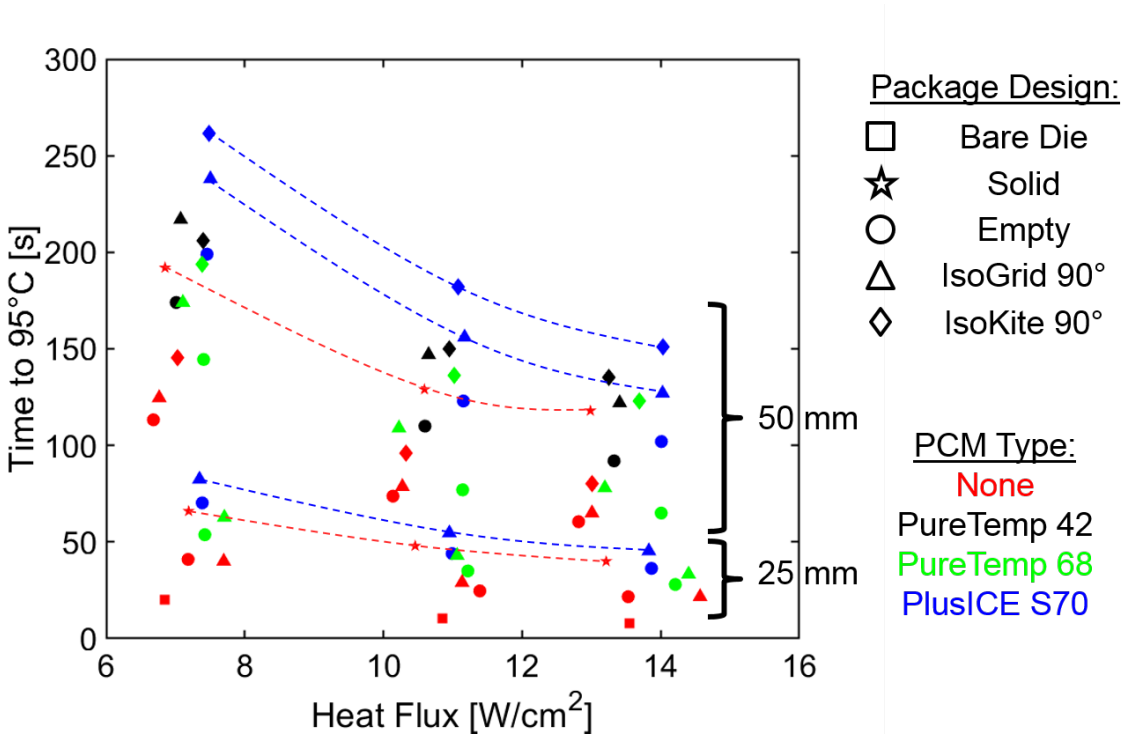

Figure 10.3. Time to 95℃ as a function of heat flux. As the heat flux is increased, the difference in performance between the package designs decreases. At a sufficiently high heat flux, the solid package would provide approximately the same performance as the composite PCM heat sink. The included lines are only meant to guide the eye, and are not representative of mathematical fitting of the data.

than 5℃ is observed in all cases, as is highlighted by the small dip and peak during its regeneration stage shown in Figure 10.4. No degradation in the behavior of the material was observed during the course of the experiments.

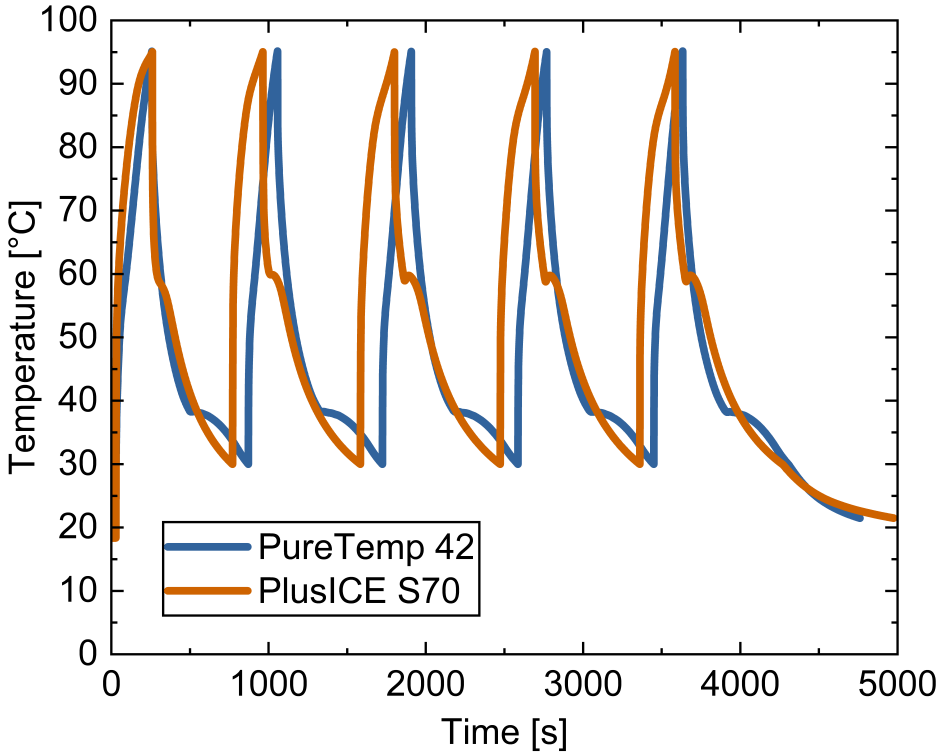

Figure 10.4. Temperature evolution during several cycles of heating for two commercial materials in the isokite packages. Repeated cycling of the PCM filled package during testing reveals that while short-term gains can be achieved with the lower melting temperature PCM, it is difficult to fully regenerate in subsequent cycles due to the elevated operating temperatures.

11. SUMMARY OF CONTRIBUTIONS ON METROLOGY FOR PCM-BASED HEAT SINKS

The thermal management evaluation platform (TMEP) is a highly capable user system providing precise control over the thermal test vehicle (TTV) and *in situ* temperature monitoring for investigating the performance of thermal management solutions. In this work I detailed the development of the TMEP and a novel composite PCM heat sink I designed to test the system. After calibration of the system sensors and characterization of the system controls, I conduct a validation study investigating the performance of enhanced composite PCM heat sinks using my own novel package design. Through this study, I show that even using off-the-shelf PCMs a marked improvement in performance and weight savings is achievable through the use of my design. This has resulted in a better understanding of effective heat sink designs for portable electronics.

11.1 Recommendations for Future Development of the PCM Packages and TTV

Through this work on phase change thermal management, I have identified several areas in which the research could be continued and improved including the following.

11.1.1 Improving the Passive Thermal Management Solution:

1. Perform studies investigating the impact of using two or more PCMs in the same package (my segmented design). Can modifying the material type or melting temperature in the hot spot areas have a significant impact on performance?

2. Perform further studies to see if there actually is an impact from the parabolic fins that are theorized to boost composite PCM performance.

3. Fabrisonic Ultrasonic Welding System

   (a) Start sealing packages with ultrasonic welder instead of Kapton tape. The welded aluminum top will help improve performance by allowing heat to spread at the top as well as the bottom.

   (b) Develop new designs and work with Professor Gilbert's group to dial in the fabrication process to successfully make these packages using ultra-sonic additive manufacturing.

4. Run longer thermal cycling tests to investigate long-term design performance and look at the stability of the off-the-shelf materials after 500 - 1000 cycles.

5. Look at incorporating PCMs into existing low power active cooling thermal management technologies. Determine to what degree these low power system could be augmented by the introduction of PCM.

6. Perform an in-depth study (closer to fundamental research) on the regeneration part of the PCM cycle. Develop models to help designers improve their understanding to of the regeneration process and better predict behavior. Is there any way to work the problem from both sides and find an optimum design for total cycle time, not just melting or regeneration.

7. Look into a PCM package design that leverages the pressure created from the void volume restriction when the PCM expands at and after melting. Could this increased pressure force PCM into something like capillary tubes to have very small volumes which would respond very quickly at the next onset of heating

11.1.2 Improving the Thermal Management Evaluation Platform:

1. Target high power density hot spot testing. Target a range of power maps and optimize the new designs for the composite PCM heat sinks to these. Run tests to investigate the effectiveness of optimal configurations over just using the standard spacing.

2. Study short time scale surges/transients as sharp power spikes with the TTV. Goal is to use data from experiments and modeling to come up with a tool to help designers address these steep transient events. After tool is complete, use it to design an optimized composite PCM package for the transient and see how much improvement is gained.

3. Small Improvements to the TMEP:

   (a) Improve individual cell power monitoring scheme instead of using averaged and scaled power right now. While not critical for the uniform power maps presented here. This will be a key piece of functionality for the system when investigating hot spots.

   (b) Speed up the data acquisition from the Keithley 2701 to better monitor transient heating on the full TTV.

   (c) Develop an improved loading fixture

      i. Needs more thermal isolation than just the PEEK block.

      ii. Needs some form of guide to keep loading direction confined to normal loading only.

      iii. Add a view area to permit infrared (IR) imaging of *in situ* melting

REFERENCES

REFERENCES

[1] LLNL. Energy Flow Chart: Estimated U.S. Energy Use in 2016, 2017.

[2] U.S. Energy Information Administration. Annual Energy Outlook 2018 with projections to 2050. Technical report, EIA, 2018.

[3] Saniya LeBlanc. Thermoelectric generators: Linking material properties and systems engineering for waste heat recovery applications. *Sustainable Materials and Technologies*, 1:26–35, 2014.

[4] A F Ioffe. Semiconductor Thermoelements and Thermoelectric Cooling. *Zeitschrift Naturforschung Teil A*, 13:703, aug 1958.

[5] Gordon E. Moore. Cramming more components onto integrated circuits. *Electronics*, 38(8):114, apr 1965.

[6] Shankar Krishnan and Suresh V. Garimella. Thermal Management of Transient Power Spikes in ElectronicsPhase Change Energy Storage or Copper Heat Sinks? *Journal of Electronic Packaging*, 126(3):308, jan 2004.

[7] Shankar Krishnan. *Transport phenomena associated with phase change in homogeneous and inhomogeneous systems*. PhD thesis, Purdue University, 2006.

[8] Unnikrishnan Vadakkan, Suresh V. Garimella, and Jayathi Y. Murthy. Transport in Flat Heat Pipes at High Heat Fluxes From Multiple Discrete Sources. *Journal of Heat Transfer*, 126(3):347, jun 2004.

[9] Shankar Krishnan, Jayathi Y. Murthy, and Suresh V. Garimella. A Two-Temperature Model for the Analysis of Passive Thermal Control Systems. *Journal of Heat Transfer*, 126(4):628, jan 2004.

[10] Ziye Ling, Zhengguo Zhang, Guoquan Shi, Xiaoming Fang, Lei Wang, Xuenong Gao, Yutang Fang, Tao Xu, Shuangfeng Wang, and Xiaohong Liu. Review on thermal management systems using phase change materials for electronic components, Li-ion batteries and photovoltaic modules. *Renewable and Sustainable Energy Reviews*, 31:427–438, mar 2014.

[11] A. T. Burkov. Measurements of Resistivity and Thermopower: Principles and Practical Realization. In David Michael Rowe, editor, *Thermoelectrics Handbook: Macro to Nano*, chapter 22, page 12. CRC Taylor and Francis, New York, 2006.

[12] Terry M. Tritt. Electrical and Thermal Transport Measurement Techniques for Evaluation of the Figure-of-Merit of Bulk Thermoelectric Materials. In David Michael Rowe, editor, *Handbook of Thermoelectrics: Macro to Nano*, chapter 23, page 30. CRC Taylor and Francis, New York, 2006.

[13] J. Martin, T. Tritt, and C. Uher. High temperature Seebeck coefficient metrology. *Journal of Applied Physics*, 108(12):121101, dec 2010.

[14] Charles C. Bidwell. Thermal Electromotive Forces in Oxides. *Physical Review*, 3(3):204–216, mar 1914.

[15] Collier S. Miers. *Towards High-Throughput, Simultaneous Characterization of Thermal and Thermoelectric Properties*. M.s.m.e., Purdue University, 2015.

[16] David G. Cahill and Ro Pohl. Thermal conductivity of amorphous solids above the plateau., mar 1987.

[17] David G. Cahill. Thermal conductivity of thin films: Measurements and understanding. *Journal of Vacuum Science & Technology A: Vacuum, Surfaces, and Films*, 7(3):1259, may 1989.

[18] David G. Cahill. Thermal conductivity measurement from 30 to 750 K: the 3ω method. *Review of Scientific Instruments*, 61(2):802–808, 1990.

[19] David G. Cahill. Erratum: Thermal conductivity measurement from 30 to 750 K: The 3ω method [Rev. Sci. Instrum. 61 , 802 (1990)]. *Review of Scientific Instruments*, 73(10):3701–3701, oct 2002.

[20] Albert Feldman. Algorithm for solutions of the thermal diffusion equation in a stratified medium with a modulated heating source. *High Temperatures - High Pressures*, 31:293–298, 1999.

[21] David G. Cahill, Kenneth Goodson, and Arunava Majumdar. Thermometry and Thermal Transport in Micro/Nanoscale Solid-State Devices and Structures. *Journal of Heat Transfer*, 124(2):223, 2002.

[22] T. Borca-Tasciuc, a. R. Kumar, and G. Chen. Data reduction in 3ω method for thin-film thermal conductivity determination. *Review of Scientific Instruments*, 72(4):2139, 2001.

[23] Chris Dames and Gang Chen. 1Ω, 2Ω, and 3Ω Methods for Measurements of Thermal Properties. *Review of Scientific Instruments*, 76(12):124902, 2005.

[24] Chris Dames. Measuring the Thermal Conductivity of Thin Films: 3 Omega and Related Electrothermal Methods. *Annual Review of Heat Transfer*, 16(1):7–49, 2013.

[25] W. J. Parker, R. J. Jenkins, C. P. Butler, and G. L. Abbott. Flash Method of Determining Thermal Diffusivity, Heat Capacity, and Thermal Conductivity. *Journal of Applied Physics*, 32(9):1679–1684, sep 1961.

[26] ASTM. ASTM D5470-12 Standard Test Method for Thermal Transmission Properties of Thermally Conductive Electrical Insulation Materials. Technical report, ASTM International, 2012.

[27] Jue Wang. System Design, Fabrication, and Characterization of Thermoelectric and Thermal Interface Materials for Thermoelectric Devices. jun 2018.

[28] Hsin Wang, Wallace D Porter, Harald Bottner, Jan Konig, Lidong Chen, Shengqiang Bai, Terry M Tritt, Alex Mayolet, Jayantha Senawiratne, Charlene Smith, Fred Harris, Patricia Gilbert, Jeff W Sharp, Jason Lo, Holger Kleinke, and Laszlo Kiss. Transport Properties of Bulk Thermoelectrics - An International Round-Robin Study, Part I: Seebeck Coefficient and Electrical Resistivity. 42(4), 2013.

[29] Hsin Wang, Wallace D Porter, Harald Bottner, Jan Konig, Lidong Chen, Shengqiang Bai, Terry M Tritt, Alex Mayolet, Jayantha Senawiratne, Charlene Smith, Fred Harris, Patricia Gilbert, Jeff W Sharp, Jason Lo, Holger Kleinke, and Laszlo Kiss. Transport Properties of Bulk Thermoelectrics - An International Round-Robin Study, Part II: Thermal Diffusivity, Specific Heat, and Thermal Conductivity. 42(4), 2013.

[30] Hugh H Woodbury, Lionel M Levinson, and Robert S Lewandowski. *Z-Meters*. 1995.

[31] H Julian Goldsmid. *Electronic refrigeration*. Pion, 1986.

[32] D M Rowe. CRC Handbook of Thermoelectrics. *New York*, 16:1251–1256, 1995.

[33] R. Amatya, P. M. Mayer, and R. J. Ram. High temperature Z-meter setup for characterizing thermoelectric material under large temperature gradient. *Review of Scientific Instruments*, 83(7):075117, jul 2012.

[34] E H Putley. Thermoelectric and Galvanomagnetic effects in Lead Selenide and Telluride. *Proceedings of the Physical Society. Section B*, 68(1):35–42, jan 1955.

[35] E H Putley. The Hall Coefficient, Electrical Conductivity and Magneto-Resistance Effect of Lead Sulphide, Selenide and Telluride. In *Proceedings of Physical Society - Section B*, volume 68, page 22, 1955.

[36] Theodore C. Harman. Special Techniques for Measurement of Thermoelectric Properties. *Journal of Applied Physics*, 29(9):1373, sep 1958.

[37] Theodore C. Harman, J. H. Cahn, and M. J. Logan. Measurement of Thermal Conductivity by Utilization of the Peltier Effect. *Journal of Applied Physics*, 30(9):1351, sep 1959.

[38] A E Bowley, L E J Cowles, G J Williams, and H Julian Goldsmid. Measurement of the Figure of Merit of a Thermoelectric Material. *Journal of Scientific Instruments*, 38(11):433, nov 1961.

[39] Zhixi Bian, Y Zhang, H Schmidt, and A Shakouri. Thin film ZT characterization using transient Harman technique. In *24th International Conference on Thermoelectrics*, pages 76–78. IEEE, 2005.

[40] Rajeev Singh, Zhixi Bian, Ali Shakouri, Gehong Zeng, Je-Hyeong Bahk, John E. Bowers, Joshua M. O. Zide, and Arthur C. Gossard. Direct measurement of thin-film thermoelectric figure of merit. *Applied Physics Letters*, 94(21):212508, 2009.

[41] L S Phillips. The Measurement of Thermoelectric Properties at High Temperatures. *Journal of Scientific Instruments*, 42(4):209, apr 1965.

[42] Eckhard Müller, J.U. Bruch, and J. Schilz. Real Condition Test of Graded Thermoelectric Elements. *Materials Science Forum*, 308-311:754–759, 1999.

[43] P. M. Mayer and R.J. Ram. Thin-film thermoelectric generator element characterization. In *ICT 2005. 24th International Conference on Thermoelectrics, 2005.*, pages 280–283. IEEE, 2005.

[44] Peter M. Mayer. *High-density thermoelectric power generation and nanoscale thermal metrology*. Phd, Massachusetts Institute of Technology, 2007.

[45] A. Muto, D. Kraemer, Q. Hao, Z. F. Ren, and G. Chen. Thermoelectric properties and efficiency measurements under large temperature differences. *Review of Scientific Instruments*, 80(9):093901, sep 2009.

[46] B. Singh, D. Shukla, P. Srivastava, and S. Patnaik. Design and calibration of Z-meter for simultaneous thermal transport measurements at high temperature. In *AIP Conference Proceedings*, volume 1591, pages 690–692. American Institute of Physics, feb 2014.

[47] Collier S. Miers and Amy M. Marconnet. Uncertainty Quantification for a High Temperature Z-Meter Characterization System. In *2018 Intersociety Conference on Thermal and Thermomechanical Phenomena in Electronic Systems (ITHERM)*, page 10, San Diego, 2018.

[48] Y S Touloukian, R W Powell, C Y Ho, and P G Klemens. *Thermophysical Properties of Matter - The TPRC Data Series. Volume 1. Thermal Conductivity - Metallic Elements and Alloys*. TPRL, 1970.

[49] Karl Jousten. *Handbook of vacuum technology*. Wiley, 1 edition, 2008.

[50] C T Murray, P Kendall, A Larson, C Harvey, and G Staus. Rumination on Design and Build of an ASTM D-5470 Thermal Interface Test Instrument. *Thermal Conductivity*, 28:309, 2006.

[51] R. Kempers, P. Kolodner, A. Lyons, and A. J. Robinson. A high-precision apparatus for the characterization of thermal interface materials. *Review of Scientific Instruments*, 80(9):095111, sep 2009.

[52] Dakotah R Thompson, Sameer R Rao, and Baratunde A Cola. A stepped-bar apparatus for thermal resistance measurements. *Journal of Electronic Packaging*, 135(4):41002, 2013.

[53] J. R. (Joseph R.) Davis and ASM International. Handbook Committee. *Metals handbook*. ASM International, 1998.

[54] Plansee. Molybdenum, 2018.

[55] Plansee. Tungsten, 2018.

[56] Juan J Valencia. Thermophysical Properties Sources and Availability of Reliable Data. In *ASM Handbook, Volume 15: Casting*, pages 468–481. ASM International, 2008.

[57] Y S Touloukian, R K Kirby, R E Taylor, and P D Desai. *Thermophysical Properties of Matter - the TPRC Data Series. Volume 12. Thermal Expansion Metallic Elements and Alloys*. 1975.

[58] B Mayr-Schmölzer, I Wesemann, R Tröber, M O 'sullivan, H Kestler, and L S Sigl. A method for measuring the high temperature emissivity of refractory metal surfaces. Technical report, 2017.

[59] Robin E. Bentley. The use of elemental thermocouples in high-temperature precision thermometry. *Measurement*, 23(1):35 – 46, jan 1998.

[60] J. V. Nicholas and D. R. White. *Traceable Temperatures*. John Wiley & Sons, Ltd, Chichester, UK, oct 2001.

[61] Thomas McGee. *Principles and Methods of Temperature Measurement*. Wiley, 1988.

[62] P H Dike. *Thermoelectric Thermometry*. Leeds & Northrup, 1954.

[63] J. A. Becker, C. B. Green, and G. L. Pearson. Properties and Uses of Thermistors-Thermally Sensitive Resistors. *Bell System Technical Journal*, 26(1):170–212, jan 1947.

[64] Ernst R.G. Eckert and Richard J. Goldstein. *Measurements in Heat Transfer*. Hemisphere Publishing Corporation, Washington, 2 edition, 1976.

[65] S. Nicoletti, S. Zampolli, I. Elmi, L. Dori, and M. Severi. Use of different sensing materials and deposition techniques for thin-film sensors to increase sensitivity and selectivity. *IEEE Sensors Journal*, 3(4):454–459, aug 2003.

[66] Charles Kittel. *Introduction to Solid State Physics*. Wiley, 8 edition, 2005.

[67] J. M. Ziman. *Electrons and Phonons: The Theory of Transport Phenomena in Solids*. Oxford University Press, London, 2 edition, 1963.

[68] J. R. Hook and H. E. Hall. *Solid State Physics*. John Wiley & Sons, New York, 2 edition, 1991.

[69] Jacob Fraden. *Handbook of modern sensors : physics, designs, and applications*. Springer-Verlag, New York, 2010.

[70] Kenneth G. Kreider, Dean C. Ripple, and William A. Kimes. Thin-film resistance thermometers on silicon wafers. *Measurement Science and Technology*, 20(045206):6, 2009.

[71] Pauline Renoux, Sigurdur Ægir Jónsson, Levente J. Klein, Hendrik F. Hamann, and Snorri Ingvarsson. Sub-wavelength bolometers: Uncooled platinum wires as infrared sensors. *Optics Express*, 19(9):8721, apr 2011.

[72] Richard M. Park and Helen M. Hoersch. ASTM-MANL-12 — Manual on the Use of Thermocouples in Temperature Measurement: 4th Edition. Technical report, ASTM, 1993.

[73] P. A. Kinzie. *Thermocouple Temperature Measurement*. John Wiley & Sons, New York, 1973.

[74] Comite Consultatif de Thermometrie. The International Temperature Scale of 1990 (ITS-90). Technical report, Comite International des Poids et Mesures, 1989.

[75] H E Bennett. *Noble Metal Thermocouples*. Johnson, Matthey & Co., 2 edition, 1958.

[76] A. S. Darling and G. L. Selman. Some Effects of Environment on the Performance of Noble Metal Thermocouples. In Harmon H. Plumb, D. I. Finch, G. W. Burns, R. L. Berger, and T. E. Van Zandt, editors, *5th Symposium on Temperature*, pages 1633–1644, Washington DC, 1972. Instrument Society of America.

[77] G. E. Glawe and A. J. Szaniszlo. Long-term drift of some noble-and refractory-metal thermocouples at 1600 K in air, argon, and vacuum. In Harmon H. Plumb, D. I. Finch, G. W. Burns, R. L. Berger, and T. E. Van Zandt, editors, *5th Symposium on Temperature*, pages 1645–1662, Washington DC, 1971. Instrument Society of America.

[78] ASTM International. *Manual on the Use of Thermocouples in Temperature Measurement*, 1970.

[79] Aleksander Sala. *Radiant Properties of Materials*. ELSEVIER/PWN, Warsaw, 1986.

[80] Y S Touloukian, R W Powell, C Y Ho, and P G Klemens. Thermophysical Properties of Matter - The TPRC Data Series. Volume 2. Thermal Conductivity - Nonmetallic Solids, 1971.

[81] OSHA. Beryllium, 2018.

[82] Ankit Rohatgi. Web Plot Digitizer, 2018.

[83] Robert C. Juvinall and Kurt M. Marshek. *Fundamentals of machine component design.* Wiley, Hoboken, NJ, USA, 4 edition, 2006.

[84] ASTM. ASTM B258-14 Standard specification for Standard Nominal Diameters and Cross-Sectional Areas of AWG Sizes of Solid Round Wires Used as Electrical Conductors. Technical report, ASTM, 2014.

[85] ASTM. ASTM C1055-03(2014) Standard Guide for Heated System Surface Conditions that Produce Contact Burn Injuries. Technical report, ASTM International, 2014.

[86] maxQ Technologies. Liquid Cooled Coldplate (001-MXQ-01). Technical report, maxQ Technologies, Tempe, AZ, 2019.

[87] Osaka Vacuum. Operation Manual: Compound Molecular Pump (TG450F). Technical report, H07737-R05, Fremont, 2012.

[88] Kurt J. Lesker. User Manual: Ionization Gauge / Dual Convection with Integrated Controller & Display - 392 Series Ionization Vacuum Gauge. Technical report, 001229-115, Jefferson Hills, 2016.

[89] David A. Bell. *Electronic Instrumentation and Measurements*. Prentice-Hall, Englewood Cliffs, NJ, 2 edition, 1994.

[90] Patrick F. Dunn. *Measurement and Data Analysis for Engineering and Science*. CRC Taylor and Francis, Boca Raton, FL, 2 edition, 2010.

[91] Keithley. *Model 2700 Multimeter/Switch System: User's Manual*, 2016.

[92] Keysight Technologies. Keysight 3458A Multimeter User's Guide. Technical report, 2017.

[93] ASTM. Standard Test Method for Thermal Transmission Properties of Thermally Conductive Electrical Insulation Materials. Technical report, ASTM, West Conshohocken, PA, 2017.

[94] M B H Mantelli and M M Yovanovich. *Thermal Contact Resistance*, volume 1, chapter 16, pages 599–638. 2002.

[95] M M Yovanovich. Thermal contact correlations. In *Spacecraft radiative transfer and temperature control*, volume 1, pages 83–95. AIAA, 1982.

[96] Jack P. Holman. *Heat Transfer*. McGraw Hill, Boston, 9 edition, 2002.

[97] David G Gilmore, editor. *Spacecraft Thermal Control Handbook*, volume 1. The Aerospace Corporation, 2 edition, 2002.

[98] G G Gubareff, J E Janssen, and R H Torborg. *Thermal Radiation Properties Survey*. Honeywell, 2 edition, 1960.

[99] Hugh W Coleman and W Glenn Steele. *Experimentation, Validation, and Uncertainty Analysis for Engineers*. Wiley, 3 edition, 2009.

[100] Semyon G Rabinovich. *Measurement Errors and Uncertainties: Theory and Practice*. Springer, 2 edition, 2000.

[101] S Marelli and B Sudret. UQLab: A framework for uncertainty quantification in MATLAB. In *2nd International Conference on Vulnerability, Risk Analysis and Management*, number ICVRAM2014, pages 2554–2563, 2014.

[102] Robert Larsen and C Crochet. Thermophysical Properties of Two Molybdenum Samples: Report to Purdue University (MTEC). Technical report, Thermophysical Properties Research Laboratory, Inc., West Lafayette, 2018.

[103] J. Prakash, H.P. Garg, and G. Datta. A solar water heater with a built-in latent heat storage. *Energy Conversion and Management*, 25(1):51–56, 1985.

[104] N.K. Bansal and D. Buddhi. An analytical study of a latent heat storage system in a cylinder. *Energy Conversion and Management*, 33(4):235–242, apr 1992.

[105] Atul Sharma and C R Chen. Solar Water Heating System with Phase Change Materials. *International Review of Chemical Engineering (I.RE.CH.E.)*, 1(4), 2009.

[106] Paras Sachdeva. Performance enhancement of solar water heater using phase change materials (PCM): A Review. *International Journal of Advance Research and Innovation*, 5(1):104–109, 2017.

[107] L.F. Cabeza, A. Castell, C. Barreneche, A. de Gracia, and A.I. Fernández. Materials used as PCM in thermal energy storage in buildings: A review. *Renewable and Sustainable Energy Reviews*, 15(3):1675–1695, apr 2011.

[108] Alvaro de Gracia and Luisa F. Cabeza. Phase change materials and thermal energy storage for buildings. *Energy and Buildings*, 103:414–419, sep 2015.

[109] Hussein Akeiber, Payam Nejat, Muhd Zaimi Abd. Majid, Mazlan A. Wahid, Fatemeh Jomehzadeh, Iman Zeynali Famileh, John Kaiser Calautit, Ben Richard Hughes, and Sheikh Ahmad Zaki. A review on phase change material (PCM) for sustainable passive cooling in building envelopes. *Renewable and Sustainable Energy Reviews*, 60:1470–1497, jul 2016.

[110] Farah Souayfane, Farouk Fardoun, and Pascal-Henry Biwole. Phase change materials (PCM) for cooling applications in buildings: A review. *Energy and Buildings*, 129:396–431, oct 2016.

[111] Yaping Cui, Jingchao Xie, Jiaping Liu, Jianping Wang, and Shuqin Chen. A review on phase change material application in building. *Advances in Mechanical Engineering*, 9(6):168781401770082, jun 2017.

[112] Raphael Menard and Jean-Sebastien Lagrange. Zero Energy Furniture, mar 2015.

[113] M. J. Hoover, P. G. Grodzka, and M. J. Oneill. Space thermal control development. Technical report, NASA, dec 1971.

[114] D. V. Hale, M. J. Hoover, and M. J. O'Neill. Phase Change Materials Handbook. Technical report, NASA Marshal Space Flight Center, Huntsville, AL, 1971.

[115] W. R. Humphries and E. I. Griggs. A design handbook for phase change thermal control and energy storage devices. Technical report, NASA Marshall Space Flight Center, Huntsville, Al, 1977.

[116] M. S. Busby and S. J. Mertesdorf. The Benefit of Phase Change Thermal Storage for Spacecraft Thermal. In *AIAA 22nd Thermophysics Conference*, page 7, Honolulu, 1987. AIAA.

[117] Ronald A. Creel. Applying Thermal Control Experiences On Apollo Lunar Rover Project To Rovers For Future Space Exploration, 2007.

[118] L. Bledjian, D. V. Hale, M. J. Hoover, and M. J. O'Neill. Phase-Change Materials. In David G. Gilmore, editor, *Spacecraft Thermal Control Handbook*, chapter 11, pages 373–403. The Aerospace Press/AIAA, El Segundo, CA, 2 edition, 2002.

[119] Flight Control Division. Lunar Roving Vehicle Systems Handbook - Rev. A. Technical report, NASA Manned Spacecraft Center, Houston, 1971.

[120] Patrick J. Shamberger. Cooling Capacity Figure of Merit for Phase Change Materials. *Journal of Heat Transfer*, 138(2):024502, sep 2016.

[121] Patrick J. Shamberger and Timothy S. Fisher. Cooling power and characteristic times of composite heatsinks and insulants. *International Journal of Heat and Mass Transfer*, 117:1205–1215, feb 2018.

[122] Kireeti Chintakrinda, Randy D. Weinstein, and Amy S. Fleischer. A direct comparison of three different material enhancement methods on the transient thermal response of paraffin phase change material exposed to high heat fluxes. *International Journal of Thermal Sciences*, 50(9):1639–1647, sep 2011.

[123] Nasiru I. Ibrahim, Fahad A. Al-Sulaiman, Saidur Rahman, Bekir S. Yilbas, and Ahmet Z. Sahin. Heat transfer enhancement of phase change materials for thermal energy storage applications: A critical review. *Renewable and Sustainable Energy Reviews*, 74:26–50, jul 2017.

[124] E. W. Bentilla, L. E. Karre, and R. F. Sterrett. Research and development study on thermal control by use of fusible materials: Final Report. Technical report, NASA, Hawthorne, CA, apr 1966.

[125] Saad Mahmoud, Aaron Tang, Chin Toh, Raya AL-Dadah, and Sein Leung Soo. Experimental investigation of inserts configurations and PCM type on the thermal performance of PCM based heat sinks. *Applied Energy*, 112:1349–1356, dec 2013.

[126] V. Dubovsky, G. Barzilay, G. Granot, G. Ziskind, and R. Letan. Study of PCM-Based Pin-Fin Heat Sinks. In *Volume 1: Heat Transfer in Energy Systems; Thermophysical Properties; Heat Transfer Equipment; Heat Transfer in Electronic Equipment*, pages 857–863. ASME, jan 2009.

[127] Rajesh Baby and C. Balaji. Experimental investigations on phase change material based finned heat sinks for electronic equipment cooling. *International Journal of Heat and Mass Transfer*, 55(5-6):1642–1649, feb 2012.

[128] Rajesh Baby and C. Balaji. Thermal optimization of PCM based pin fin heat sinks: An experimental study. *Applied Thermal Engineering*, 54(1):65–77, may 2013.

[129] C. Balaji, Praneet Mungara, and Parw Sharma. Optimization of size and shape of composite heat sinks with phase change materials. *Heat and Mass Transfer*, 47(5):597–608, may 2011.

[130] Siva P. Gurrum, Yogendra K. Joshi, and Jungho Kim. Thermal Management of High Temperature Pulsed Electronics Using Metallic Phase Change Materials. *Numerical Heat Transfer: Part A: Applications*, 42(8):777–790, 2002.

[131] Shankar Krishnan, Suresh V. Garimella, and Sukhvinder S. Kang. A novel hybrid heat sink using phase change materials for transient thermal management of electronics. *IEEE Transactions on Components and Packaging Technologies*, 28(2):281–289, jun 2005.

[132] Candice A. Bauer and R. A. Wirtz. Thermal Characterization of a Compact, Passive Thermal Energy Storage Device. In *Undergraduate Research and Design in Heat Transfer*, page 7, Orlando, 2000. ASME/IMECE.

[133] KULR. PCM Heat Sink, 2018.

[134] Colas Hasse, Hébert Sallée, Rémy Dendievel, André Bontemps, and Manuel Grenet. Realization, test and modelling of honeycomb wallboards containing a Phase Change Material. *Energy and Buildings*, 43(1):232–238, 2010.

[135] Yvan Dutil, Daniel R. Rousse, Nizar Ben Salah, Stéphane Lassue, and Laurent Zalewski. A review on phase-change materials: Mathematical modeling and simulations. *Renewable and Sustainable Energy Reviews*, 15(1):112–130, jan 2011.

[136] Yoram Kozak, Boris Abramzon, and Gennady Ziskind. Experimental and numerical investigation of a hybrid PCMair heat sink. *Applied Thermal Engineering*, 59(1-2):142–152, sep 2013.

[137] M. Merzlyakov and C. Schick. Thermal conductivity from dynamic response of DSC. *Thermochimica Acta*, 377(1-2):183–191, oct 2001.

[138] Jiajun Wang, Lianfang Feng, Julio M. Ottino, and Richard Lueptow. Inertial Effects on Chaotic Advection and Mixing in a 2D Cavity Flow. *Industrial & Engineering Chemistry Research*, 48(5):2436–2442, mar 2009.

[139] Sadegh Motahar, Nader Nikkam, Ali A. Alemrajabi, Rahmatollah Khodabandeh, Muhammet S. Toprak, and Mamoun Muhammed. Experimental investigation on thermal and rheological properties of n-octadecane with dispersed TiO2 nanoparticles. *International Communications in Heat and Mass Transfer*, 59:68–74, dec 2014.

[140] Jifen Wang, Huaqing Xie, and Zhong Xin. Thermal properties of heat storage composites containing multiwalled carbon nanotubes. *Journal of Applied Physics*, 104(11):113537, dec 2008.

[141] Jifen Wang, Huaqing Xie, Zhong Xin, Yang Li, and Lifei Chen. Enhancing thermal conductivity of palmitic acid based phase change materials with carbon nanotubes as fillers. *Solar Energy*, 84(2):339–344, feb 2010.

[142] Da Hee Choi, Juhyuk Lee, Hiki Hong, and Yong Tae Kang. Thermal conductivity and heat transfer performance enhancement of phase change materials (PCM) containing carbon additives for heat storage application. *International Journal of Refrigeration*, 42:112–120, jun 2014.

[143] F. Frusteri, V. Leonardi, S. Vasta, and G. Restuccia. Thermal conductivity measurement of a PCM based storage system containing carbon fibers. *Applied Thermal Engineering*, 25(11-12):1623–1633, aug 2005.

[144] F. Frusteri, V. Leonardi, and G. Maggio. Numerical approach to describe the phase change of an inorganic PCM containing carbon fibres. *Applied Thermal Engineering*, 26(16):1883–1892, nov 2006.

[145] Ali Karaipekli, Ahmet Sar, and Kamil Kaygusuz. Thermal conductivity improvement of stearic acid using expanded graphite and carbon fiber for energy storage applications. *Renewable Energy*, 32(13):2201–2210, oct 2007.

[146] Yi-Hsien Wang and Yue-Tzu Yang. Three-dimensional transient cooling simulations of a portable electronic device using PCM (phase change materials) in multi-fin heat sink. *Energy*, 36(8):5214–5224, aug 2011.

[147] Yash Ganatra and Amy Marconnet. Passive Thermal Management Using Phase Change Materials: Experimental Evaluation of Thermal Resistances. In *Volume 1: Thermal Management*, page V001T09A064. ASME, jul 2015.

[148] Yash Ganatra, Javieradrian Ruiz, John A. Howarter, and Amy Marconnet. Experimental investigation of Phase Change Materials for thermal management of handheld devices. *International Journal of Thermal Sciences*, 129:358–364, jul 2018.

[149] Marc Hodes, Randy D. Weinstein, Stephen J. Pence, Jason M. Piccini, Lou Manzione, and Calvin Chen. Transient Thermal Management of a Handset Using Phase Change Material (PCM). *Journal of Electronic Packaging*, 124(4):419, dec 2002.

[150] Zhaoxia Luo, Hyejung Cho, Xiaobing Luo, and Kyung-il Cho. System thermal analysis for mobile phone. *Applied Thermal Engineering*, 28(14-15):1889–1895, oct 2008.

[151] F.L. Tan and C.P. Tso. Cooling of mobile electronic devices using phase change materials. *Applied Thermal Engineering*, 24(2-3):159–169, feb 2004.

[152] Fabrisonic. Solid-State Welding at Low Temperature, 2018.

[153] ANSI. ANSI/ASME B4.1-1967 (R2009) Preferred Limits Fits Cylindrical Parts. Technical report, ANSI/ASME, 2009.

[154] Junbo Feng, Yao Chen, John Blair, Hamza Kurt, Ran Hao, D S Citrin, Christopher J Summers, and Zhiping Zhou. Fabrication of annular photonic crystals by atomic layer deposition and sacrificial etching. *Journal of Vacuum Science & Technology B, Nanotechnology and Microelectronics: Materials, Processing, Measurement, and Phenomena*, 27:568, 2009.

[155] Special Metals. INCONEL ® alloy X-750. Technical report, SMC-067, 2004.

APPENDICES

A. THERMOCOUPLE FABRICATION STEPS

1. Clean wires a nitric acid wash followed by a 200 proof ethanol rinse. Triple solvent clean of alumina.
2. Place the ends of the two thermoelements side-by-side, mount in double carbon arc welding mounting fixture, DO NOT TWIST ENDS.
3. Start the flow of the argon shielding gas, then strike the arc between the two carbon electrodes just long enough for the bead to be formed.
4. 99.8% pure alumina, double-bore (127 μm ID), insulation tubes (794 μm OD) (OMEGA TRX-005132-6) are used in all areas that will experience temperatures >60℃, the remaining areas are insulated with fiberglass sleeving (OMEGA FBGS-N-30-100 (Natural/White) and FBGS-N-30-100 (Red)). Note, these are not the ANSI standard colors for type S thermocouple insulation (ANSI Standard is Black/Red for Positive/Negative), but the natural color was chosen over black as it introduced fewer contaminants to the system
5. Following the insertion of the individual Pt/Pt-10%Rh leads through the double bore tubes, the tip with the thermocouple junction is sealed in high-temperature, high-purity alumina potting cement (Ceramabond 569) (agitated/outgassed during mixing to reduce porosity and increase thermal conductivity). This electrically isolates the junction tip from the metal bars and serves as a contamination barrier between the molybdenum and the platinum.
6. After tube tip is sealed and cured, it is gently polished to remove any burs or rough/uneven edges
7. Each probe is then chemically etched to reduce the probe diameter to fit precisely in the respective installation hole on the reference bar. The probes are undersized by a maximum of 11.43 μm following a standard locational clearance fit (LC1)

[153]. The chemical etching is accomplished using a buffered oxide etch (BOE). Care must be taken to avoid exposure of the thermocouple leads to the BOE, which is why the leads are gently coiled into a PTFE bag and the bag is carefully sealed with Kapton® tape. This ensures that the thermocouple legs are not damaged during the etching of the alumina sheath. The BOE concentration is 1:6 ($HF : H_2O = 1 : 6$), which has a published etch rate for alumina of 100 nm/min at room temperature [154]. This very slow etch rate allows the probes to be slowly brought the the correct diameter and the best fit to be obtained in the reference bar for each probe sheath. The probes are etched one at a time in a PTFE beaker with a PTFE lid that is drilled to hold the probe stationary in the middle of the BOE in the beaker at the appropriate depth. Following removal of the probe from the BOE beaker, it is thoroughly rinsed with ultra-pure water for two minutes at a flow rate of at least one gallon per minute. The probe is then dried by placing on top of a double thick layer of clean room wipes and using a clean nitrogen gun to remove the water. Pressure for the Nitrogen regulator should be set between 10-15 psi. This process is repeated until a precision fit is obtained for all six thermocouple probes in the reference bar. After the desired fit has been achieved, the Kapton® tape and the PTFE bag are removed. The probe is then cleaned again by wiping down with 200 proof ethanol.

8. The entire probe assembly (all six at once) are then annealed for 1 hour at 1100℃ to remove cold work and relax the thermocouple leads

9. Following this anneal and controlled cooling to room temperature. The ceramic sheathed portion of the assembly is inserted into the furnace to achieve a temperature between 1050 - 1100℃, then quickly withdrawn from the furnace (over a few seconds) and allowing it to quickly cool in air. This is an insulator limited quench in that the thermal diffusivity of the alumina dominates the cooling rate and is thus slower than if the thermocouple bare wire was quenched. Quenching of bare wire can result in brittleness due to hardening during the rapid quench. This quench of the type S thermocouple is done to minimize the drift for later

high-temperature operation in the Z-Meter. In a quenched state and fixed installation position, the drift for type S thermocouples is greatest above 1000℃, where it is ~ 0.1℃ during the first 100 hours of operation (above 1000℃).

B. HIGH TEMPERATURE SPRING FABRICATION PROCEDURE

SAFETY WARNING: ALL LATHE OPERATIONS DONE WITH THE LATHE POWER DISCONNECTED!

High temperature springs can be fabricated by selecting or machining an appropriately sized smooth steel rod as an arbor to wind our spring around. Note that the winding arbor diameter should be a little smaller than the target value due to wire spring back which opens the diameter a little after the winding is released and also that dimensional changes will also occur after the annealing process, so a couple of iterations may be required. Next the wire will need some way to be secured to the arbor, the best way is to drill a hole through the diameter of the arbor on one end that is just big enough for the Inconel wire we are using to fit through. An alternative is to clamp the wire against the side of the arbor when they are installed in the lathe chuck if this can be done securely without causing the arbor to be off-center for the lathe rotation. We then create a friction control device for the wire feed by sliding a small length of plastic tubing over the end of the Inconel wire and mounting this tube in the tool holder on the cross-slide of the lathe using the set screw to clamp the tube and control how much friction is added to the wire sliding through the holder. This is important because it allows us to keep the wire taught while we are wrapping the wire around the arbor and will permit us to use the lathe cross-slide to control the pitch of the winding. Next, to secure the wire to the winding arbor, we slide the Inconel wire through the hole in the diameter of the arbor and make a hard 90° bend in the wire on the opposite side to prevent it from slipping out. Mount the arbor in the lathe, support the other end of the arbor in a chuck mounted in the tailstock and position the tool holder close to he location where the wire is secured into the rod. Based on the load rating you desire for your spring, set the number of coils per inch by setting up the change gears for the lathe like you are cutting single-point threads. We

recommend doing some test runs with steel wire of the same diameter as the Inconel wire to avoid waste of the costly material. Once the lathe setting are determined and the Inconel wire is being used, start hand rotating the lathe chuck counter-clockwise (so that the wire is coiled from the tool holder over the top of the arbor, but leave the halfnut disengaged to wind two tight coils to start the spring, then engage the lathe halfnut and keep rotating to form the compression coils. Disengage the lathe halfnut again about two wire diameters short of our desired stop location and wind two more touching coils to finish the spring. It is critical to have your settings well defined, and use a repeatable method of stops to ensure that each spring manufactured has a load as close to the others as possible. Then trim the wire being fed from the tool holder and cut the wire being secured through the arbor on the side opposite of the 90° bend. At this point, your spring should slide off the end of the arbor (after the tailstock support is moved out of the way). Now trim the coiled ends to leave approximatley one tight coil before the regularly spaced pitch starts in the middle of the spring, then grind the ends of the spring flat to finish off the spring. The next step is to stress relieve the springs with an annealing step to make sure they hold their shape well.

The Society of Automotive Engineers (SAE) recommends the following triple heat treatment for Inconel alloy X-750 [wire, spring temper] (AMS5699) designed for springs in service requiring maximum relaxation resistance between 450 - 700℃. First heat the cold coiled springs to 1150℃ and hold for 2 hours, but due to furnace limitations, we heat to 1100℃ and hold for 4 hours (solution treating), then air cool (AC). Next, heat to 850℃ and hold for 24 hours (stabilization treating), then AC. Finally, heat to 700℃ and hold for 20 hours (precipitation treating), then AC. Springs should be protected from sagging during the triple heat treatment. This is accomplished by placing the springs on an arbor which makes a snug fit with the inner diameter of the coiled spring [155]. The heat treatments are done in a Lindberg/Blue M Mini-Mite tube furnace (TF55035A-1), fitted with an alumina process tube which improves the temperature uniformity over the use with direct filament exposure. The process tube can also be used to carry out furnace processes in atmospheres other

than air. The most uniform part of the chamber is in the direct center of the furnace. The process tube extends more than five tube diameters past the end of the hot zone, which helps to maximize hot zone uniformity; however, if possible only use the center 70% of the furnace hot zone to ensure sufficient temperature uniformity during the heat treatment. In other words, try to avoid using the last 15% of the hot zone on both sides of the furnace as an area where the springs are being heat treated on the arbor. Only insert one arbor at a time and it is best practice to suspend the arbor in the middle of the alumina tube by using two annulus shapped supports, one at either end of the arbor. The outer diameter of the annulus should be approximately: $OD_{Annulus} \approx ID_{ProcessTube}$ - (5% - 10%).

It is typically recommended to use the springs with the oxide layer on. If they must be cleaned, treat in a reducing bath of sodium hydride (NaH) followed by a water quenching and rinsing provides a good surface [155]. If you use NaH make sure you fully understand all safety procedures and are wearing appropriate personal protective equipment (PPE) at all times.

C. BAR ALIGNMENT PROCEDURE

Bar alignment is checked after bringing the bars into contact by holding a short straight-edge[1] along the axial direction of the two bars with the straight edge centered at the bar interface. With the straight edge held along the bar, the user checks to see if any light is visible between the bar surface and the straight edge. If there is light visible on for one bar and it is a consistent thickness gap along that bar, then it indicates that the bars need to be shifted into alignment to eliminate this gap. It is a good standard practice to check this at three points on the bar separated by approximately 120°. After the bars are aligned, all components are carefully tightened working from bolt-to-bolt, tightening a little at a time to avoid shifting the system out of alignment. After the bolts are all at their final installation torque values, the bars are checked once more to verify alignment. This process can be repeated as need to realign the bars after any system component in series with either bar is changed. While taking advantage of the tolerance stacking for minute adjustments to insure perfect positioning of the meter bars works very well for axial alignment, it does not address the problem of the parallelism of the bar faces.

When checking the axial alignment of the bars, if there is a gap between the bar and straight edge, but it is not a consistent thickness along the bar, this indicates that there is a parallelism problem between the faces. However, sometimes the parallel misalignment can be so small that it would be hard to see with the naked eye, for this reason a more precise method of detection is required. When checking the parallelism of the top and bottom bar faces, the bars should be separated by a very small distance, approximately 0.001 - 0.010 in., but the exact distance does not matter. Once the bars are separated, the user takes a parallel feeler gauge (do not use tapered feeler

[1]The straight edge used is simply a precisely machined bar for this purpose. It is made from 316SS, measures 3.000 (L) × 0.750 (W) × 0.150 in. (T). It is machined to keep the long edges flat to within ± 0.001 in..

gauges) and finds the smallest gap between the edges of the two bars by moving up in sizes until the gauge slides around the perimeter everywhere except for a single location. If there is any difference in fit between locations around the perimeter, then this indicates that the bar faces are not parallel.

For example, if a 0.001 in. thick gauge fits tightly in one location, but then freely slides everywhere else, then this indicates that the locations where the gauge is loose are higher than the tight location. To bring the bar faces back into parallel, the user should find a mounting bolt in series with the bar (above or below depending on the top versus bottom bars), loosen this bolt slightly, then install a shim of appropriate thickness to bring the two faces closer to parallel. The thickness of the required shim can be determined by measuring the height difference between the point where the thickness gauge fits tightly and where it is loose, which is accomplished by using the other thicknesses in the feeler gauge. A first order estimation of the thickness for the required shim is approximately $1/2 \cdot (th_2 - th_1)$, where th_1 is the thickness of the gauge material where the shim gets stuck and th_2 is the largest thickness of gauge material that will fit between the faces of the bars (should be separated from the sticking position by 180° around the bars). However, in reality, the shim is not being applied directly above the misalignment, and the offset (vertically and horizontally) will require the thickness of the correction shim to be further reduced to account for the geometric mounting factors in the system. After a shim is installed, the axial alignment of the bars must be checked again, then the parallelism of the bars can be rechecked. This process is completed until the feeler gauge can slide all the way around the perimeter of the bar interfaces, but the next size thicker, 0.0015 in., will not fit between the bar interfaces. When this is achieved, the parallelism alignment of the bars is 12.7 μm (0.0005 in.); however, this does not yet meet the parallelism requirement of 5 μm to comply with ASTM D5470. In order to further measure the parallelism between these bar faces, a difference in thickness between gauges of 0.0002 in. must be used. This is a smaller step difference than found on any known feeler gauges, but it can easily be accomplished using a Class X go/no-go plug gauge. This

plug gauge consists of a handle with one pin on either end. The "go" end is a pin of $\varnothing$0.2500 in., while the "no-go" end houses a pin of $\varnothing$0.2502 in. Now the user must just position the bars so that the "go" gauge can move between the two faces of the bars, but the "no-go" gauge cannot be inserted. If the "no-go" gauge fits anywhere between the bar faces after being sized to the "go" gauge, then the bar faces are not parallel to within 5 μm and further shimming is required to bring the parallelism into tolerance.

D. RADIATION SHIELD ALIGNMENT PROCEDURE

Concentric alignment of the upper bar shield bank to the CLS shield bank is crucial because there is little clearance between the inside of the upper bar bank and the surface of the bar. Relative positioning of the two shield banks for assembly is done using alignment rods. The clearance gap between the outer diameter of the upper bar horizontal shield layers and the inner diameter of the CLS bank is 0.060 inches. A rod diameter of 0.045 - 0.052 inches is required to properly center the two shield banks, while still providing sufficient clearance to remove the rods without scratching the polished surfaces of the shield assembly. A length of 4.75 - 5.50 inches is recommended for rod length to allow full clearance of the CLS shield bank and enough rod exposure for easy removal. Alignment rods can be purchased as $^{3}/_{64}$ inch diameter rotary shafts, but due the cost of these shafts and their limited use, an alternative method is developed.

A 36 inch length of $^{1}/_{16}$ inch stainless steel welding rod is selected and cut into seven equal portions, approximately 5 inches in length. The welding rod diameter is oversized for this application, so each rod is mounted in a drill chuck, then sanded and polished using aluminum oxide sandpaper, starting with 600 grit, then progressing to 800 grit, and finally polishing with 1,200 grit, this process should take several minutes per rod. Note it is imperative that the drill be speed or power limited to avoid injury. In this case, a basic corded hand drill is mounted in a bench vise and plugged into a Variac[1], which limits the power. If a cordless drill is used, make sure it has slip clutch or torque control, and set this to the lowest setting that still permits light sanding pressure to be applied during rotation. After each rod is the correct size, the portion of the rod mounted in the drill, which is still has a $^{1}/_{16}$ inch diameter, is trimmed away, and the ends are lightly sanded to remove any burs that might scratch

[1]Variac is a trade name commonly used for a variable autotransformer.

the heat shield surfaces. The rods are then subjected to a triple solvent wipe down, to remove any surface contaminants and oils, which involves using a hydroentangled, nonwoven cleanroom wipe (TechniCloth© TX609) folded into quarters and wetted with solvent to wipe down the rod starting with toluene, then acetone, and finishing with isopropanol. A new wipe is used for each chemical. Wipes may be used to clean multiple rods provided a clean quarter of the cloth is used each rod.

The rods need to be distributed around the perimeter of the shield to keep the assemblies concentric. The equal spacing of the rods is also challenging as they have to stay in place while the two shields are aligned vertically. The easiest way to complete this assembly is to secure two 24 inch long parallel strips of 3/4 inches wide Kapton® tape to a clean work surface with approximately 3.5 inches between the outer edges of the two strips and the adhesive side facing up. Place the first rod 2 inches from the left end of the strip, with one end of the rod flush with the outer edge of the tape making sure the rod is approximately perpendicular to the two tape strips. The spacing for the remaining rods is determined by dividing the circumference of the inner face of the CLS shield bank divided by the number of spacing rods used,

$$\Delta x_{rod} = C/n = \pi \cdot d_{i,CLS}/n, \tag{D.1}$$

where D_i is the inner diameter of the CLS shield bank and n is the number of rods used. The inner diameter of the CLS shield bank is 2.120 inches, which gives a circumference of 6.660 inches. When divided by the seven rods we prepared, this gives a rod spacing of 0.950 inches. Then, take two more pieces of tape and cover the first two pieces, adhesive sides contacting the rods and press together to seal. This creates a flexible sheet that is used to align the two shield banks, without needing to hold all of the rods in place separately.

Place the CLS bank on a clean surface with one of the open ends facing up. Carefully insert the flexible sheet of rods inside the inner most heat shield of the CLS bank with the end where the rods are flush with Kapton® inserted first. Spread the rod sheet out to line the perimeter of the heat shield, a small amount of Kapton® tape can be used to hold the ends of the rod sheet in place if needed, but this should be

applied at the end sitting on the table, where the rods are flush. This avoids any interference of the tape with the alignment region. There should be a small protrusion of alignment rods from the top of the shields when done. Next, prepare the set screws used to join the two shield assemblies by starting them in the threaded of the CLS bank from the outside towards the inside. Install each such that the threads engage and it is held in place, but make sure it does not enter the inner cylinder surface to avoid scratching the other shield bank during installation. Finally, carefully insert the upper bar shield bank with the horizontal shields going in first and align the threaded holes between the two shields. Use one hand to hold the upper bar shields in place while using a ball-end hex driver to interlock the two shield banks. It is important to go slowly here and tighten each set screw gradually working between the fasteners in a criss-cross pattern until the two shield banks are secure.

Check the alignment by first visually inspecting and verifying that the banks appear to be centered and that all of the alignment rods are indeed passing between the two banks. Then pick up the shield assembly, and test that all the rods move freely when pulling from the end of the rods flush with the tape. If all rods are free to slide out, carefully remove the alignment rods and the shield assembly is complete. If any of the rods bind or cannot be freely removed, this means that the shield assembly is not fully centered and the set screws must be adjusted. The amount misalignment possible in this assembly is at most a few thousands of an inch as dictated by the tolerance of the threaded holes and set screws.

Since this alignment only has to be addressed whenever the two shield are being assembled it is unlikely that it will have to be redone by future users as the shields can be removed together as a single unit from the system to access the bars, but if infrared (IR) measurement systems are added to the system in the future more of the upper bar will need to be visible. A modified design of the upper bar shield bank will be required, which is shorter to permit the IR detector to see more of the bar surface. In such a case the alignment procedure of the shield banks will prove useful.

E. Z-METER PART DRAWINGS

Load Frame

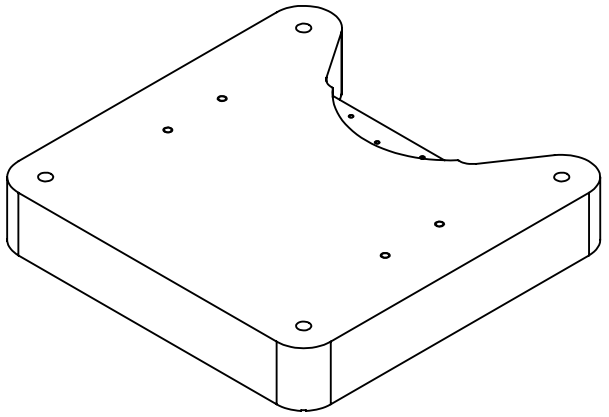

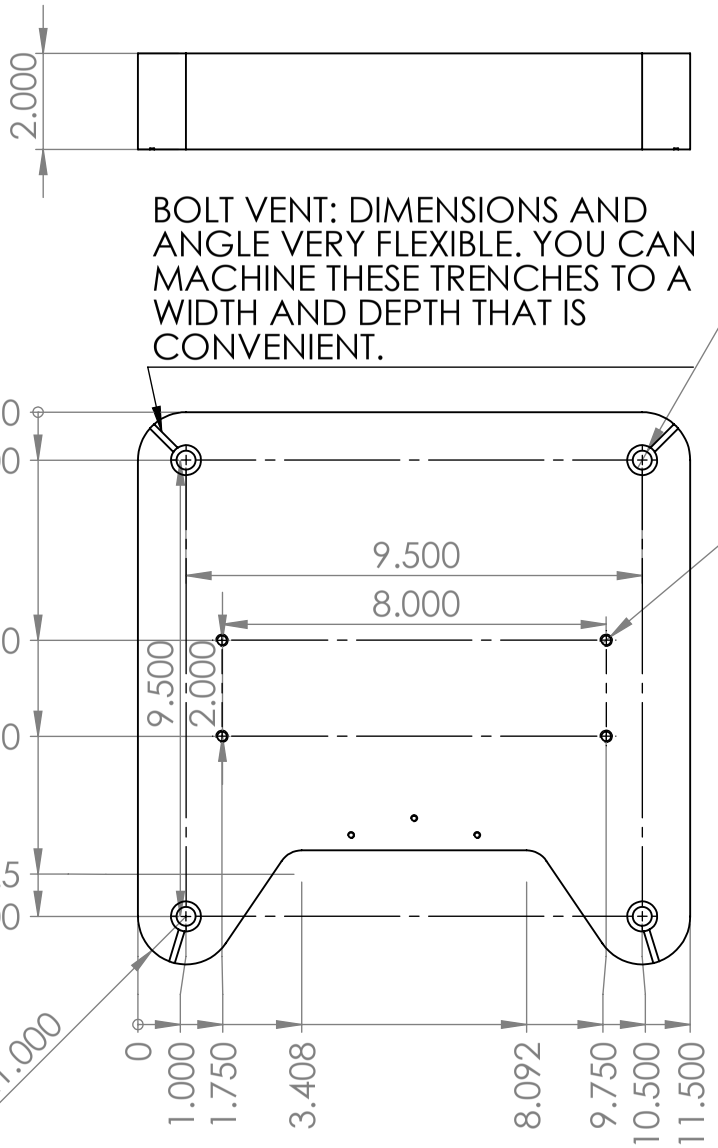

DATE: 09/02/16			
TITLE: BOTTOM FIXTURE PLATE v7			
Collier Miers			
MATERIAL: 6061	SIZE A	DWG. NO.	QTY: 1
FINISH:	SCALE: 1:4		SHEET 1 OF 2

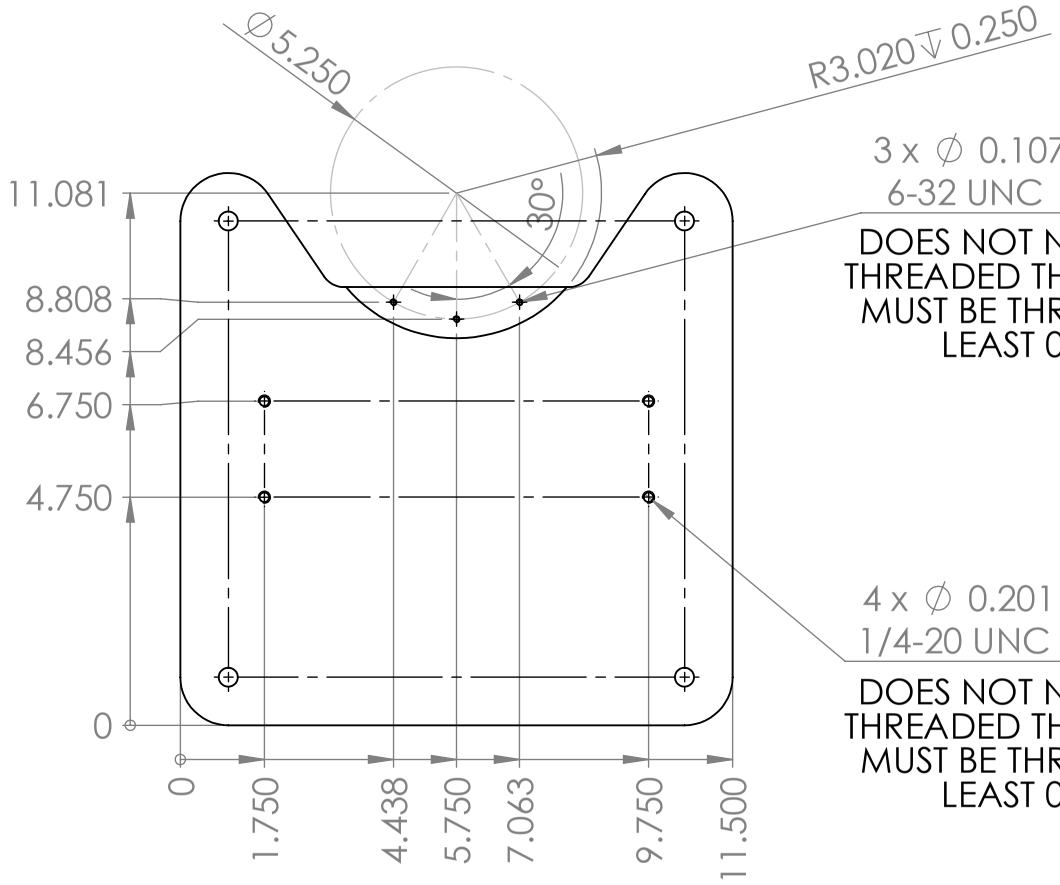

3 x ∅ 0.107 THRU ALL
6-32 UNC THRU ALL

DOES NOT NEED TO BE THREADED THRU ALL BUT MUST BE THREADED AT LEAST 0.500".

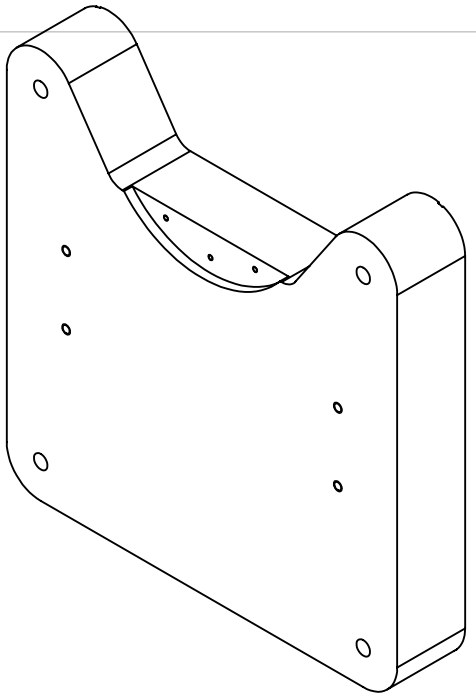

4 x ∅ 0.201 THRU ALL
1/4-20 UNC THRU ALL

DOES NOT NEED TO BE THREADED THRU ALL BUT MUST BE THREADED AT LEAST 0.625".

DATE: 09/02/16			
TITLE: BOTTOM FIXTURE PLATE v7			
Collier Miers			
MATERIAL: 6061	SIZE A	DWG. NO.	QTY: 1
FINISH:	SCALE: 1:4		SHEET 2 OF 2

NOTE:
STOCK FOR THIS PART ROUGHLY
6" DIAM x 0.3" THICK

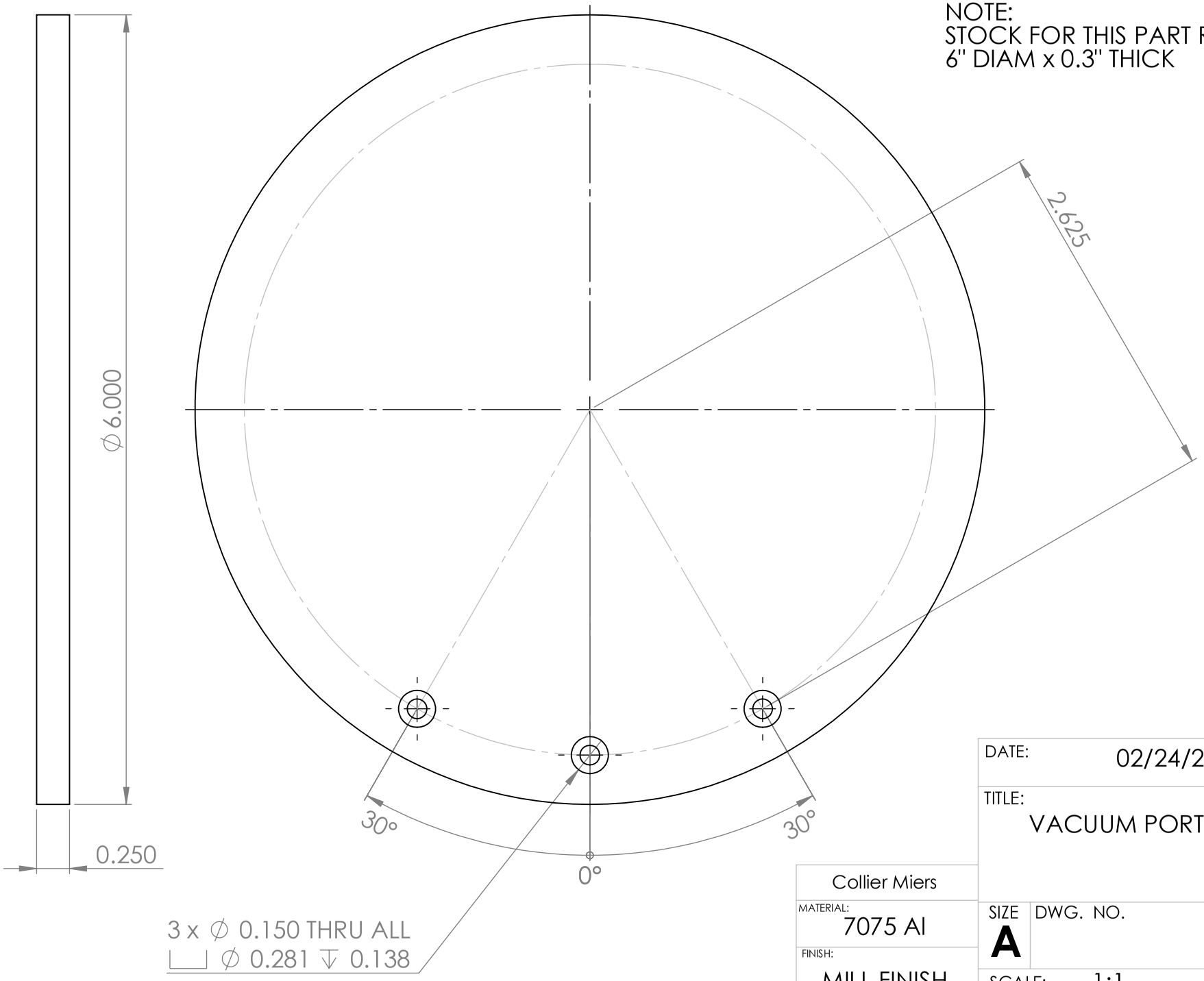

DATE:	02/24/2017
TITLE:	VACUUM PORT BAFFEL
Collier Miers	
MATERIAL:	7075 Al
FINISH:	MILL FINISH
SIZE	A
DWG. NO.	
QTY:	1
SCALE:	1:1
SHEET 1 OF 1	

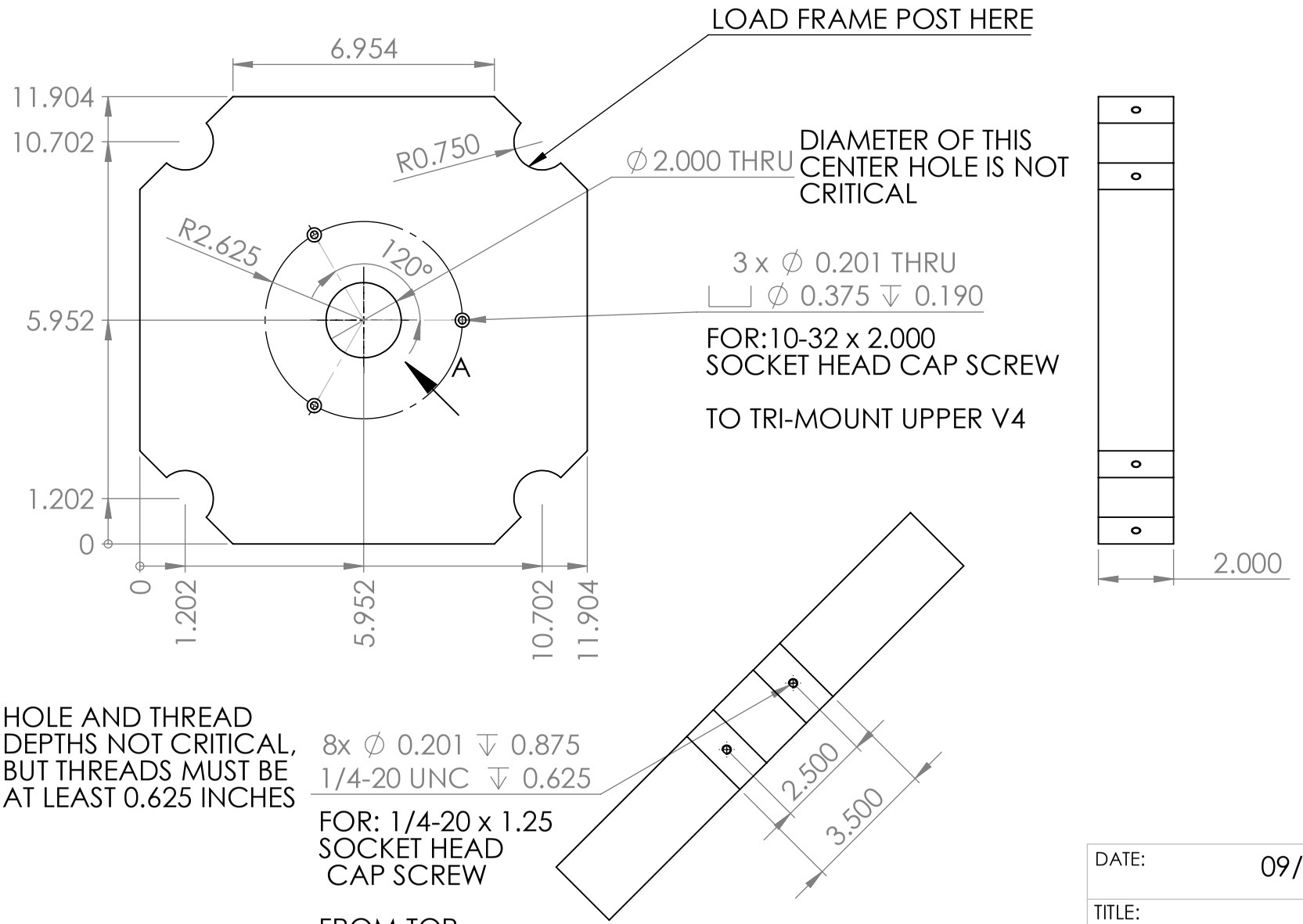

DATE:	09/02/16
TITLE:	TOP PLATEN v11
Collier Miers	
MATERIAL:	6061
FINISH:	
SIZE	A
DWG. NO.	
QTY:	1
SCALE:	1:4
SHEET 1 OF 1	

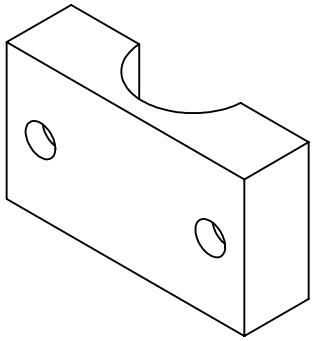

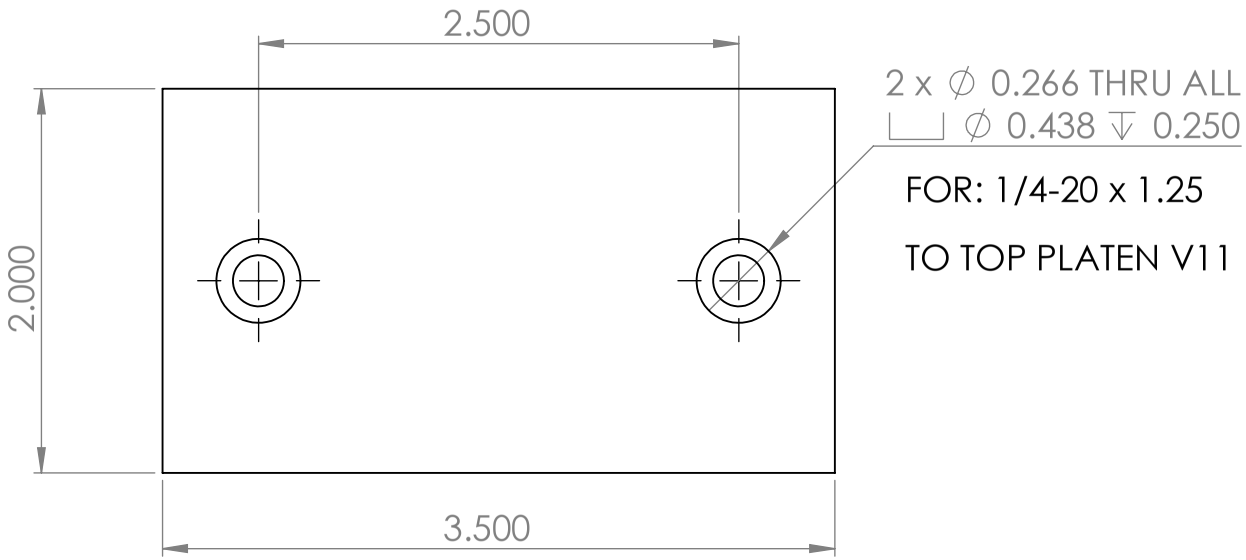

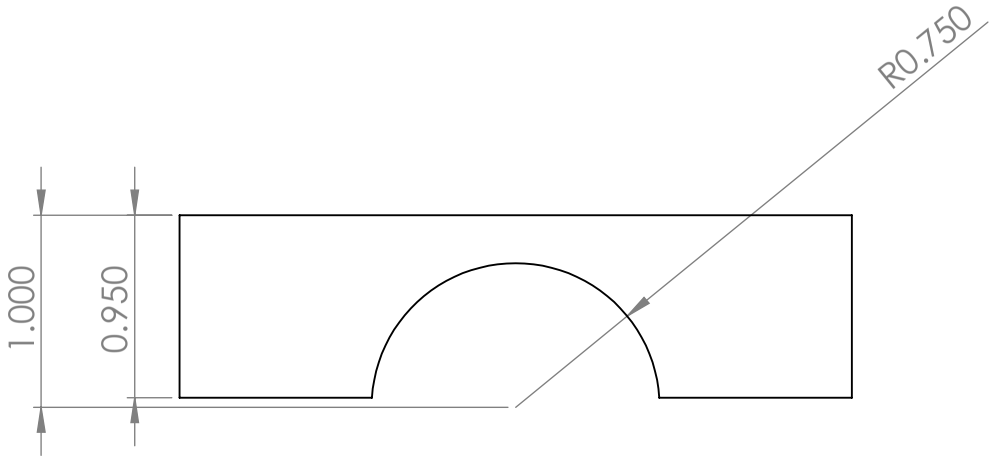

DATE: 09/02/16			
TITLE: TOP PLATEN CLAMP v2			
Collier Miers			
MATERIAL: 6061	SIZE A	DWG. NO.	QTY: 4
FINISH:	SCALE: 1:1		SHEET 1 OF 1

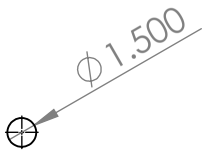

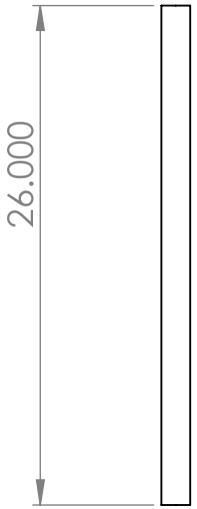

NOTE: OUTSIDE (RADIAL FACE) OF STOCK IS ALREADY POLISHED. AXIAL FACES DO NOT NEED TO BE POLISHED.

ONLYTHE BOTTOM FACE HAS A HOLE, THE TOP FACE IS BLANK.

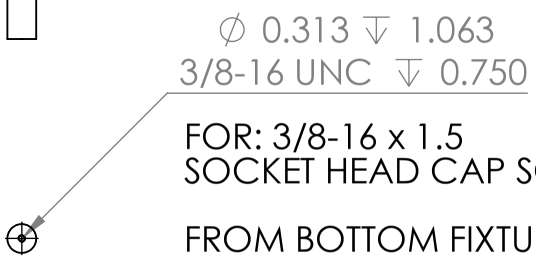

THREAD DEPTH IS NOT CRITICAL, BUT SHOULD BE GREATER THAN 0.750 INCHES.

FOR: 3/8-16 x 1.5
SOCKET HEAD CAP SCREW

FROM BOTTOM FIXTURE PLATE V7

DATE: 09/02/16			
TITLE: LOAD FRAME POST			
Collier Miers			
MATERIAL: 304 SS	SIZE A	DWG. NO.	QTY: 4
FINISH: POLISHED	SCALE: 1:10		SHEET 1 OF 1

NOTE: CHAMFER DIMENSIONS ARE NOT CRITICAL. PLEASE CHAMFER ENOUGH TO REMOVE CORNER AND AVOID INTERFERENCE WITH WELDS INSIDE SERVICE WELL OF VACUUM CHAMBER.

THREADED DEPTH IS NOT CRITICAL, BUT NEEDS TO BE GREATER THAN 0.750 INCHES

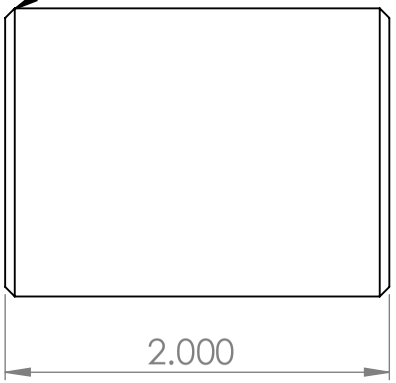

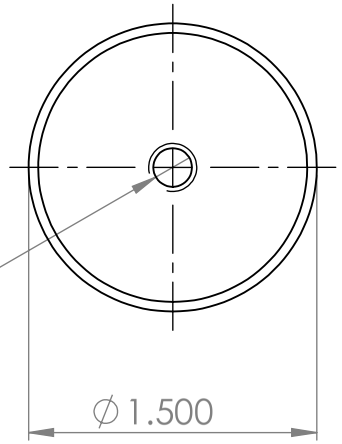

FOR: 1/4-20 x 0.750
FLAT HEAD CAP SCREW

FROM SPACER BAR V2

NOTE: STOCK FOR THESE PARTS IS THE EXTRA MATERIAL FROM CUTTING THE LOAD FRAME POSTS TO LENGTH. OUTSIDE (RADIAL FACE) OF BAR IS ALREADY POLISHED, AXIAL FACES DO NOT NEED TO BE POLISHED.

DATE: 09/02/16			
TITLE: SPACER CYLINDER v2			
Collier Miers			
MATERIAL: 304 SS	SIZE A	DWG. NO.	QTY: 8
FINISH: POLISHED	SCALE: 1:1		SHEET 1 OF 1

NOTE: END RADIUS IS NOT CRITICAL.

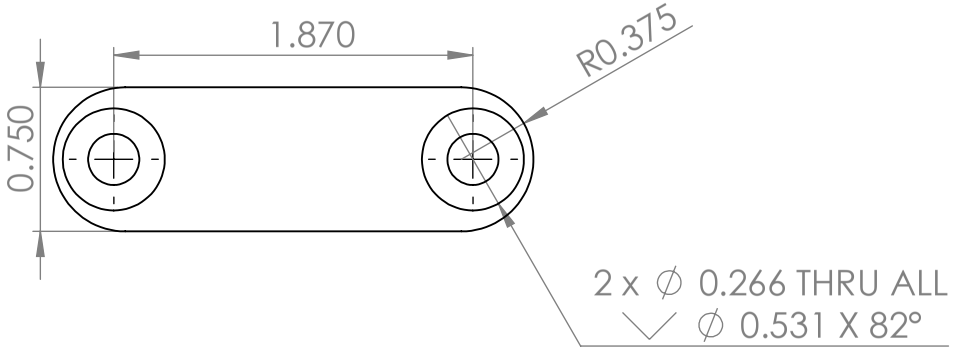

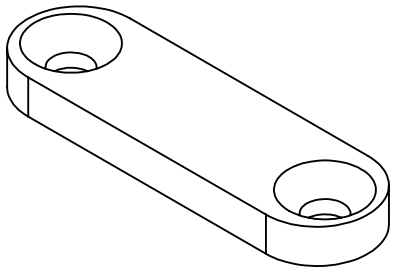

FOR: 1/4-20 x 3/4
FLAT HEAD CAP SCREW

TO SPACER CYLINDER V2

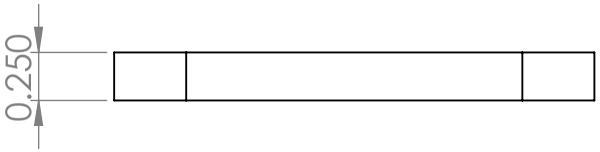

DATE: 09/02/16			
TITLE: SPACER CYLINDER BAR v2			
Collier Miers			
MATERIAL: 6061	SIZE A	DWG. NO.	QTY: 4
FINISH:	SCALE: 1:1		SHEET 1 OF 1

Thermal Isolation Platforms

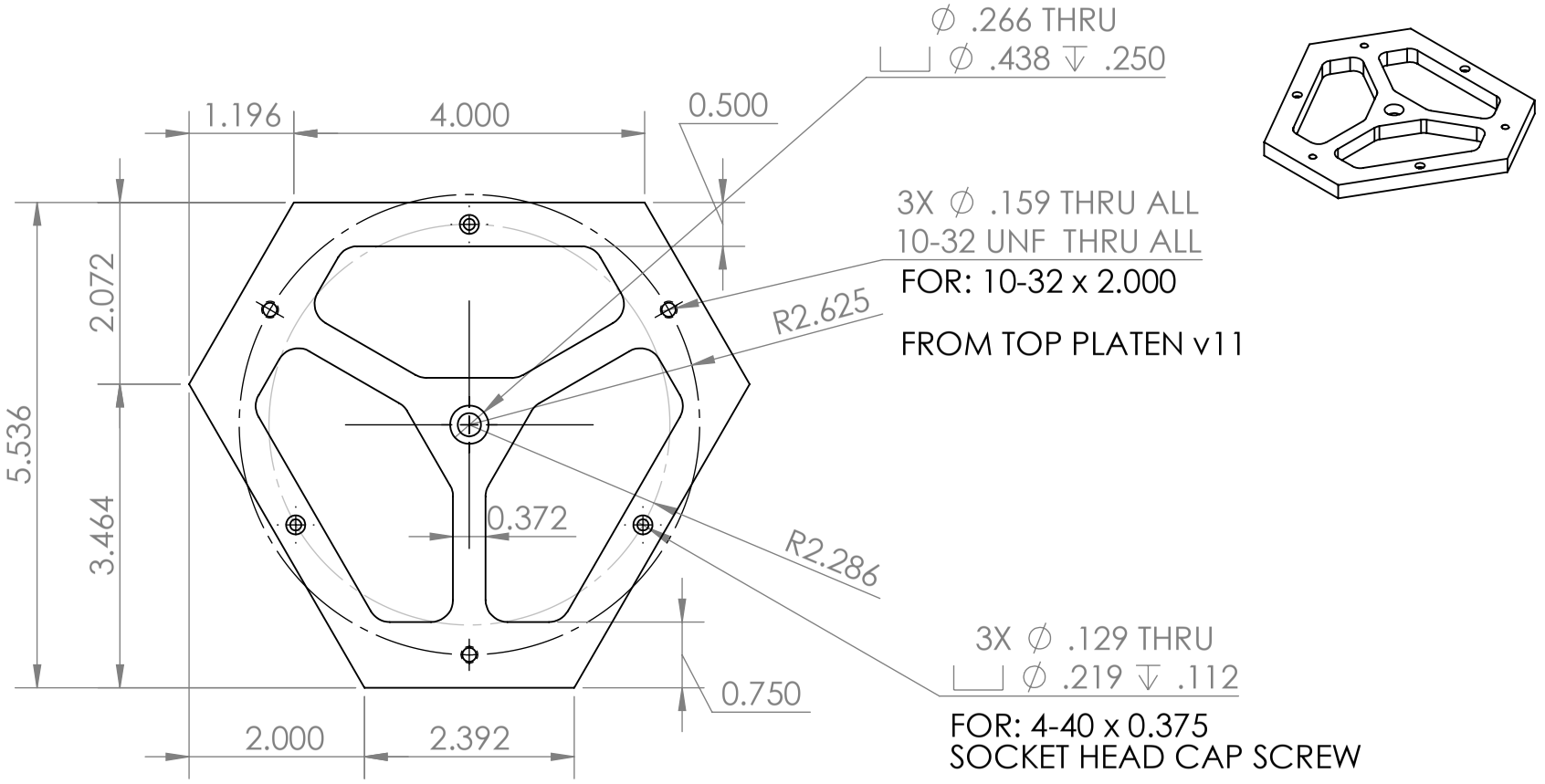

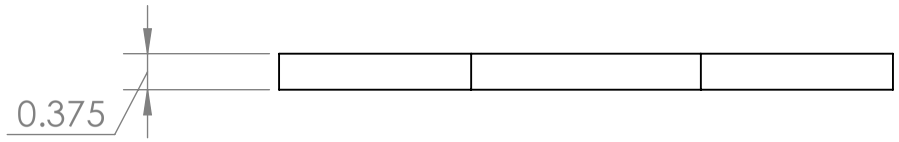

DATE: 09/02/16			
TITLE: TRI-MOUNT UPPER v4			
COLLIER MIERS			
MATERIAL: 304 SS	SIZE A	DWG. NO.	QTY: 1
FINISH:	SCALE: 1:2		SHEET 1 OF 5

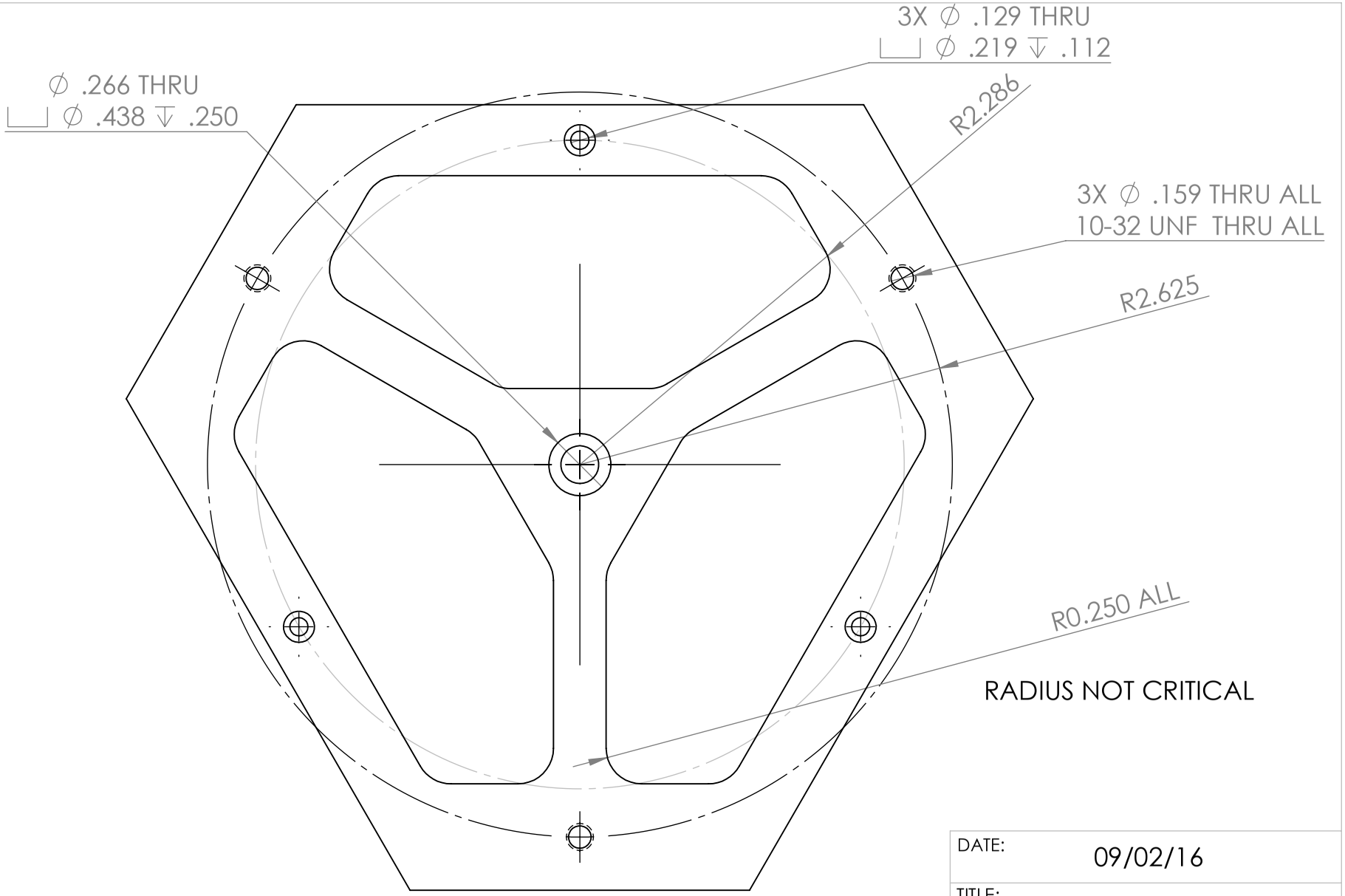

DATE: 09/02/16			
TITLE: TRI-MOUNT UPPER v4			
COLLIER MIERS			
MATERIAL: 304 SS	SIZE A	DWG. NO.	QTY: 1
FINISH:	SCALE: 1:1		SHEET 2 OF 5

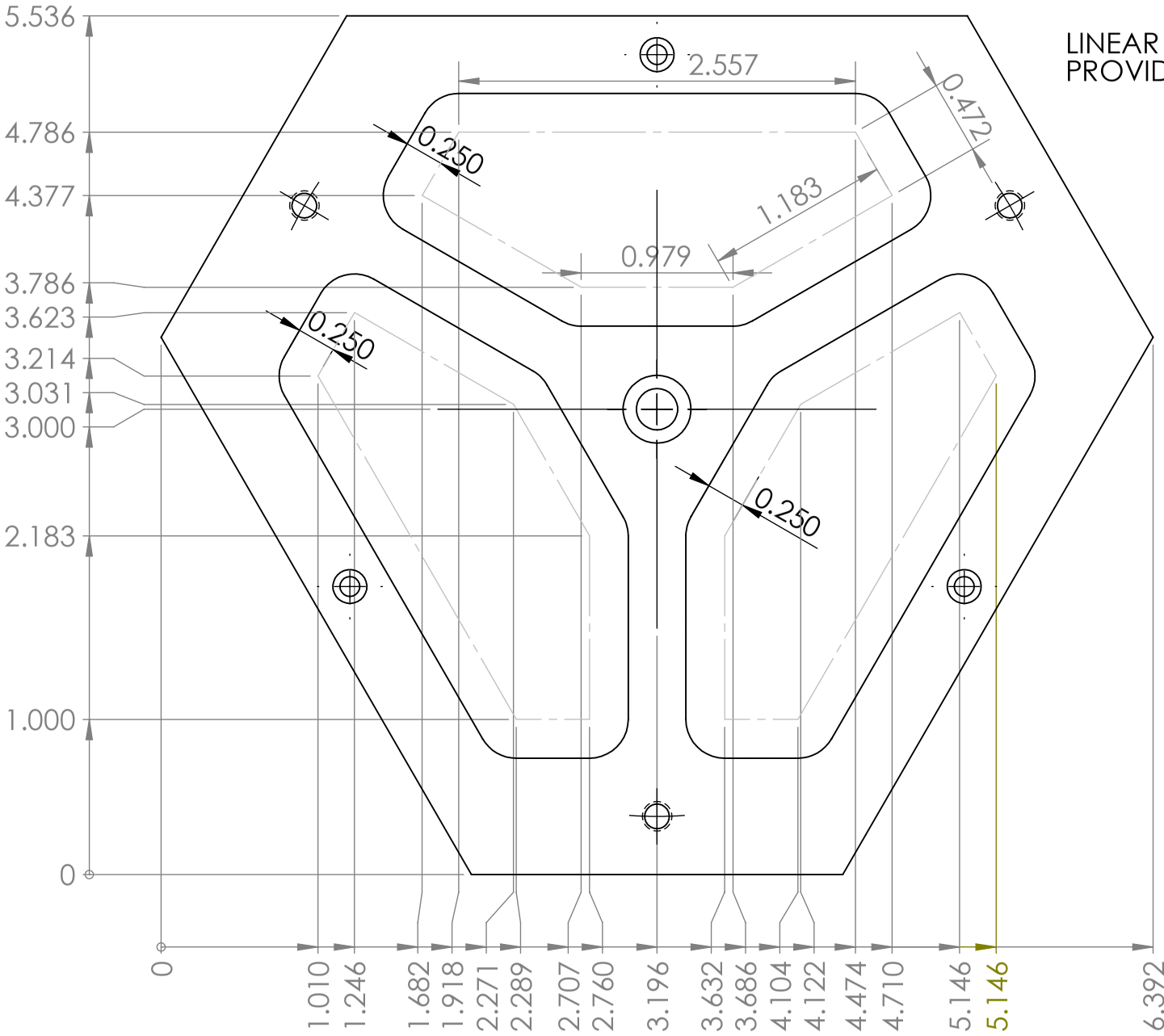

LINEAR POCKET DIMENSIONS
PROVIDED FOR REFERENCE.

DATE:	10/18/2016
TITLE:	TRI-MOUNT UPPER v4
Collier Miers	
MATERIAL: 304SS	
FINISH:	
SIZE A	DWG. NO.
QTY: 1	
SCALE: 1:1	SHEET 3 OF 5

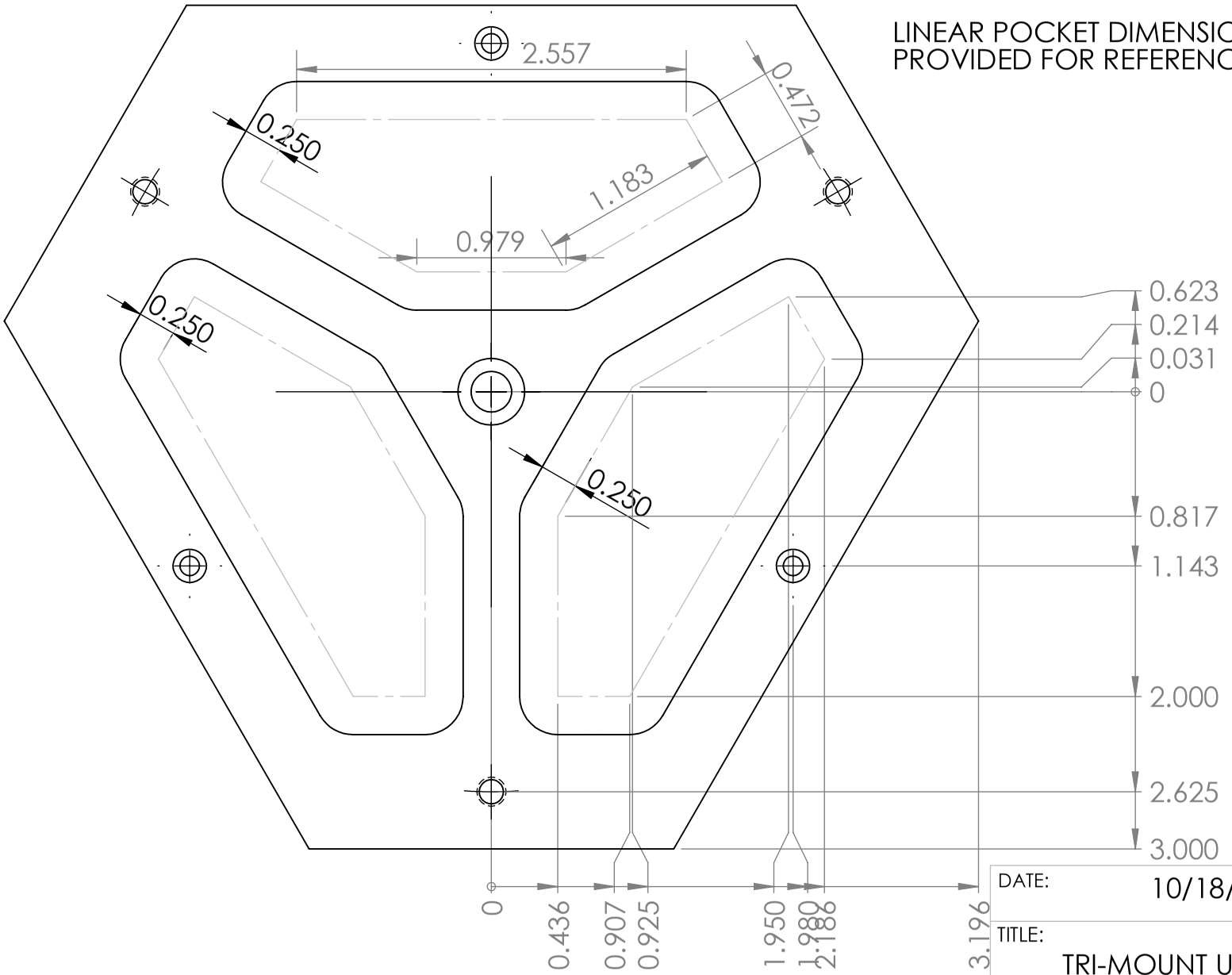

DATE:	10/18/2016
TITLE:	TRI-MOUNT UPPER v4
Collier Miers	
MATERIAL: 304SS	
FINISH:	
SIZE A	DWG. NO.
QTY: 1	
SCALE: 1:1	SHEET 4 OF 5

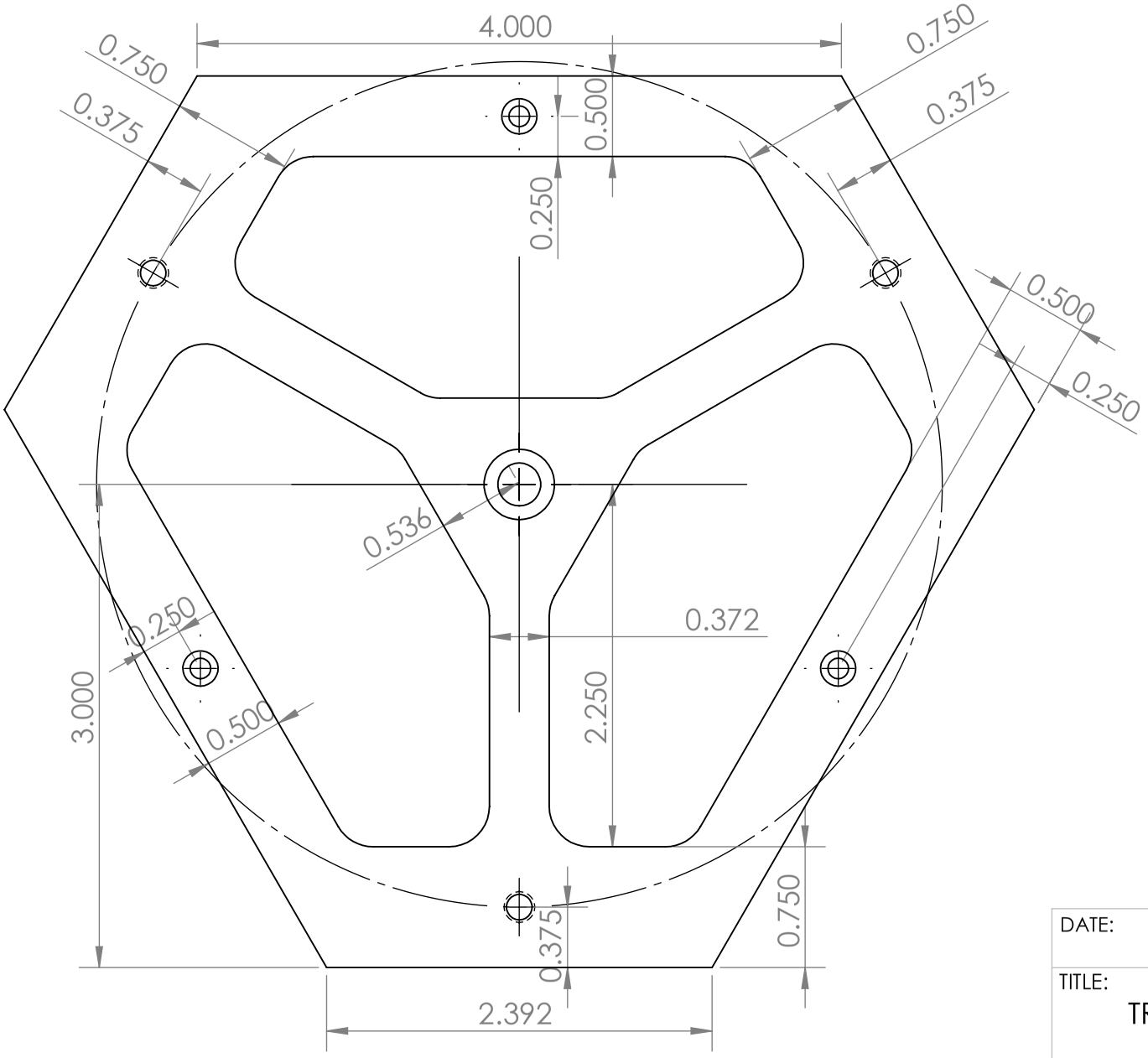

DATE: 07/08/16			
TITLE: TRI-MOUNT UPPER v4			
Collier Miers			
MATERIAL: 304SS	SIZE A	DWG. NO.	QTY: 1
FINISH:	SCALE: 1:1		SHEET 5 OF 5

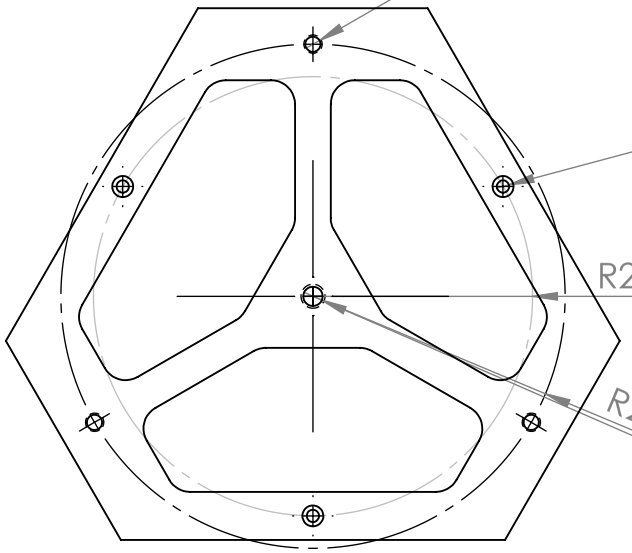

3X ∅ .159 THRU ALL
10-32 UNF - 2B THRU ALL

FOR: 10-32 x 2.00
SOCKET HEAD CAP SCREW

FROM FIXTURE RING v3

3X ∅ .129 THRU
⌴ ∅ .219 ↧ .112

FOR: 4-40 x 0.375
SOCKET HEAD CAP SCREWS

TO FUTEK LOAD CELLS (BOTTOM)

∅ .201 THRU ALL
1/4-20 UNC THRU ALL

FROM TRI-MOUNT UPPER v4

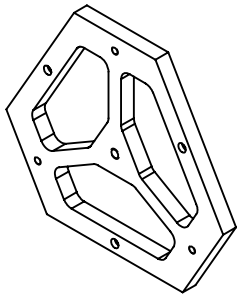

SAME DIMENSIONS AS TRI-MOUNT UPPER v4,
BUT HOLES ARE DIFFERENT TYPE HERE.

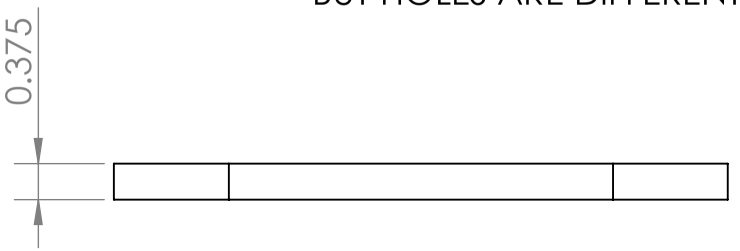

DATE: 09/02/16			
TITLE: TRI-MOUNT LOWER v4			
COLLIER MIERS			
MATERIAL: 304 SS	SIZE A	DWG. NO.	QTY: 1
FINISH:	SCALE: 1:2		SHEET 1 OF 1

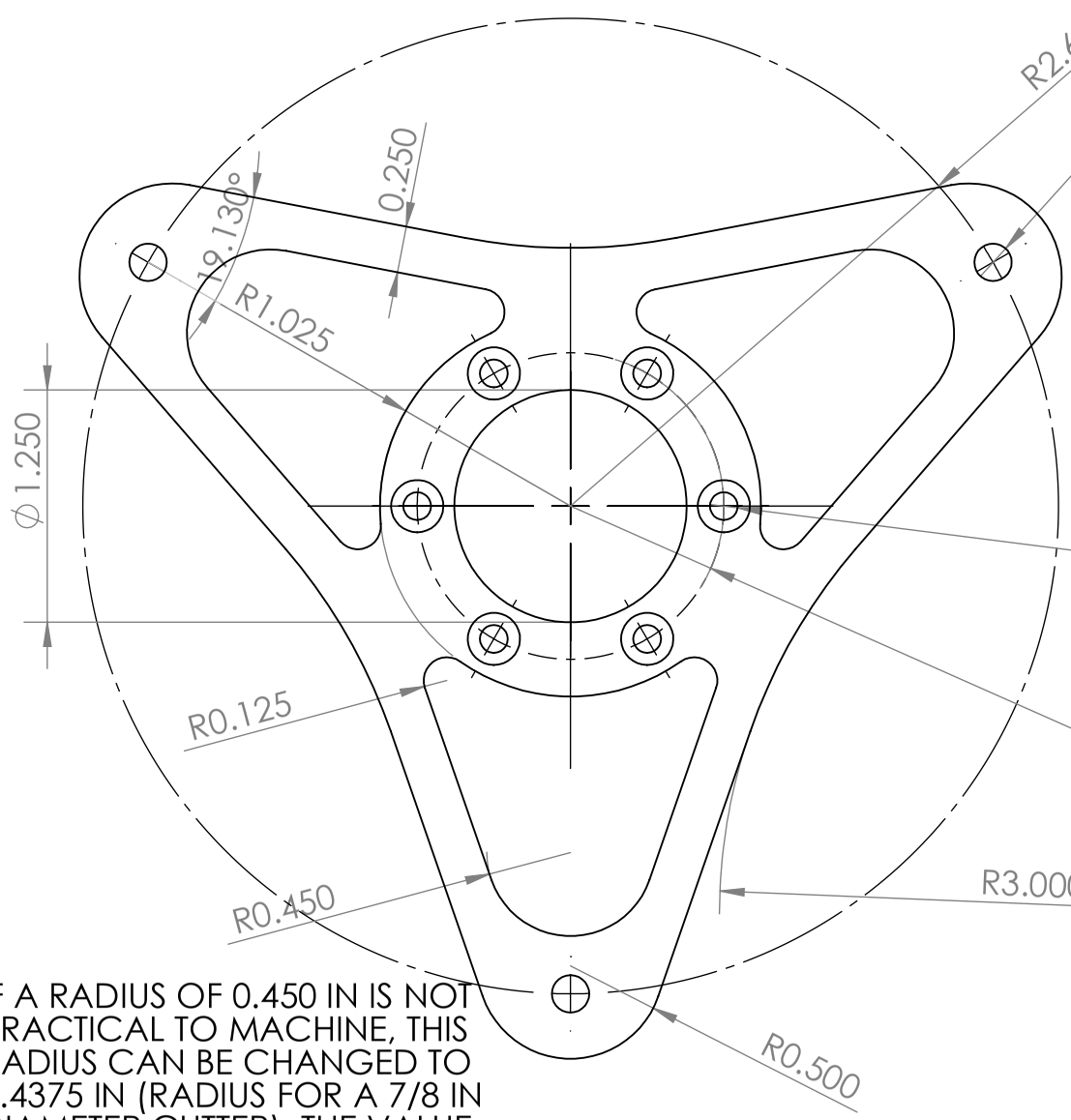

3X ⌀ .201 THRU ALL
⌴ ⌀ .375 ↧ .190

COUNTERBORE ON BACK FACE

FOR: 10-32 x 2.000
SOCKET HEAD CAP SCREW

TO TRI-MOUNT LOWER v4

6X ⌀ .150 THRU ALL
⌴ ⌀ .281 ↧ .138

FOR: 6-32
SOCKET HEAD CAP SCREW

TO CERAMIC HEATER LOADING SHROUD v3

IF A RADIUS OF 0.450 IN IS NOT PRACTICAL TO MACHINE, THIS RADIUS CAN BE CHANGED TO 0.4375 IN (RADIUS FOR A 7/8 IN DIAMETER CUTTER). THE VALUE OF THE RADIUS IS NOT CRITICAL.

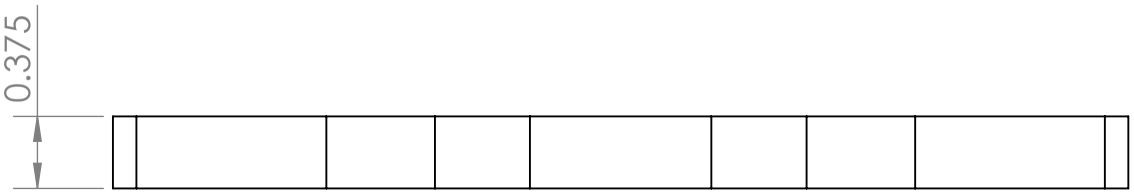

DATE: 09/02/16			
TITLE: FIXTURE RING v3			
COLLIER MIERS			
MATERIAL: 304 SS	SIZE A	DWG. NO.	QTY: 1
FINISH:	SCALE: 1:1		SHEET 1 OF 2

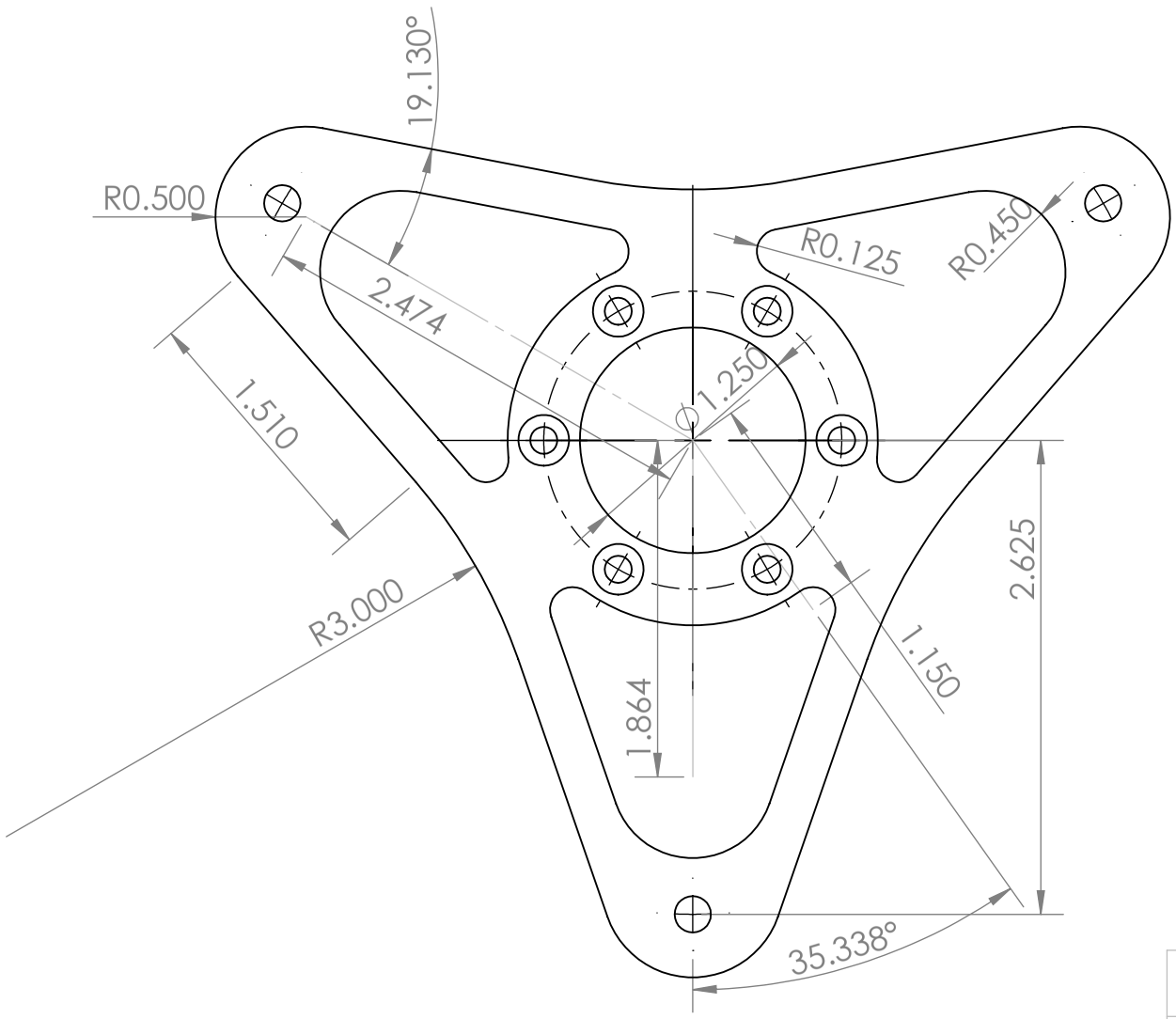

	DATE: 07/08/16		
	TITLE: FIXTURE RING v3		
Collier Miers			
MATERIAL: 304 SS	SIZE A	DWG. NO.	QTY: 1
FINISH:	SCALE: 1:1		SHEET 2 OF 2

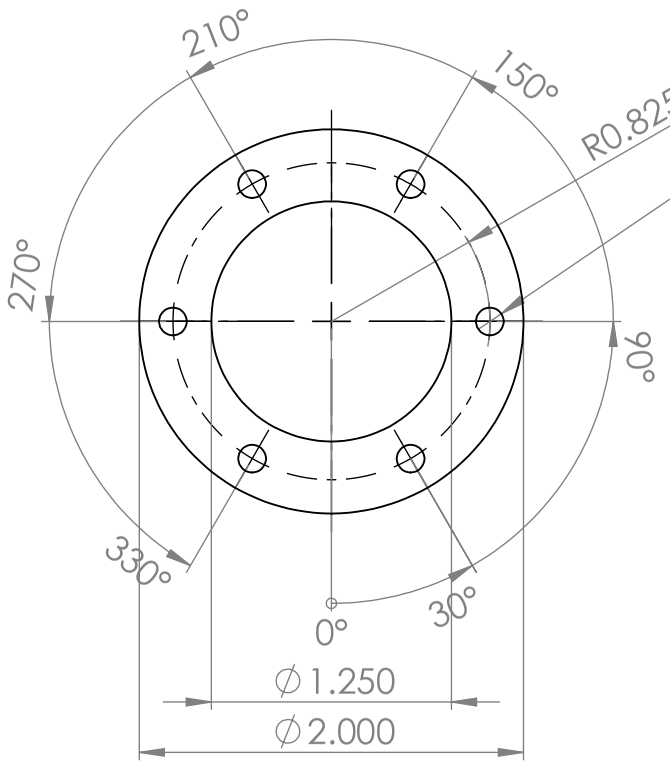

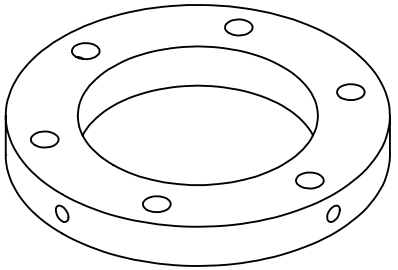

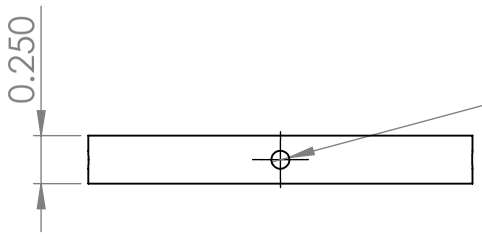

4 x ∅ 0.094 ↧ 0.125

SPACED AT 90 DEG
AROUND THE COLLAR

DATE: 03/23/17			
TITLE: HEAT SHIELD ADAPTOR COLLAR			
Collier Miers			
MATERIAL: 304 SS	SIZE A	DWG. NO.	QTY: 1
FINISH:	SCALE: 1:1		SHEET 1 OF 1

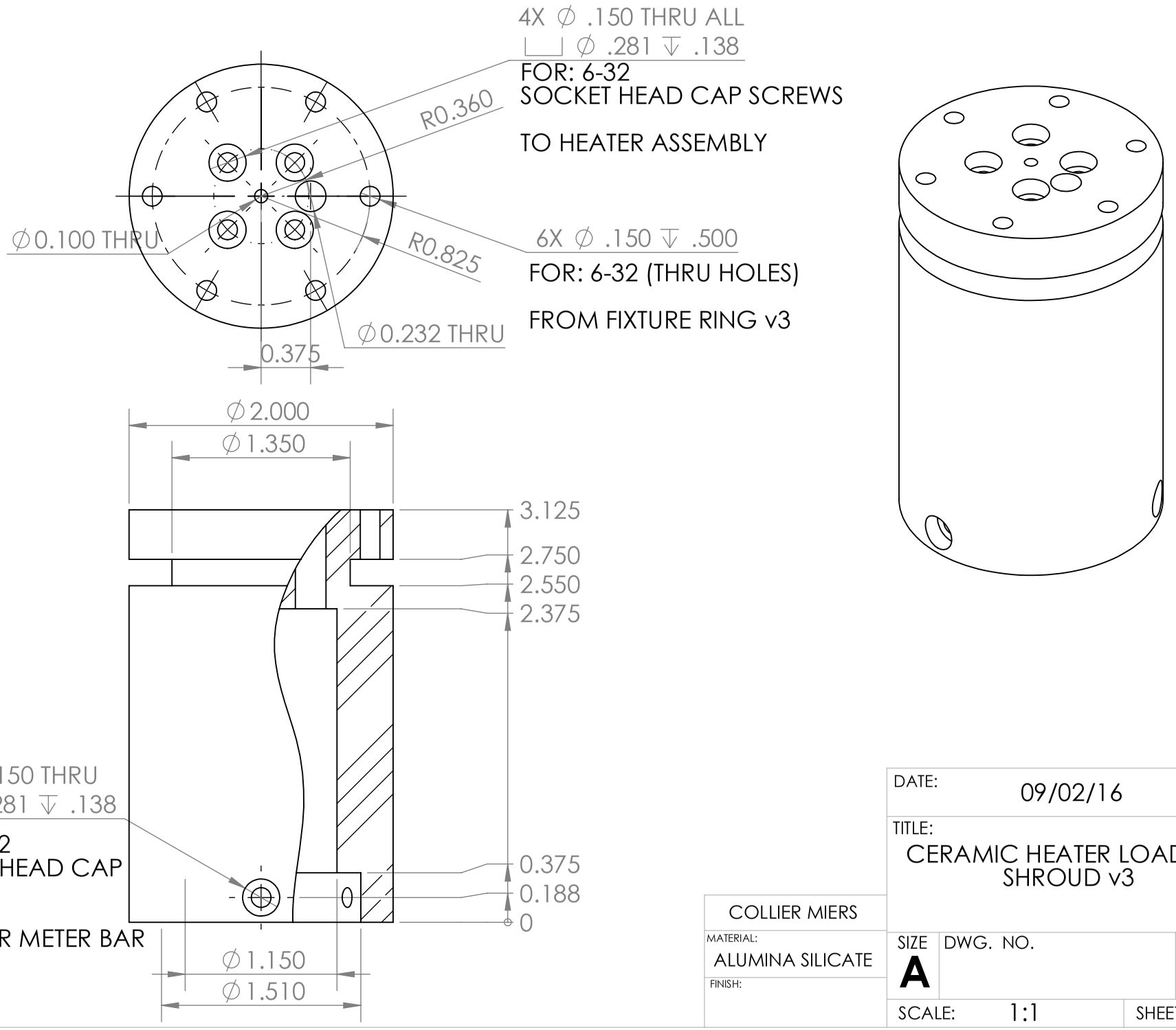

DATE: 09/02/16			
TITLE: CERAMIC HEATER LOADING SHROUD v3			
COLLIER MIERS			
MATERIAL: ALUMINA SILICATE	SIZE A	DWG. NO.	QTY: 1
FINISH:	SCALE: 1:1		SHEET 1 OF 1

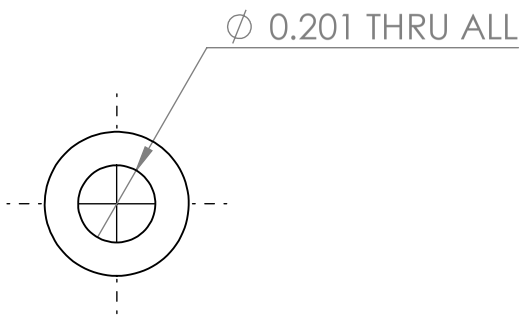

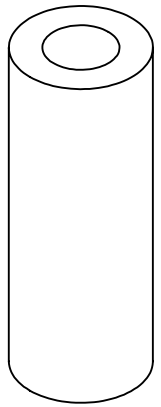

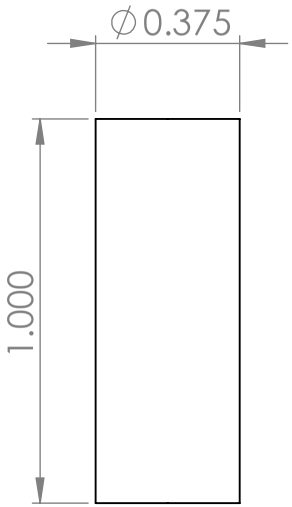

THESE ALUMINA SILICATE THERMAL STANDOFFS WILL BE CUT FROM THE 0.375" DIAMETER X 6" LENGTH STOCK PIECES. THE OUTER DIAMETER IS NOT CRITICAL, SO IF THE STOCK VARIES SLIGHTLY FROM THE SPECIFIED OD, THAT IS FINE.

ID IS A THRU HOLE FOR A #10 BOLT.

BREAK ALL EDGES TO AVOID CHIPPING OF CERAMIC DURING INSTALL.

	DATE: 12/01/16		
	TITLE: THERMAL STANDOFFS		
Collier Miers			
MATERIAL: Al2SiO5	SIZE A	DWG. NO.	QTY: 6
FINISH:	SCALE: 2:1		SHEET 1 OF 1

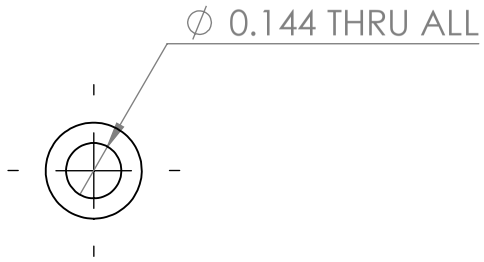

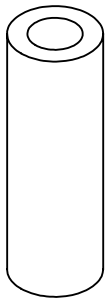

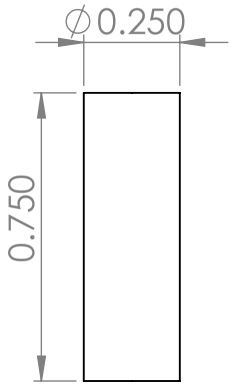

THESE ALUMINA SILICATE THERMAL STANDOFFS WILL BE CUT FROM THE 0.250" DIAMETER X 3.000" LENGTH STOCK PIECES. THE OUTER DIAMETER IS NOT CRITICAL, SO IF THE STOCK VARIES SLIGHTLY FROM THE SPECIFIED OD, THAT IS FINE.

ID IS A THRU HOLE FOR A #6 BOLT.

BREAK ALL EDGES TO AVOID CHIPPING OF CERAMIC DURING INSTALL.

DATE: 12/01/16			
TITLE: HEATER SHROUD STANDOFF			
Collier Miers			
MATERIAL: Al2SiO5	SIZE A	DWG. NO.	QTY: 8
FINISH:	SCALE: 2:1		SHEET 1 OF 1

Meter Bars and Mounting Fixtures

SURFACE ROUGHNESSES ARE GIVEN IN MICROINCHES.

SIDE SURFACES SHOULD BE POLISHED TO A BRIGHT FINISH TO REDUCE THE EMISSIVITY, BUT A SPECIFIC SURFACE ROUGHNESS IS NOT SPECIFIED.

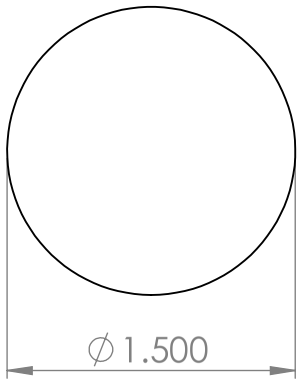

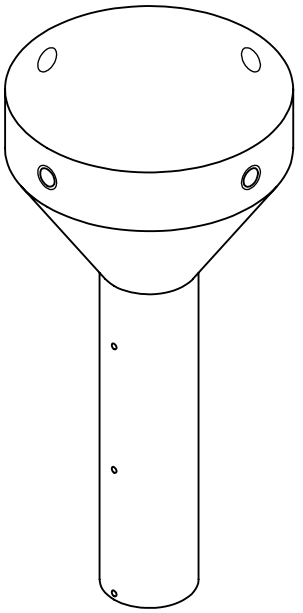

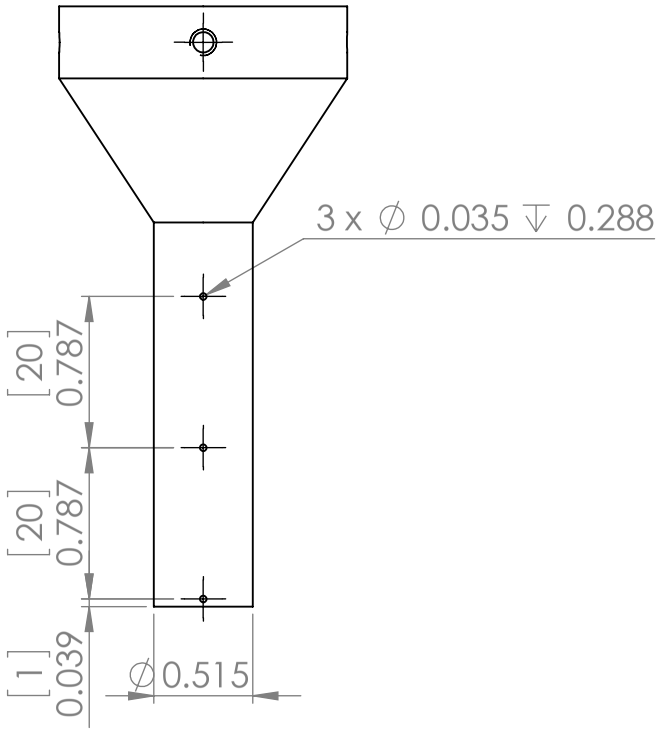

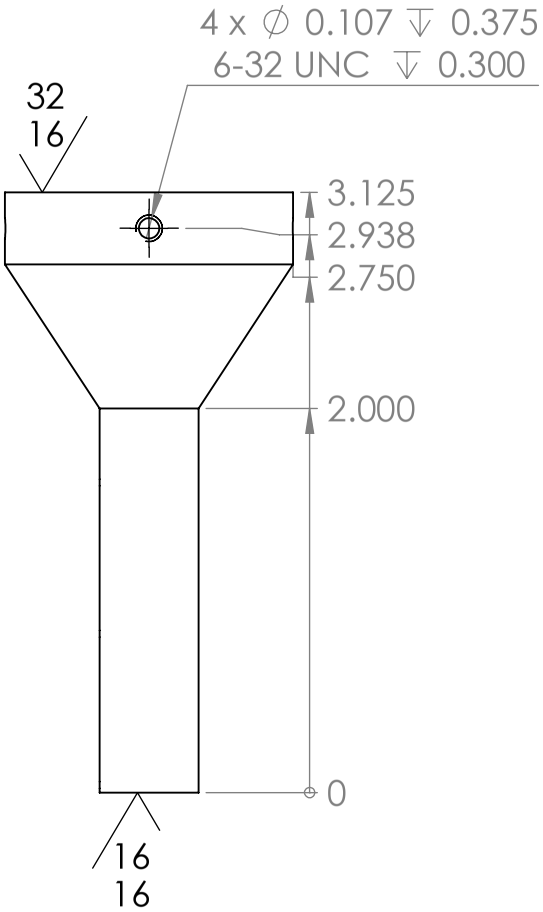

SPACING BETWEEN THERMOCOUPLE MOUNTING HOLES IS CRITICAL AS IT IS USED TO DETERMINE THE HEATFLUX THROUGH THE BAR.

DATE: 12/01/16			
TITLE: UPPER METER BAR v15			
Collier Miers			
MATERIAL: MOLYBDENUM	SIZE A	DWG. NO.	QTY: 1
FINISH: POLISHED	SCALE: 1:1		SHEET 1 OF 2

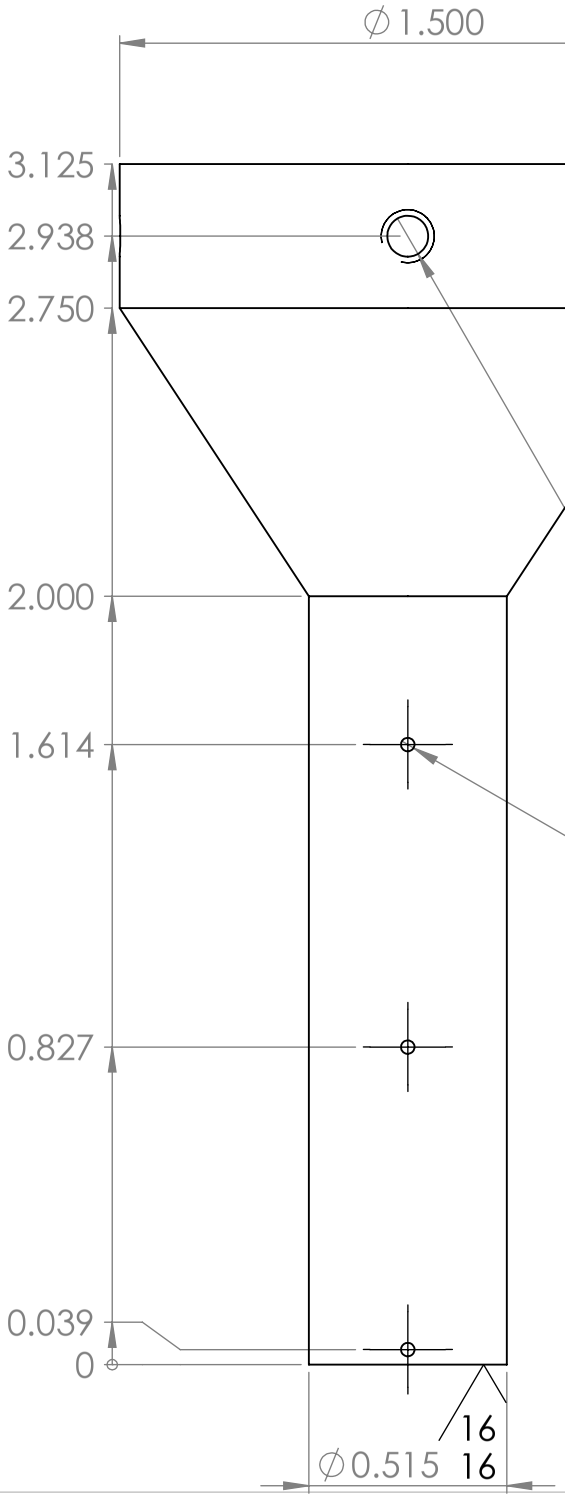

SURFACE ROUGHNESSES ARE GIVEN IN MICROINCHES.

SIDE SURFACES SHOULD BE POLISHED TO A BRIGHT FINISH TO REDUCE THE EMISSIVITY, BUT A SPECIFIC SURFACE ROUGHNESS IS NOT SPECIFIED.

SPACING BETWEEN THERMOCOUPLE MOUNTING HOLES IS CRITICAL AS IT IS USED TO DETERMINE THE HEATFLUX THROUGH THE BAR.

DATE: 12/01/16			
TITLE: UPPER METER BAR v15			
Collier Miers			
MATERIAL: MOLYBDENUM	SIZE A	DWG. NO.	QTY: 1
FINISH: POLISHED	SCALE: 2:1		SHEET 2 OF 2

SURFACE ROUGHNESSES ARE GIVEN IN MICROINCHES.

SIDE SURFACES SHOULD BE POLISHED TO A BRIGHT FINISH TO REDUCE THE EMISSIVITY, BUT A SPECIFIC SURFACE ROUGHNESS IS NOT SPECIFIED.

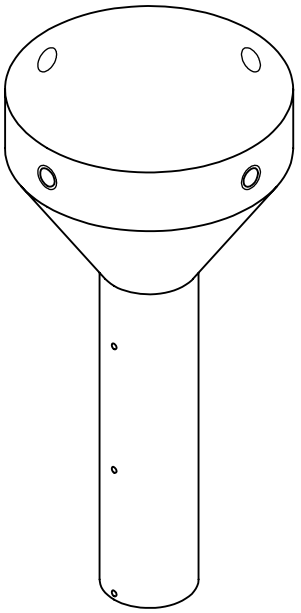

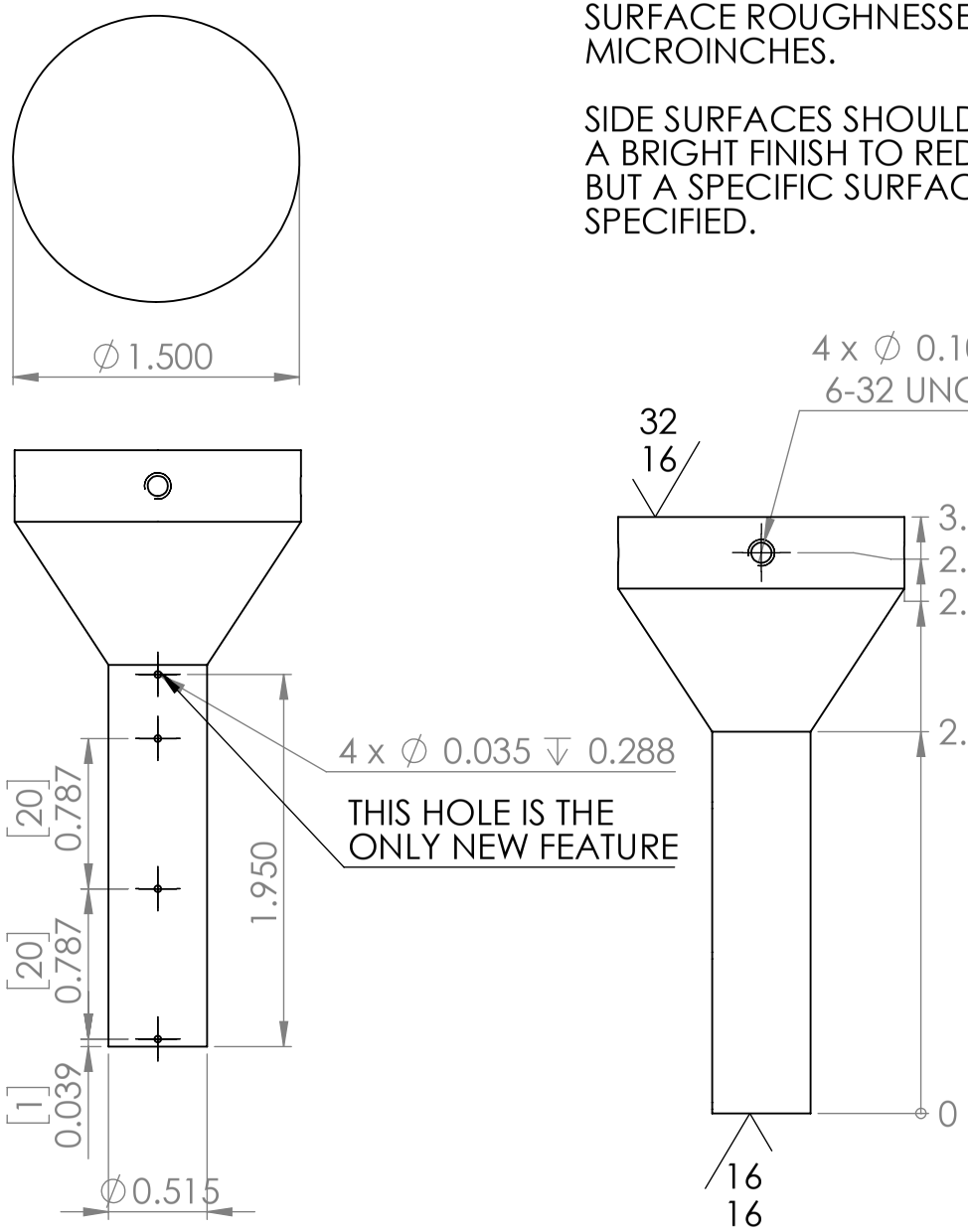

SPACING BETWEEN THERMOCOUPLE MOUNTING HOLES IS CRITICAL AS IT IS USED TO DETERMINE THE HEATFLUX THROUGH THE BAR.

DATE: 12/01/16			
TITLE: UPPER METER BAR v16			
Collier Miers			
MATERIAL: MOLYBDENUM	SIZE A	DWG. NO.	QTY: 1
FINISH: POLISHED	SCALE: 1:1		SHEET 1 OF 1

SPACING BETWEEN THERMOCOUPLE MOUNTING HOLES IS CRITICAL AS IT IS USED TO DETERMINE THE HEATFLUX THROUGH THE BAR.

SURFACE ROUGHNESSES ARE GIVEN IN MICROINCHES.

SIDE SURFACES SHOULD BE POLISHED TO A BRIGHT FINISH TO REDUCE THE EMISSIVITY, BUT A SPECIFIC SURFACE ROUGHNESS IS NOT SPECIFIED.

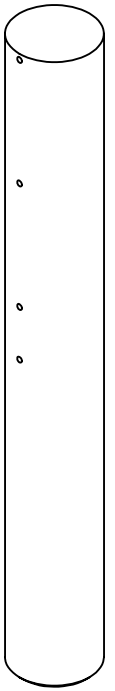

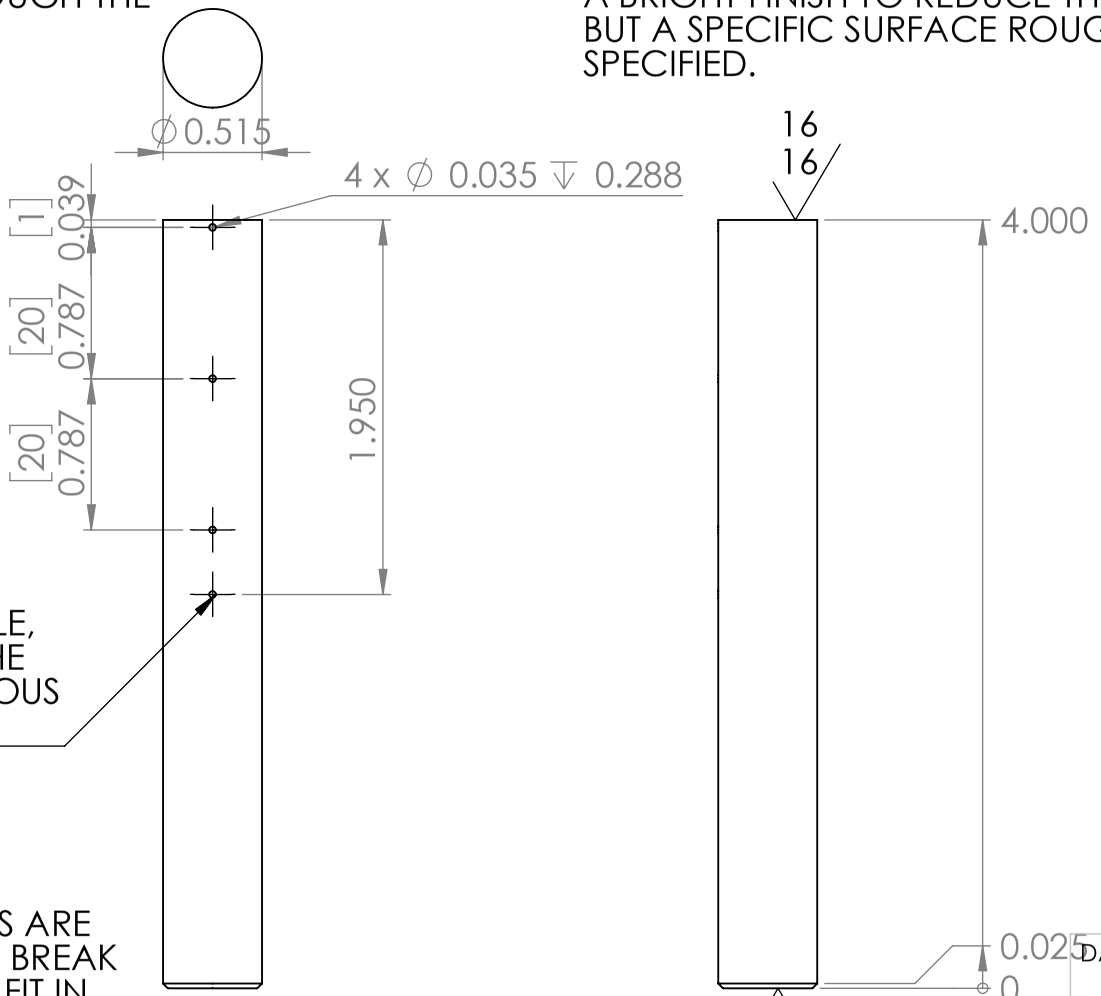

THIS IS THE NEW HOLE, DIMENSIONS ARE THE SAME AS THE PREVIOUS HOLES.

BOTTOM CHAMFERS ARE NOT CRITICAL, JUST BREAK EDGES FOR GOOD FIT IN COPPER HOLDER.

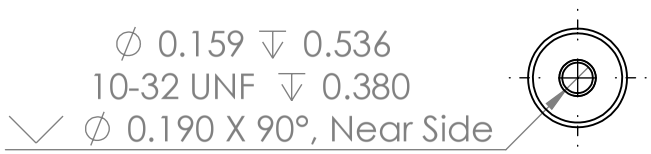

DATE: 12/01/16			
TITLE: LOWER METER BAR			
Collier Miers			
MATERIAL: MOLYBDENUM	SIZE A	DWG. NO.	QTY: 1
FINISH: POLISHED	SCALE: 1:1		SHEET 1 OF 2

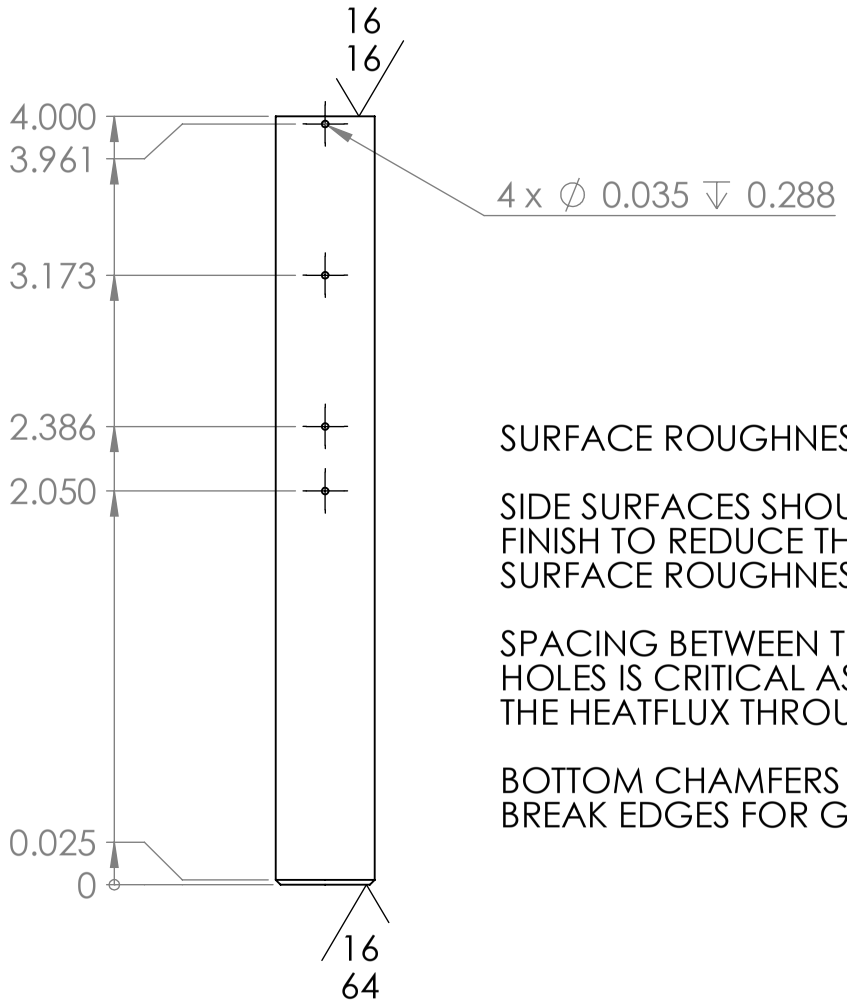

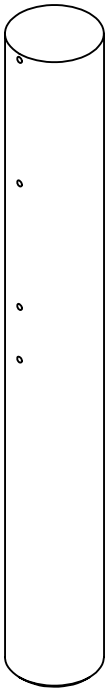

SURFACE ROUGHNESSES ARE GIVEN IN MICROINCHES.

SIDE SURFACES SHOULD BE POLISHED TO A BRIGHT FINISH TO REDUCE THE EMISSIVITY, BUT A SPECIFIC SURFACE ROUGHNESS IS NOT SPECIFIED.

SPACING BETWEEN THERMOCOUPLE MOUNTING HOLES IS CRITICAL AS IT IS USED TO DETERMINE THE HEATFLUX THROUGH THE BAR. SEE SHEET 1.

BOTTOM CHAMFERS ARE NOT CRITICAL, JUST BREAK EDGES FOR GOOD FIT IN COPPER HOLDER.

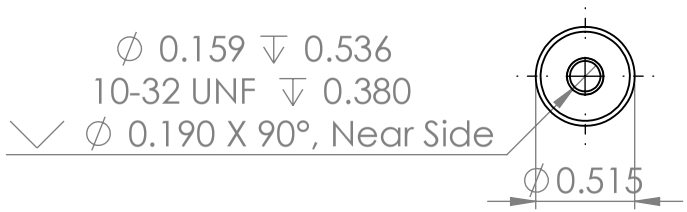

DATE: 12/01/16			
TITLE: LOWER METER BAR			
Collier Miers			
MATERIAL: MOLYBDENUM	SIZE A	DWG. NO.	QTY: 1
FINISH: POLISHED	SCALE: 1:1		SHEET 2 OF 2

<MOD-DIAM>0.515<HOLE-DEPTH>2.000

THIS HOLE IS FOR THE LOWER MOLYBDENUM METER BAR, WHICH HAS A DIAMETER OF 0.515 IN, SO THE CLEARANCE ON THIS HOLE SHOULD BE JUST OVER THAT TO ALLOW A CLOSE FIT DURING ASSEMBLY.

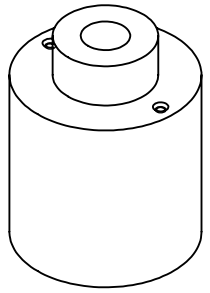

2 x <MOD-DIAM> 0.089 <HOLE-DEPTH> 0.349
4-40 UNC <HOLE-DEPTH> 0.224
<HOLE-SINK><MOD-DIAM> 0.162 X 90°, Near Side

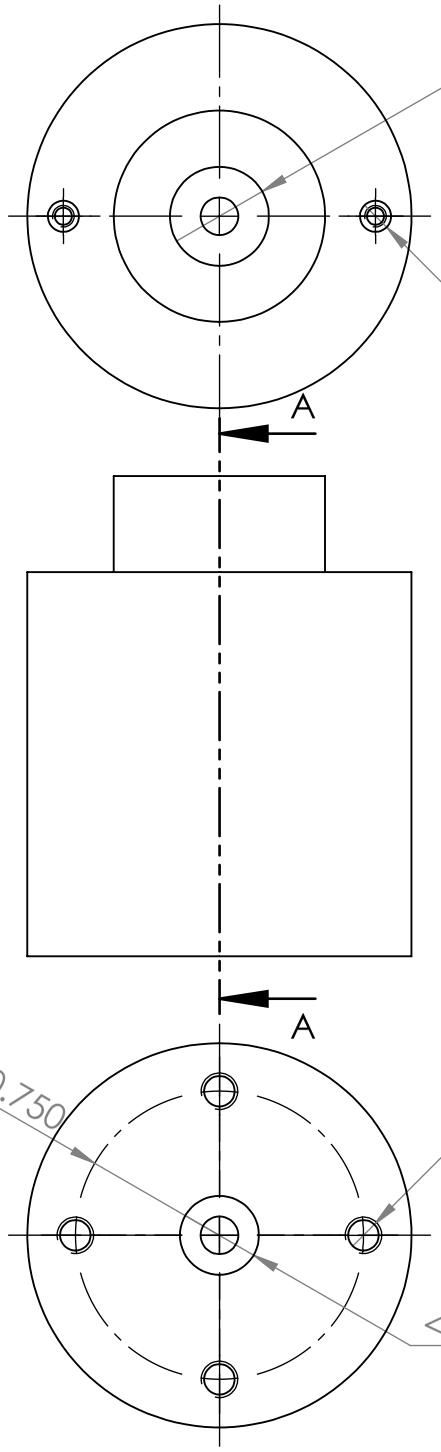

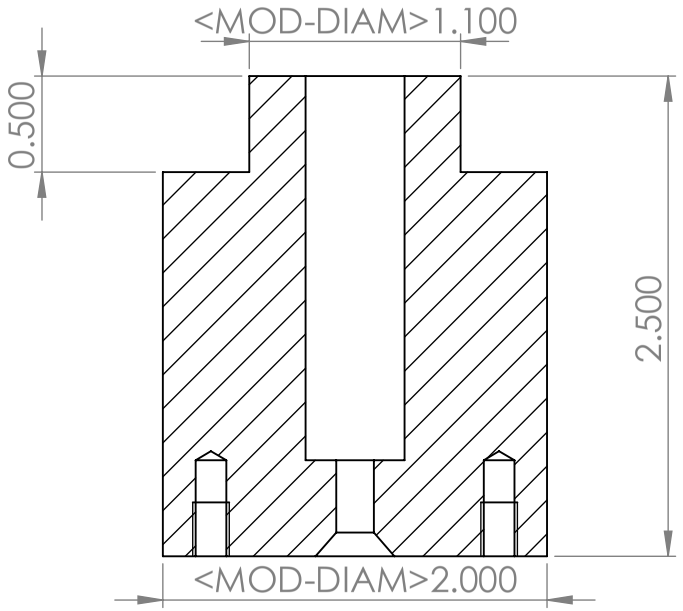

SECTION A-A

4 x <MOD-DIAM> 0.159 <HOLE-DEPTH> 0.500
10-32 UNF <HOLE-DEPTH> 0.280

<MOD-DIAM> 0.196 THRU ALL
<HOLE-SINK><MOD-DIAM> 0.411 X 82°

	DATE: 03/15/17		
	TITLE: COPPER BAR MOUNT v3		
Collier Miers			
MATERIAL: C101 Copper	SIZE A	DWG. NO.	QTY: 1
FINISH: POLISHED	SCALE: 1:1		SHEET 1 OF 1

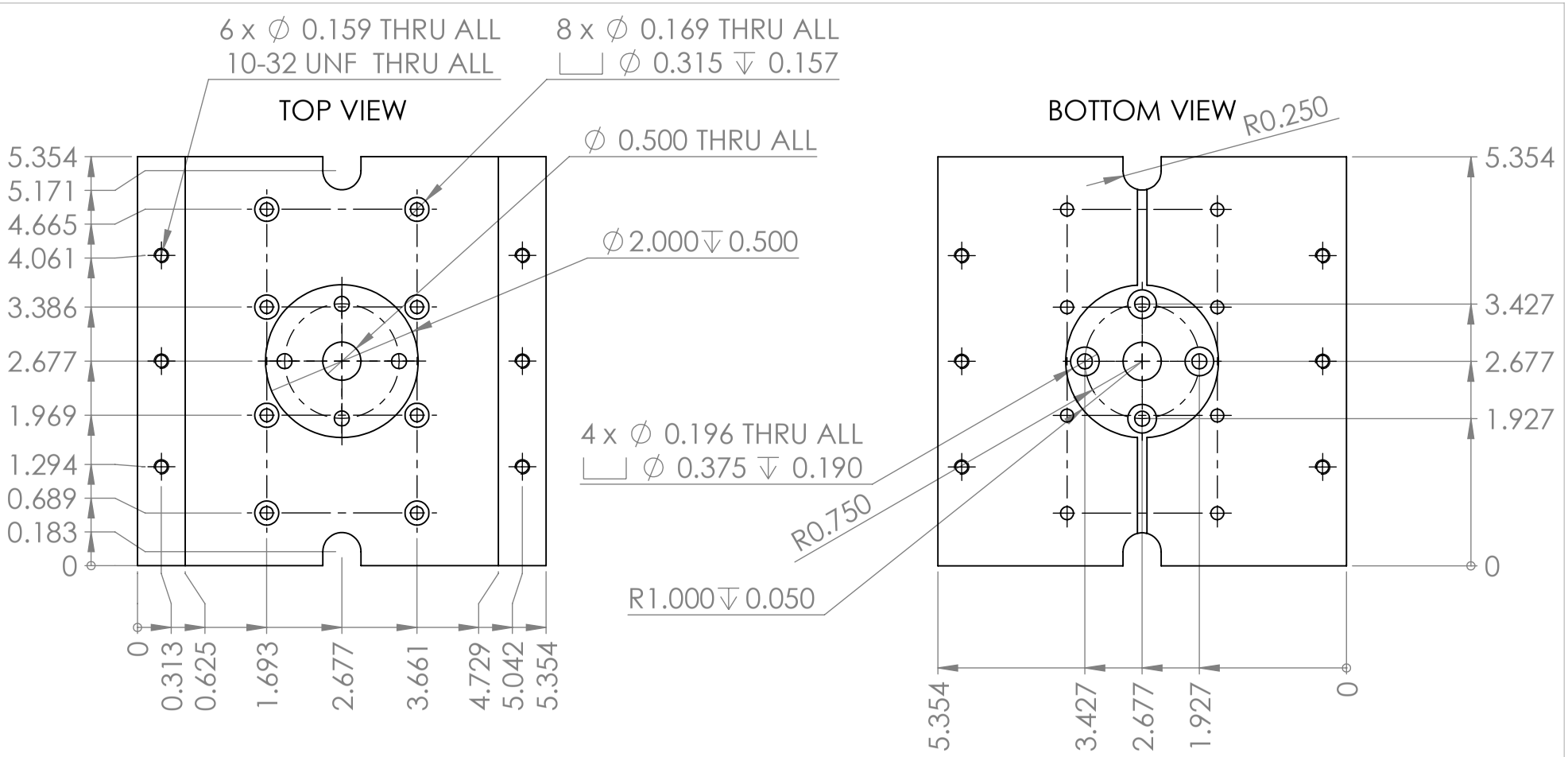

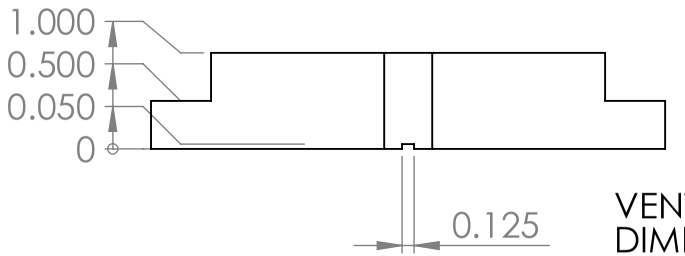

VENTING CHANNEL DIMENSION IS NOT CRITICAL.

DATE: 02/14/17			
TITLE: COPPER BASE PLATE_v2			
Collier Miers			
MATERIAL: C101 Copper	SIZE A	DWG. NO.	QTY: 1
FINISH:	SCALE: 1:2		SHEET 1 OF 1

NOTE: IF THIS SURFACE PROVES TO BE TOO THIN, PLEASE LET ME KNOW. IT IS NOT CRITICAL TO THE STRUCTURE AND CAN LIKELY BE REMOVED.

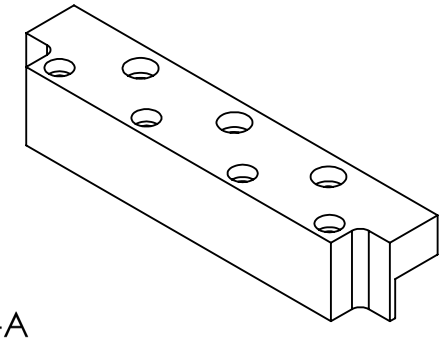

SECTION B-B

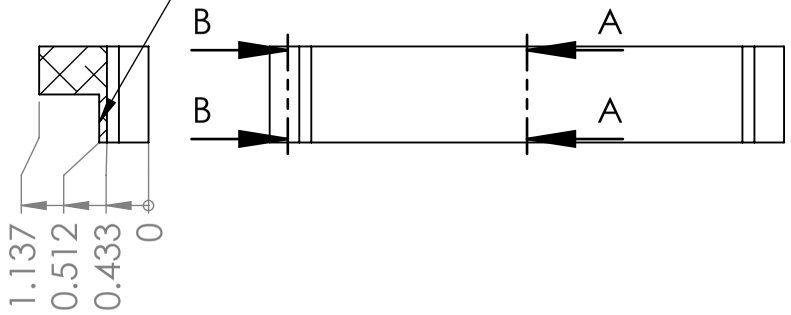

SECTION A-A

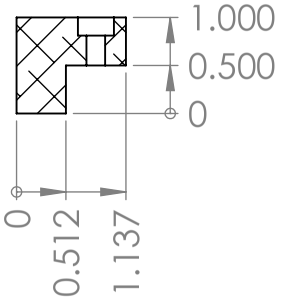

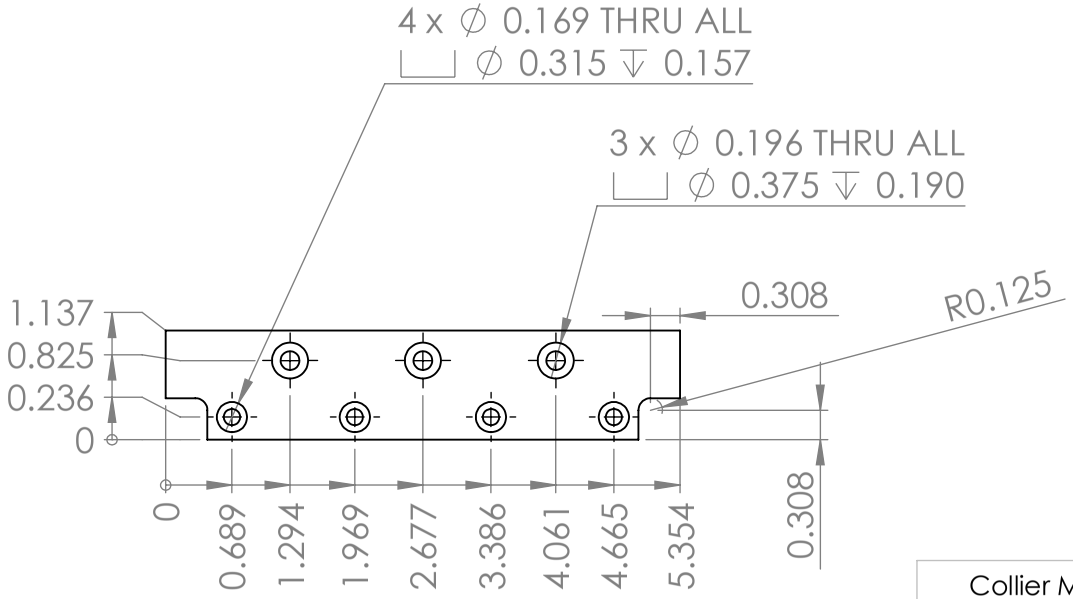

	DATE: 02/14/17		
	TITLE: MOUNTING BARS FOR BASE		
Collier Miers			
MATERIAL: 6061 Al	SIZE A	DWG. NO.	QTY: 2
FINISH:	SCALE: 1:2		SHEET 1 OF 1

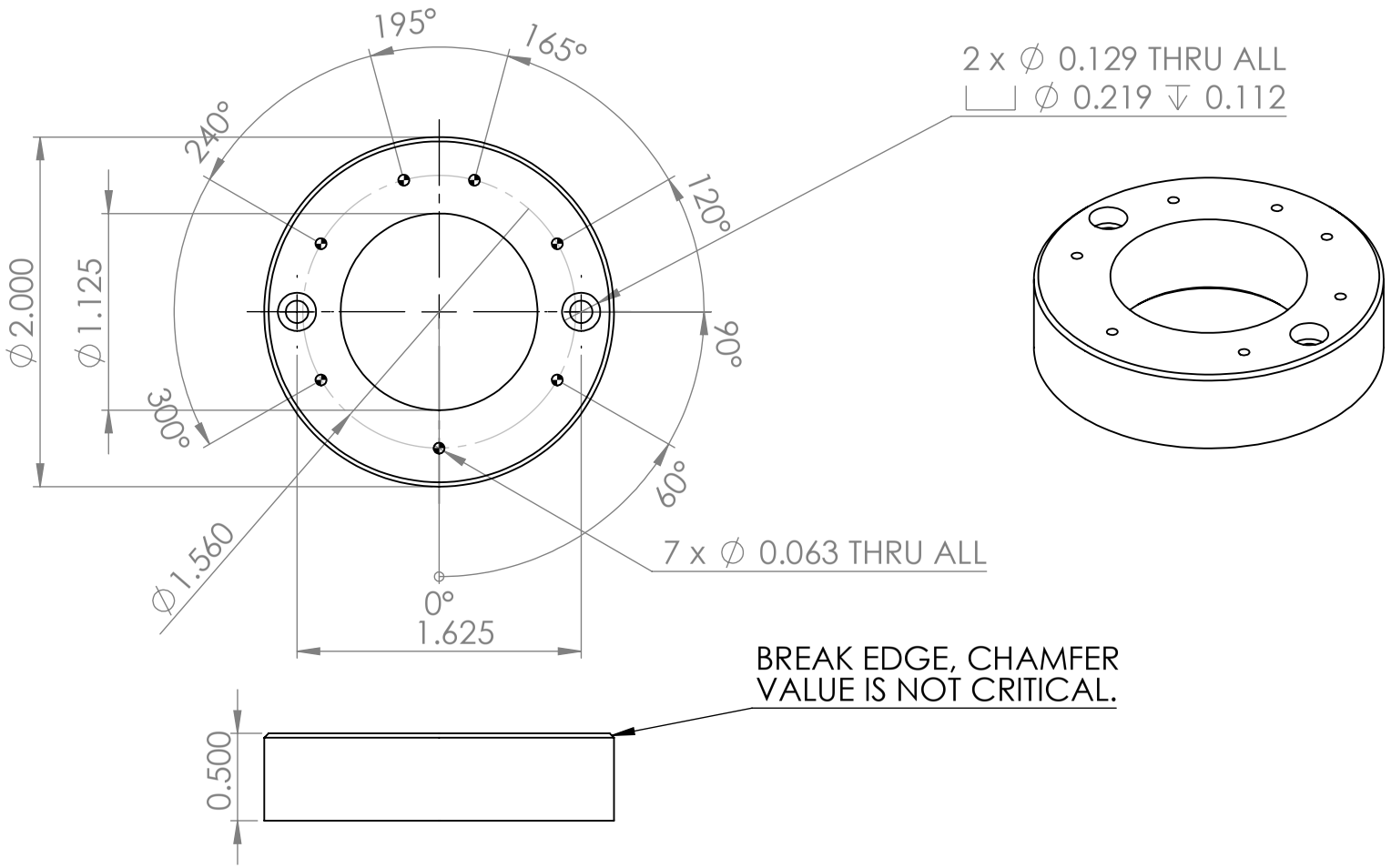

DATE: 03/15/17		
TITLE: LOWER SHIELD BANK MOUNTING COLLAR		
Collier Miers		
MATERIAL: ALUMINA FINISH: SILICATE	SIZE: A	DWG. NO.
	QTY: 1	
SCALE: 1:1	SHEET 1 OF 1	

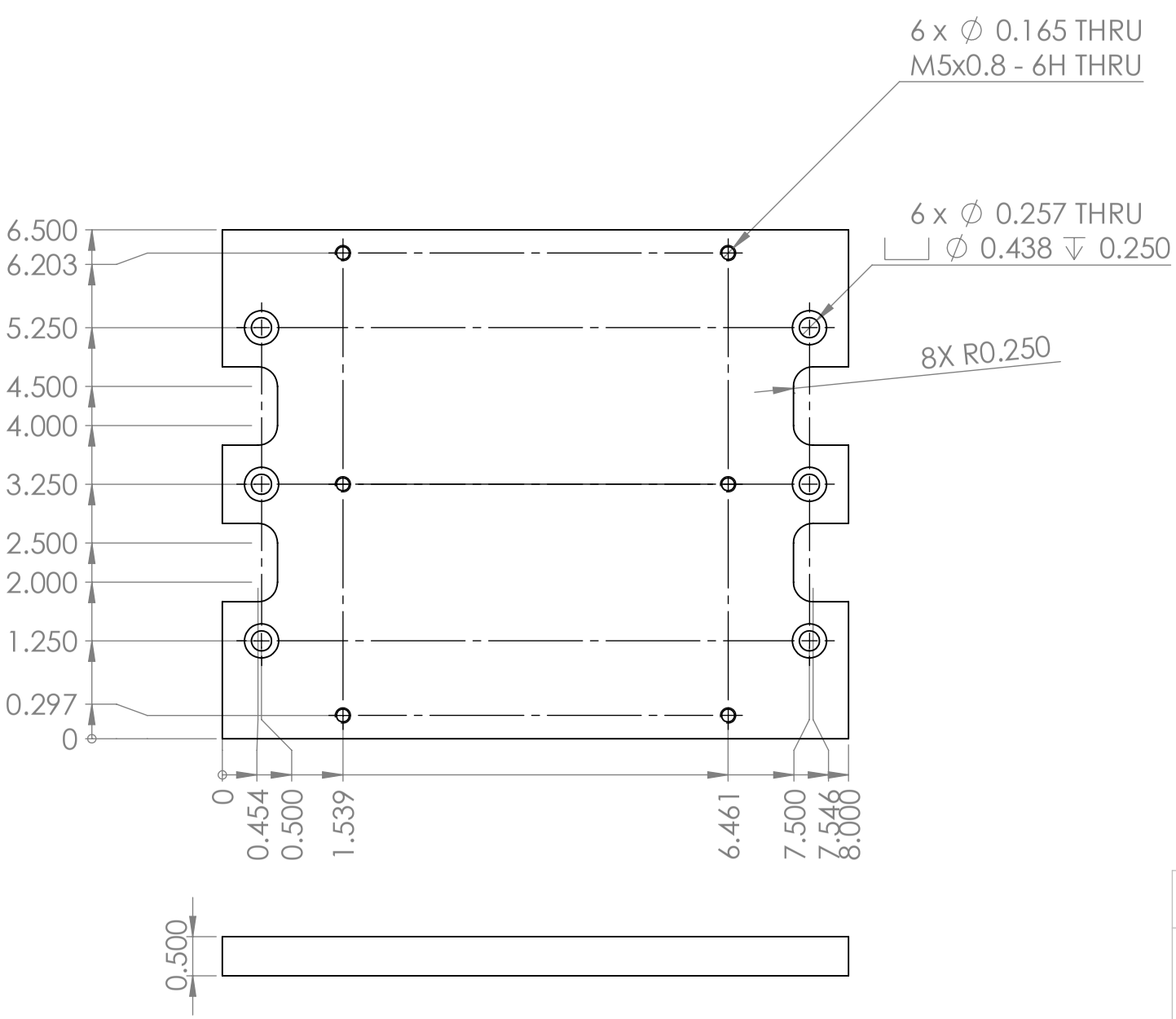

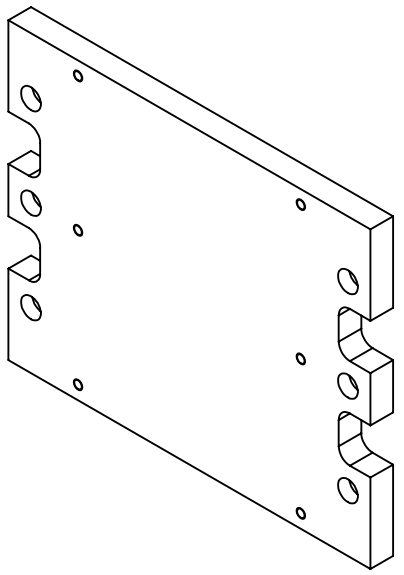

DATE: 12/01/16			
TITLE: LABJACK-TO-COLDPLATE ADAPTOR			
Collier Miers			
MATERIAL: ULTEM 1000	SIZE A	DWG. NO.	QTY: 1
FINISH:	SCALE: 1:2		SHEET 1 OF 1

Cold Junction

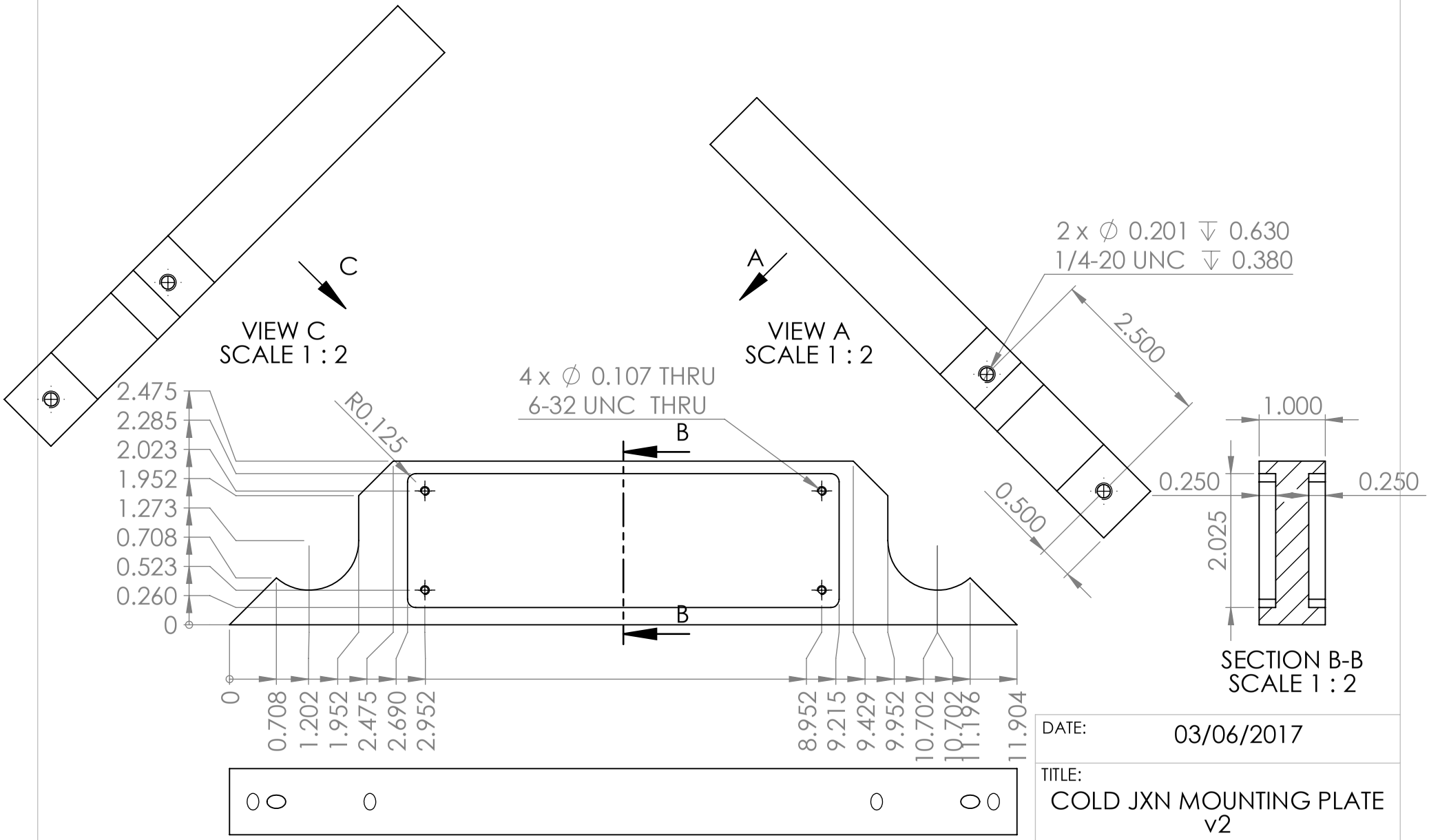

DATE:	03/06/2017
TITLE:	COLD JXN MOUNTING PLATE v2
Collier Miers	
MATERIAL:	6061 Al
FINISH:	
SIZE	A
DWG. NO.	
QTY:	1
SCALE:	1:2
SHEET 1 OF 1	

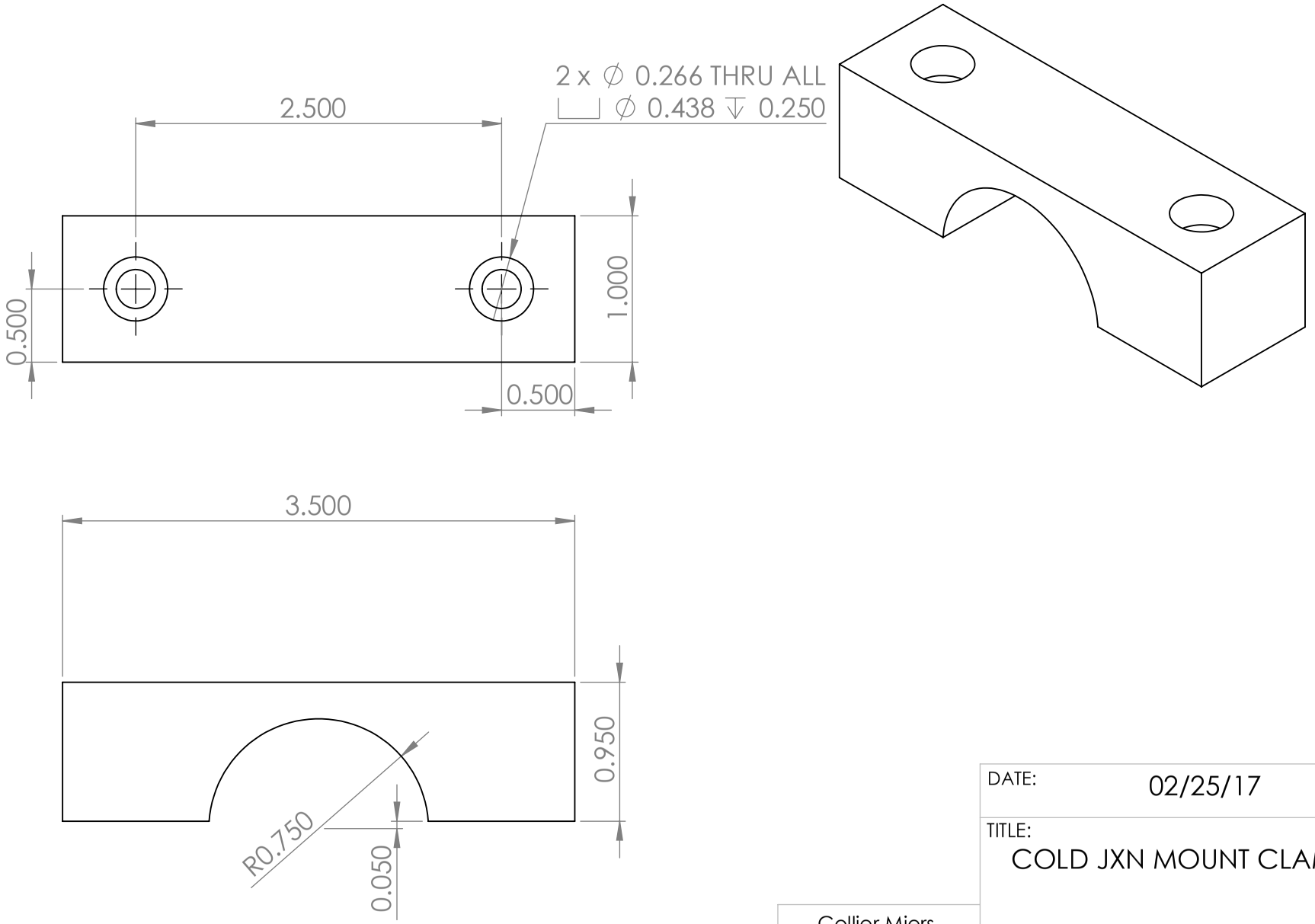

DATE: 02/25/17			
TITLE: COLD JXN MOUNT CLAMP			
Collier Miers			
MATERIAL: 6061 Al	SIZE A	DWG. NO.	QTY: 2
FINISH:	SCALE: 1:1		SHEET 1 OF 1

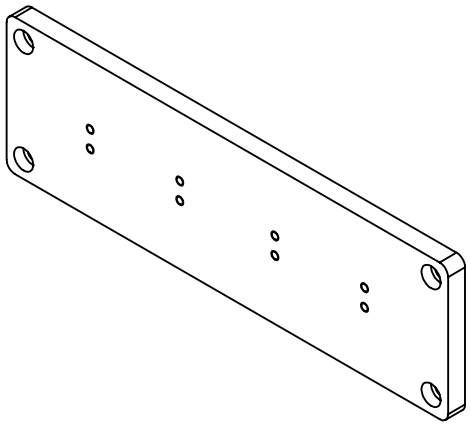

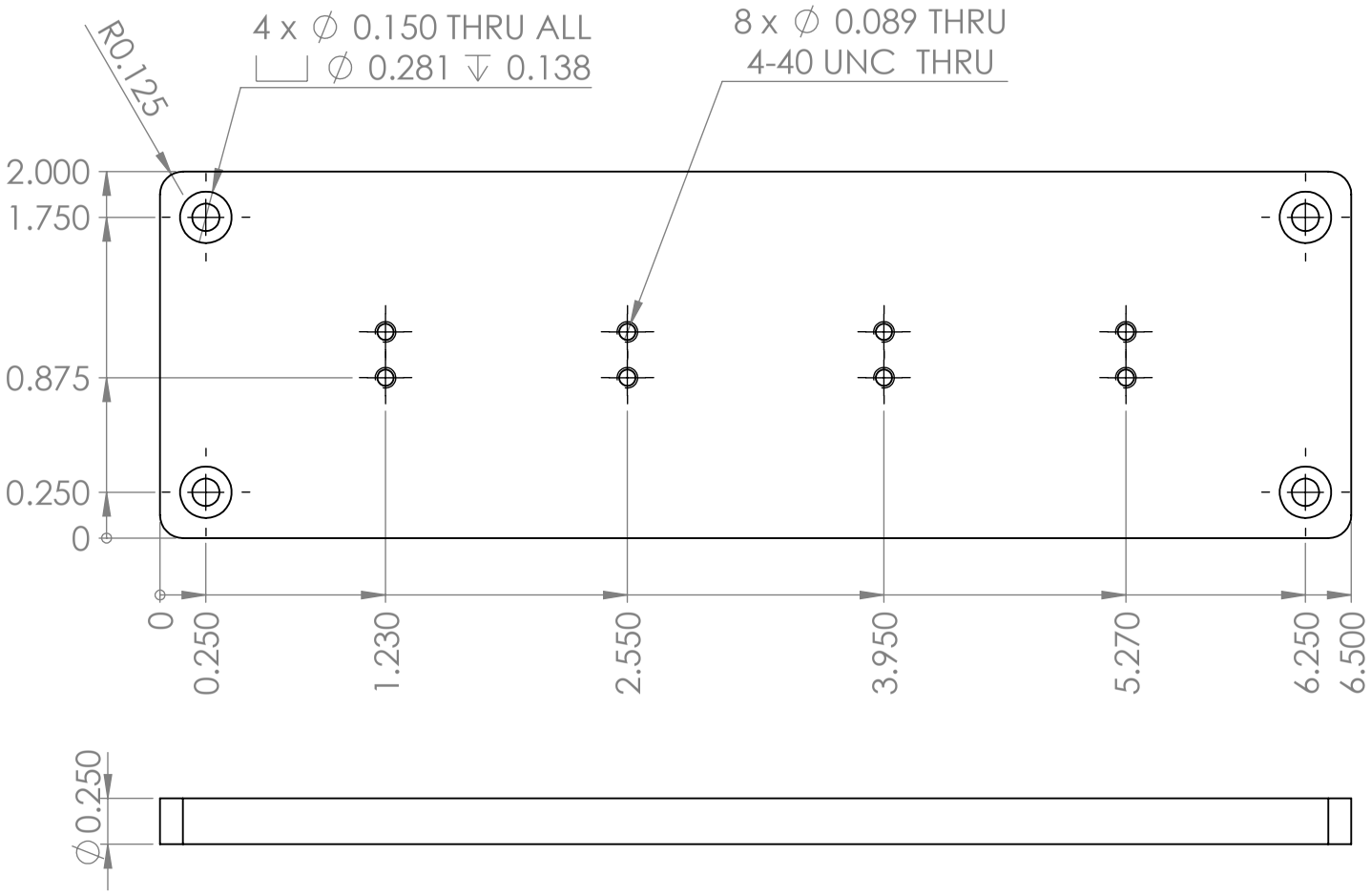

DATE: 02/25/17			
TITLE: COLD JXN HEAT SPREADER			
Collier Miers			
MATERIAL: COPPER	SIZE A	DWG. NO.	QTY: 2
FINISH:	SCALE: 1:1		SHEET 1 OF 1

Heat Shields

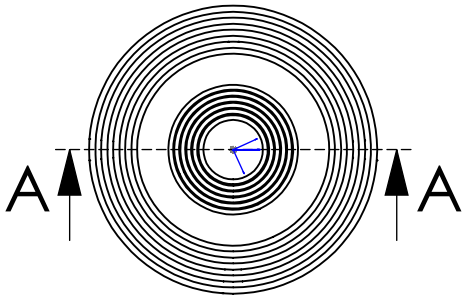

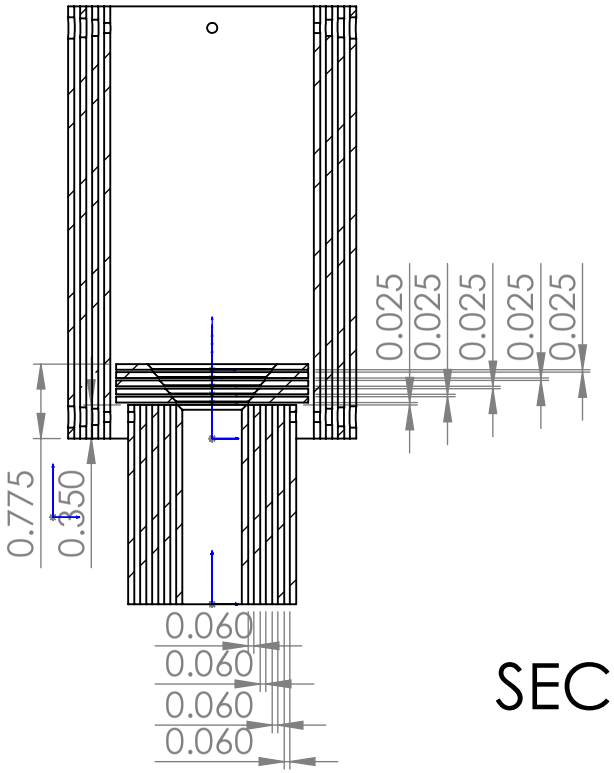

SECTION A-A

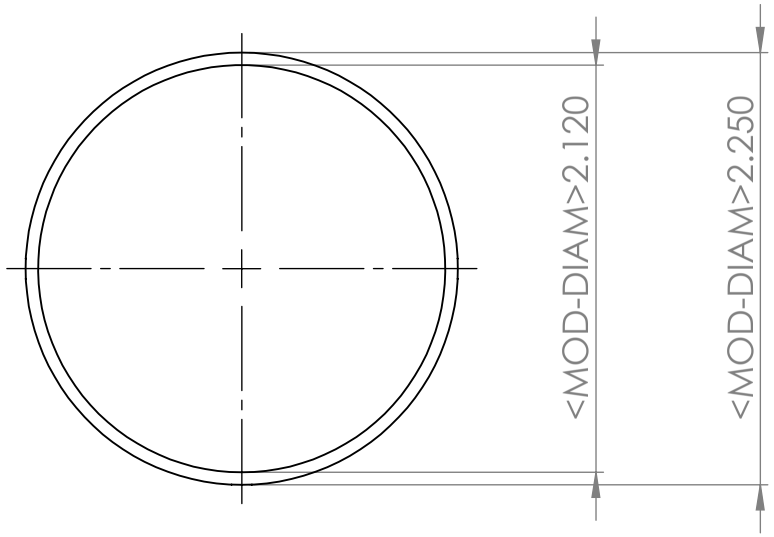

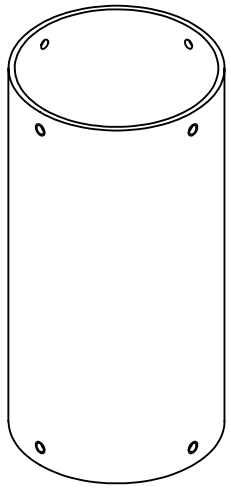

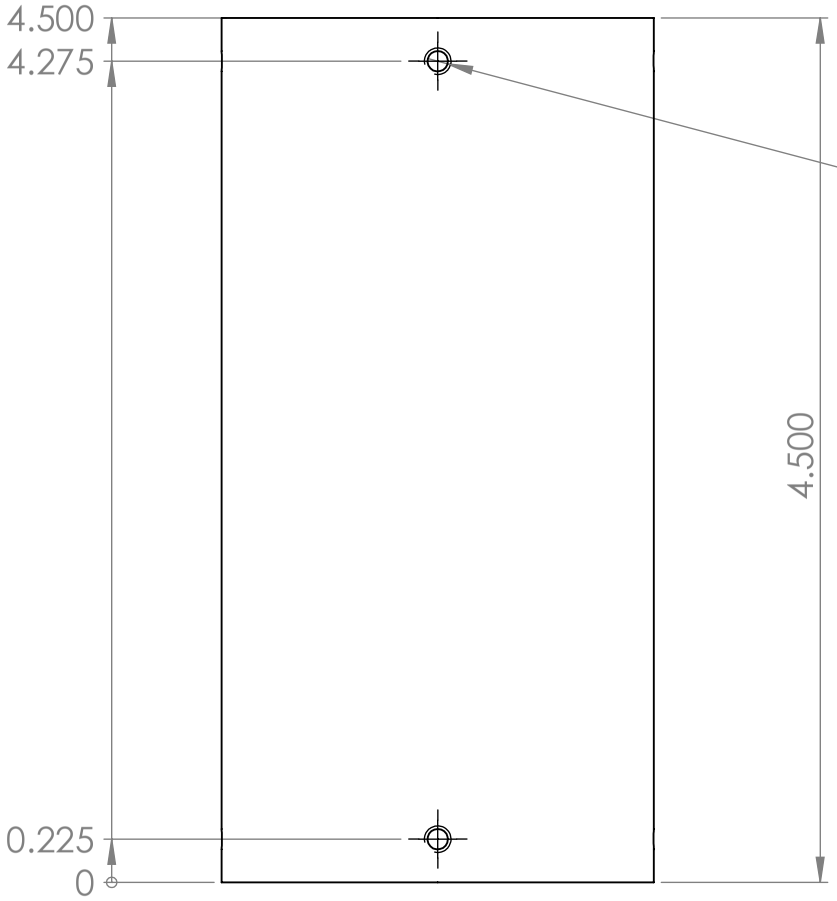

8x <MOD-DIAM> 0.107 THRU ALL
6-32 UNC THRU ALL

DATE: 03/15/17			
TITLE: HEAT SHIELD 1.1			
Collier Miers			
MATERIAL: 304 SS	SIZE A	DWG. NO.	QTY: 1
FINISH: POLISHED	SCALE: 1:1		SHEET 1 OF 1

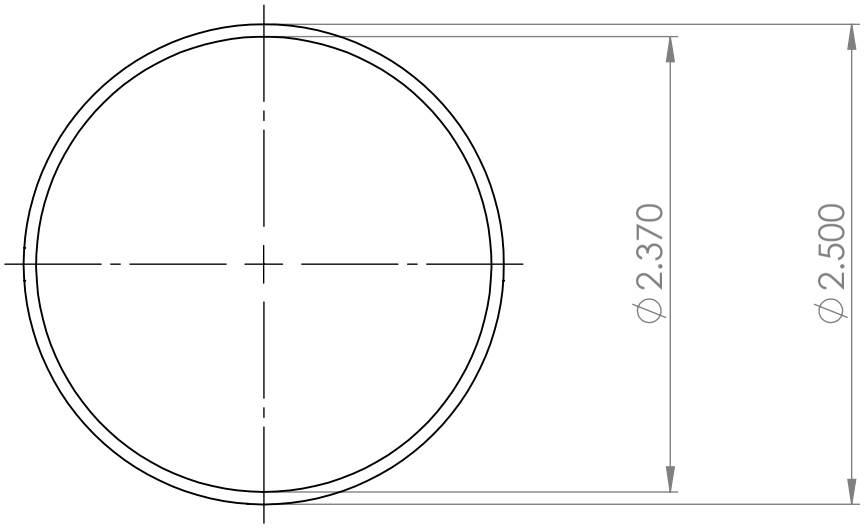

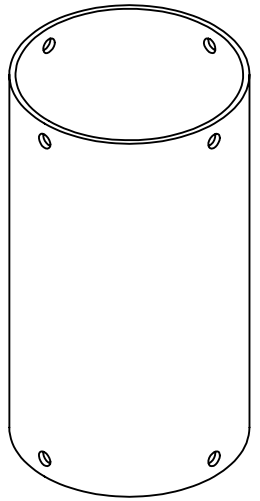

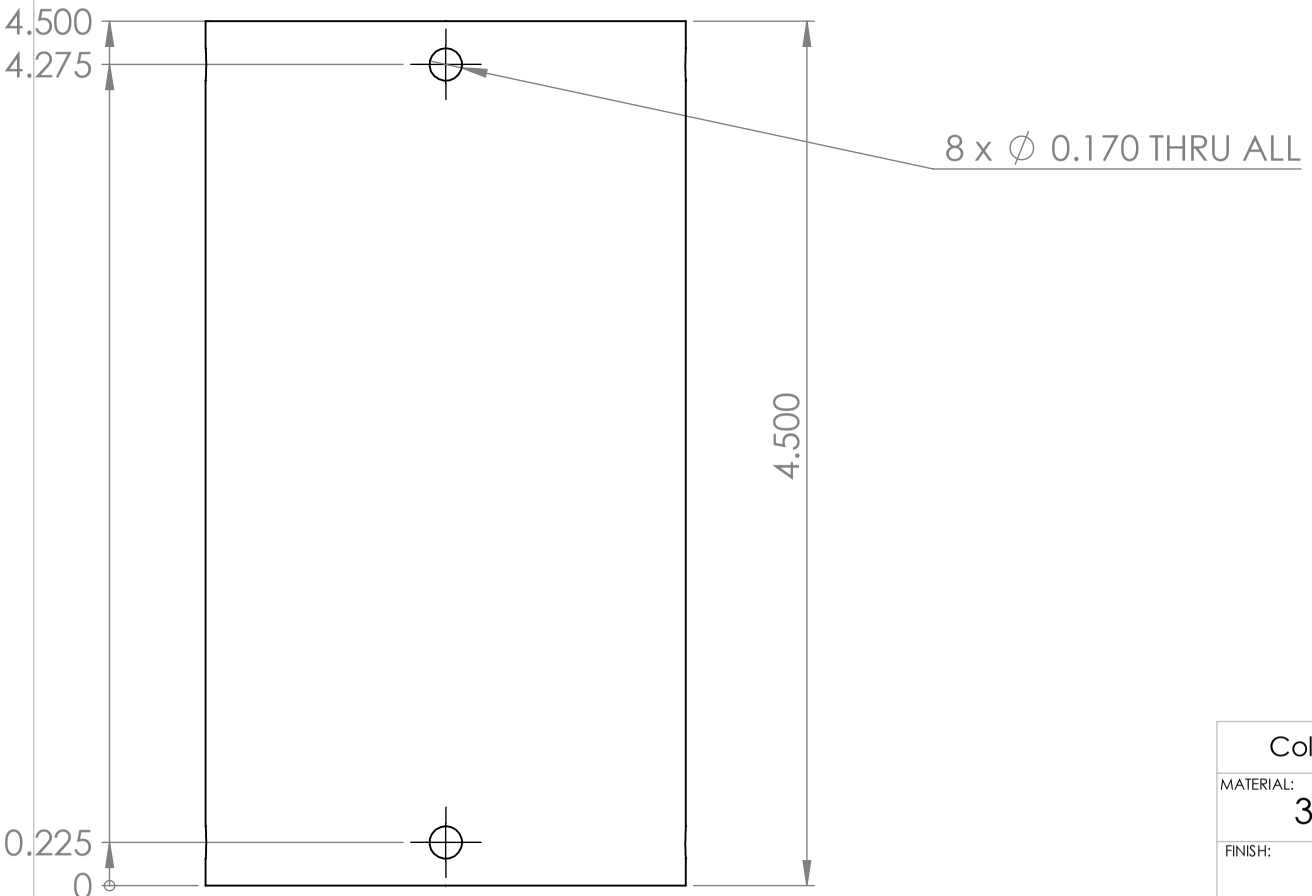

DATE: 03/15/17			
TITLE: HEAT SHIELD 1.2			
Collier Miers			
MATERIAL: 304 SS	SIZE A	DWG. NO.	QTY: 1
FINISH:	SCALE: 1:1		SHEET 1 OF 1

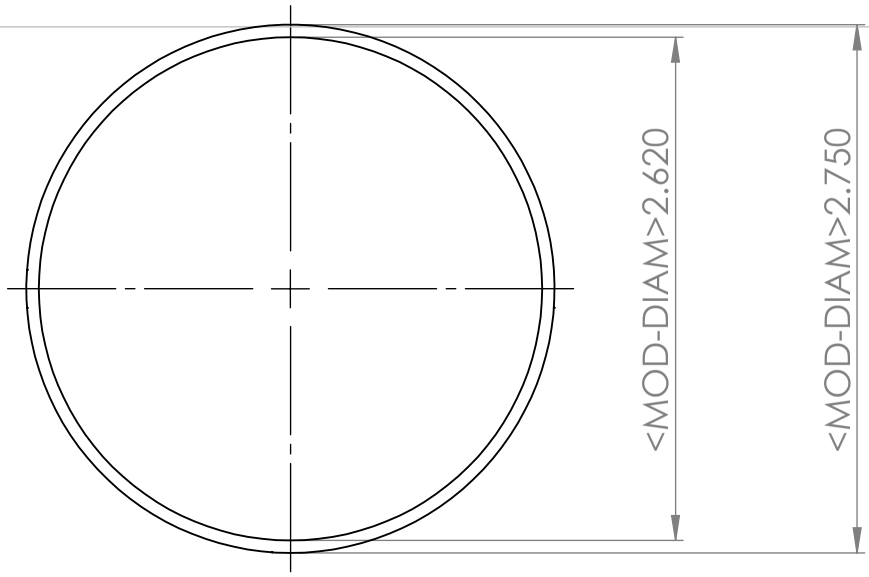

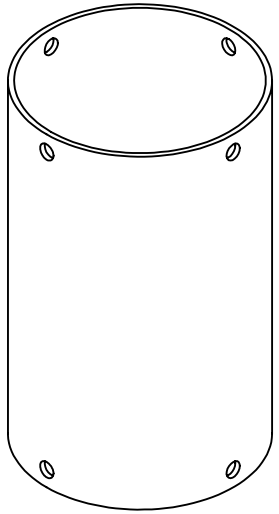

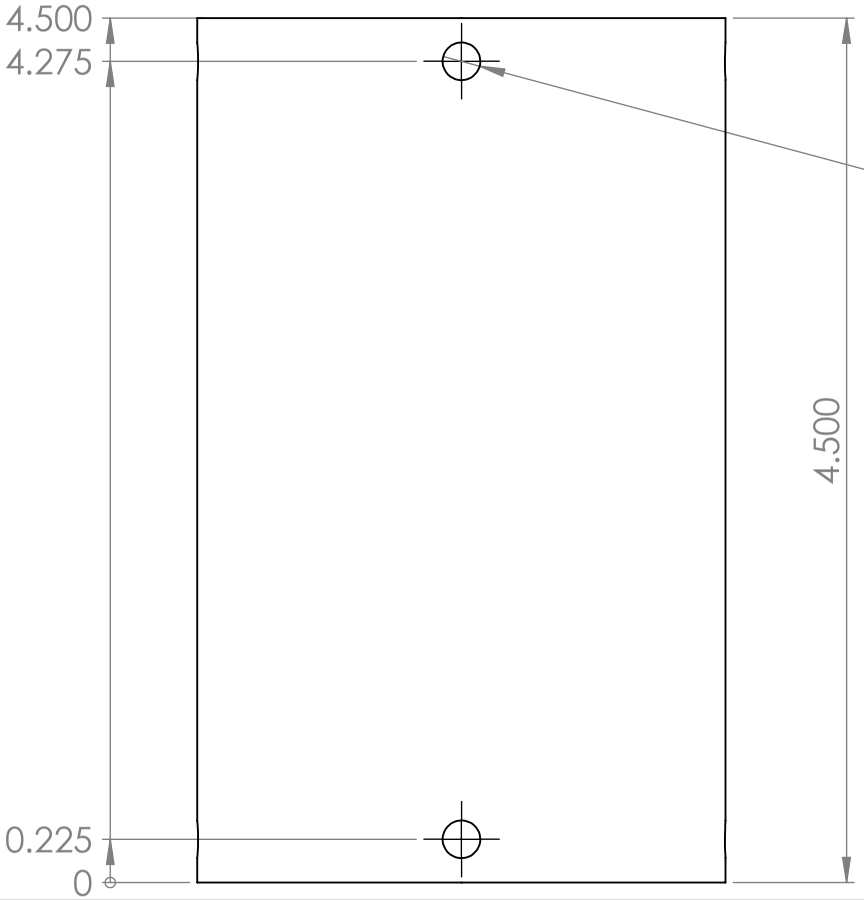

DATE: 03/15/17			
TITLE: HEAT SHIELD 1.3			
Collier Miers			
MATERIAL: 304 SS	SIZE A	DWG. NO.	QTY: 1
FINISH: POLISHED	SCALE: 1:1		SHEET 1 OF 1

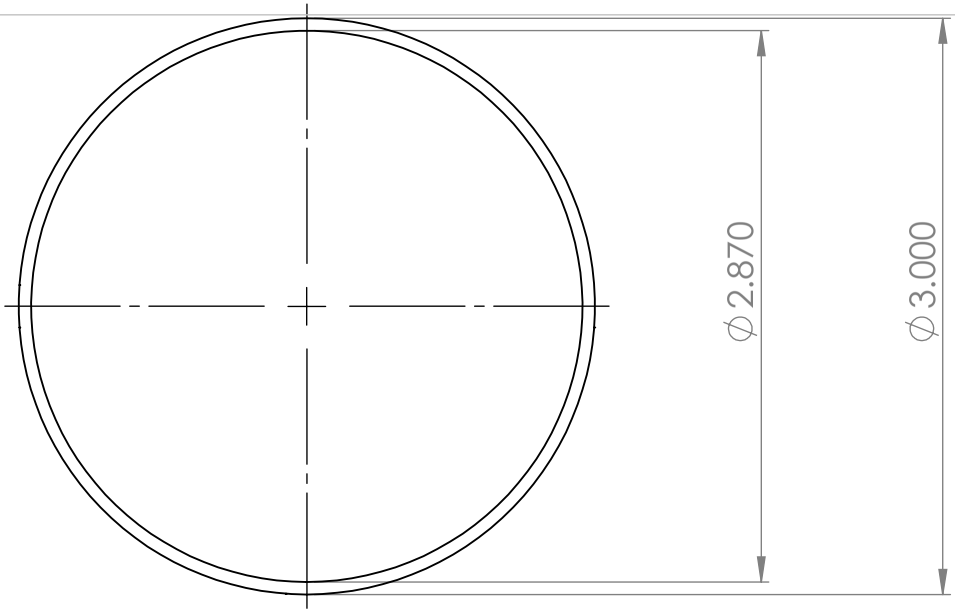

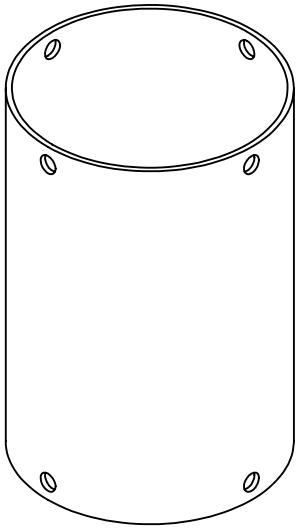

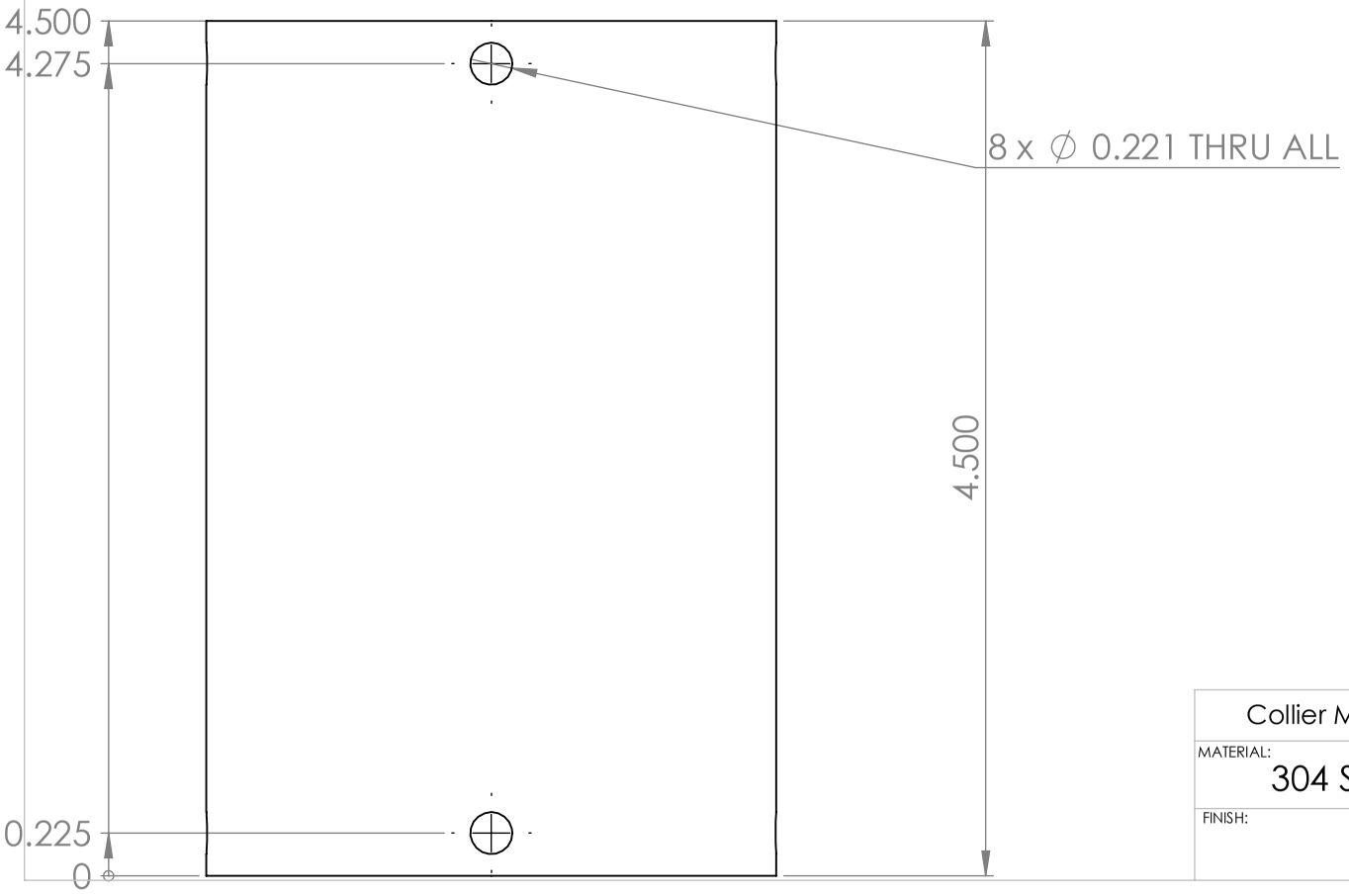

Collier Miers	DATE: 03/15/17		
	TITLE: HEAT SHIELD 1.4		
MATERIAL: 304 SS	SIZE A	DWG. NO.	QTY: 1
FINISH:	SCALE: 1:1		SHEET 1 OF 1

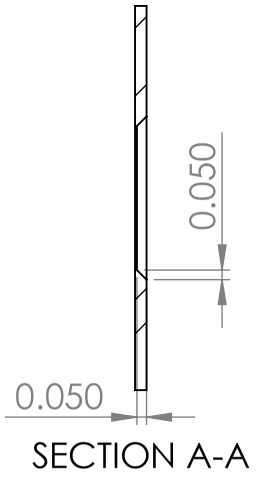

SECTION A-A

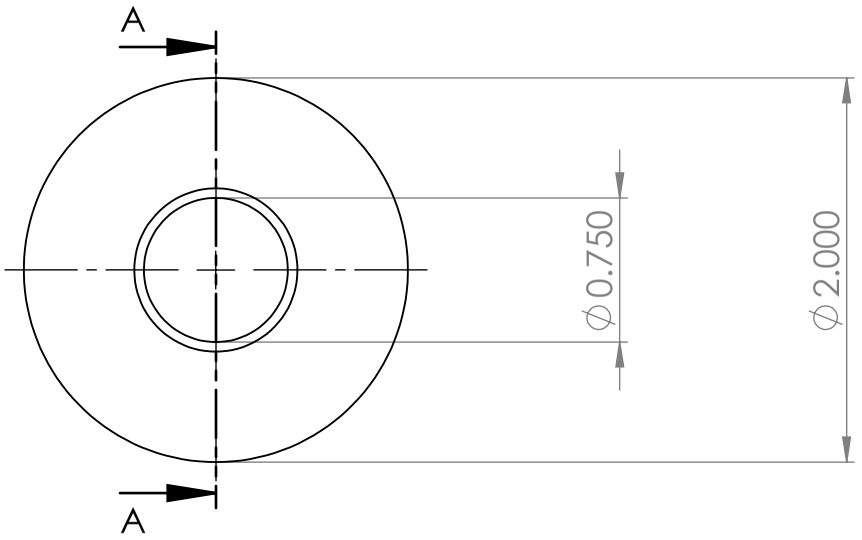

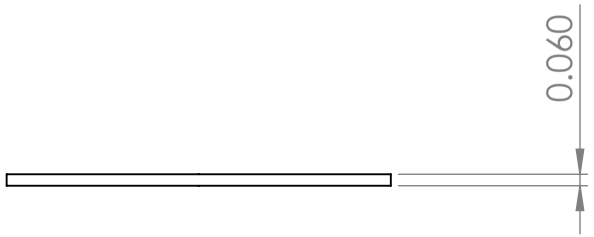

DATE: 03/15/17			
TITLE: HEAT SHIELD 2.1			
Collier Miers			
MATERIAL: 304 SS	SIZE A	DWG. NO.	QTY: 1
FINISH: POLISHED	SCALE: 1:1		SHEET 1 OF 1

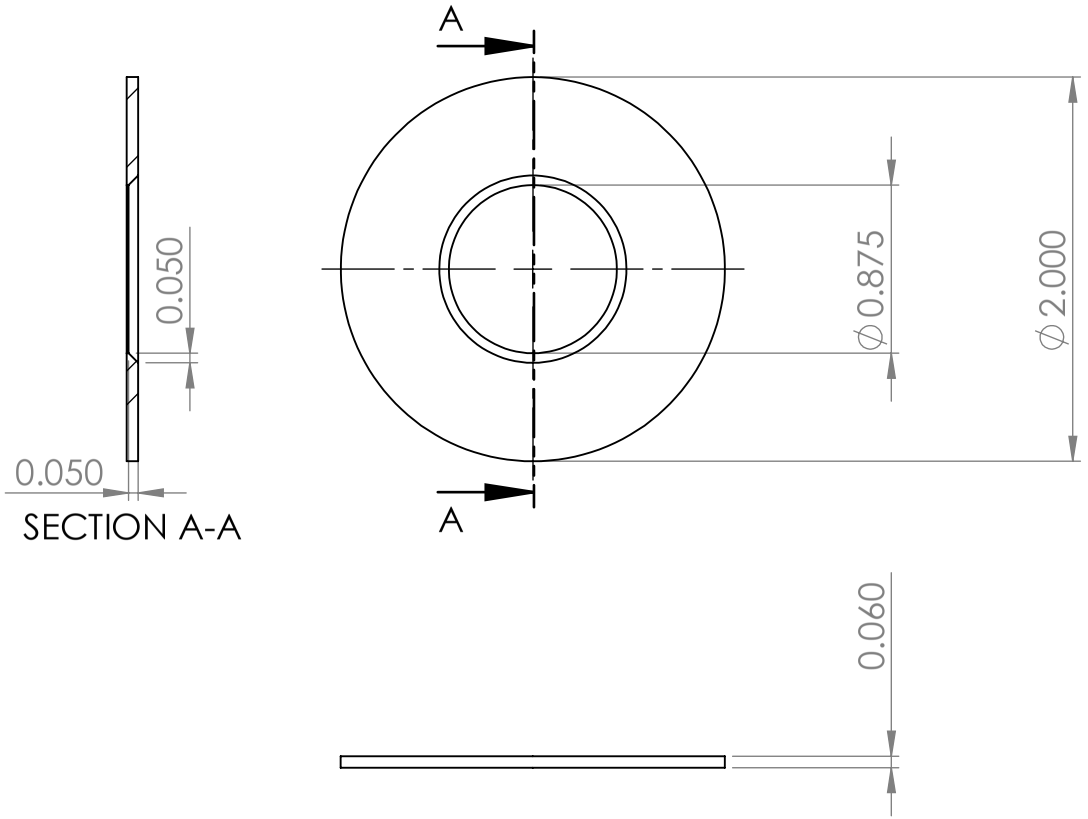

DATE: 03/15/17			
TITLE: HEAT SHIELD 2.2			
Collier Miers			
MATERIAL: 304 SS	SIZE A	DWG. NO.	QTY: 1
FINISH: POLISHED	SCALE: 1:1		SHEET 1 OF 1

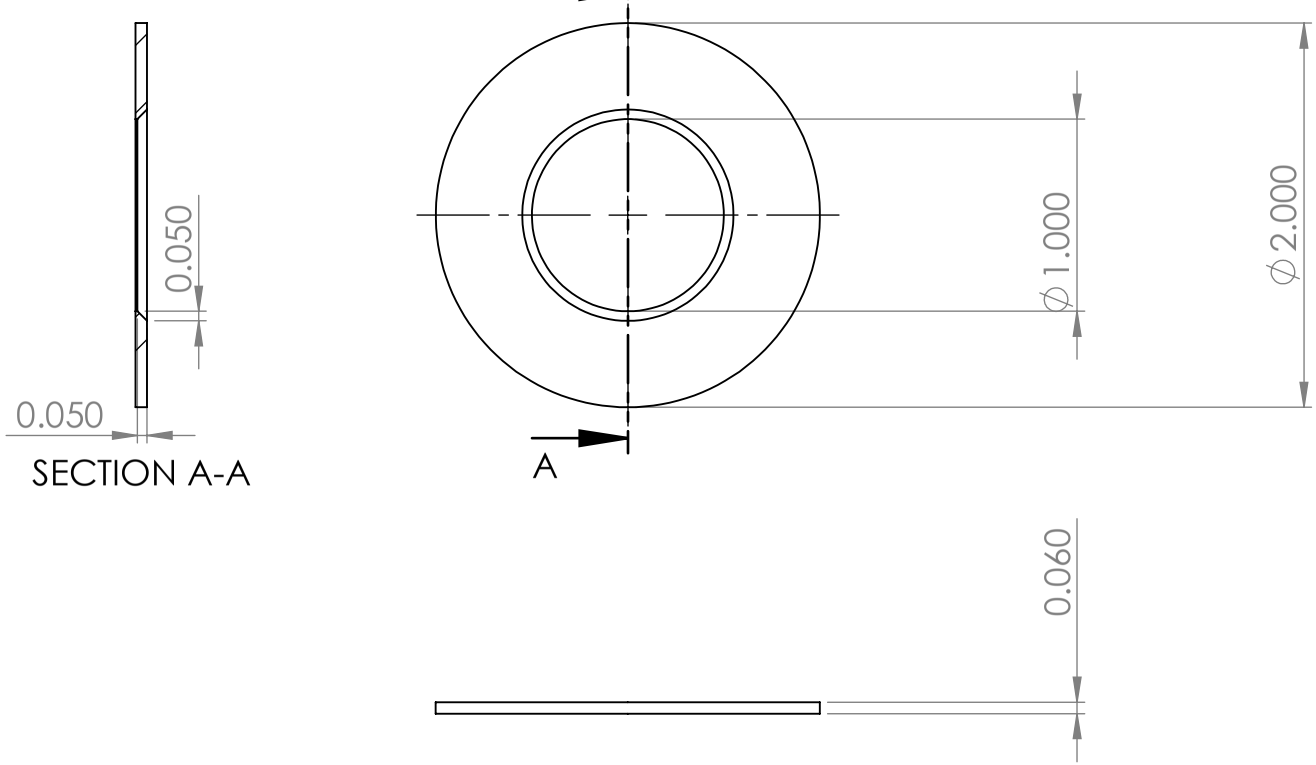

DATE: 03/15/17			
TITLE: HEAT SHIELD 2.3			
Collier Miers			
MATERIAL: 304 SS	SIZE A	DWG. NO.	QTY: 1
FINISH: POLISHED	SCALE: 1:1		SHEET 1 OF 1

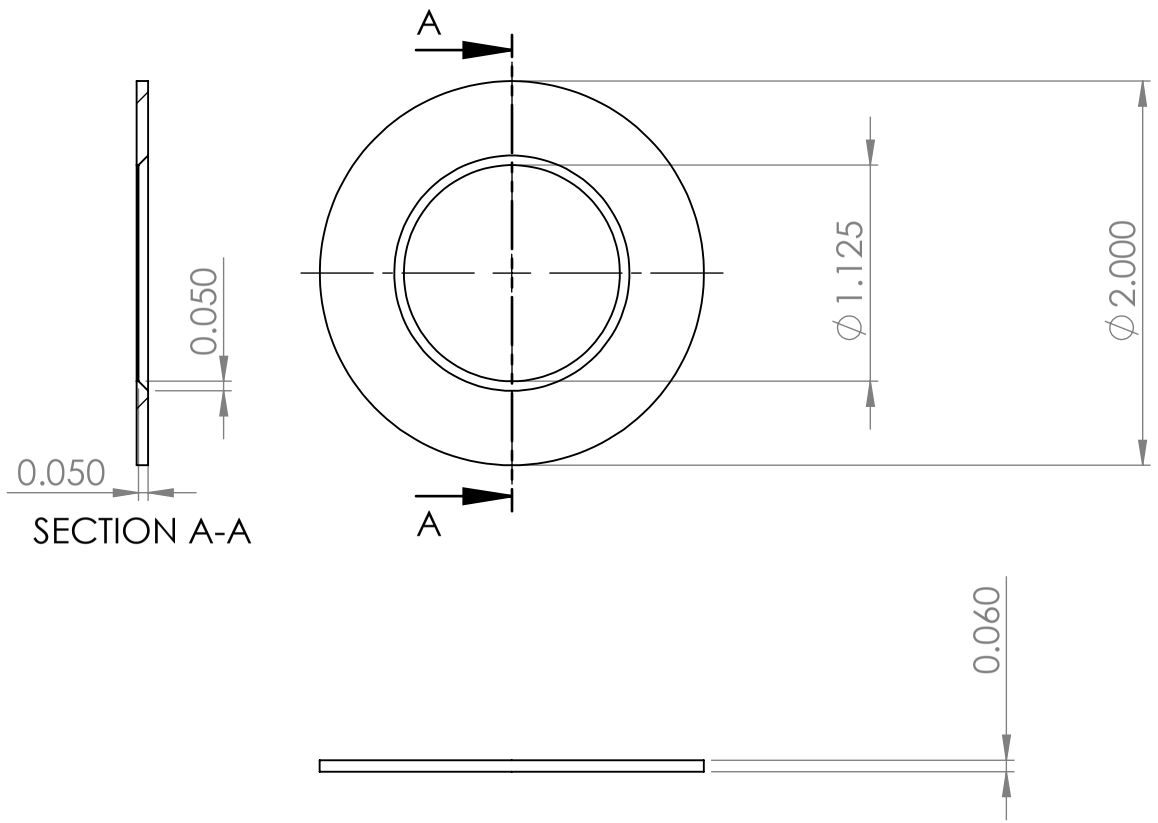

DATE: 03/15/17			
TITLE: HEAT SHIELD 2.4			
Collier Miers			
MATERIAL: 304 SS	SIZE A	DWG. NO.	QTY: 1
FINISH: POLISHED	SCALE: 1:1		SHEET 1 OF 1

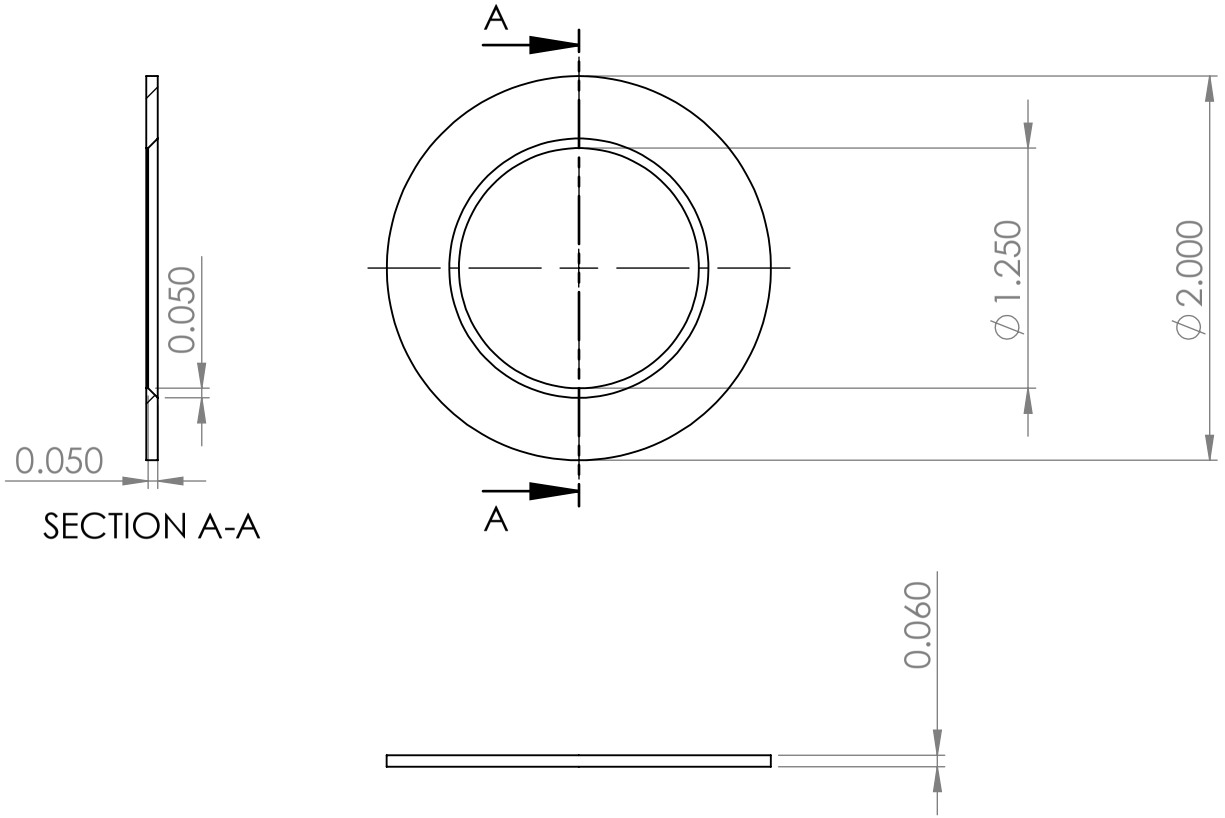

DATE: 03/15/17			
TITLE: HEAT SHIELD 2.5			
Collier Miers			
MATERIAL: 304 SS	SIZE A	DWG. NO.	QTY: 1
FINISH: POLISHED	SCALE: 1:1		SHEET 1 OF 1

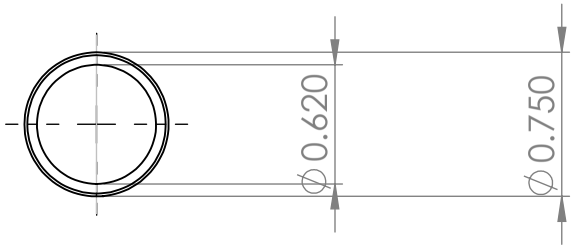

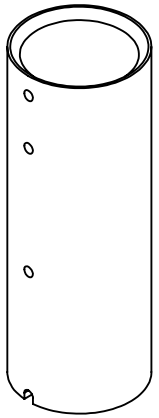

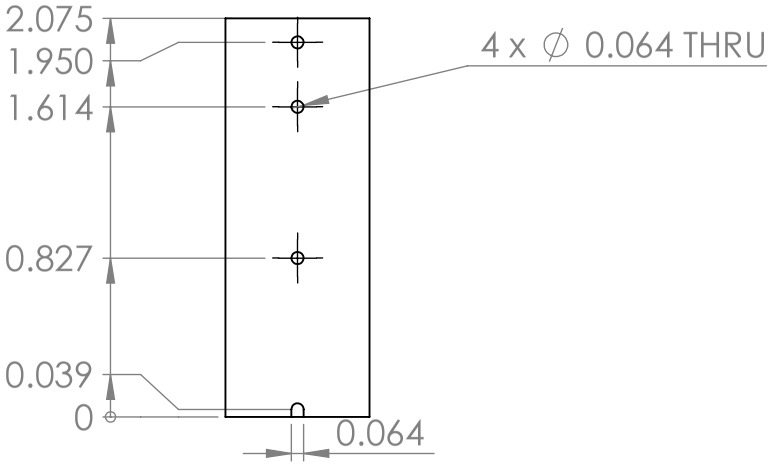

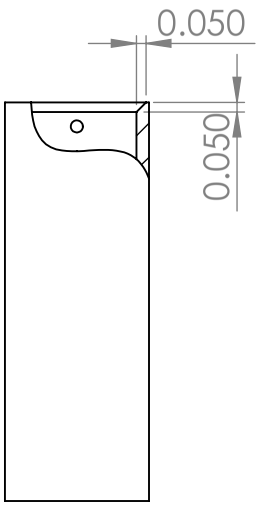

DATE: 03/15/17			
TITLE: HEAT SHIELD 3.1			
Collier Miers			
MATERIAL: 304 SS	SIZE A	DWG. NO.	QTY: 1
FINISH:	SCALE: 1:1		SHEET 1 OF 1

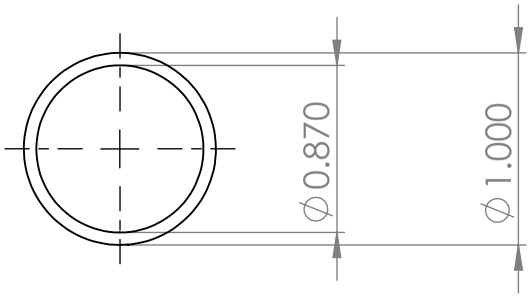

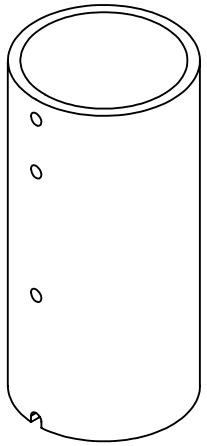

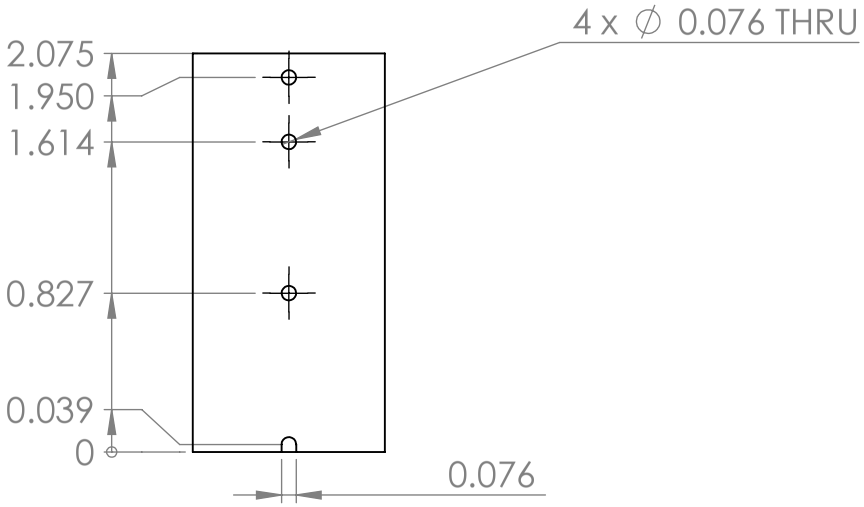

DATE: 03/15/17			
TITLE: HEAT SHIELD 3.2			
Collier Miers			
MATERIAL: 304 SS	SIZE A	DWG. NO.	QTY: 1
FINISH:	SCALE: 1:1		SHEET 1 OF 1

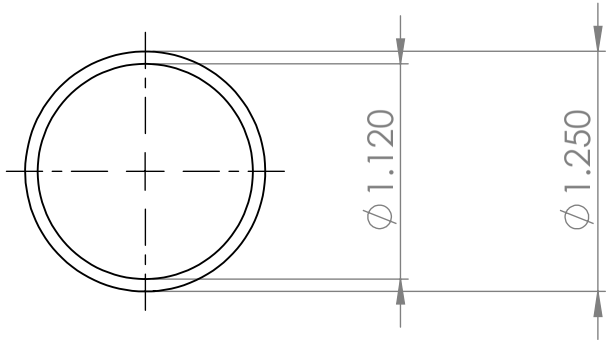

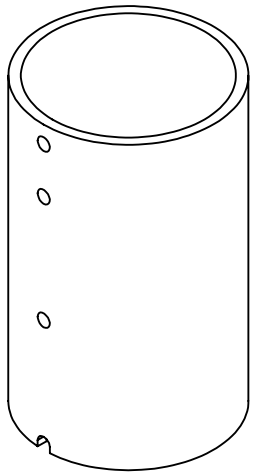

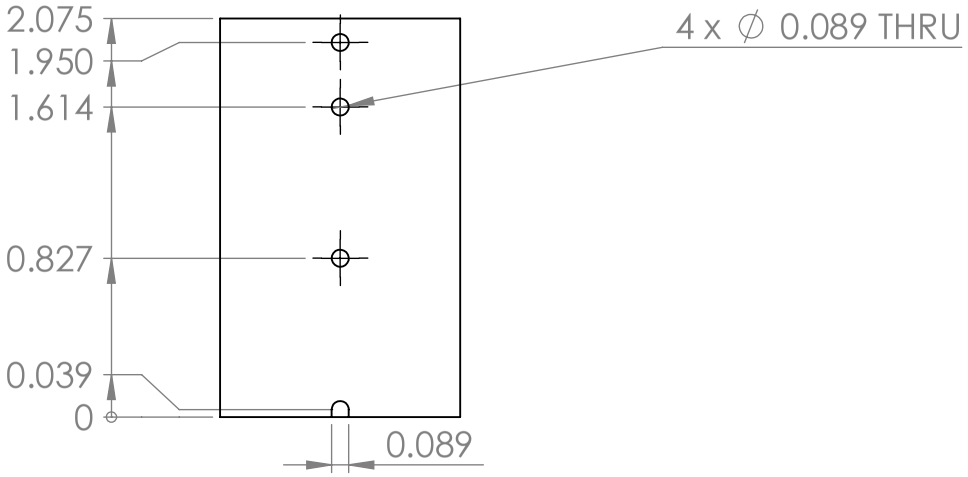

DATE: 03/15/17			
TITLE: HEAT SHIELD 3.3			
Collier Miers			
MATERIAL: 304 SS	SIZE A	DWG. NO.	QTY: 1
FINISH: POLISHED	SCALE: 1:1		SHEET 1 OF 1

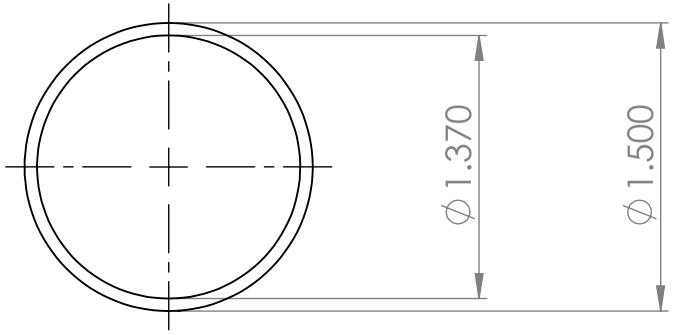

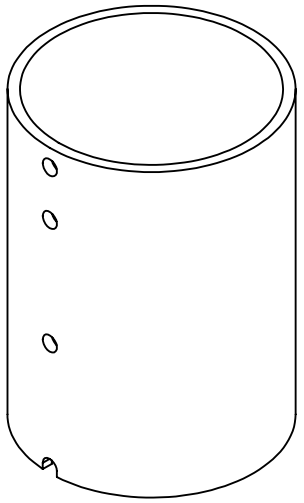

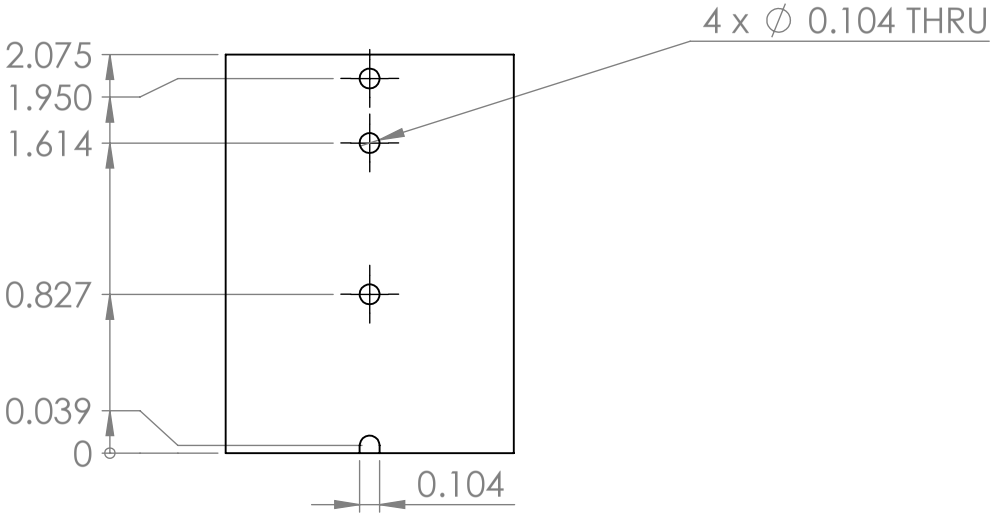

DATE: 03/15/17			
TITLE: HEAT SHIELD 3.4			
Collier Miers			
MATERIAL: 304 SS	SIZE A	DWG. NO.	QTY: 1
FINISH:	SCALE: 1:1		SHEET 1 OF 1

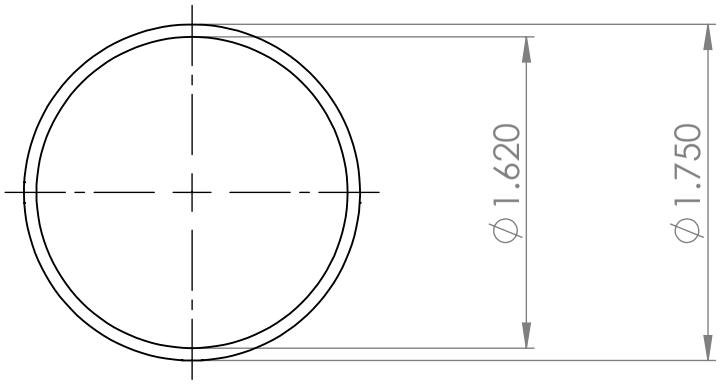

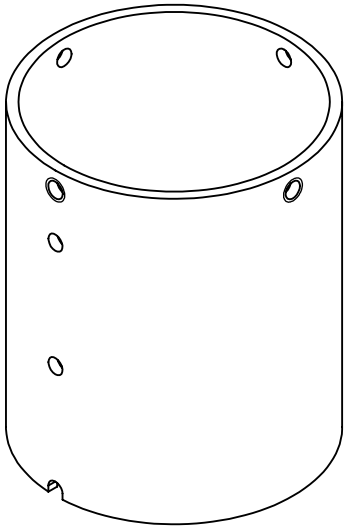

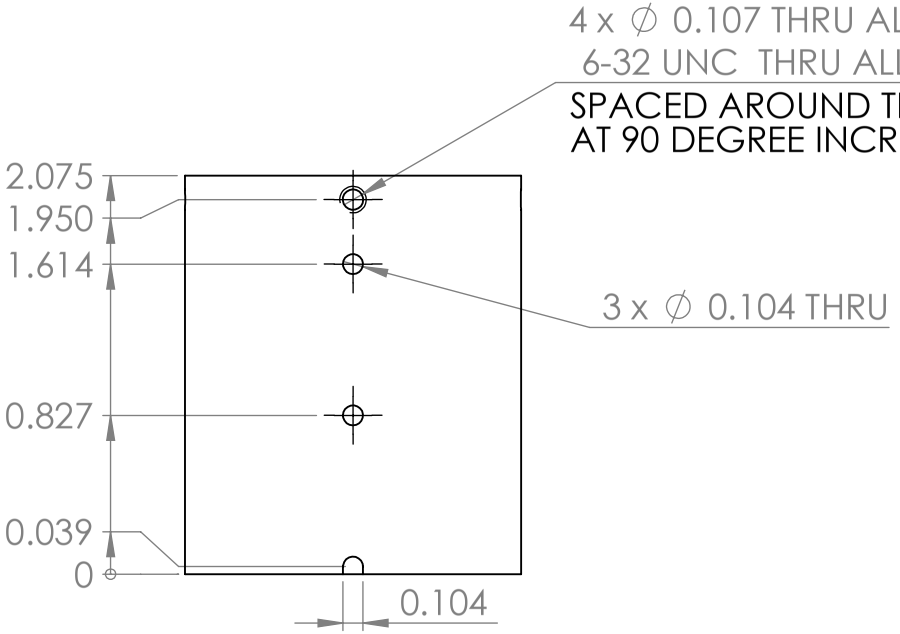

DATE: 03/15/17			
TITLE: HEAT SHIELD 3.5			
Collier Miers			
MATERIAL: 304 SS	SIZE A	DWG. NO.	QTY: 1
FINISH: POLISHED	SCALE: 1:1		SHEET 1 OF 1

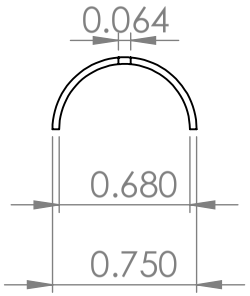

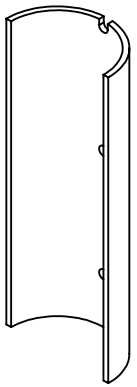

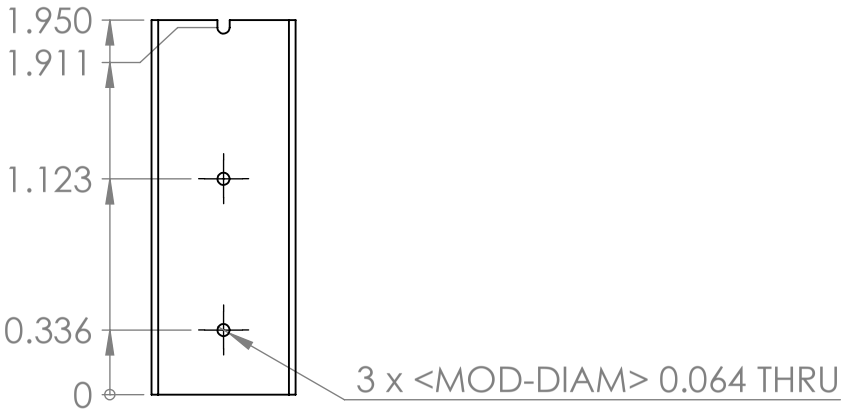

DATE: 03/15/17			
TITLE: HEAT SHIELD 4.1B			
Collier Miers			
MATERIAL: 304 SS	SIZE A	DWG. NO.	QTY: 1
FINISH: POLISHED	SCALE: 1:1		SHEET 1 OF 1

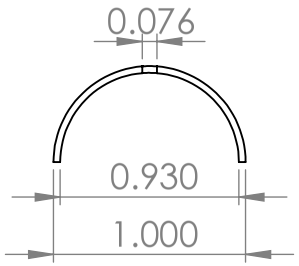

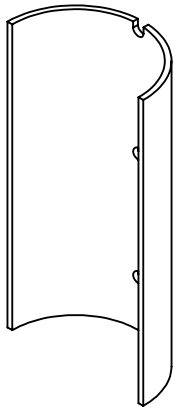

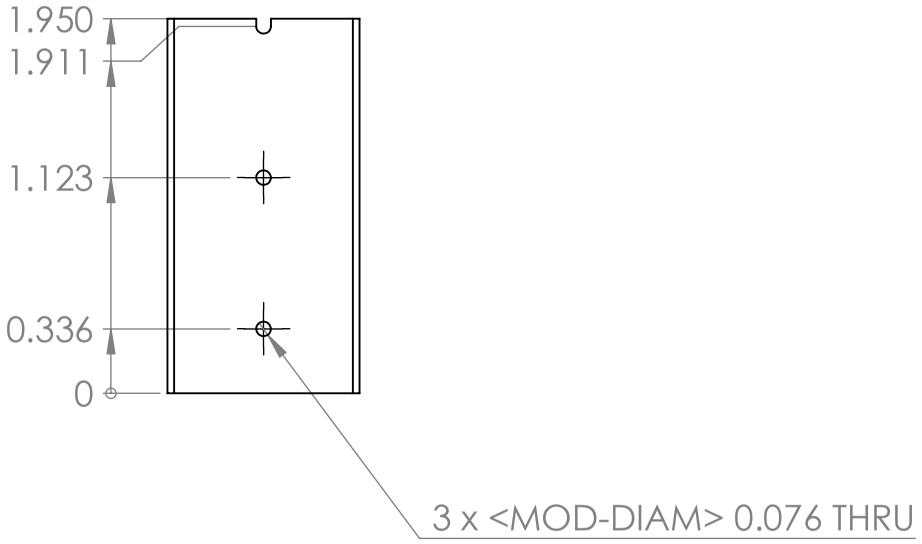

DATE: 03/15/17			
TITLE: HEAT SHIELD 4.2B			
Collier Miers			
MATERIAL: 304 SS	SIZE A	DWG. NO.	QTY: 1
FINISH: POLISHED	SCALE: 1:1		SHEET 1 OF 1

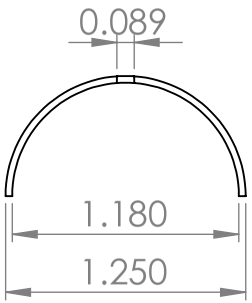

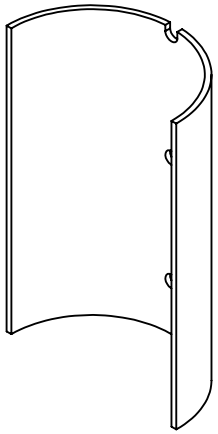

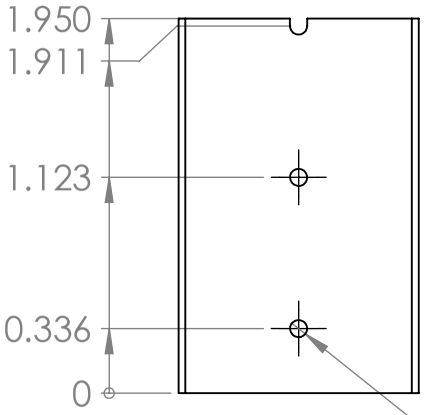

3 x <MOD-DIAM> 0.089 THRU

DATE: 03/15/17			
TITLE: HEAT SHIELD 4.3B			
Collier Miers			
MATERIAL: 304 SS	SIZE A	DWG. NO.	QTY: 1
FINISH: POLISHED	SCALE: 1:1		SHEET 1 OF 1

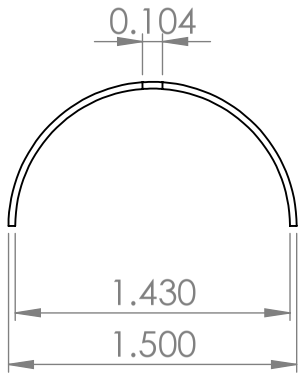

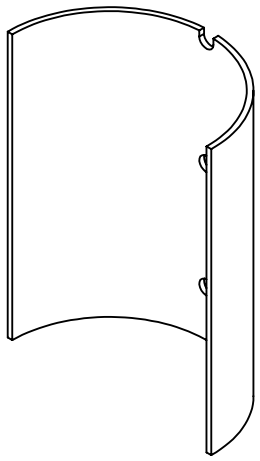

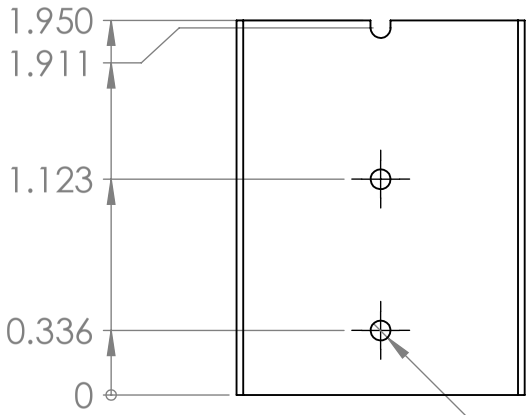

DATE: 03/15/17			
TITLE: HEAT SHIELD 4.4B			
Collier Miers			
MATERIAL: 304 SS	SIZE A	DWG. NO.	QTY: 1
FINISH: POLISHED	SCALE: 1:1		SHEET 1 OF 1

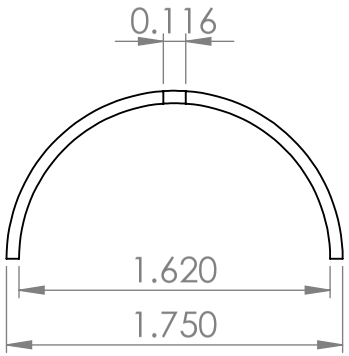

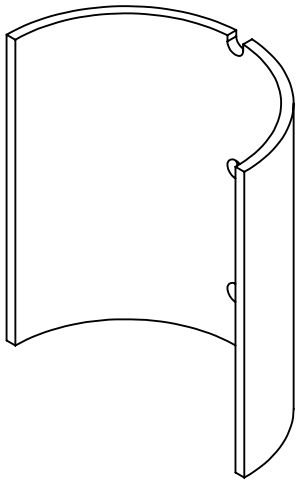

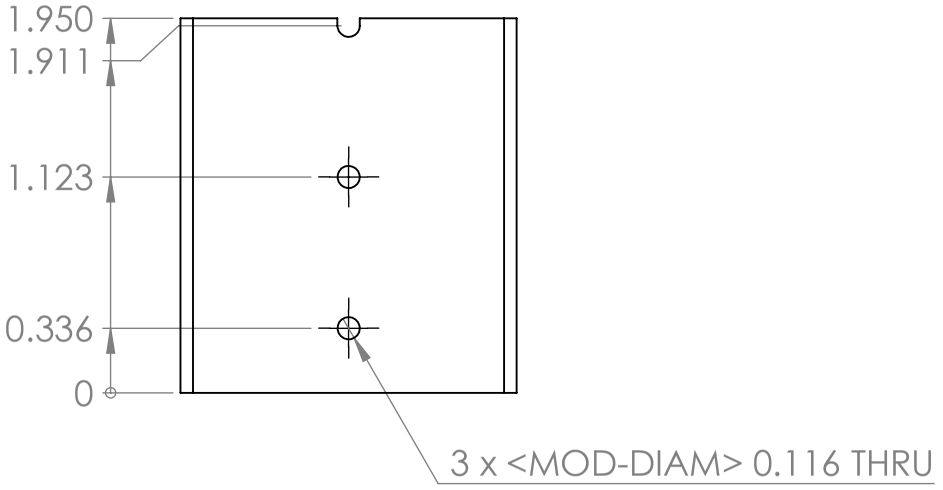

DATE: 03/15/17			
TITLE: HEAT SHIELD 4.5B			
Collier Miers			
MATERIAL: 304 SS	SIZE A	DWG. NO.	QTY: 1
FINISH: POLISHED	SCALE: 1:1		SHEET 1 OF 1

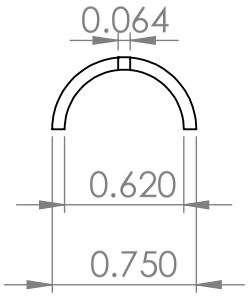

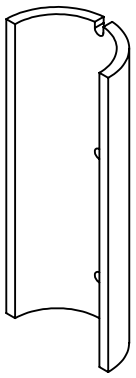

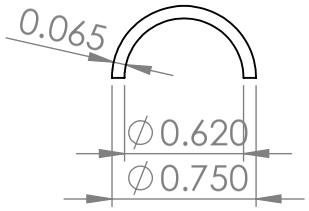

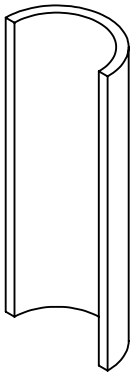

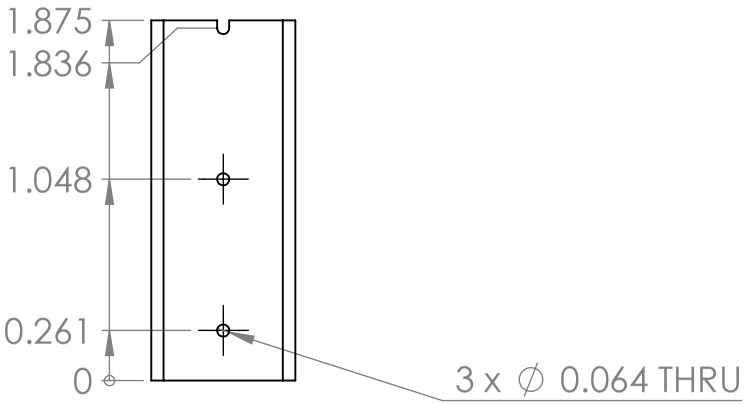

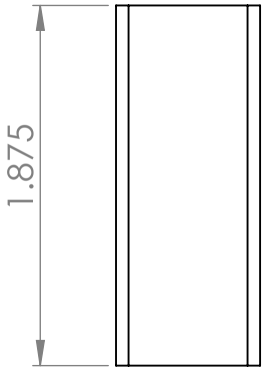

DATE: 03/15/17			
TITLE: HEAT SHIELD 4.1			
Collier Miers			
MATERIAL: 304 SS	SIZE A	DWG. NO.	QTY: 1
FINISH:	SCALE: 1:1		SHEET 1 OF 1

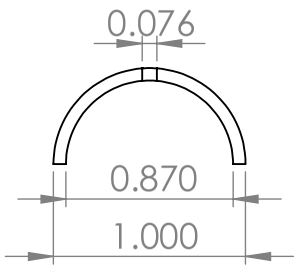

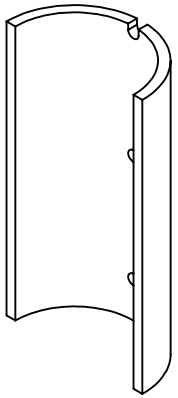

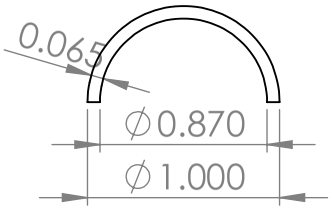

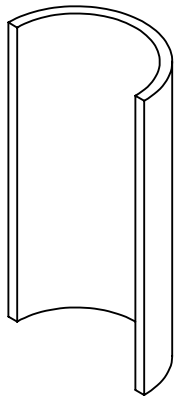

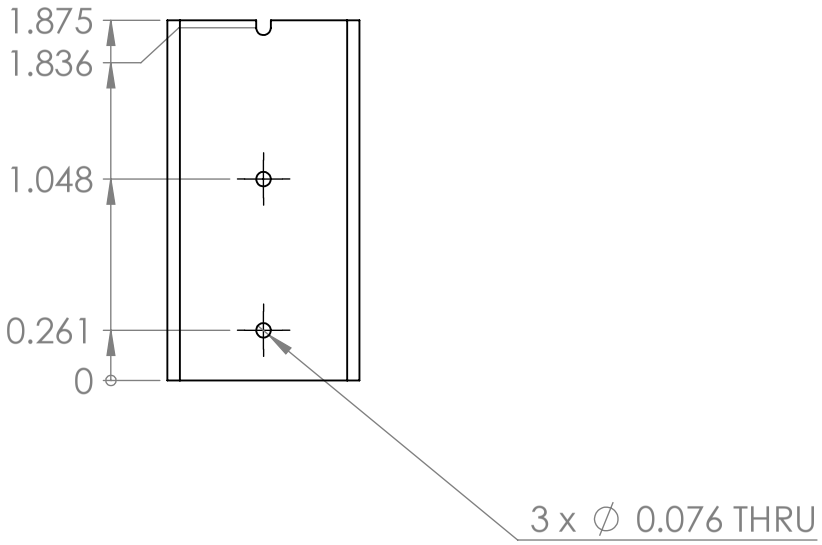

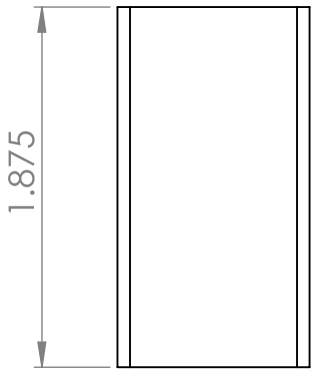

DATE: 03/15/17			
TITLE: HEAT SHIELD 4.2			
Collier Miers			
MATERIAL: 304 SS	SIZE A	DWG. NO.	QTY: 1
FINISH:	SCALE: 1:1		SHEET 1 OF 1

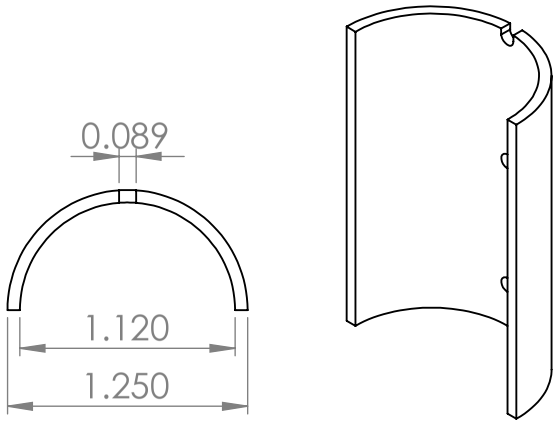

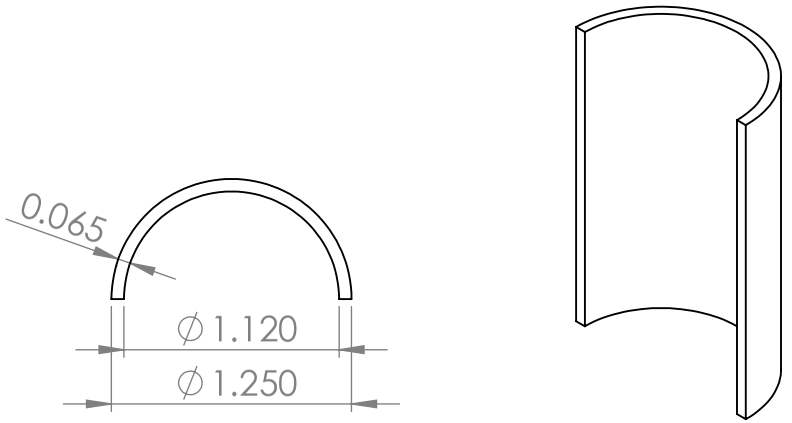

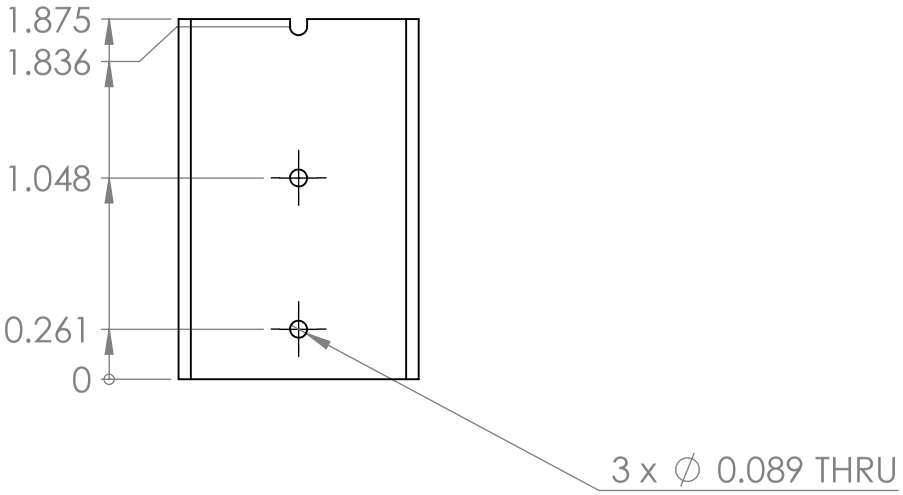

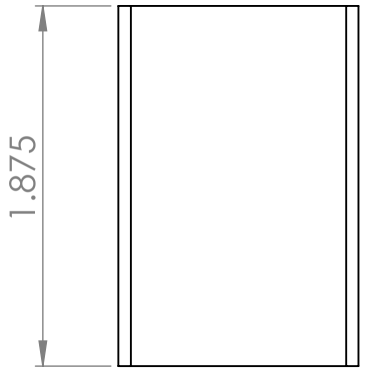

DATE: 03/15/17			
TITLE: HEAT SHIELD 4.3			
Collier Miers			
MATERIAL: 304 SS	SIZE A	DWG. NO.	QTY: 1
FINISH: POLISHED	SCALE: 1:1		SHEET 1 OF 1

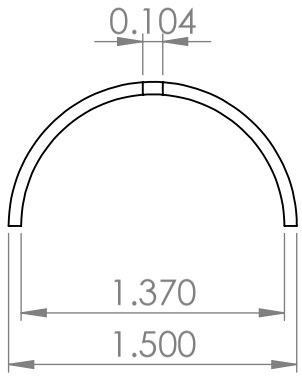

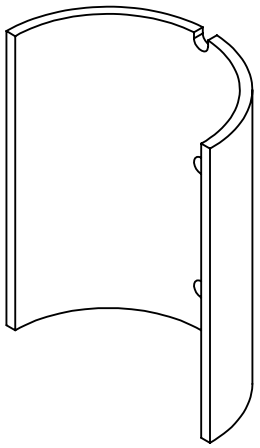

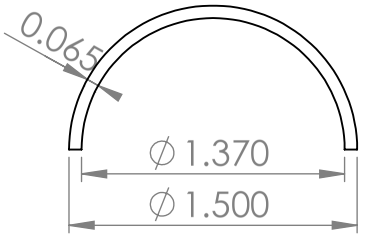

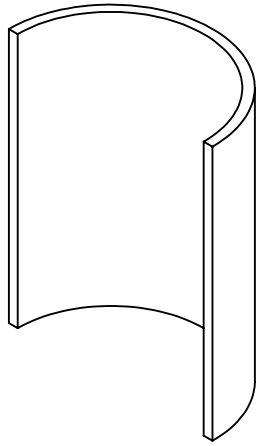

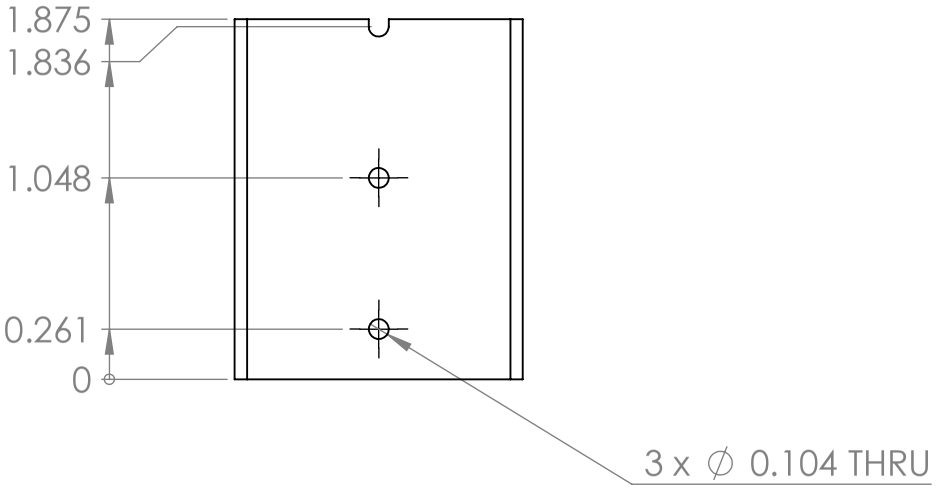

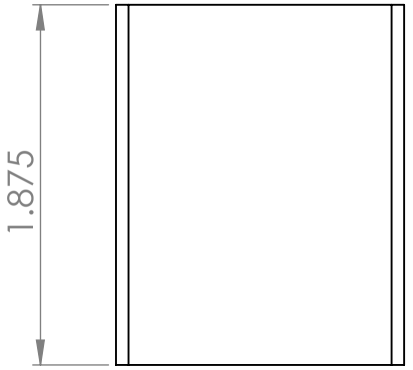

DATE: 03/15/17			
TITLE: HEAT SHIELD 4.4			
Collier Miers			
MATERIAL: 304 SS	SIZE A	DWG. NO.	QTY: 1
FINISH:	SCALE: 1:1		SHEET 1 OF 1

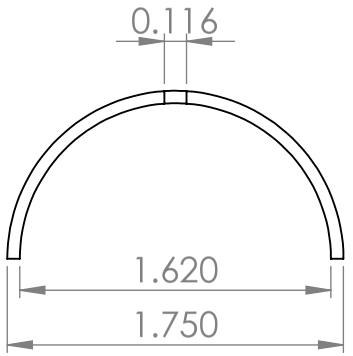

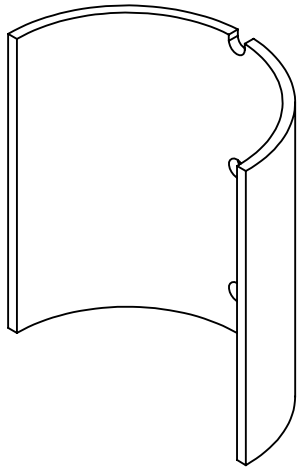

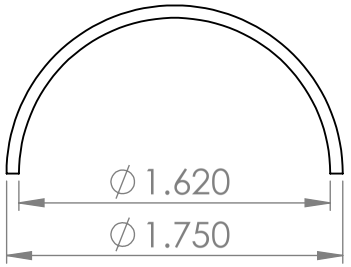

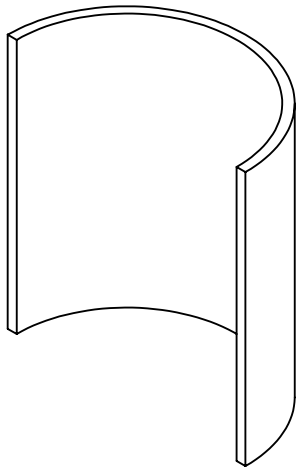

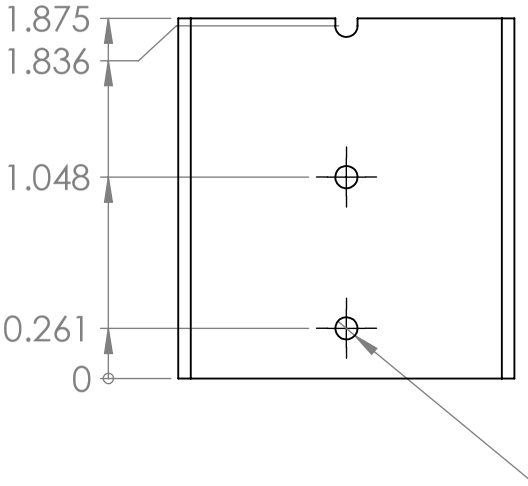

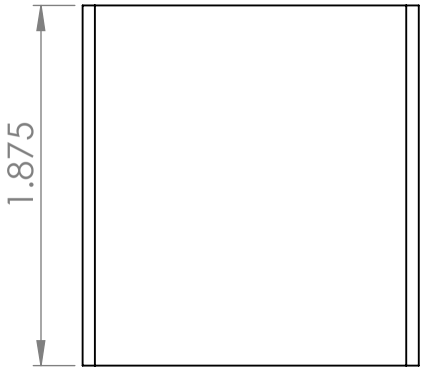

DATE: 03/15/17			
TITLE: HEAT SHIELD 4.5B			
Collier Miers			
MATERIAL: 304 SS	SIZE A	DWG. NO.	QTY: 1
FINISH: POLISHED	SCALE: 1:1		SHEET 1 OF 1

Tubing Assemblies

TOP

RIGHT

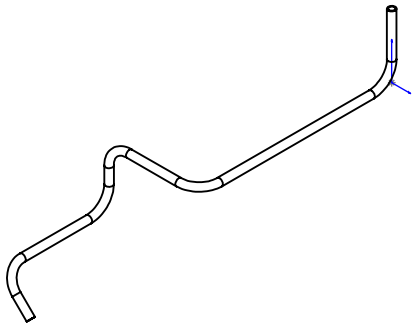

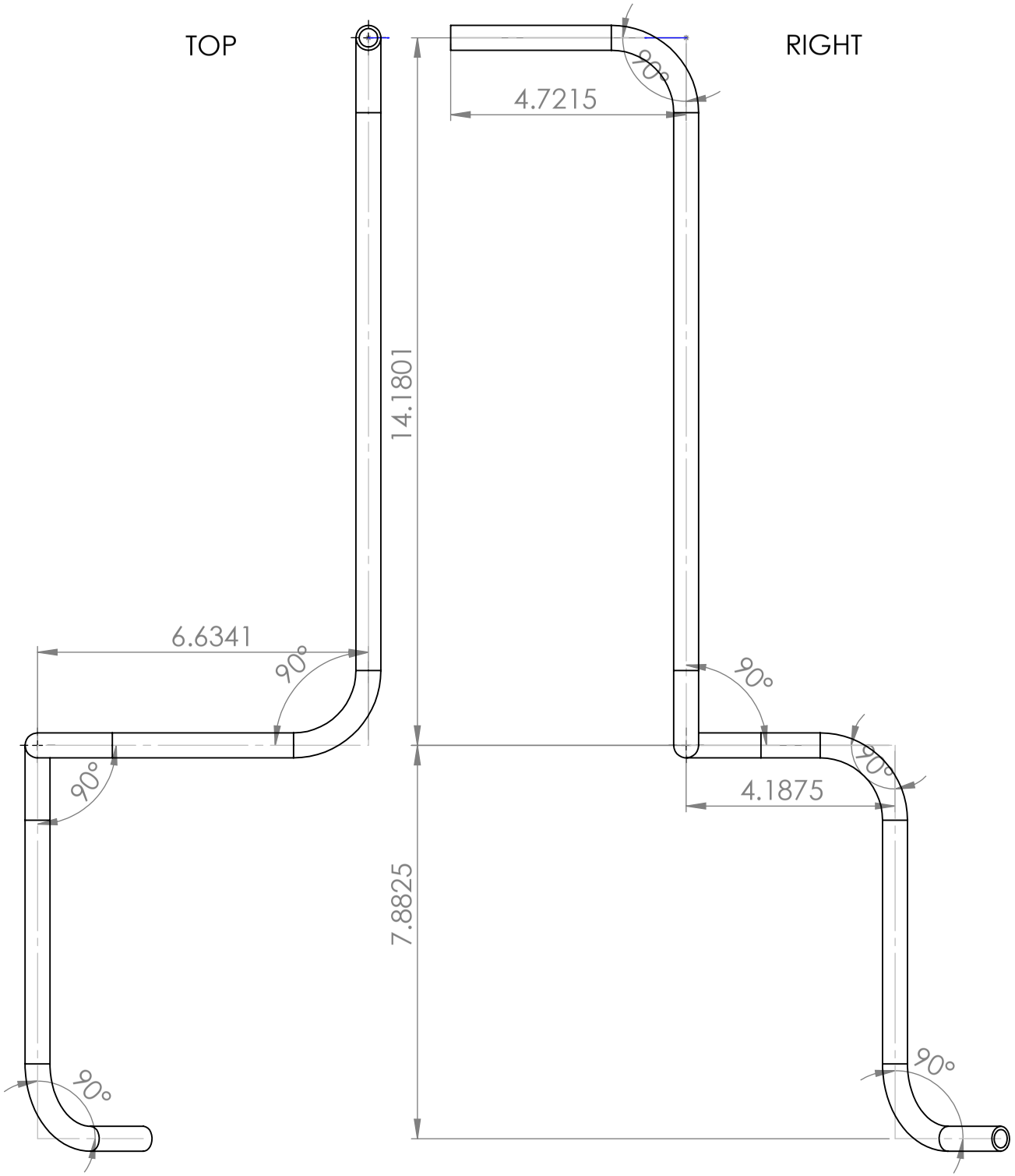

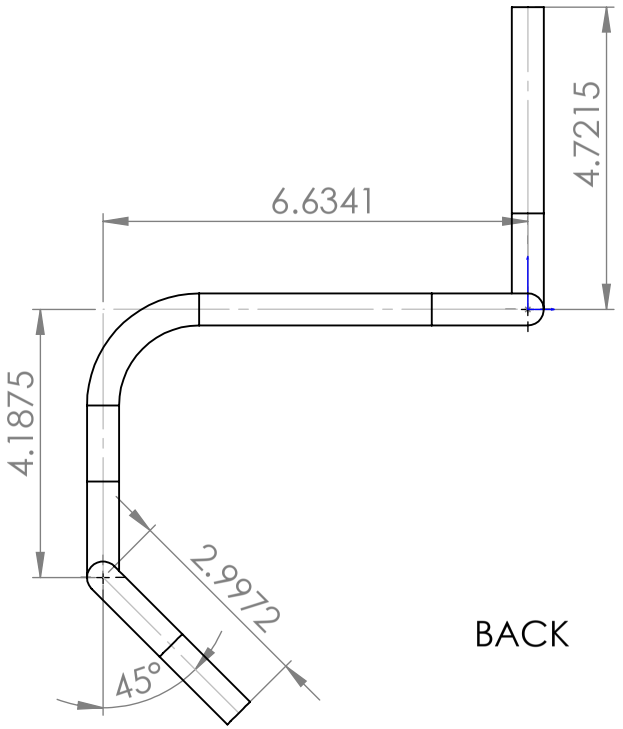

BACK

HotSide_ExternalTubingRun_Final

SCALE: 1:3

MAT'L: 304 SS

BY: COLLIER MIERS

BOTTOM VIEW MIDDLE JOG

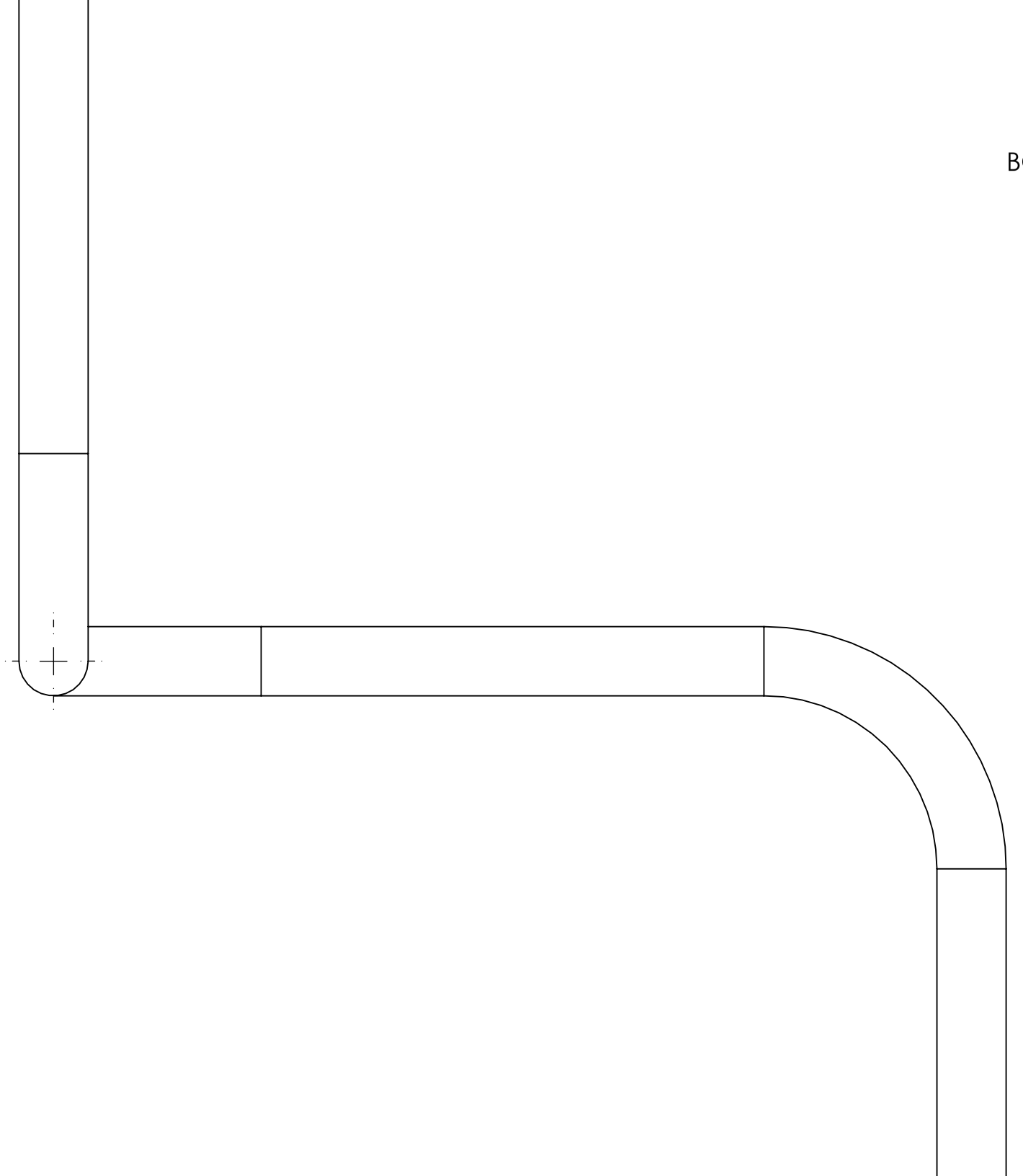

SCALE: 1:1

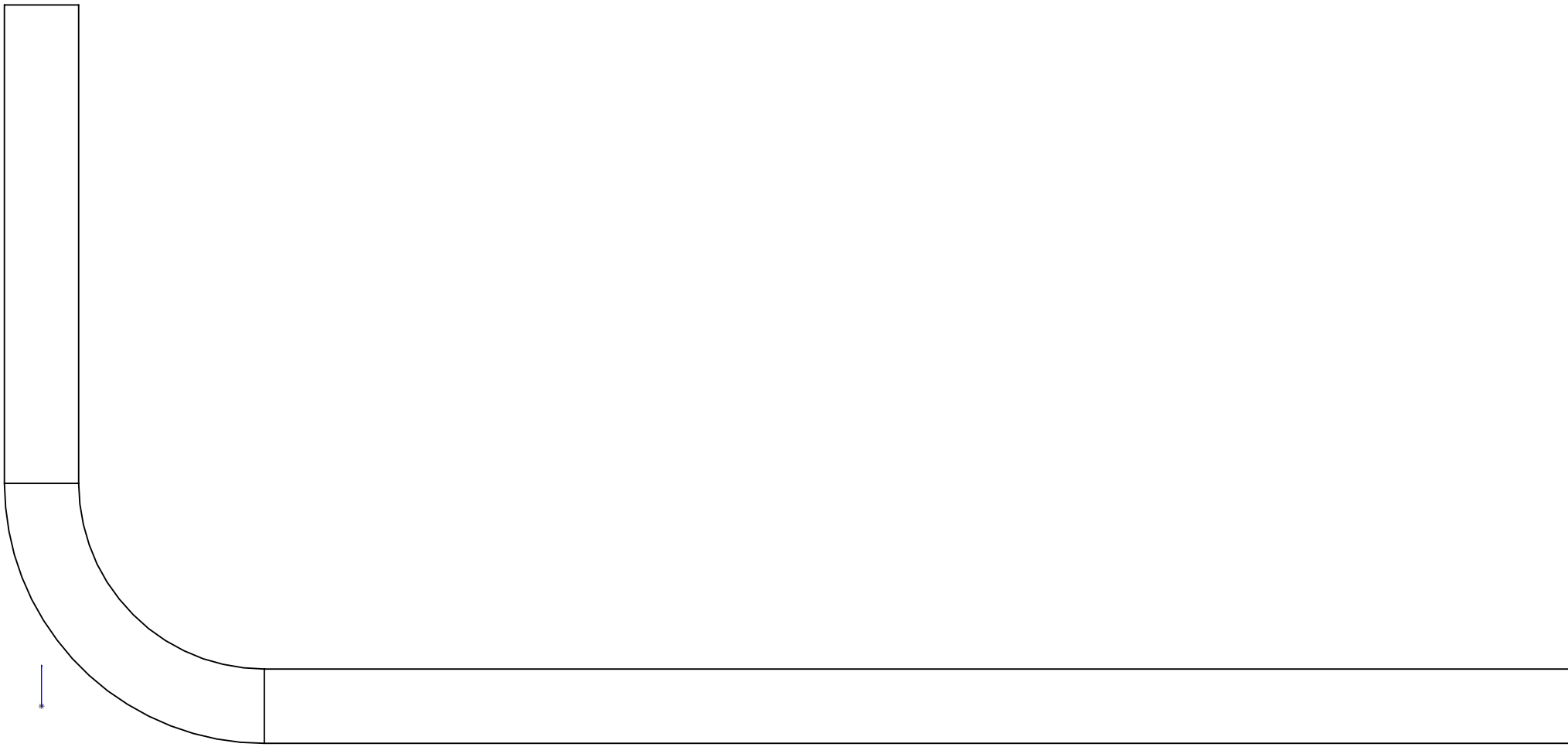

RIGHT VIEW (CHAMBER CONNECTION)

SCALE 1:1

LEFT VIEW MIDDLE JOG

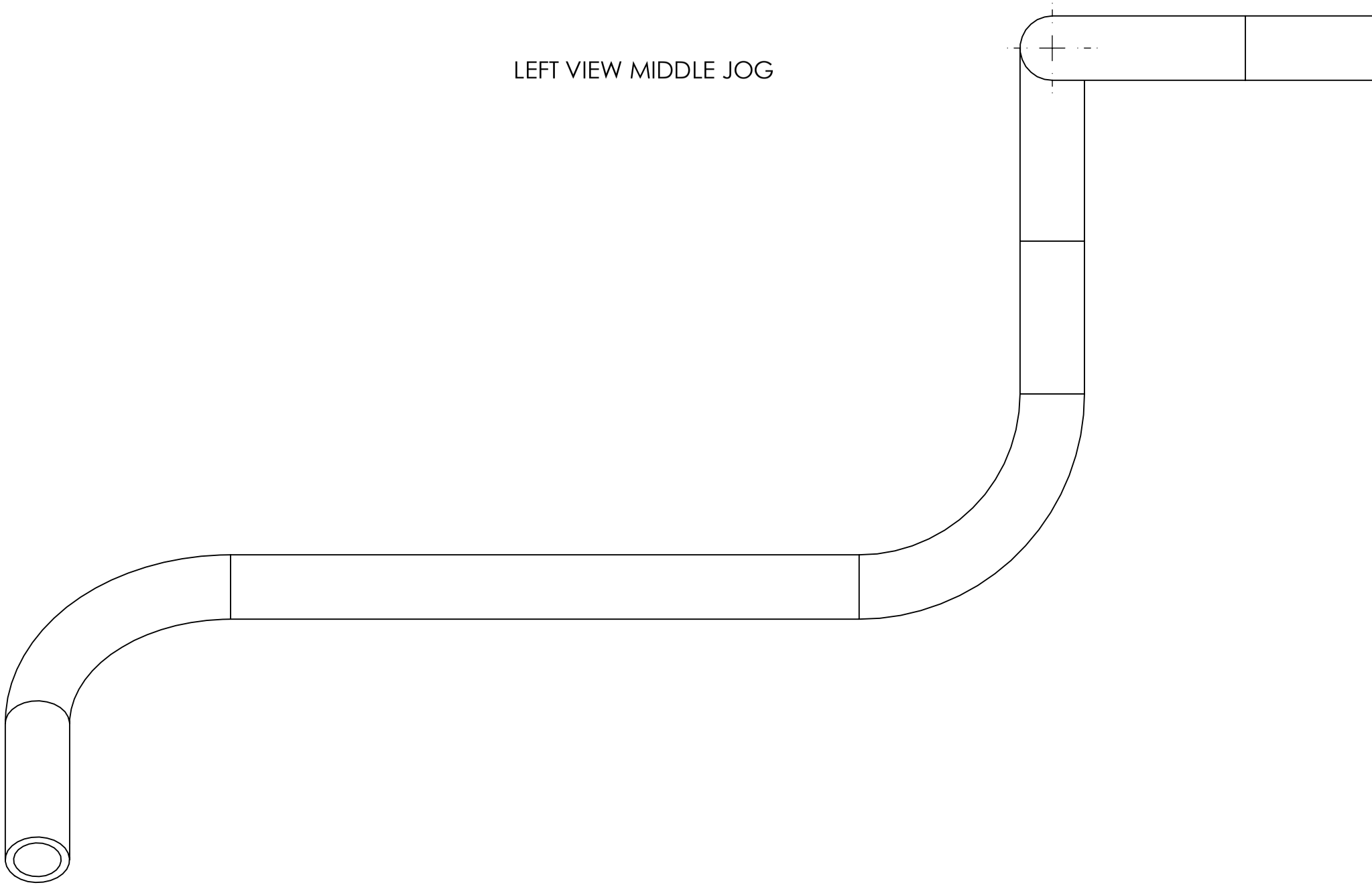

SCALE 1:1

FRONT VIEW

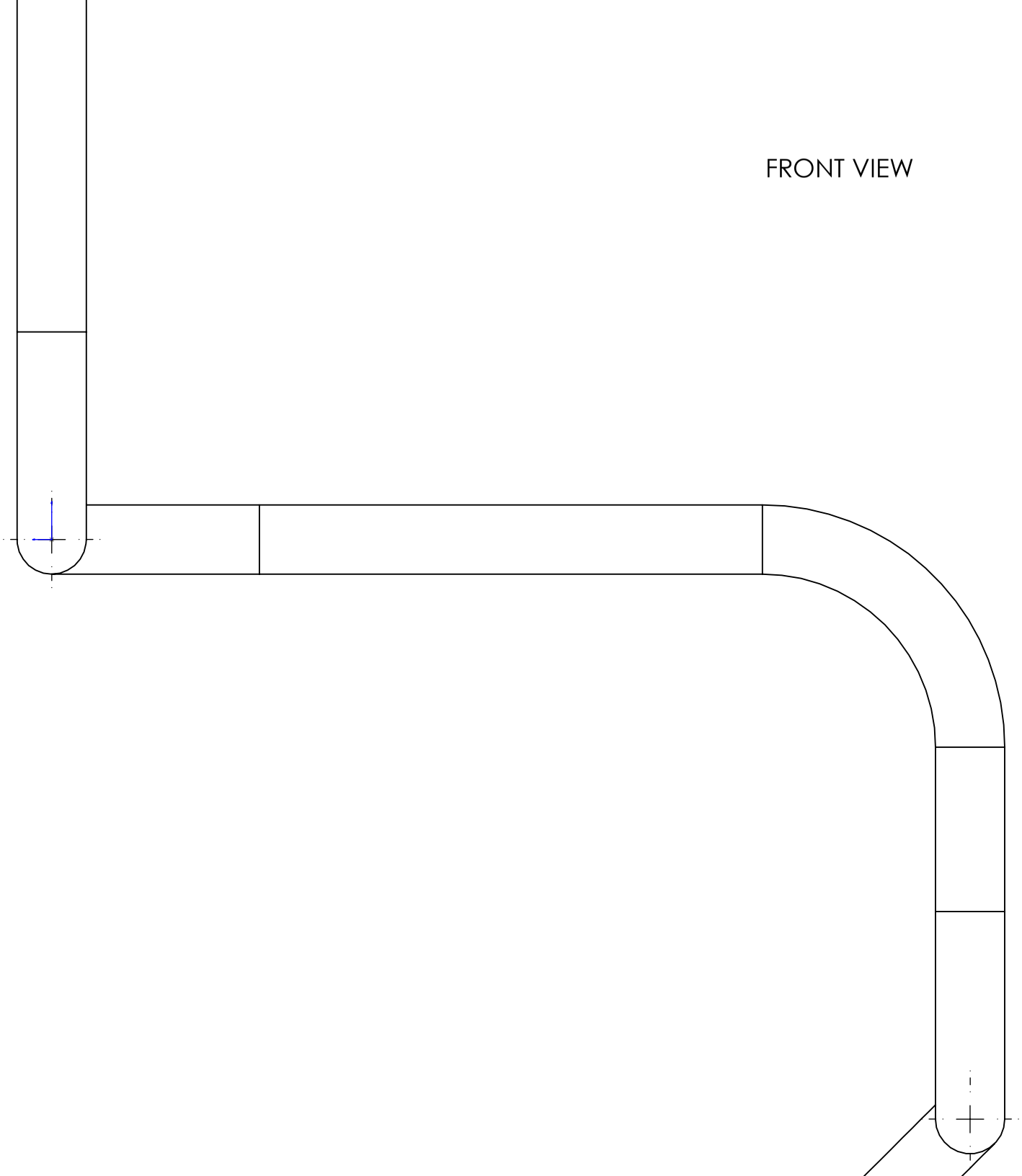

SCALE 1:1

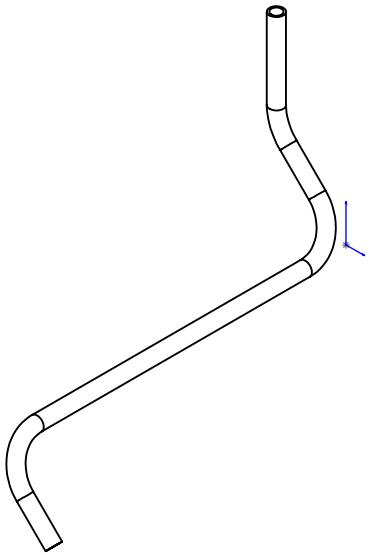

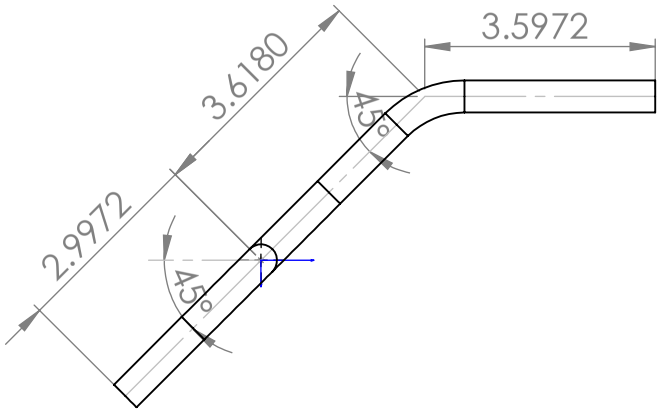

BACK

TOP

ColdSide_ExternalTubingRun_Final
SCALE: 1:3
MAT'L: 304 SS
BY: COLLIER MIERS

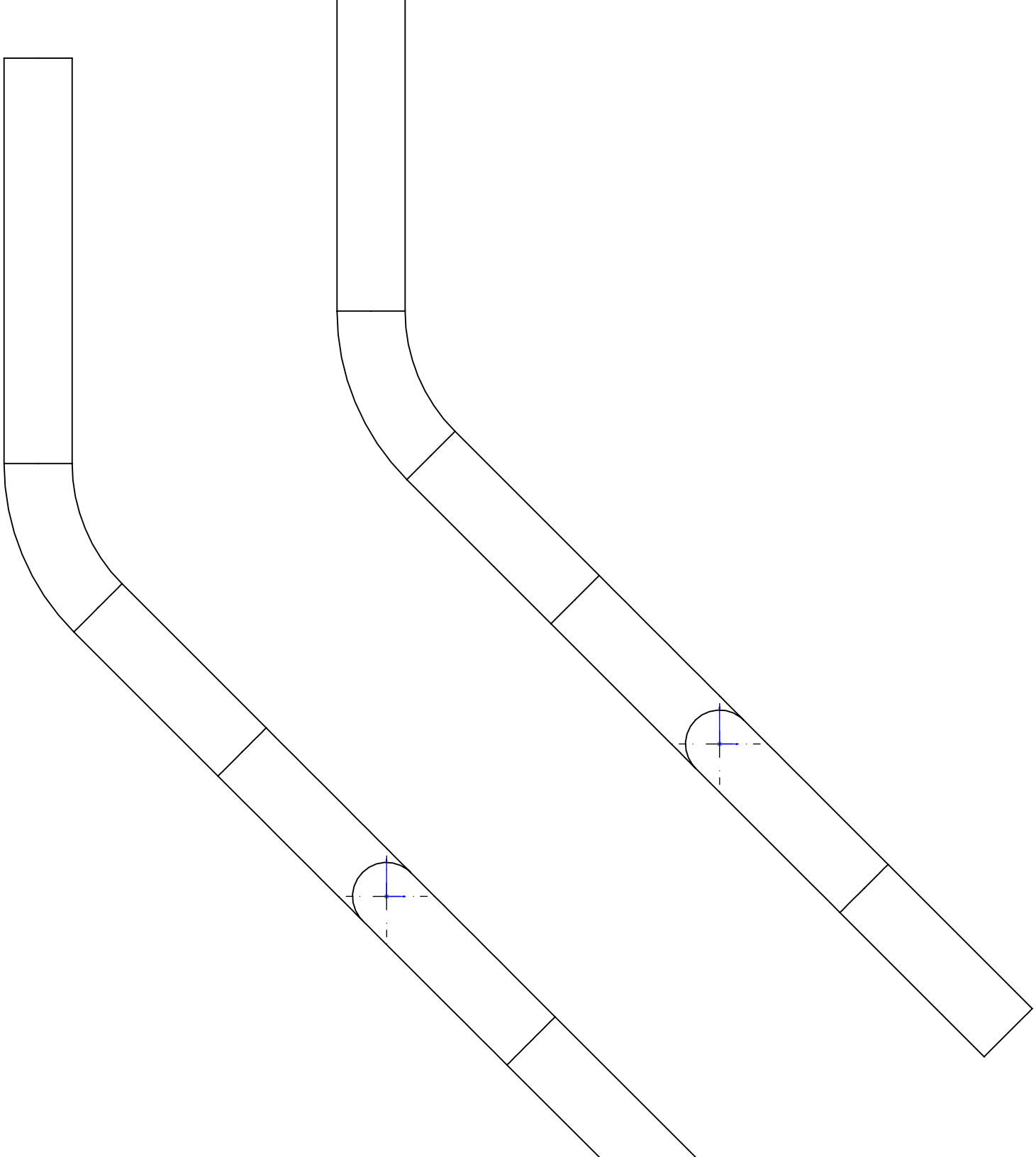

SCALE: 1:1

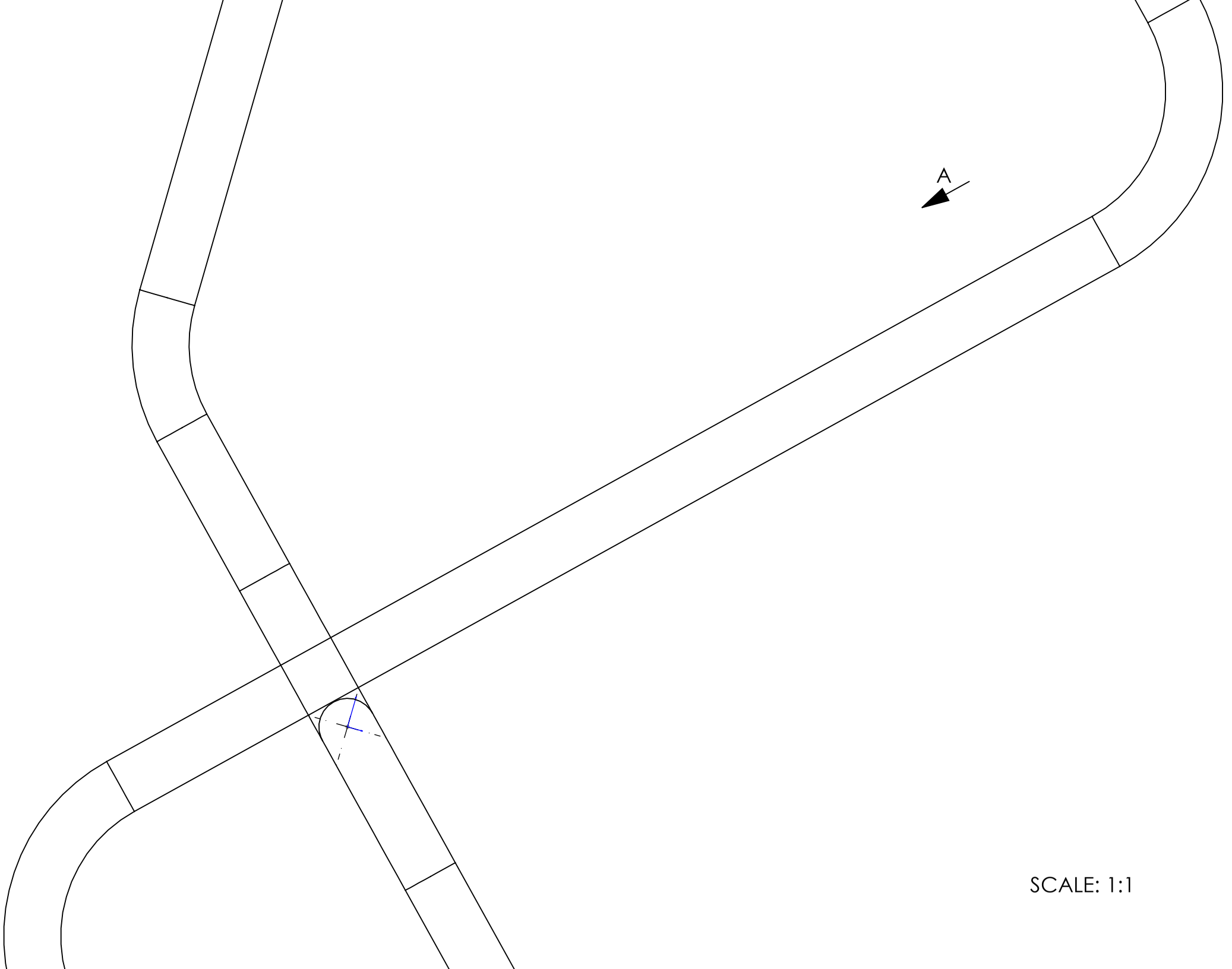

SCALE: 1:1

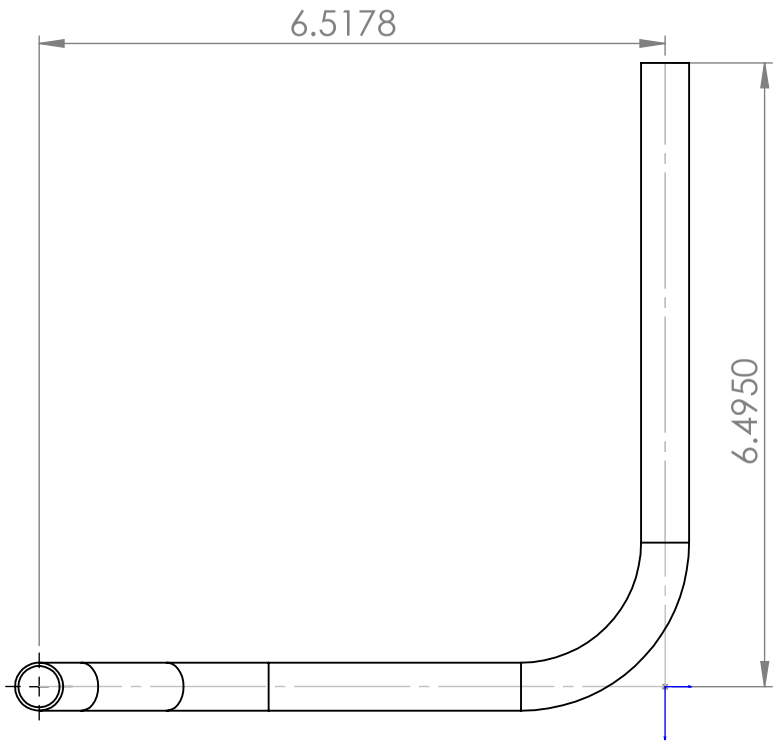

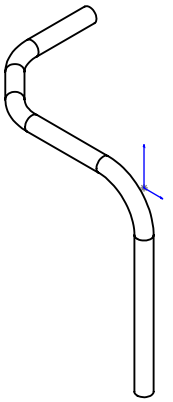

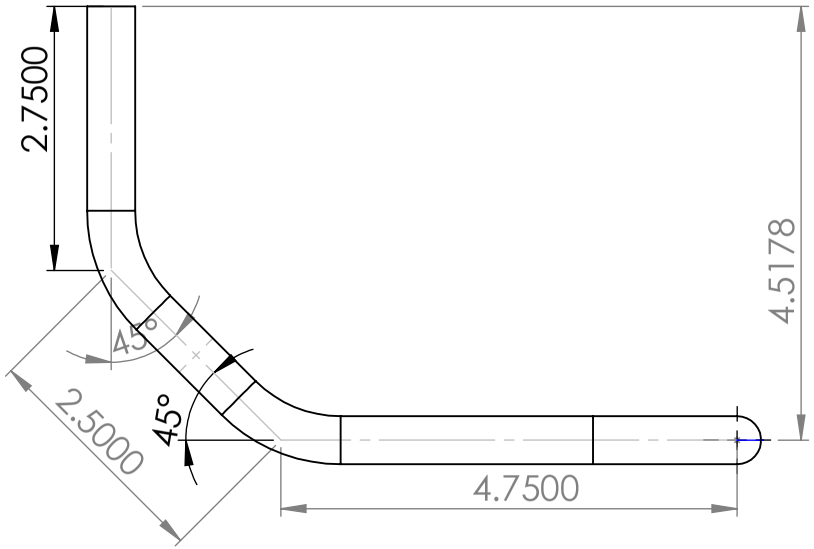

IN-VAC HOTSIDE TUBE ASSEMBLY

SCALE: 1:2

MAT'L: 304 SS

BY: COLLIER MIERS

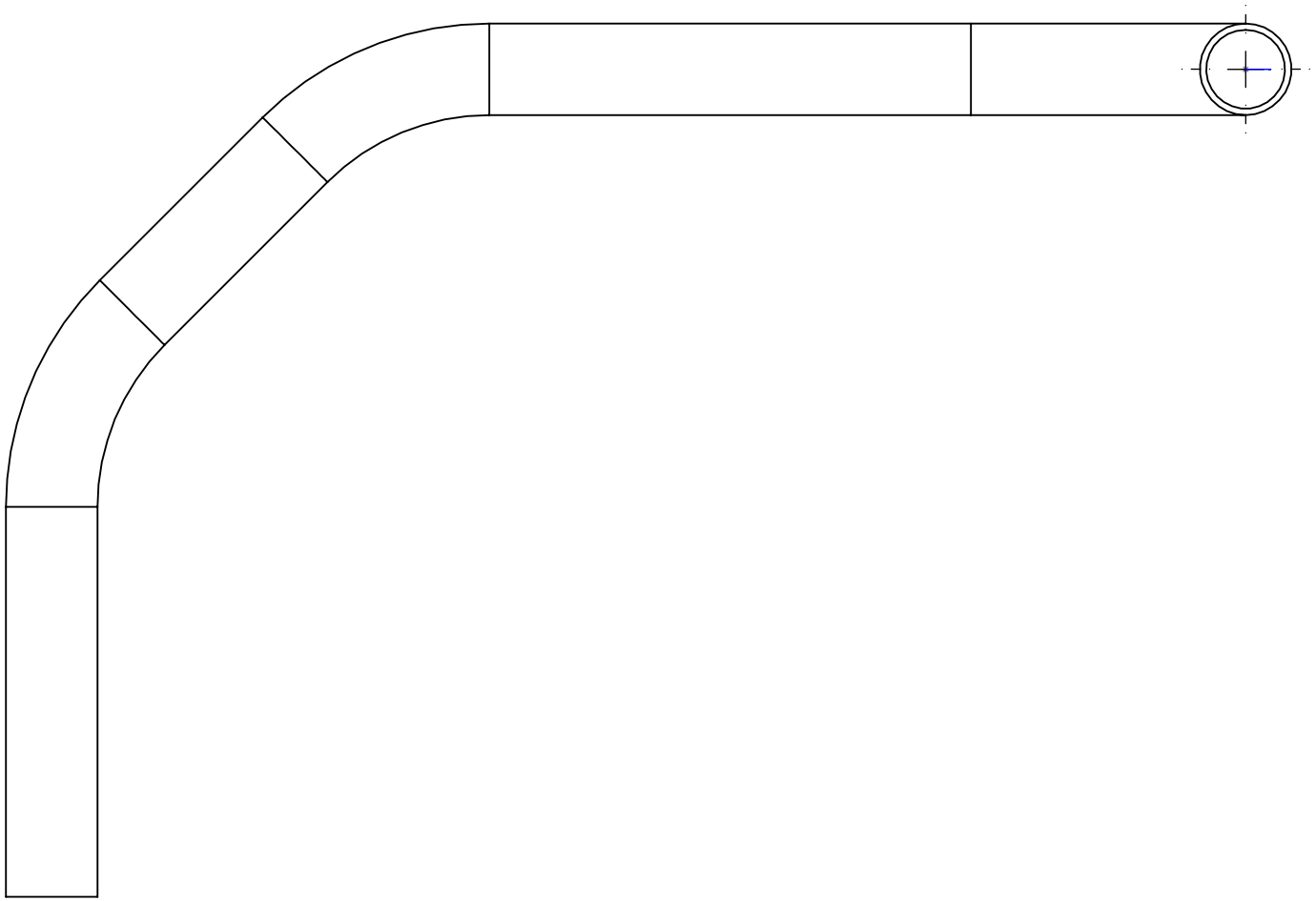

SCALE: 1:1

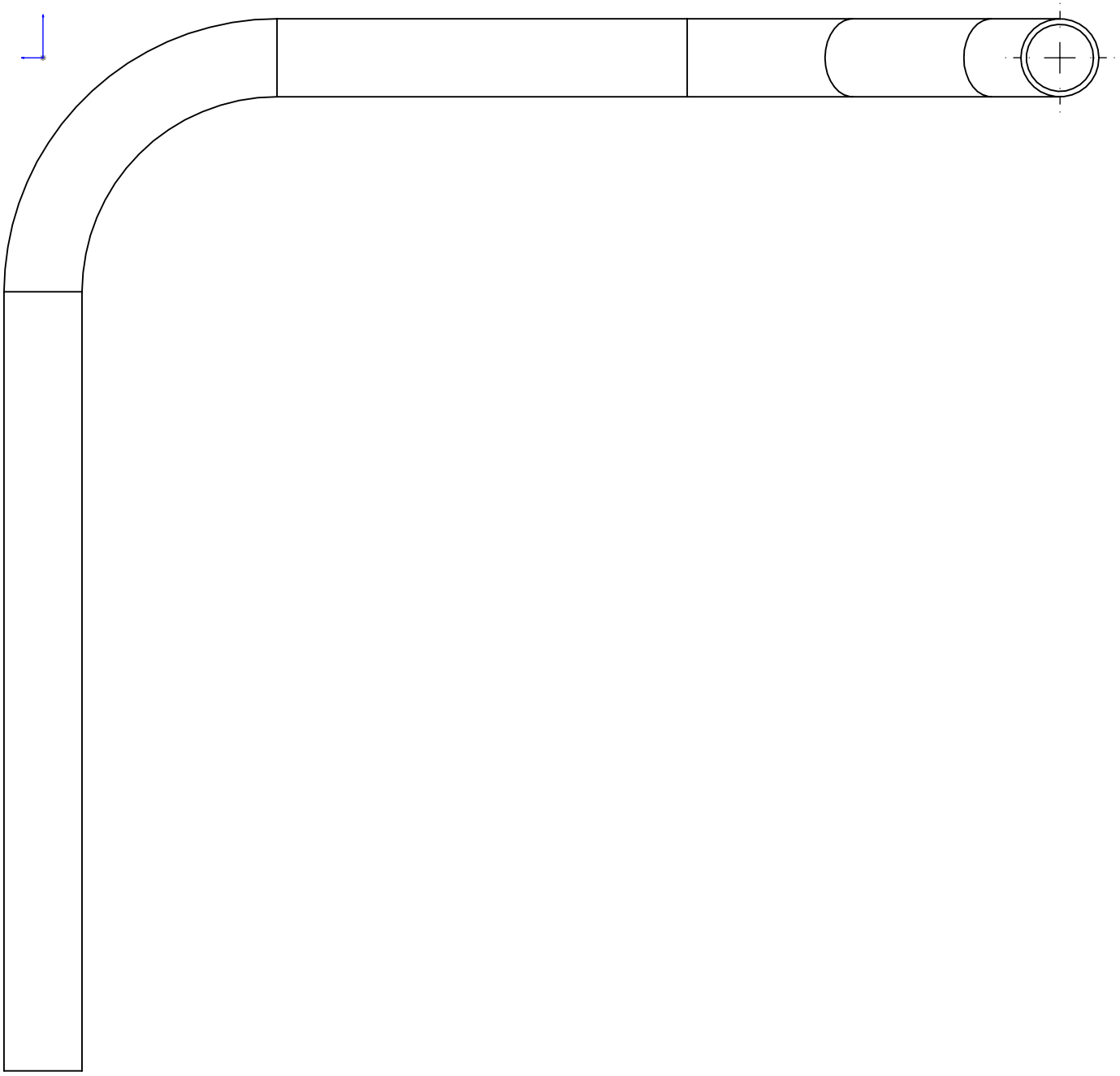

SCALE: 1:1

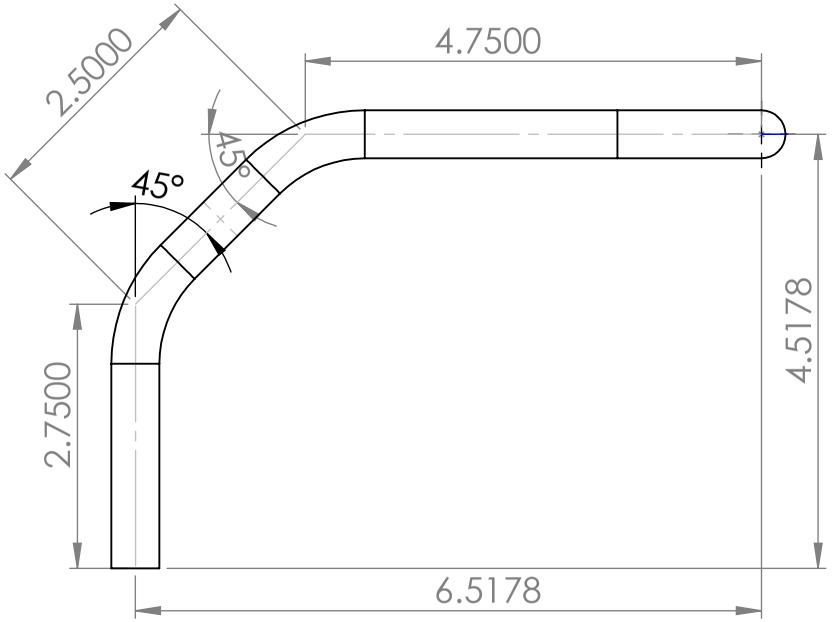

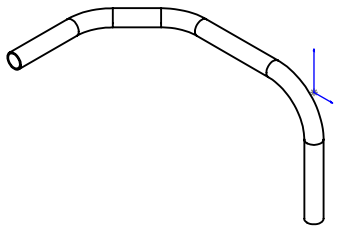

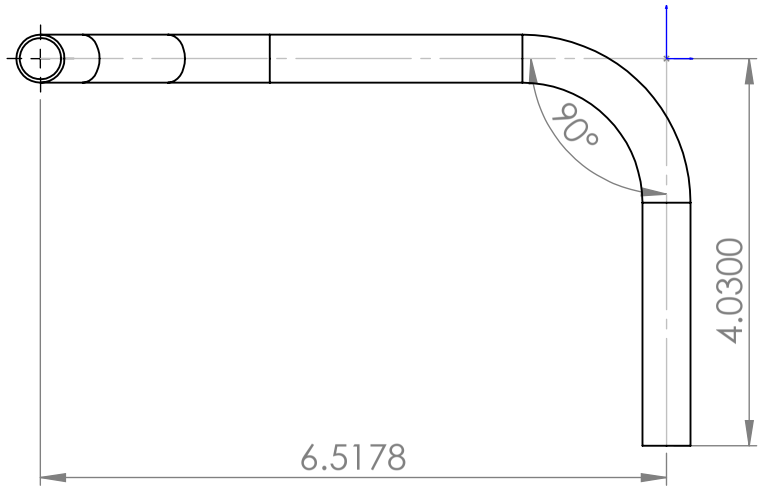

IN-VAC COLDSIDE TUBE ASSEMBLY

SCALE: 1:2

MAT'L: 304 SS

BY: COLLIER MIERS

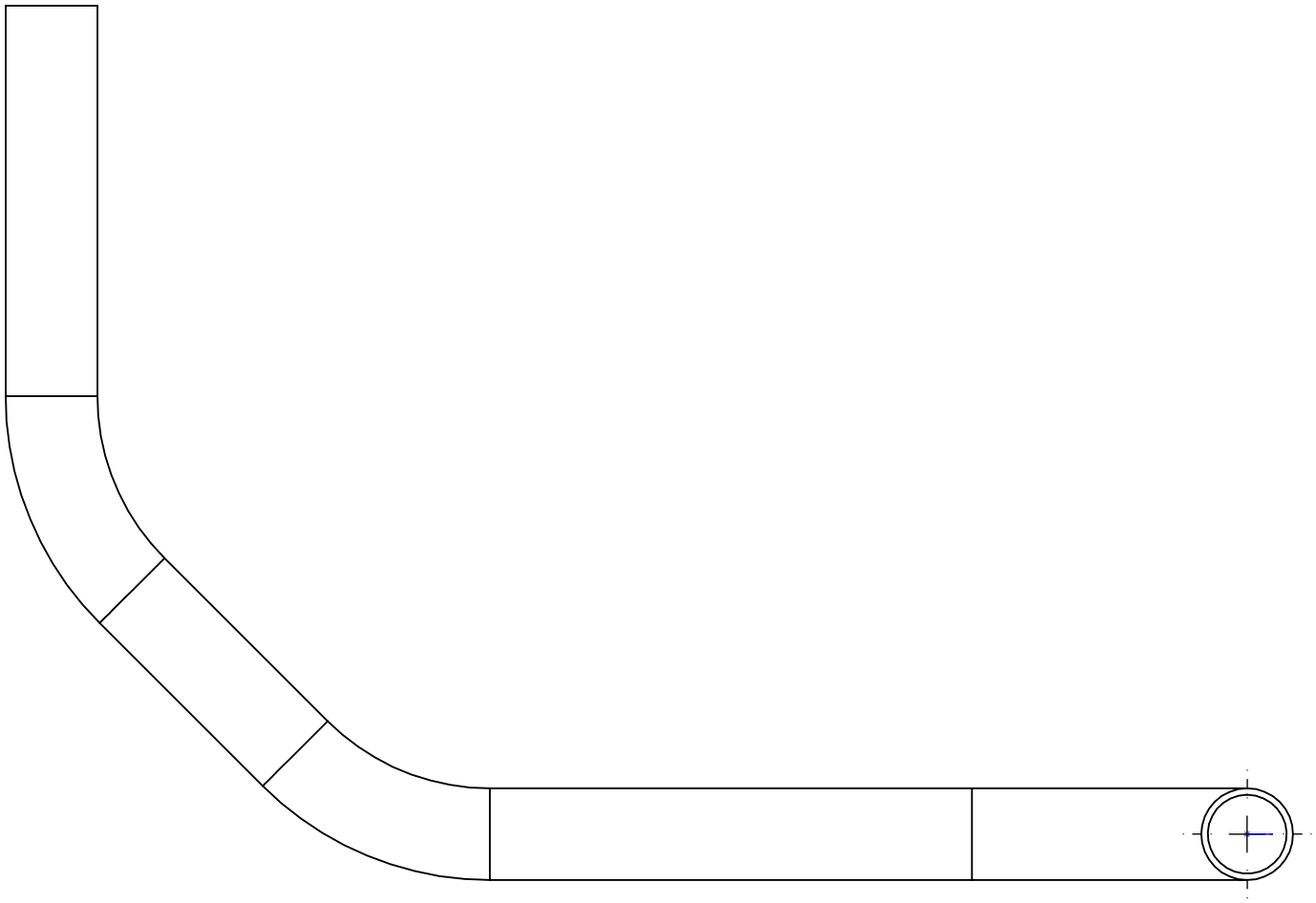

SCALE: 1:1

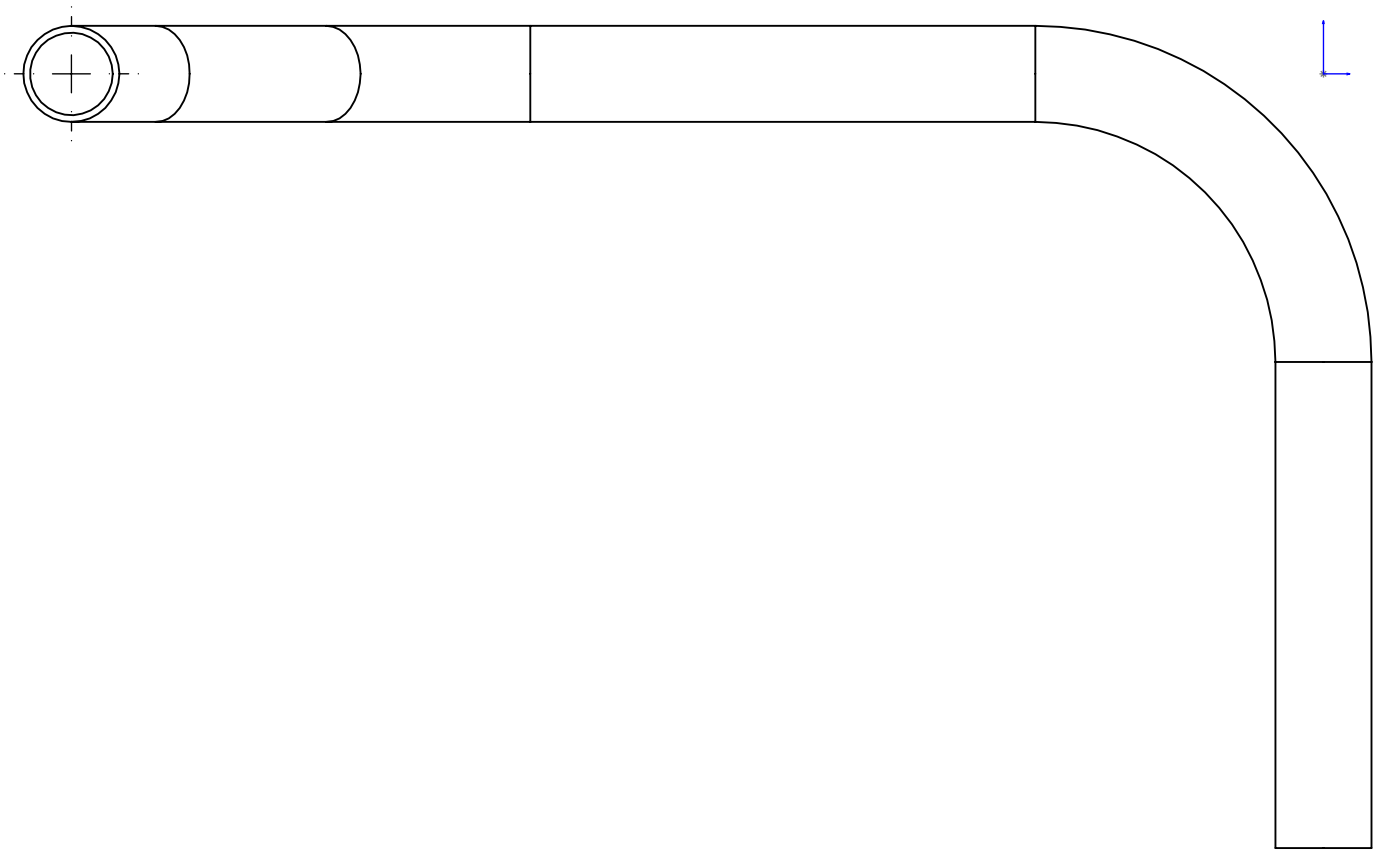

SCALE: 1:1

F. Z-METER WIRING DIAGRAMS

Vacuum Service Well Port Identification

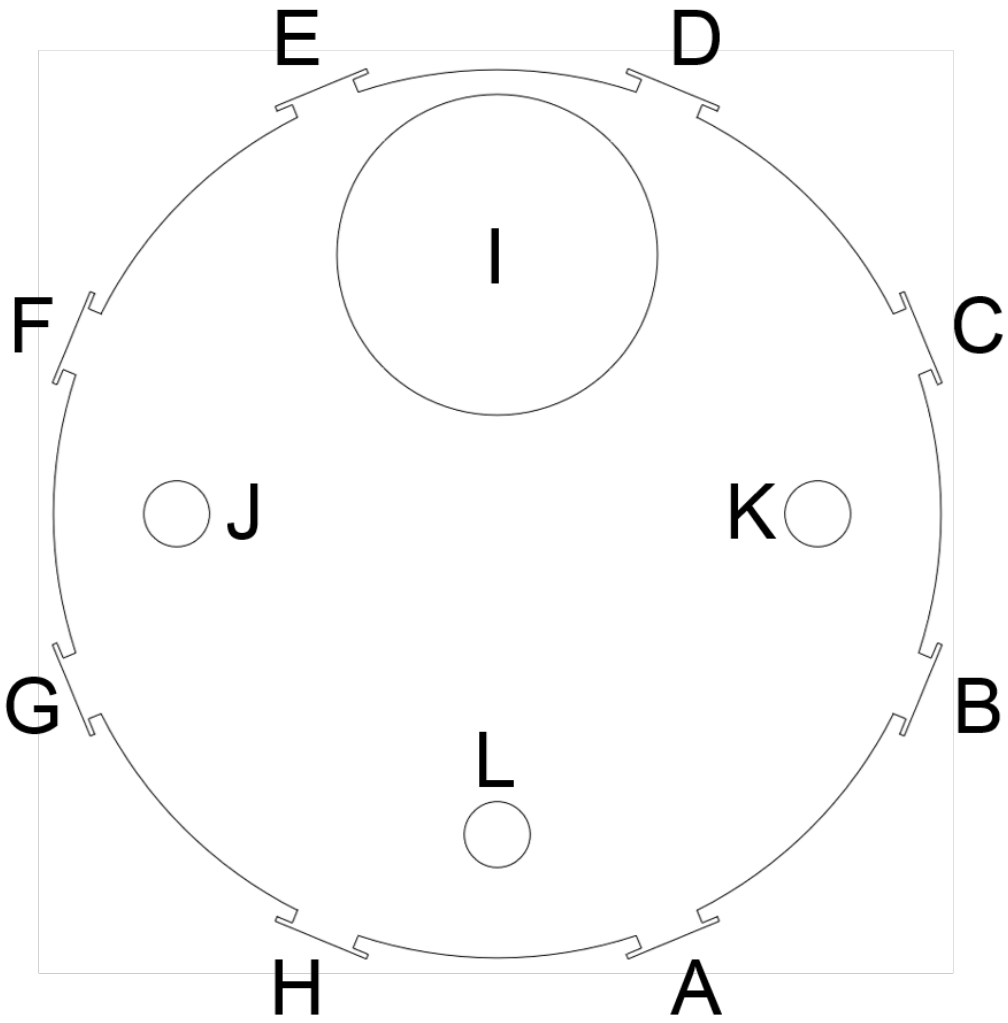

Figure F.1. Top view of Kurt J. Lesker vacuum service well (P/N: SW1808SUQ) with utility ports labeled. These labels correspond to the cable naming convention and service as a reference for easy linking between the physical port location and associated wiring diagrams.

Table F.1. Utility port identification labels for the Kurt J. Lesker service well (P/N: SW1808SUQ). These labels correspond to the cable naming convention and service as a reference for easy linking between the physical port location and associated wiring diagrams. In addition to this, the name/description and part number are given for the feed through installed at each utility port location.

Port:	Name/Description:	Manufacturer:	Part No.:	Port Type:
A	Circular Connector (10 pin)	Kurt J. Lesker	IFDRG107018B	KF 40
B	Type K Push-On (5 TC Pairs)	Kurt J. Lesker	TFT5KP00008B	KF 40
C	BNC Single-Ended (x4)	Kurt J. Lesker	IFTBG042038B	KF 40
D	Circular Connector (32 pin)	Kurt J. Lesker	IFDRG327018B	KF 40
E	Circular Connector (32 pin)	Kurt J. Lesker	IFDRG327018B	KF 40
F	Ionization Vacuum Gauge	Kurt J. Lesker	KJLC392402YD	KF 40
G	Convection Vacuum Gauge	Kurt J. Lesker	KJL275316	KF 40
H	Ferro-Magnetic Rotary F/T	Kurt J. Lesker	KLFDTM025716	KF 40
I*	Turbo Molecular Pump	Osaka Vacuum	TG450FCAB	DN 160 CF
J	Liq. F/T, 1/2" OD, VCO-VCO (x1)	Kurt J. Lesker	LFT8B14MCMC	KF 40
K	Liq. F/T, 1/2" OD, VCO-VCO (x1)	Kurt J. Lesker	LFT8B14MCMC	KF 40
L	High Voltage Power F/T	Kurt J. Lesker	EFT02V5068B	KF 40

Port A: Circular Connector (10 pin)

Insert Arrangement: 12-10

Plug (ATM) P/N: FTACIR10AC

Cabling (ATM): 24 AWG, tinned copper, 3 conductor, FEP insulation, Beldfoil® (100%) + tinned copper braid (85%) shield, FEP jacket - Belden 83503

Plug (VAC) P/N: FTACIR10V

Cabling (VAC): 29 AWG, silver plated copper, 4 conductor, spiral shielded, Teflon® Cable - 10' included leads with FUTEK LSB200 (QSH01649) load cells

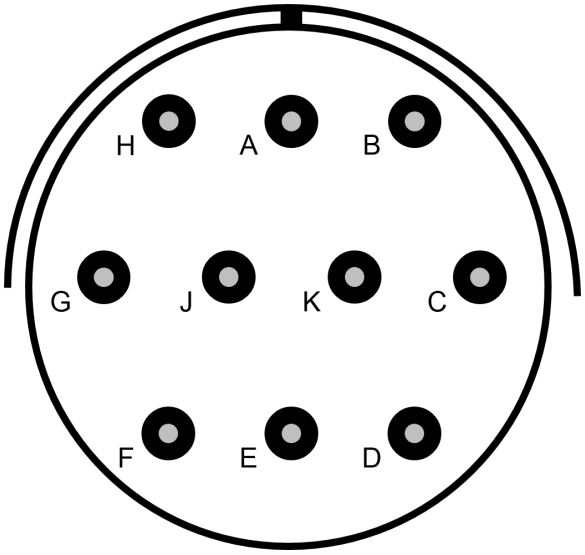

Figure F.2. Pin-out for port A circular connector.

Table F.2. Load cell installation location by S/N. This is important as there is a different calibration for each load cell (cataloged by S/N).

Load Cell No.:	Location:	S/N:
1	Front	690326
2	Right	690325
3	Left	690327

Table F.3. Port A: Pin-out connections and wiring.

Pin:	**VAC Connection:**	**VAC Cable:**	**ATM Connection:**	**ATM Cable:**
A	- EXCITE (LC 1-3)	LC 1-3.Black	HP 6111A.V(-)	ZMETER.A-4 Black
B	GND	LC 1-3.Shields	Shield GND Busbar	ZMETER.A-5 Black
C	- SIGNAL (LC 3)	LC 3.White	Keithley 2700.(7708)-140(-)	ZMETER.A-3 Black
D	+ SIGNAL (LC 3)	LC 3.Green	Keithley 2700.(7708)-140(+)	ZMETER.A-3 Red
E	- SIGNAL (LC 2)	LC 2.White	Keithley 2700.(7708)-139(-)	ZMETER.A-2 Black
F	+ SIGNAL (LC 1)	LC 1.Green	Keithley 2700.(7708)-138(+)	ZMETER.A-1 Red
G	GND	LC 1-3.Shields	Shield GND Busbar	ZMETER.A-5 Red
H	+ EXCITE (LC 1-3)	LC 1-3.Red	HP 6111A.V(+)	ZMETER.A-4 Red
J	+ SIGNAL (LC 2)	LC 2.Green	Keithley 2700.(7708)-139(+)	ZMETER.A-2 Red
K	- SIGNAL (LC 1)	LC 1.White	Keithley 2700.(7708)-138(-)	ZMETER.A-1 Black

Port B: Type K Thermocouple F/T

Push-on Crimp Connectors P/Ns:

Chromel (+): FTATC056C (Lesker)

Alumel (-): FTATC056A (Lesker)

Cabling (ATM): 20 AWG (solid) type-K extension grade thermocouple wire, PVC insulation, PVC jacket. P/N: EXPP-K-20 (Omega)

Cabling (VAC): 24 AWG (solid) type-K (SLE) thermocouple wire, Kapton® insulation, Kapton® jacket. P/N: 5TC-KK-K-24-72 (Omega)

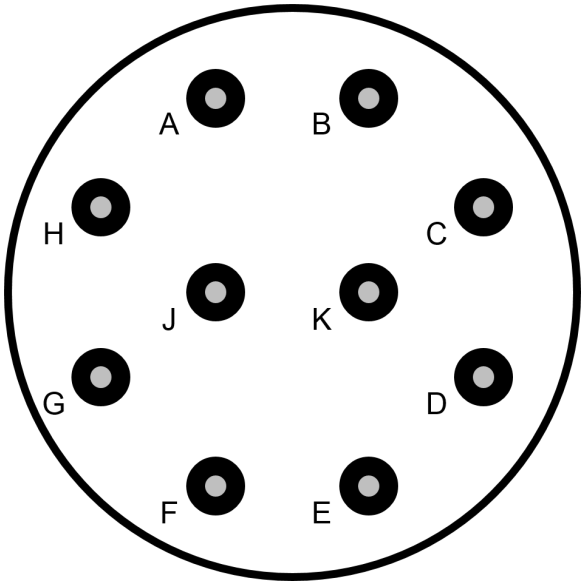

Figure F.3. Pin-out for port B thermocouple F/T.

Table F.4. Port B: Pin-out connections and wiring. Please note: the heater control thermocouple is split at the input connector to the heater control of HWL.101303-23B, and then run to the Keithley.2700.(7708)-117 terminals.

Pin:	**VAC Connection:**	**ATM Connection:**	**ATM Cable:**
A	+ Heatshield Back	Keithley 2700.(7708)-120(+)	ZMETER.B-2 Yellow
B	- Heater Current Lead Insulation	HWL 101303-23B.Limit(-)	ZMETER.B-5 Red
C	+ Heater Current Lead Insulation	HWL 101303-23B.Limit(+)	ZMETER.B-5 Yellow
D	- Trimount Upper (LC Top)	Keithley 2700.(7708)-118(-)	ZMETER.B-4 Red
E	+ Trimount Upper (LC Top)	Keithley 2700.(7708)-118(+)	ZMETER.B-4 Yellow
F	- Trimount Lower (LC Bottom)	Keithley 2700.(7708)-119(-)	ZMETER.B-3 Red
G	+ Trimount Lower (LC Bottom)	Keithley 2700.(7708)-119(+)	ZMETER.B-3 Yellow
H	- Heatshield Back	Keithley 2700.(7708)-120(-)	ZMETER.B-2 Red
J	- Heater Control	Keithley 2700.(7708)-117(-)	ZMETER.B-1 Red
	- Heater Control	HWL 101303-23B.Control(-)	ZMETER.B-1 Red
K	+ Heater Control	Keithley 2700.(7708)-117(+)	ZMETER.B-1 Yellow
	+ Heater Control	HWL 101303-23B.Control(+)	ZMETER.B-1 Yellow

Port C: BNC Single-Ended (x4)

Plug (ATM) P/N: FTABNC (Lesker) [Same as Amphenol RF P/N: 031-2]
Cabling (ATM): 20 AWG Coax (stranded - 19x33) RG-58 A/U - Belden 8259
Plug (VAC) P/N: FTASSC094 (Lesker)
Cabling (VAC): ⌀ 121.92 μm (0.0048 in.) OSI Tungsten hs-86 electrode wire, braided fiberglass insulation sleeve FBGS-N-30-100 (Omega)

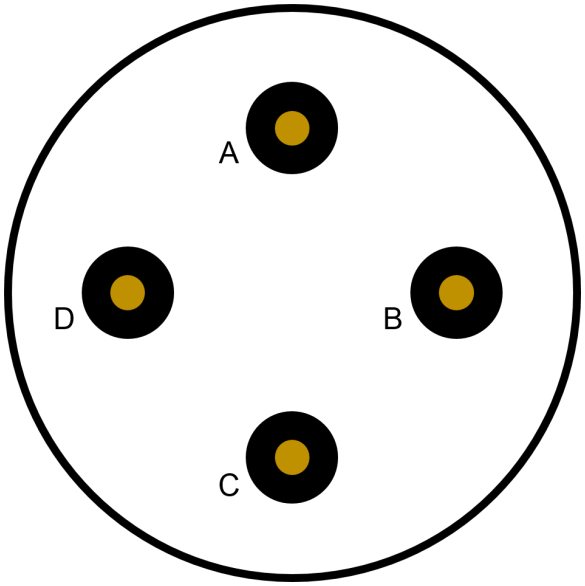

Figure F.4. Pin-out for port C BNC F/T.

Table F.5. Port C: Pin-out connections and wiring.

Pin:	**VAC Connection:**	**ATM Connection:**	**ATM Cable:**
A	Current Lower Bar	Keithley 6221.Guard (Inner Shield)	ZMETER.C-1
B	Current Upper Bar	Keithley 6221.Force (Core)	ZMETER.C-2
C	Voltage Lower Bar	Agilent 3458A.Input.Lo	ZMETER.C-3
D	Voltage Upper Bar	Agilent 3458A.Input.Hi	ZMETER.C-4

Port D: Circular Connector (32 pin)

Insert Arrangement: 18-32

Plug (ATM) P/N: FTACIR32AC (Lesker) [Same as MS3476L18-325 (Deutsch)]

Cabling (ATM): 24 AWG (stranded - 28x0.10) ultra pure oxygen free copper, polypropylene conductor insulation, x8 twisted pairs per cable - individually jacketed (PVC composite) and shielded (24 μm aluminum/polyester foil, $>$ 150%), overall jacket (PVC composite). x2 cables per connector to give x16 twisted pairs per circular connector. Bend radius: 122 mm (4.80 in.). Color Code: IEC 189-2 appendix A

Plug (VAC) P/N: FTACIR32V (Lesker)

Cabling (VAC): 24 AWG (solid), silver plated copper wire

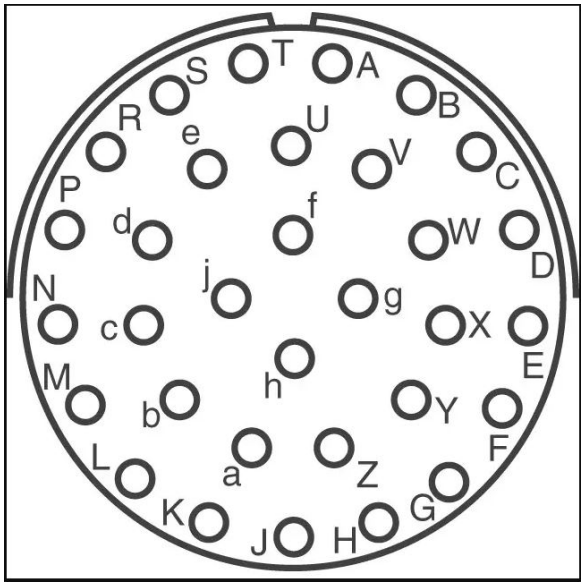

Figure F.5. Pin-out for port D circular connector.

Table F.6. Port D (1/2): Pin-out connections and wiring. Cable conductor designation: CABLE.TWISTED PAIR.COLOR(±)

Pin:	**VAC Connection CJC No.**	**ATM Connection:**	**ATM Cable:**
A	9	Keithley 2700.(7708)-105(+)	ZMETER.D-1.02.white(+)
B	10	Keithley 2700.(7708)-105(-)	ZMETER.D-1.02.orange(-)
C	13	Keithley 2700.(7708)-107(+)	ZMETER.D-1.03.white(+)
D	14	Keithley 2700.(7708)-107(-)	ZMETER.D-1.03.green(-)
E	17	Keithley 2700.(7708)-109(-)	ZMETER.D-1.04.brown(-)
F	18	Keithley 2700.(7708)-109(+)	ZMETER.D-1.04.white(+)
G	23	Keithley 2700.(7708)-112(-)	ZMETER.D-1.05.grey(-)
H	24	Keithley 2700.(7708)-112(+)	ZMETER.D-1.05.white(+)
J	25	Keithley 2700.(7708)-113(-)	ZMETER.D-2.02.orange(-)
K	26	Keithley 2700.(7708)-113(+)	ZMETER.D-2.02.white(+)
L	27	Keithley 2700.(7708)-114(-)	ZMETER.D-2.03.green(-)
M	28	Keithley 2700.(7708)-114(+)	ZMETER.D-2.03.white(+)
N	31	Keithley 2700.(7708)-116(-)	ZMETER.D-2.04.brown(-)
P	32	Keithley 2700.(7708)-116(+)	ZMETER.D-2.04.white(+)
R	3	Keithley 2700.(7708)-102(+)	ZMETER.D-2.05.white(+)
S	4	Keithley 2700.(7708)-102(-)	ZMETER.D-2.05.grey(-)

Table F.7. Port D (2/2): Pin-out connections and wiring. Cable conductor designation: CABLE.TWISTED PAIR.COLOR(±)

Pin:	**VAC Connection CJC No.**	**ATM Connection:**	**ATM Cable:**
T	7	Keithley 2700.(7708)-104(+)	ZMETER.D-1.08.red(+)
U	8	Keithley 2700.(7708)-104(-)	ZMETER.D-1.08.green(-)
V	11	Keithley 2700.(7708)-106(+)	ZMETER.D-1.07.red(+)
W	12	Keithley 2700.(7708)-106(-)	ZMETER.D-1.07.orange(-)
X	19	Keithley 2700.(7708)-110(-)	ZMETER.D-1.06.blue(-)
Y	20	Keithley 2700.(7708)-110(+)	ZMETER.D-1.06.red(+)
Z	21	Keithley 2700.(7708)-111(-)	ZMETER.D-2.08.green(-)
a	22	Keithley 2700.(7708)-111(+)	ZMETER.D-2.08.red(+)
b	29	Keithley 2700.(7708)-115(-)	ZMETER.D-2.07.orange(-)
c	30	Keithley 2700.(7708)-115(+)	ZMETER.D-2.07.red(+)
d	5	Keithley 2700.(7708)-103(+)	ZMETER.D-2.06.red(+)
e	6	Keithley 2700.(7708)-103(-)	ZMETER.D-2.06.blue(-)
f	15	Keithley 2700.(7708)-108(+)	ZMETER.D-1.01.white(+)
g	16	Keithley 2700.(7708)-108(-)	ZMETER.D-1.01.blue(-)
h	2	Keithley 2700.(7708)-101(-)	ZMETER.D-2.01.blue(-)
j	1	Keithley 2700.(7708)-101(+)	ZMETER.D-2.01.white(+)

Port E: Circular Connector (32 pin)

Insert Arrangement: 18-32

Plug (ATM) P/N: FTACIR32AC (Lesker) [Same as MS3476L18-325 (Deutsch)]

Cabling (ATM): 24 AWG (stranded - 28x0.10) ultra pure oxygen free copper, polypropylene conductor insulation, x8 twisted pairs per cable - individually jacketed (PVC composite) and shielded (24 μm aluminum/polyester foil, $>$ 150%), overall jacket (PVC composite). x2 cables per connector to give x16 twisted pairs per circular connector. Bend radius: 122 mm (4.80 in.). Color Code: IEC 189-2 appendix A

Plug (VAC) P/N: FTACIR32V (Lesker)

Cabling (VAC):

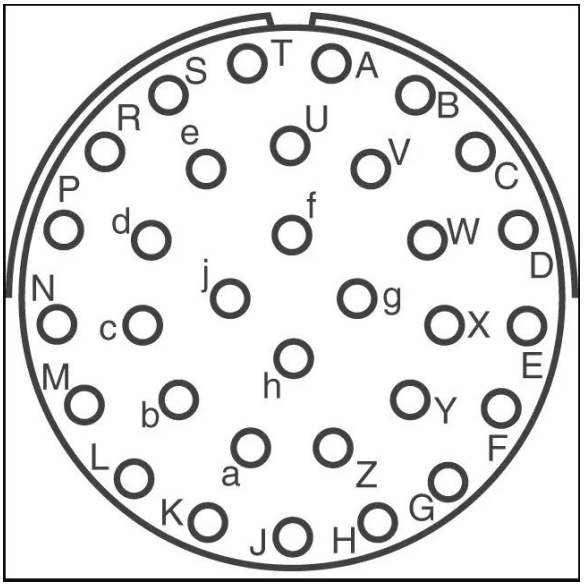

Figure F.6. Pin-out for port E circular connector.

Table F.8. Port E (1/2): Pin-out connections and wiring. RTD assignment designation: RTD.I/V(±). Cable conductor designation: CABLE.TWISTED PAIR.COLOR(±)

Pin:	**VAC Connection RTD No.**	**ATM Connection:**	**ATM Cable:**
A	ii.I(+)	Keithley 2700.(7708)-105(+)	ZMETER.E-1.02.white(+)
B	ii.I(-)	Keithley 2700.(7708)-105(-)	ZMETER.E-1.02.orange(-)
C	i.I(+)	Keithley 2700.(7708)-107(+)	ZMETER.E-1.03.white(+)
D	i.I(-)	Keithley 2700.(7708)-107(-)	ZMETER.E-1.03.green(-)
E	viii.I(+)	Keithley 2700.(7708)-109(-)	ZMETER.E-1.04.brown(-)
F	viii.I(-)	Keithley 2700.(7708)-109(+)	ZMETER.E-1.04.white(+)
G	viii.V(-)	Keithley 2700.(7708)-112(-)	ZMETER.E-1.05.grey(-)
H	vii.I(+)	Keithley 2700.(7708)-112(+)	ZMETER.E-1.05.white(+)
J	vii.I(-)	Keithley 2700.(7708)-113(-)	ZMETER.E-2.02.orange(-)
K	vi.V(-)	Keithley 2700.(7708)-113(+)	ZMETER.E-2.02.white(+)
L	vi.I(-)	Keithley 2700.(7708)-114(-)	ZMETER.E-2.03.green(-)
M	vi.I(+)	Keithley 2700.(7708)-114(+)	ZMETER.E-2.03.white(+)
N	iv.I(-)	Keithley 2700.(7708)-116(-)	ZMETER.E-2.04.brown(-)
P	iv.I(+)	Keithley 2700.(7708)-116(+)	ZMETER.E-2.04.white(+)
R	iii.V(-)	Keithley 2700.(7708)-102(+)	ZMETER.E-2.05.white(+)
S	iii.I(-)	Keithley 2700.(7708)-102(-)	ZMETER.E-2.05.grey(-)

Table F.9. Port E (2/2): Pin-out connections and wiring. RTD assignment designation: RTD.I/V(±). Cable conductor designation: CABLE.TWISTED PAIR.COLOR(±)

Pin:	**VAC Connection RTD No.**	**ATM Connection:**	**ATM Cable:**
T	iii.I(+)	Keithley 2700.(7708)-104(+)	ZMETER.E-1.08.red(+)
U	ii.V(+)	Keithley 2700.(7708)-104(-)	ZMETER.E-1.08.green(-)
V	ii.V(-)	Keithley 2700.(7708)-106(+)	ZMETER.E-1.07.red(+)
W	i.V(+)	Keithley 2700.(7708)-106(-)	ZMETER.E-1.07.orange(-)
X	i.V(-)	Keithley 2700.(7708)-110(-)	ZMETER.E-1.06.blue(-)
Y	viii.V(+)	Keithley 2700.(7708)-110(+)	ZMETER.E-1.06.red(+)
Z	vii.V(+)	Keithley 2700.(7708)-111(-)	ZMETER.E-2.08.green(-)
a	vii.V(-)	Keithley 2700.(7708)-111(+)	ZMETER.E-2.08.red(+)
b	vi.V(+)	Keithley 2700.(7708)-115(-)	ZMETER.E-2.07.orange(-)
c	iv.V(-)	Keithley 2700.(7708)-115(+)	ZMETER.E-2.07.red(+)
d	iv.V(+)	Keithley 2700.(7708)-103(+)	ZMETER.E-2.06.red(+)
e	iii.V(+)	Keithley 2700.(7708)-103(-)	ZMETER.E-2.06.blue(-)
f	v.I(+)	Keithley 2700.(7708)-108(+)	ZMETER.E-1.01.white(+)
g	v.I(-)	Keithley 2700.(7708)-108(-)	ZMETER.E-1.01.blue(-)
h	v.V(-)	Keithley 2700.(7708)-101(-)	ZMETER.E-2.01.blue(-)
j	v.V(+)	Keithley 2700.(7708)-101(+)	ZMETER.E-2.01.white(+)